Fossil Energy Program Annual Progress Report

April 1999 – March 2000

Oak Ridge National Laboratory

ORNL/TM-2000/175

Fossil Energy Program Annual Progress Report for April 1999 Through March 2000

Roddie R. Judkins
Program Manager

Paul T. Carlson
Technical Assistant

July 2000

Prepared for the
DOE Office of Fossil Energy
(AA, AB, AC, AW, AZ, SA)

Prepared by the
OAK RIDGE NATIONAL LABORATORY
Oak Ridge, Tennessee 37831-6285
Managed by
UT-BATTELLE, LLC
for the
U.S. DEPARTMENT OF ENERGY
under Contract DE-AC05-00OR22725

CONTENTS

CONTENTS

CONTENTS

ABREVIATIONS AND ACRONYMS

ABF	aerosol beam focusing
ACRS	acoustic cavity resonance detector
AIChE	American Institute of Chemical Engineers
AIMSI	Advanced Integrated Management Services, Inc.
ANL	Argonne National Laboratory
APCVD	atmospheric pressure chemical vapor deposition
API	American Petroleum Institute
AR	Advanced Research
AR&TD	Advanced Research and Technology Development
ARM	Advanced Research Materials
ASTM	American Society for Testing and Materials
BCC	background-corrected count
BTEXH	benzene, toluene, ethylbenzene, xylenes, and hexanoic acid
CAPP	Canadian Association of Petroleum Producers
CCD	charge-coupled device
CCI	Community College Institute (DOE)
CCT	Clean Coal Technology
CEA	Completion Engineering Association
CFB	circulating fluidized bed
CRADA	cooperative research and development agreement
CSIC	Consejo Superior de Investigaciones Cientificas
CTE	coefficient of thermal expansion
CVD	chemical vapor deposition
CVI	chemical vapor infiltration
D&D	decommissioning and dismantlement
DEA	Drilling Engineering Association
DIPPR®	Design Institute for Physical Property Data
DOE	U.S. Department of Energy
DSC	differential scanning calorimeter
E&P	exploration and production
EBC	environmental barrier coating
ECAS	Environmental Compliance Assistance System
EDS	energy-dispersive spectroscopy
EDX	energy-dispersive X-ray
EIS	environmental impact statement
EPMA	electron probe microanalysis
FEG-SEM	field-emission gun scanning electron microscopy
FIB	focused ion beam
FID	flame ionization detector
GDP	gross domestic product
GRI	Gas Research Institute
HVOF	high-velocity oxy-fuel
ICP/AES	inductively couples plasma atomic emission spectroscopy
INEEL	Idaho Engineering and Environmental Laboratory
JEA	Jacksonville Electric Authority
LIPS	laser-induced plasma emission spectroscopy
MSDS	Material Safety Data Sheet
NEPA	National Environmental Policy Agency
NETL	National Energy Technology Laboratory (DOE)

NGOTP	Natural Gas and Oil Technology Partnership
NIPER	National Institute for Petroleum and Energy Research
NPTO	National Petroleum Technology Office
NROM	naturally occurring radioactive material
ODS	oxide-dispersion strengthened
ORNL	Oak Ridge National Laboratory
OSHA	Occupational Safety and Health Administration
PAH	polyaromatic hydrocarbons
PDF	probability density function
PEG	polyethylene glycol
PERF	Petroleum and Environmental Research Forum
PERF	Petroleum Environmental Research Forum
PM	powder metallurgical
PS	plasma spray
RE	reactive element
SEM	scanning electron microscopy
SEM/EDX	scanning electron microscope/energy-dispersive X-ray
SPR	Strategic Petroleum Reserve
SRS	Savannah River Site
STEM	scanning transmission electron microscopy
TPH	total petroleum hydrocarbons
USGS	U.S. Geological Survey
UV	ultraviolet
VLE	vapor-liquid equilibrium
XRD	X-ray diffraction
XRF	X-ray fluorescence
YAG	yttrium aluminum garnet
YSZ	yttria-stabilized zirconia

FOSSIL ENERGY PROGRAM ANNUAL PROGRESS REPORT FOR APRIL 1999 THROUGH MARCH 2000[1]

Roddie R. Judkins, Program Manager
Paul T. Carlson, Technical Assistant

INTRODUCTION

This report covers progress made at Oak Ridge National Laboratory (ORNL) on research and development projects that contribute to the advancement of fossil energy technologies. Projects on the ORNL Fossil Energy Program are supported by the U.S. Department of Energy (DOE) Office of Fossil Energy, the DOE National Energy Technology Laboratory (NETL), the DOE Fossil Energy Clean Coal Technology (CCT) Program, the DOE National Petroleum Technology Office, and the DOE Fossil Energy Office of Strategic Petroleum Reserve (SPR).

The ORNL Fossil Energy Program research and development activities cover the areas of coal, clean coal technology, gas, petroleum, and support to the SPR. An important part of the Fossil Energy Program is technical management of all activities on the DOE Fossil Energy Advanced Research (AR) Materials Program. The AR Materials Program involves research at other DOE and government laboratories, at universities, and at industrial organizations.

MATERIALS RESEARCH AND DEVELOPMENT

Materials research and development activities at ORNL include development of ceramic composites for high-temperature applications; new alloys with unique mechanical properties for advanced fossil energy systems; development of functional materials, such as ceramic filters, ceramic membranes, activated carbon materials, and solid oxide fuel cell materials; and corrosion research to understand the behavior of materials in coal-processing environments. Transfer of technology developed on this program is enhanced through interactions with industry and by joint research programs with interested end-users.

[1]Research sponsored by the U.S. Department of Energy, Office of Fossil Energy, under contract DE-AC05-00OR22725 with UT-Batttelle, LLC.

ENVIRONMENTAL ANALYSIS SUPPORT

Activities in environmental analysis support included assistance to the NETL at Morgantown and Pittsburgh in reviewing and preparing documents required by the National Environmental Policy Act (NEPA) for projects selected for the CCT Program. An important activity for the CCT Program was the preparation of an environmental impact statement (EIS) for a new circulating fluidized bed (CFB) combustor fueled by coal and petroleum coke to repower an existing steam turbine at JEA's (formerly the Jacksonville Electric Authority's) Northside Generating Station in Jacksonville, Florida.

BIOPROCESSING RESEARCH

Work on the Fossil Energy Bioprocessing Research Program has focused on determining environmentally acceptable endpoints for petroleum hydrocarbon residuals in soil from a risk-based perspective. Various studies have shown that various chemicals present in petroleum hydrocarbon mixtures may be able to permeate into soil particles.

FOSSIL FUEL SUPPLIES MODELING AND RESEARCH

The fossil fuel supplies modeling and research effort focuses on SPR planning and management. Topics covered include planning for an Asian Pacific emergency oil stockpile, reassessing the benefits of expanding the size of the SPR, updating models for SPR risk analysis, and fill-draw planning.

OIL AND GAS PRODUCTION

Research in oil and gas production at ORNL is represented by activities in three research divisions: Chemical Technology, Computer Science and Mathematics, and Environmental Sciences. The areas of study involve enzymatic upgrading of crude oils, physical properties of produced water, measurements of wax points in crude oils and petroleum fluids, an evaluation of the hydrocarbon potential of part of the Appalachian basin, the application of nuclear fuel reprocessing technology to the separation of petroleum and water down hole in an oil well, the application of global optimization methods to residual statics in seismic imaging, in situ characterization of metals in gas and aerosol phases, maintenance of an environmental compliance system, ozone treatment of soluble organics in produced water, the fundamental chemistry of heavy oils and industrial chemicals, advanced techniques for improving the biological quality of petroleum-contaminated soils, an ecological framework to evaluate the impacts of the releases at petroleum exploration and production sites, and the use of neural networks in oilfield parameter estimation.

Related activities include interfaces with the Petroleum Environmental Research Forum (PERF), which supports cooperative research and development of technology for environmental pollution control and waste treatment for the petroleum industry. Nineteen major companies are members of PERF, and they have 22 active projects valued at $40M under way.

HIGH-TEMPERATURE, FIBER-REINFORCED COMPOSITES

T. M. Besmann, R. A. Lowden, J. C. McLaughlin, and E. Lara-Curzio

ABSTRACT

Very high temperature composite materials for fossil-fuel applications will require crystalline reinforcing fibers. The development of SiC fibrils is under way, but these materials are not yet available. It is expected that, unlike polymer precursor-derived fibers, the fibrils will not be weaveable and that short fibers will thus be used. In order to understand fundamental issues related to the use of short fibers, chopped Nicalon-reinforced composites were produced by infiltrating slurry-molded preforms with SiC using forced-flow, thermal gradient chemical vapor infiltration. Issues such as the need for fiber coatings, attainable fiber loading, ultimate density, and mechanical properties were explored.

INTRODUCTION

The goal of producing composites capable of sustaining operations in coal-fired systems to 1400°C will require development of new materials. In particular, there is a need for fiber-reinforced composites that have the refractoriness, strength, and toughness required for applications such as heat exchanger tubes. Currently, tubular shapes can be produced by using forced-flow, thermal-gradient chemical vapor infiltration (CVI) to deposit a SiC matrix throughout a continuous ceramic fiber preform. Such materials can, in principle, meet the requirements of the proposed applications. Currently, however, there are no continuous fiber materials that retain adequate strength to the target temperature range. These fibers are typically prepared from polymer precursors that produce a largely amorphous product. The crystallization of the fibers at high temperatures as well as other interactions that degrade properties make the fibers unsuitable for use at temperatures much above 1100°C. A project within the Fossil Energy Advanced Research Materials Program is developing crystalline SiC fibrils that do not suffer from degradation under these conditions. The fibrils can be multiple centimeters in length; however, they are often not straight and have a very high modulus, which would be expected of crystalline SiC. Therefore, the fibrils cannot be woven into cloth or other forms for producing layups and three-dimensional shapes. It is thus the goal of the current effort that techniques be developed to utilize short fibers to produce composite materials that meet programmatic goals. At this point in the development of SiC fibrils, there is insufficient material for use in developing techniques for producing composites. Therefore, to proceed with development of techniques for producing composite components, other SiC-based fibers prepared from polymer precursors (Nicalon) were used.

EXPERIMENTAL

Chopped fibers with lengths of ~1.3 cm were prepared from ceramic-grade and Hi-Nicalon for use in preforms. These were slurry-molded with polyethylene glycol binder into 10-cm blanks. The blanks were warm-pressed to increase fiber density.

Preforms 4.5 cm in diameter and 0.5 in. thick were cut from the blanks and loaded into graphite holders. The fibers within the preforms were then precoated with carbon by using an isothermal, low-pressure CVI step. The preforms were then densified with SiC by using forced-flow, thermal-gradient CVI. Fiber loadings of 27% were obtained and material with an overall density of 92 vol. % was produced. The samples were characterized by scanning electron microscopy (SEM), and their mechanical properties were evaluated by four-point flexure testing of bars cut from the disks.

RESULTS AND DISCUSSION

Table 1 summarizes the results of properties and testing of the chopped-fiber composites. The fiber loading in excess of 0.2 volume fraction is below that which is typically achieved for cloth layups but is well within the range for dispersed-phase reinforcements. The final void fraction of the infiltrated composites was quite high, larger than those for typical cloth layup materials.

Table 1. Results of the fabrication and testing of the short-fiber composite specimens.

Nicalon Fiber Type	Fiber Vol. Fraction	Carbon Interface Thickness	Final Void Fraction	Avg. Flexure Strength
Ceramic-Grade	0.249	none	0.08	68±12 MPa
Hi-Nicalon	0.210	~300 nm	0.13	227±29 MPa
Hi-Nicalon	0.263	~200 nm	0.12	205±30 MPa

The carbon interface thickness was intentionally varied in order to determine whether interface coatings were needed and to make an initial determination as to whether thickness variation produced noticeable effects. Fig. 1 is a typical flexure curve for the ceramic-grade Nicalon samples that had no interface coating. The curve is representative of brittle fracture with no fiber pull out. The very low strength of this material (see Table 1) indicates that not only was the material brittle, but it is likely that the fibers were attacked by the chloride-containing forced-flow CVI precursors, causing them to lose strength.

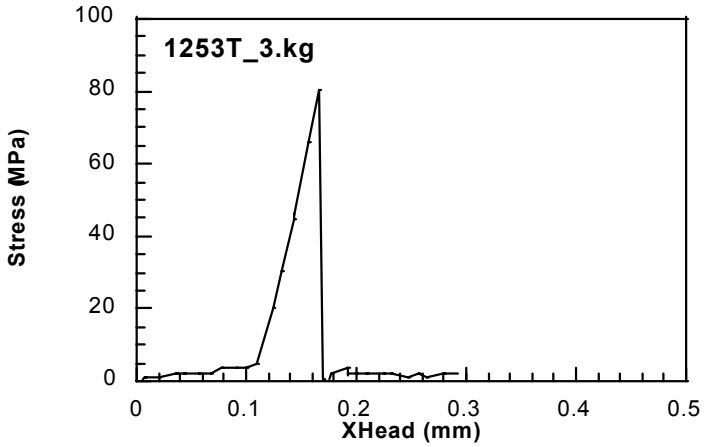

Fig. 1. Flexure curve for a ceramic-grade Nicalon sample with no carbon interface coating.

Facture surfaces for a ceramic-grade Nicalon sample are seen in Fig. 2. The densification has proceeded well, filling much of the inter-fiber volume. There is little pull-out, with the matrix fracture surfaces appearing to be relatively in-plane with the sheared fibers. Pull out lengths are well below the values of the fiber diameter, indicating brittle failure, as confirmed by the flexure curves. The surface features were uniform across fracture surfaces, indicating that the material had volumetrically isotropic properties.

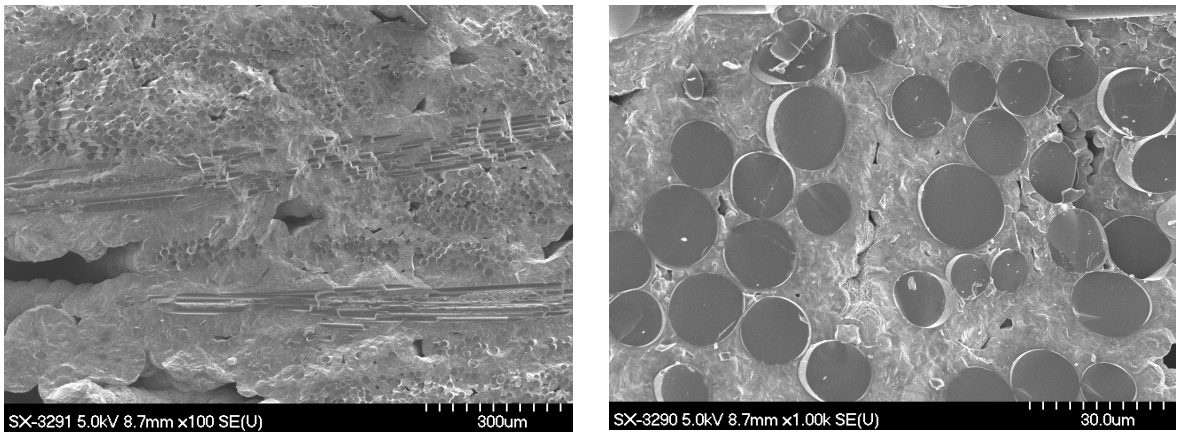

Fig. 2. Fracture surfaces of ceramic-grade Nicalon samples.

A typical flexure curve for the Hi-Nicalon samples is seen in Fig. 3. The curves were not discernibly different for the samples with fibers coated by ~200 or ~300 nm of carbon. The substantial strain-to-failure indicates that the material is relatively tough and displays significant fiber pullout. The strengths were also fairly high, indicating that the fibers retained much of their properties.

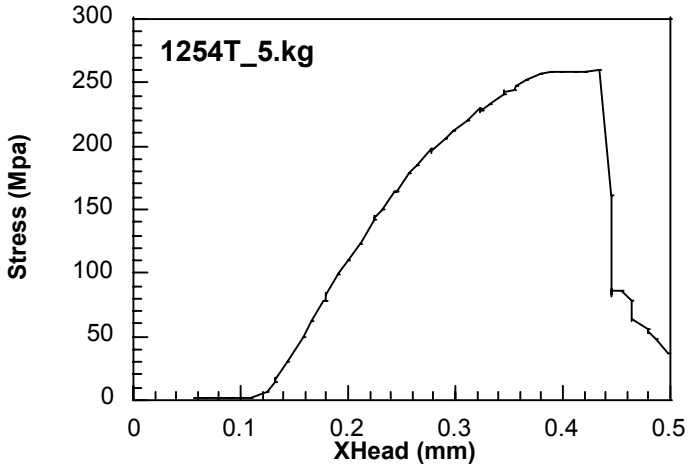

Fig. 3. Flexure curve for a typical Hi-Nicalon sample, indicating substantial strain tolerance.

The fracture surfaces of the Hi-Nicalon samples indicate considerable pull out, as expected from the nature of the flexure curves (Fig. 4). The pull out is seen uniformly across fracture surfaces, indicating relatively uniform fiber coatings, and therefore relatively uniform material properties. Pull out lengths are multiples of the fiber diameter but are not exceptionally long. This indicates that they are probably nearly optimal for maximizing toughness and strength.

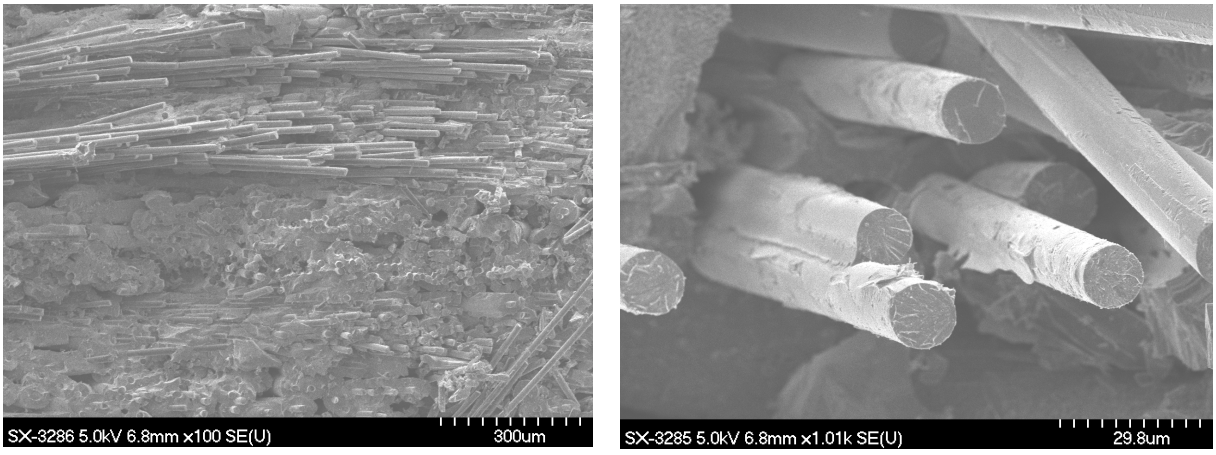

Fig. 4. Fracture surfaces of Hi-Nicalon samples.

CONCLUSIONS

The current work demonstrates that composites with attractive mechanical properties can be prepared from short-fiber preforms. Fiber loadings, while relatively modest, were sufficient to convey the toughness of the material. Fiber interface coatings were required to retain the properties of the polymer precursor-derived fibers and to allow for fiber pull out. It remains to be demonstrated whether this will remain so when crystalline SiC fibrils are used.

CORROSION-RESISTANT Si-BASED COMPOSITES

R. A. Lowden, B. L. Armstrong, J. C. McLaughlin, D. A. Butz, and J. McDavid

BACKGROUND

Silicon carbide-based materials in the form of sintered SiC, siliconized SiC, or SiC-matrix composites are being examined for use in components such as heat exchangers or hot-gas filters for industrial waste incinerators and advanced fossil- or biomass-fueled power systems. Silicon-based ceramics are typically protected by a slow-growing silica surface scale that limits oxygen diffusion and thus prevents further attack of the substrate. Unfortunately, these SiO_2 scales are susceptible to volatilization by high-temperature reactions with water vapor and fluxing by hot corrosion in the presence of alkali salt deposits, such as molten Na_2SO_4. The long-term durability of Si-based ceramic components is thus limited, necessitating the use of protective coatings or the development of materials with improved stability in these harsh environments.

In order to utilize the attractive properties of SiC, systems are being developed that combine oxide and non-oxide ceramics to take advantage of the properties of both families of materials. For example, oxide ceramic coatings are being deposited on SiC and silicon nitride ceramics to protect the bulk materials from corrosion. The oxide coatings commonly called “environmental barrier coatings (EBCs), however, do not completely prevent oxygen diffusion and thus a silica layer is formed between the substrate and protective oxide coating. It is believed that the silica layer will continue to grow with time, albeit very slowly, and eventually will cause the protective coatings to fail and spall during thermal cycling.

One solution to this is the development of Si-based coatings and/or matrices that form protective oxides other than silica. It is hypothesized that composite coatings of SiC and compounds containing aluminum such as aluminum nitride, would form aluminosilicate surface layers upon oxidation. The composition would be optimized to produce mullite, which is chemically and mechanically stable in contact with SiC. The SiC composite coatings would be deposited employing chemical vapor deposition (CVD) techniques and thus could be used as a surface layer, as the matrix, or as a bond coat. Other possible compositions include SiC and Si_3N_4 with additions of hafnium, zirconium, and other metals that would form silicates that are compatible with SiC-based materials. The deposition of SiC and Si_3N_4 composite coatings is being pursued. Thermochemical analysis of the deposition of these composite coatings has been conducted to determine deposition “windows.” A furnace has been modified to permit the introduction of the necessary reactants. Initial experiments involving the introduction of aluminum-containing compounds to SiC are being conducted.

Another approach to improving the environmental stability of these materials is to not simply apply a surface layer, but to substitute an oxide material for a portion of the matrix. In the preferred embodiment, the oxide is used as the final portion of the matrix (i.e., the material nearest to the surfaces and most likely to be exposed to an external atmosphere). A skeletal structure of SiC fibers, interface coating, and SiC matrix is formed but not fully densified. The open porosity is then filled with an oxide that is thermochemically and thermomechanically compatible with the bulk material. This approach is similar in many ways to the silicon melt infiltration process. The process overcomes some of the concerns associated with thin external coatings, although a final seal coating may be necessary to completely close surface porosity. Oxides such as mullite, zircon, and selected phosphates are suitable candidates. Chemical vapor deposition has been used to infiltrate porous substrates with oxides; however, the process is very slow. Alternate techniques such as sol-gel and slurry impregnation are better suited for infiltration of the large pores with oxide ceramics and are thus being explored.

Initially, the impregnation of SiC composites with mullite is being examined. Variations in powder particle size, infiltration technique, and processing conditions are being investigated. Early efforts are focusing on uniformity of infiltration and corrosion resistance. Once these factors are optimized for mullite, other oxides will be examined, and processing conditions will be varied for maximum retained strength.

INTRODUCTION

Recent exposures of SiC/SiC composites and monolithic Si_3N_4 to actual and simulated combustion environments (e.g., engine tests at Solar Turbines and in the ORNL steam rig) have revealed unacceptable levels of corrosion, and thus significantly reduced lifetimes for components.[1] The rapid recession rates were attributed to a combination of elevated temperature (1200°C), high pressure (10 atm), and the presence of water vapor (~15 %), which accelerates the corrosion process through a number of mechanisms. Under these conditions (burning of natural gas), the integrity of the SiC/SiC composite component would be rapidly compromised. The presence of additional contaminants found in other fuels would only exacerbate the problem.

Thus the development of protective coating systems has become essential for enabling the long-term application of SiC, Si_3N_4, and SiC/SiC components in combustion environments. Recent efforts in the development of EBCs have focused on oxide surface layers. Numerous factors, such as thermal expansion and chemical compatibility and stability, must be considered in the selection of the appropriate oxide composition.[2] Because of these requirements, the majority of the candidates for EBCs for the protection of Si-based ceramics and composites are from the aluminosilicate family of oxide ceramics.

Many of the materials have been evaluated in other programs, with promising results found for materials such as mullite ($Al_6Si_2O_{13}$) and celsian.[3,4] Plasma-sprayed systems containing these materials are being investigated for protecting SiC/SiC composites from corrosion in the gas turbine environment. The EBC systems of current interest are complex combinations of materials with multiple layers and mixtures of materials. The utilization of EBCs for protecting ceramics is a relatively new concept; thus, much must be done to fully understand the processing, stability, and performance of these systems.

An issue of concern regarding oxide EBCs applied to silicon-containing ceramics and ceramic composites is the formation of silica at the EBC-substrate interface. An oxide EBC cannot prevent oxygen diffusion to the substrate. Formation of a silica layer at this boundary is inevitable. This layer will become a weak link in the system. Silica is not thermochemically or thermomechanically stable in the given systems. Cracks will form in this layer and will eventually cause spalling and failure.

A solution is the utilization of a matrix or bond coating that forms a more thermochemically and thermomechanically stable compound upon oxidation. Silicates such as mullite and zircon are being investigated as EBCs and thus meet the necessary criteria. It is hypothesized that the silicon-based ceramics such as SiC and Si_3N_4 could be combined with aluminum- or zirconium-containing materials to produce composites that form adherent and compatible scales. Upon oxidation these composites would form layers of mullite or zircon and not silica, creating a more stable system. It may be possible to produce a material that is self-protecting and does not need an EBC.

TECHNICAL APPROACH

A review and an analysis of the thermochemical stability of materials of interest and mixtures thereof were conducted to examine the potential to form oxide scales other than silica (Table 1). Desired compositions include mixtures of silicon carbide and aluminum nitride, and silicon nitride and aluminum nitride. There are many concerns regarding the corrosion of mixtures of materials, such as preferential oxidation of one phase over another. In the given systems, the AlN could oxidize more quickly than the Si-containing ceramics, which may prevent the formation of mullite or cause cracking and failure during thermal cycling. Therefor it is also difficult to form mullite from silica and alumina therefore if these phases form separately; the subsequent formation of mullite would not be possible. Mullite should be formed during the oxidation of mixtures of SiC + AlN and Si3N4 + AlN (see Table 1). In addition, it appears that mullite will also form for mixtures of alumina and SiC, thus alleviating concerns regarding preferential oxidation in the SiC + AlN system.

Hot-pressed mixtures of SiC + AlN and Si_3N_4 + AlN were prepared to examine the feasibility of forming a mullite scale during oxidation. Compositions containing the appropriate amounts of silicon and aluminum necessary to form stoichiometric mullite were selected. Powders were blended and

hot-pressed employing typical ceramic processing techniques and under conditions usually used for the given materials. Test specimens were cut and ground and were oxidized in air at temperatures from 950 to 1350°C.

Reaction	ΔHf	ΔGf
$2\ Al + 3/2\ O_2 = Al_2O_3$	-1125.2	-797.5
$Si + O_2 = SiO_2$	-899.0	-644.5
$Zr + O_2 = ZrO_2$	-1082.7	-816.6
$2\ AlN + 3/2\ O_2 = Al_2O_3 + N_2$	-686.4	-593.4
$SiC + 2\ O_2 = SiO_2 + CO_2$	-215.4	-93.4
$Si_3N_4 + 3\ O_2 = 3\ SiO_2 + 2\ N_2$	-217.9	-187.2
$ZrC + 2\ O_2 = ZrO_2 + CO_2$	-245.2	-118.2
$2\ SiC + 6\ AlN + 17/2\ O_2 = Al_6Si_2O_{13} + 2\ CO_2 + 3\ N_2$	**-462.6**	**-360.7**
$2\ Si_3N_4 + 18\ AlN + 39/2\ O_2 = 3\ Al_6Si_2O_{13} + 11\ N_2$	**-224.5**	**-195.6**
$SiC + ZrC + 4\ O_2 = ZrSiO_4 + 2\ CO_2$	-236.5	-105.9
$Si_3N_4 + 3\ ZrN + 6\ O_2 = 3\ ZrSiO_4 + 7/2\ N_2$	-233.3	-192.0
$2\ SiC + 3\ Al_2O_3 + 4\ O_2 = Al_6Si_2O_{13} + 2\ CO_2$	**-210.8**	**-98.9**

Table 1. A review of the thermochemical information for materials of interest
[Values for 1200°C in kJ/mole]

The ultimate product of this research is a CVD coating or matrix that forms mullite upon oxidation. Thermochemical analysis of the CVD of mixtures of SiC + AlN and Si_3N_4 + AlN was conducted employing SOLGASMIX-PV. Deposition phase diagrams were calculated for gas mixtures containing methyltrichlorosilane (CH_3SiCl_3 or MTS), aluminum trichloride ($AlCl_3$), ammonia (NH_3), and hydrogen (H_2) or silicon tetrachloride ($SiCl_4$), methane (CH_4), $AlCl_3$, NH_3, and H_2 for SiC + AlN; and $SiCl_4$, $AlCl_3$, NH_3, and H_2 for Si_3N_4 + AlN. Gas ratios and concentrations similar to those used for the chemical vapor infiltration of SiC were used in the analysis. A total of 231 points was calculated for each diagram using 6 elements, 87 gas species, and 14 condensed phases. Temperatures from 500 to 1500°C and pressures of 50, 100, and 745 torr were examined.

RESULTS AND DISCUSSION

Powder mixtures containing SiC + AlN and Si_3N_4 + AlN were readily hot-pressed to densities approaching 100%. Specimens from the compacts were heated in air to temperatures of 950, 1204, and 1350°C and for times as long as 160+ h. Post-treatment analysis of the specimen surfaces by X-ray diffraction found mullite as noted by the double peaks at ~ 26° 2θ (Figs. 1 and 2). Alumina was found at the surface of the SiC + AlN specimens heated at lower temperatures and shorter times. Mullite began to

form as temperature and time were increased. Only mullite was observed at the surface of the Si_3N_4 + AlN mixtures regardless of treatment (Fig. 2).

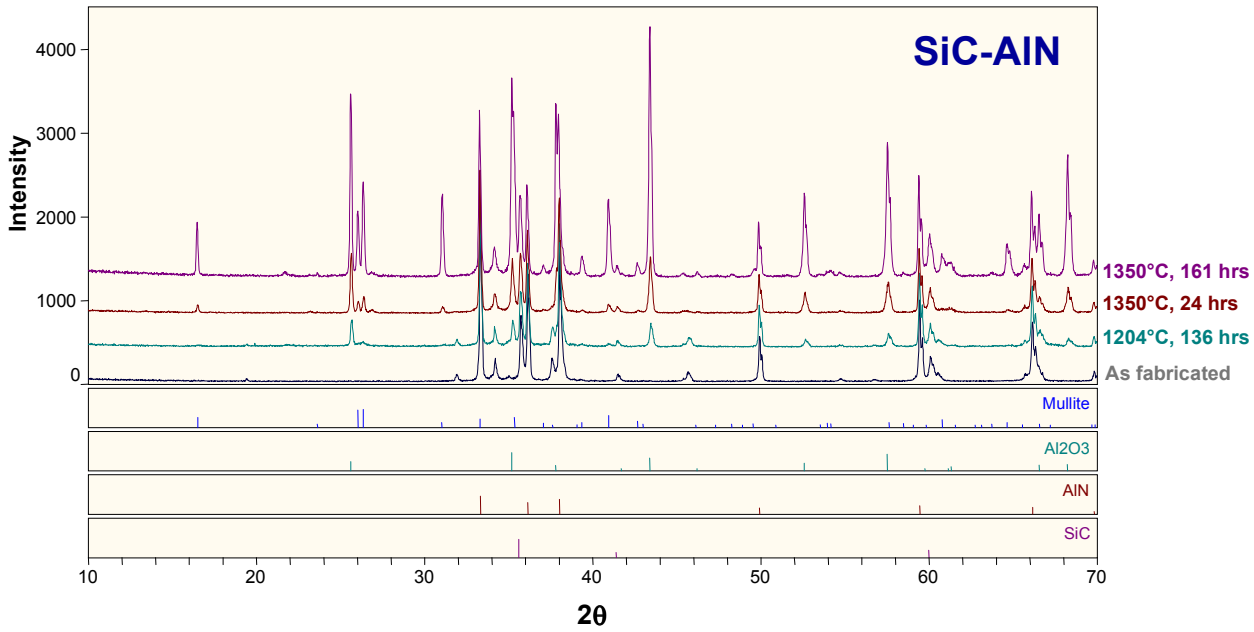

Fig. 1. X-ray diffraction analysis of hot-pressed SiC + AlN samples after exposure to air at different temperatures and for varying times.

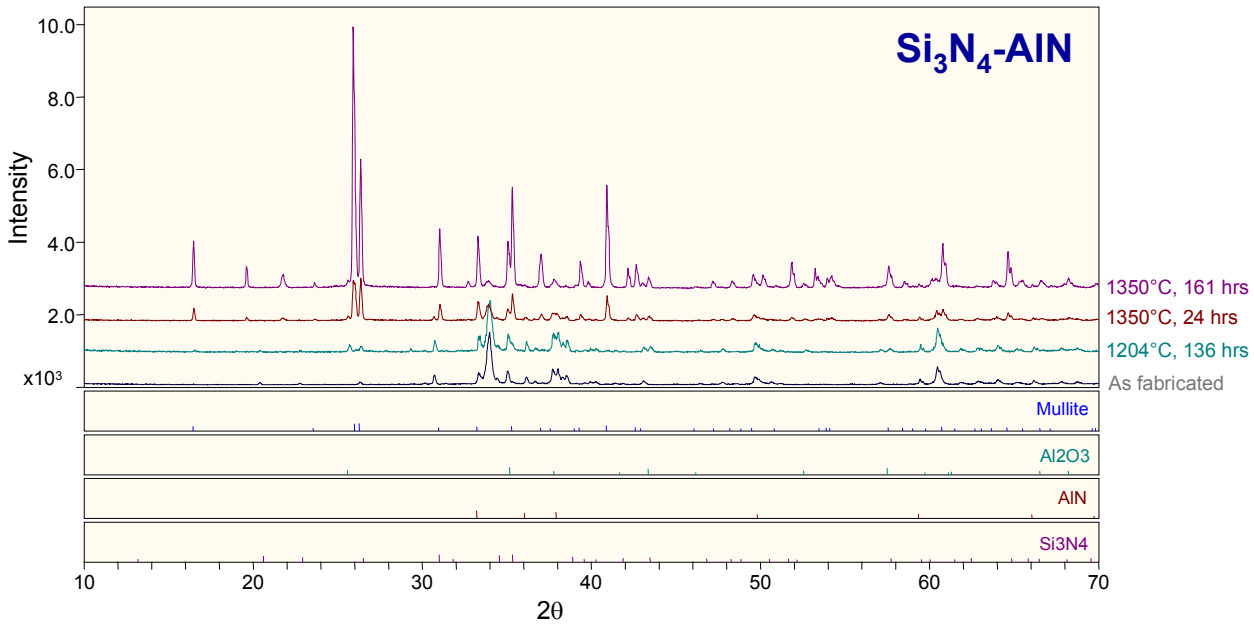

Fig. 2. X-ray diffraction analysis of hot-pressed Si_3N_4 + AlN samples after exposure to air at different temperatures and for varying times.

Thermochemical equilibrium analysis of the CVD of SiC +AlN and Si_3N_4 + AlN revealed windows of opportunity for the fabrication of coating with the desired compositions (Figs. 3 and 4). The calculations predict large regions of potential for the Si_3N_4 + AlN system deposited produce and from gas mixtures containing $SiCl_4$, $AlCl_3$, NH_3, and H_2 (Fig. 3). Although the results presented in Fig. 3 are for a pressure of 50 torr, similar regions were found for other pressures.

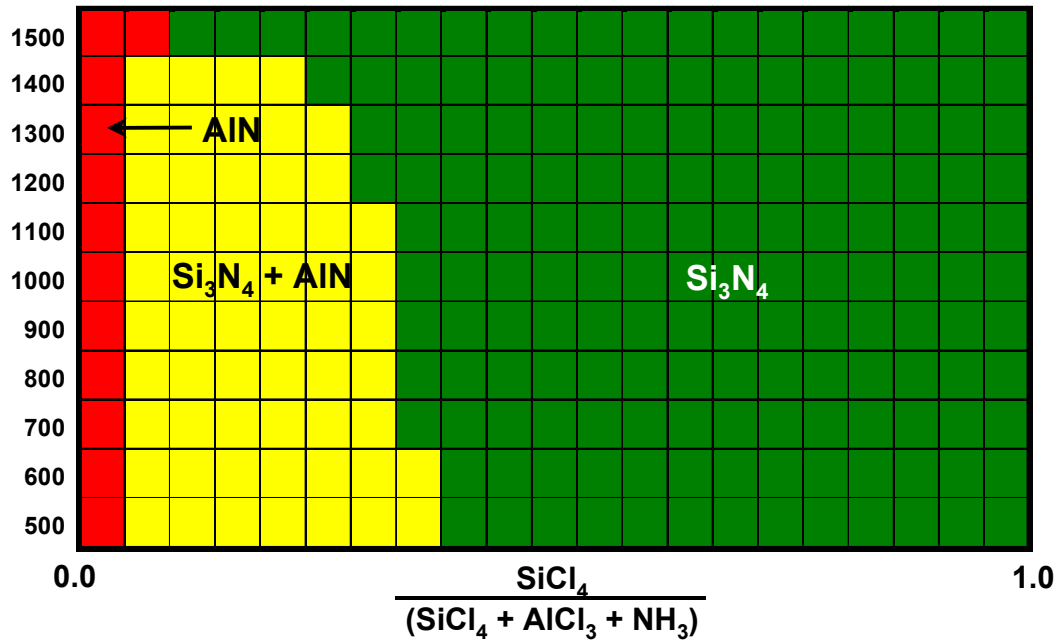

Fig. 3. Thermochemical equilibrium analysis of the deposition of Si_3N_4 + AlN at 50 torr from gas mixtures containing $SiCl_4$, $AlCl_3$, NH_3, and H_2.

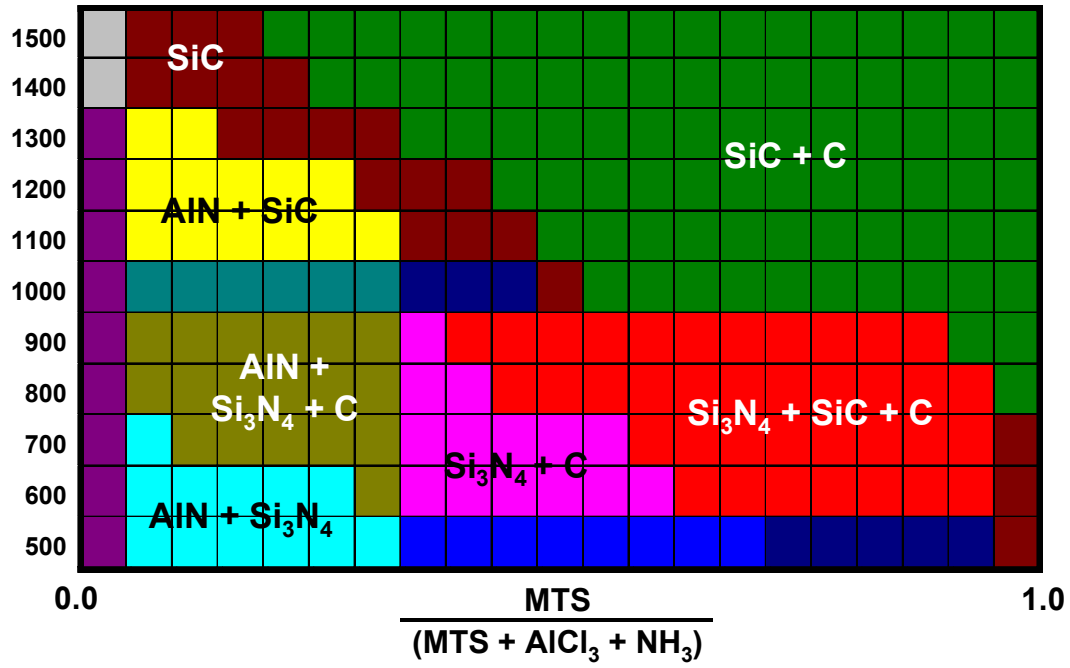

Fig. 4. Thermochemical equilibrium analysis of the deposition of SiC + AlN at 50 torr from gas mixtures containing MTS, $AlCl_3$, NH_3, and H_2.

The results for the SiC + AlN system are more interesting. Small regions of opportunity for the deposition of the desired composition from mixtures containing MTS, $AlCl_3$, NH_3, and H_2 are predicted (Fig. 4). The formation of Si_3N_4 is preferred at low carbon concentrations; thus additional calculations were performed to explore higher carbon concentrations. This would be accomplished experimentally by adding methane to the reactant gas mixture. The addition of extra carbon expanded the region in which SiC + AlN should deposit. A furnace with the appropriate gas-handling and chlorination systems has been constructed to investigate the deposition of the desired coating compositions. The results of the thermochemical analysis will be used to guide the experiments.

CONCLUSIONS

Si-containing ceramics are not stable in many combustion environments. The "protective" silica layer that forms on the surface in oxidizing atmospheres and inhibits further attack of the underlying material can be volatilized in the presence of moisture or react with other compounds to form low-viscosity glasses. Oxide surface layers or coatings, now called "environmental barrier coatings" (EBCs), are being examined to extend the life of Si-containing ceramics in hazardous environments. Unfortunately, EBCs do not prevent the diffusion of oxygen to the surface of the substrate, and the silica that forms at the EBC-bond coat or substrate interface for Si-containing ceramics and composites will limit component life and will degrade performance. Modifications to the substrate surface or bulk materials are being examined. The enhancements are designed to produce materials that form oxides other than silica in corrosive environments and involve the addition of Al- and Zr-containing compounds to Si-based ceramics. Compositions that form mullite, such SiC + AlN and Si_3N_4 + AlN, are of primary interest. Initial efforts utilized hot-pressed mixtures to prove feasibility. Mullite was easily formed on the specimens through oxidation in air. CVD and other techniques are also being investigated to provide flexibility in processing and expanded applicability. Thermochemical analysis of the CVD of the aforementioned mixtures revealed conditions that should produce coatings with the desired compositions.

ACKNOWLEDGMENTS

This project is being conducted in collaboration with the Supporting Technologies Task of the CFCC Program.

REFERENCES

1. K. L. More, P. F. Tortorelli, M. K. Ferber, and J. R. Keiser, "Observations of Accelerated Oxidation of SiC at High Water Vapor Pressures," *J. Am. Ceram. Soc*. in press.
2. K. N. Lee and R. A. Miller, "Development and Environmental Durability of Mullite and Mullite/YSZ Dual Layer Coatings for SiC and Si_3N_4 Ceramics," *Surface Coating Technology* **86**[87] 142-148 (1996).

3. K. L. More et. al., "Exposure of Ceramics and Ceramic Matrix Composites in Simulated and Actual Combustor Environments," ASME Paper 99-GT-292, American Society of Mechanical Engineers, New York, 1999.
4. J. A. Haynes, M. J. Lance, K. M. Cooley, M. K. Ferber, R. A. Lowden, and D. P. Stinton, "CVD Mullite Coatings in High-Temperature, High-Pressure Air-H_2O," *J. Am. Ceram. Soc.* **83**[3], 657-659 (2000).

ADVANCED STAINLESS STEELS FOR RECUPERATOR APPLICATIONS

R. W. Swindeman, P. J. Maziasz, and B. A. Pint
J. P. Montague, Solar Turbines, Inc. San Diego, CA

INTRODUCTION

Basic concepts of alloy design and fabrication technology are being applied to the development of high-performance recuperator materials for simple-cycle gas turbines systems. A cooperative research and development agreement (CRADA) with Solar Turbines, Inc., for this purpose has two goals. The first goal is to enhance the strength of type 347 stainless steel foil to permit an extension of the operating conditions for existing designs to long times at 650°C. The second goal is to develop a stainless steel with improved strength and oxidation resistance that will permit an increase in operating temperature beyond 650°C.

DISCUSSION OF CURRENT ACTIVITIES

The activities had three thrust areas. These included (1) alloy design and fabrication technology, (2) corrosion, and (3) mechanical behavior. Type 347 stainless steel and advanced stainless steels were included in each thrust area.

Several modifications of type 347 stainless steel were examined to explore the influence of chromium, nickel, niobium, and carbon. Sheets produced from the experimental compositions were processed together with commercial material to produce 0.1-mm foils of varying grain size and microstructure. Products with microstructures judged to be optimum for recuperator fabrication were then selected for further evaluation. Experimental alloys were produced for comparison with higher chromium alloys such as 20Cr-25Ni-Nb stainless steel and 310 stainless steel. Again, processing variables were examined to permit the selection of microstructures judged to be optimum with respect to commercial fabrication schedules.

Corrosion studies included studies of oxidation in dry air and in moist air containing several concentrations of water vapor. Cyclic oxidation tests were conducted to beyond 7000 h over a temperature range needed to accelerate oxidation rates while preserving the appropriate oxidation mechanism. Models capable of predicting oxidation lifetime were developed for the 347 stainless steel. Work was begun to develop similar models for the higher chromium steels.

Creep tests were performed on foil specimens. Testing was in the range of 677 to 732°C, and times for the strong alloys were extended to well beyond 10,000 h. It was found that foils from materials with optimized microstructures exhibited creep strengths that exceeded the requirements for the primary goal (650°C operation).

Efforts were made to adjust the composition and fabrication schedules for optimum properties, and a portion of a commercial heat of 347 stainless steel meeting the target composition was processed according to recommended schedules. Samples from the commercial heat were scheduled for testing before the termination of the CRADA. A small heat of an advanced higher chromium stainless steel was ordered.

Activities on this CRADA are scheduled for completion by the end of the fiscal year. The technology will be transferred to parallel research in support of microturbine development.

DEVELOPMENT OF ADVANCED CORROSION-RESISTANT Fe-Cr-Ni AUSTENITIC STAINLESS ALLOY WITH IMPROVED HIGH-TEMPERATURE STRENGTH AND CREEP RESISTANCE

P.J. Maziasz and R.W. Swindeman M. Harper, G.D. Smith, and H.W. Sizek, Special Metals, Inc.

INTRODUCTION

Improving the combination of oxidation/corrosion resistance and high-temperature strength for austenitic stainless alloys for heat-exchanger tubing applications is an essential part of any strategy for achieving improved efficiency for fossil power generation. Alloy 803 is an improved alloy developed recently by INCO (now Special Metals, Inc.), with more Cr and Ni than the alloy 800 group of alloys (800H and 800HT) for better oxidation and corrosion resistance, but with enough Fe to keep it relatively cost-effective[1]. This cooperative research and development agreement (CRADA) project, begun in February 1999, is a direct result of INCO's now Special Metals, Inc.'s desire to impart microstructure-based improvements in creep-resistance into the 803 base alloy that were similar to those achieved by ORNL investigators on somewhat similar alloys for different applications[2,3,4]. Alloy 803 is a wrought high-performance Fe-25Cr-35Ni austenitic stainless alloy with very good oxidation and carburization resistance that has use for piping and tubing in chemical and petrochemical processing applications as well as fossil energy applications.

PROGRESS AND RESULTS

An initial set of modified 803 alloy compositions were identified relative to the 803 base material, and six alloys were vacuum-melted and cast as 4-in.-diameter bars at Special Metals. These were then homogenized and hot-worked into plate at Special Metals, and then processed further into cold-finished plate at ORNL. Microcharaterization was conducted at ORNL, and oxidation and mechanical properties testing was performed at Special Metals. The high-temperature corrosion testing of the new alloys showed that two alloys were much better than the other six, and that these two modified alloys had similar oxidation and carburization resistance but reduced sulfidation resistance relative to the unmodified 803. Initial creep-rupture screening of the new alloys at 1500°F and 10 ksi showed that the same two new alloys were much better than the others and were similar to the unmodified 803 alloy, but with improved rupture ductility. These two modified alloys were given another modified processing schedule at ORNL, which then boosted the improvements in creep-rupture resistance and ductility, depending

on the details of the modified processing. These upgrades, termed 803mod1 and 803mod2, ranged from 2 to15 times more rupture resistant, with rupture ductility of 50% or more. Microstructural analysis of aged and of creep-tested specimens clearly confirmed that differences in precipitation behavior within the grains and at grain boundaries during high-temperature exposure were responsible for the relative better strength of 803mod1 and 803mod2 after the initial processing experiments. Analysis of the modified alloys after subsequent processing experiments is in progress.

Based on these initial, successful results, a second set of alloys having minor alloy compositional modifications based on the 803mod1 and 803mod2 alloys were cast and processed into plate and are currently being evaluated in creep and corrosion screening tests. This project will assess the potential for scale-up, and will identify critical field tests for in-service evaluation of corrosion resistance for the next year.

MILESTONES

The milestone (ORNL 5(L)-1) this year of providing final processing for six new modified heats of alloy 803 produced at Special Metals, and of characterizing the microstructures of those modified alloys after processing and short-term aging was achieved as scheduled on November 30, 1999.

REFERENCES

1. P. Ganesan, J. A. Plyburn, and C. S. Tassen, "Incoloy Alloy 803, A Cost Effective Alloy for High Temperature Service," pp. 191-198 in *Heat-Resistant Materials II*, eds. K. Natesan, P. Ganesan, and G. Lai, ASM-International, Materials Park, Ohio (1995).
2. R.W. Swindeman and P. J. Maziasz, "The Mechanical and Microstructural Stability of Austenitic Stainless Steels Strengthened by MC-Forming Elements," pp. 33-42 in *Creep: Characterization, Damage and Life Assessment*, ed. D. A. Woodford, C. H. A. Townley, and M. Ohnami, ASM-International, Materials Park, Ohio (1992).
3. R. W. Swindeman and P. J. Maziasz, "The Effect of MC Forming Additions and 10% Cold Work on the High Temperature Strength of 20Cr-30Ni-Fe Alloys," pp. 251-259 in *Heat-Resistant Materials,* eds. K. Natesan and D. J. Tillack, ASM-International, Materials Park, Ohio (1991).
4. P. J. Maziasz, R. W. Swindeman, J. P. Montague, M. Fitzpatrick, P.F. Browning, J. F. Grubb, and R. C. Klug, "Improved Creep-Resistance of Austenitic Stainless Steels for Compact Gas-Turbine Recuperators," *Materials at High Temperatures* **16**(4) 207-212 (1999).

DEVELOPMENT OF IRON ALUMINIDES

M. L. Santella, R. E. Howell, E. A. Franco-Ferreira, and G. M. Goodwin

INTRODUCTION

Iron-aluminum alloys, particularly those near and above the Fe_3Al composition (14-24 wt % Al), have exceptional environmental resistance to reducing and oxidizing atmospheres. Their environmental resistance properties coupled with their low cost relative to stainless steels and nickel-based alloys has created interest in using Fe_3Al alloys in various fossil energy applications such as boilers. Unfortunately, their low strength, low creep resistance, and limited ductility from ambient to moderately elevated temperatures limits their use as structural alloys. However, the environmental resistance of the Fe_3Al alloys can still be exploited by using them as claddings on low alloy steels as is commonly done with stainless steels and nickel-based alloys. Boiler tube cladding is often done by welding processes, and it is known that weld overlay claddings with up to 10 wt % Al can be produced with relative ease. Weld deposits with higher than 10 wt % Al are highly susceptible to cracking.

Published data from corrosion tests show that low alloy steels that were weld clad with 5 to10 wt % Al can have excellent environmental resistance in certain simulated boiler conditions even compared with stainless steels. The maximum environmental resistance benefits of Fe-Al alloys are obtained, however, at Al concentrations exceeding 14 wt %. The evaluation of wire arc spray deposits reported here represents an attempt to evaluate methods by which Fe-Al deposits with greater than 14 wt % Al can be obtained by processes that would be feasible for cladding boiler tubes.

MATERIALS AND EXPERIMENTAL DETAILS

Deposits of an Fe-Al alloy were made using an electric wire arc spray process. A schematic outline of the process is shown in Fig. 1. The consumable materials used in the process are metal wires and high-pressure air or gas. Two metal wires are fed simultaneously to a gun containing contact electrodes that provide a current path through the wire tips. Resistance heating causes the wires to melt. The molten metal is then formed into a spray plume by the high-pressure gas. The wire arc spray process is simple, versatile, and portable. It can deposit metal at very high rates and it can be applied to large structures. In the overall spectrum of thermal spray processes, it is relatively unsophisticated, but this means it is relatively easy to deploy, especially for field applications.

The wire used to make the deposits was produced by and purchased from Stoody Company (Bowling Green, Kentucky). The wire had a nominal composition of Fe-26Al-0.25Mo-0.25Zr-0.1C wt %, and it was a composite of an Al wire sheathed in Fe with additional alloying elements added to the sheath as

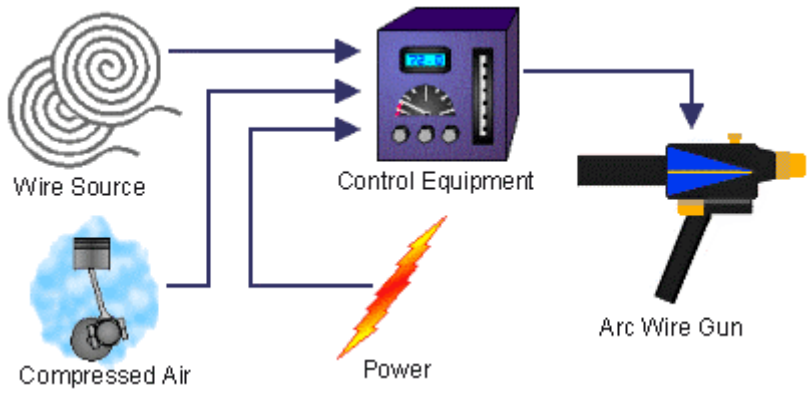

Fig. 1. Schematic outline showing key elements of the electric wire arc spray process.

powders. A photograph illustrating the construction of the wire is given as Fig. 2. The finished diameter of the wire was 1.6 mm (1/16 in.).

Fig. 2. Construction of Fe-Al composite wire consisting of an Al wire wrapped in an Fe sheath.

Four deposits were made using the atmospheric conditions shown in Table 1. The deposits were sprayed onto steel surfaces that were prepared to intentionally promote debonding. The debonded coatings, an example of which is shown in Fig. 3, were in the thickness range of 1 to 1.5 mm and had surfaces that were relatively rough. Specimens of the debonded coatings were then used for an evaluation of oxidation behavior without the need to account for the behavior of the substrate material. The specimens were oxidized in still air at either 500°C or 900°C for either 24 h or 100 h. Half of the specimens were also

Table 1. Atmospheric conditions used to make wire arc spray deposits

Coating ID	Deposition condition
AS9901	Air propellant with no shielding
AS9902	Nitrogen propellant with no shielding
AS9903	Nitrogen propellant with N shielding
AS9904	Nitrogen propellant in a N-filled glove box

Fig. 3. Photograph wire arc spray coating that spontaneously debonded from its substrate.

given a pretreatment of 1000°C in air for 1 h to promote full reaction and homogenization of the deposited metal. Specimen weights before and after exposure were compared to assess oxidation behavior.

Selected specimens were also examined in a scanning electron microscope (SEM) to determine the microstructural features associated with oxidation and to assess homogeneity of the deposits.

RESULTS

The results from chemical analysis of the deposits are given in Table 2. The Al concentrations of the deposits were all less than the nominal of 26 wt %, and those sprayed in the more oxidizing conditions experienced higher Al losses. The Al losses were expected, not only because of oxidation, but from aporization as well. The Mo concentrations of the deposits were below the detection limit of the X-ray fluorescence method used for the analyses. The Zr concentrations were substantially higher than the nominal of 0.25 wt %. These variations may be the result of optimizing the wire composition for welding

applications rather than for a thermal spray process. The deposits all contained substantial concentrations of O and N as expected due to their reactivity with the major elements in the wire. The O concentrations were higher for the deposits made with air propellant or no shielding. The N concentrations were relatively constant regardless of atmospheric conditions.

Table 2. Chemical analysis results from wire arc spray deposits.

	Analyzed wt %			
Element	**AS9901**	**AS9902**	**AS9903**	**AS9904**
Al	18.35	21.99	24.65	24.37
Cr	0.02	0.02	0.02	0.02
Fe	78.19	75.89	74.28	74.44
Mn	0.06	0.08	0.10	0.10
Mo	<0.01	<0.01	<0.01	<0.01
Si	<0.01	0.01	0.01	0.01
Zr	0.63	0.57	0.63	0.64
C	0.02	0.03	0.05	0.06
O	2.56	1.22	0.087	0.138
N	0.110	0.127	0.109	0.138

Results from the evaluation of oxidation behavior will only be presented for the deposits made under the least protective conditions (AS9901) and the most protective conditions (AS9904) because they adequately illustrate the range of behavior. The weight gain data, expressed as mg/cm^2, for these two deposits are given in Figs. 4 and 5. Weight gains increased with either exposure temperature or holding time at temperature for both sets of specimens. For the specimens that were pretreated at 1000°C, the incremental weight gains were considerably less than those for the directly exposed specimens. However, at each exposure condition, the total weight gains were nearly identical regardless of whether or not specimens received the 1000°C pretreatment. The weight gain data also indicate that there was no advantage to producing the deposits in the more protective confines of a N-filled glove box. The microstructures of the deposits exposed at 900°C for 100 h were examined in the SEM as this represented the most severe oxidation conditions and a temperature that was more relevant to boiler operation conditions. The microstructures before and after exposure are shown in Figs. 6. and 7. The microstructures of specimens that were pretreated at 1000°C were virtually identical to those of specimens that were directly exposed, so only the later are shown. These figures collectively illustrate the irregular nature of the coating surfaces. The darker phases in these micrographs are oxides, and the black features are cracks or unbonded interfaces between individual sprayed particles.

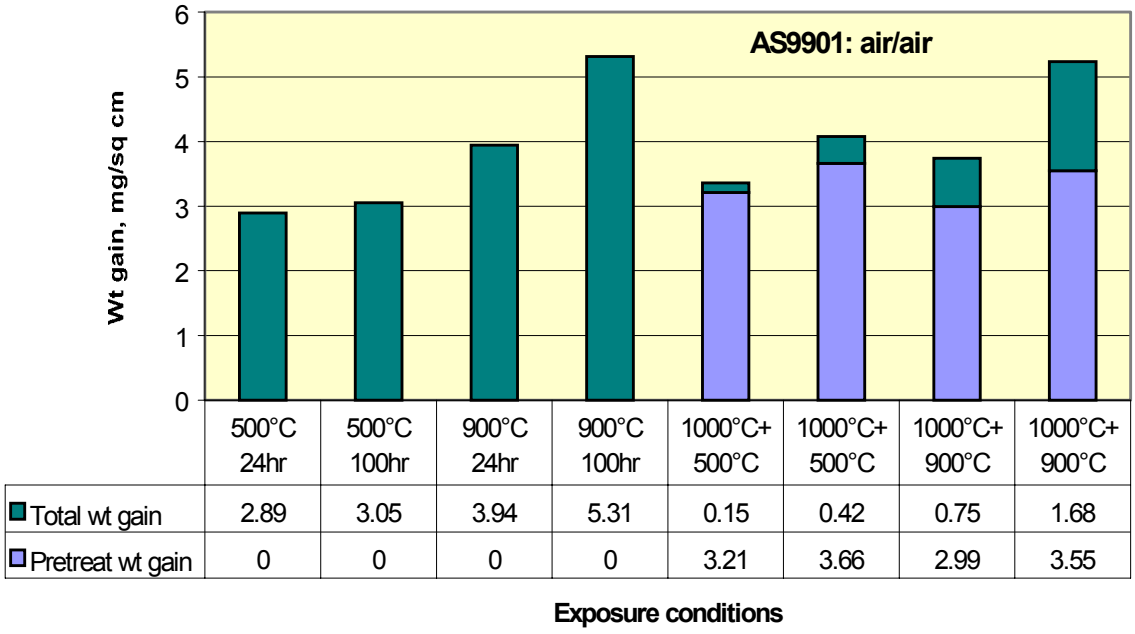

Fig. 4. Weight gain results for arc spray deposit made with air propellant and no shielding.

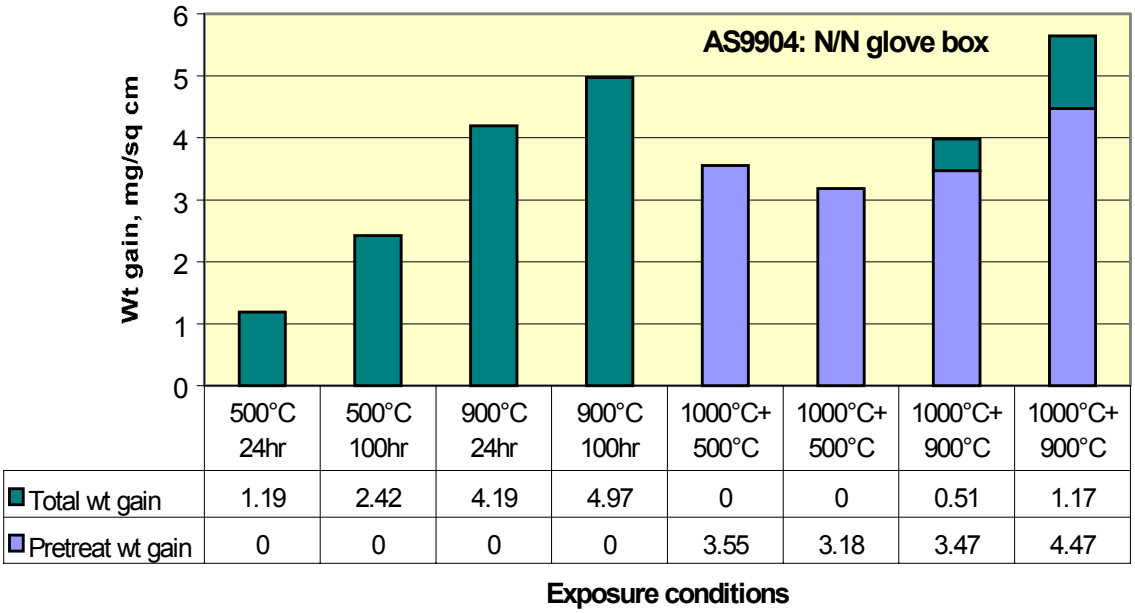

Fig. 5. Weight gain results for arc spray deposit made with N propellant in a N-filled glove box.

Fig. 6 shows that the deposit made in air contained oxides throughout its thickness, even in the as-deposited condition. The contrast of the metallic matrix suggests that its chemical composition was relatively uniform, and this was confirmed by microchemical analysis using the energy dispersive

spectroscopy (EDS) system on the SEM. The exposure at 900°C dramatically increased the amount of oxides throughout the thickness of the deposit. Microchemical analysis indicated that most of the oxides were aluminum oxide. The large particle in the upper right corner of the exposed microstructure was an iron oxide. However, very few iron oxide particles were observed, and they were always found on the surfaces of the deposits.

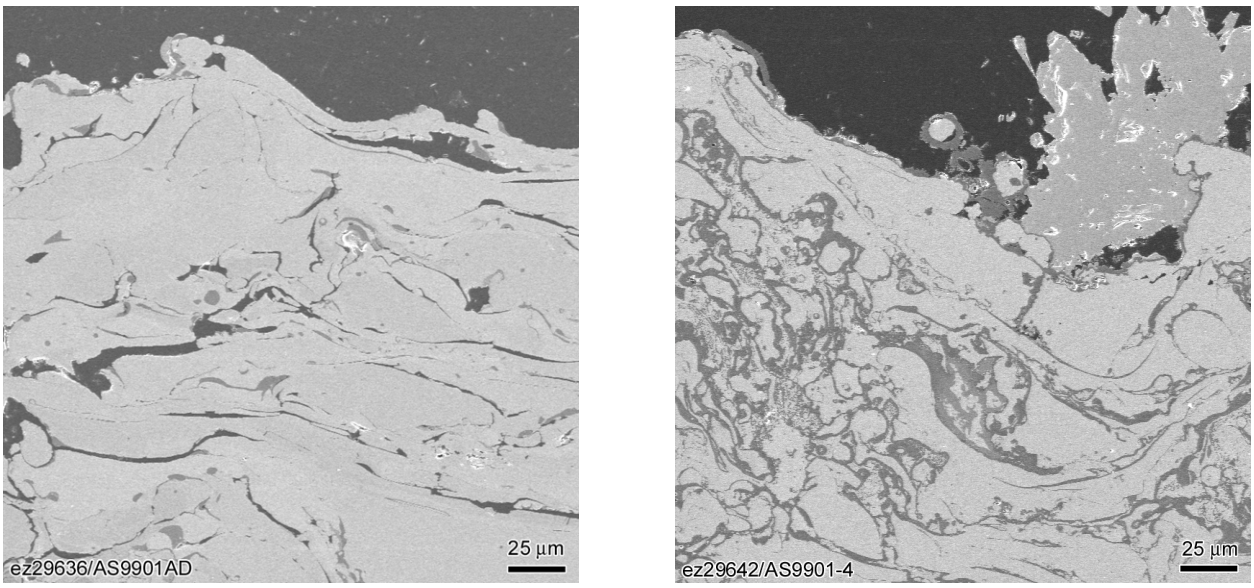

Fig. 6. SEM micrographs of wire arc spray deposits made in air: as-deposited (left) and after exposure in air at 900°C for 100 h (right).

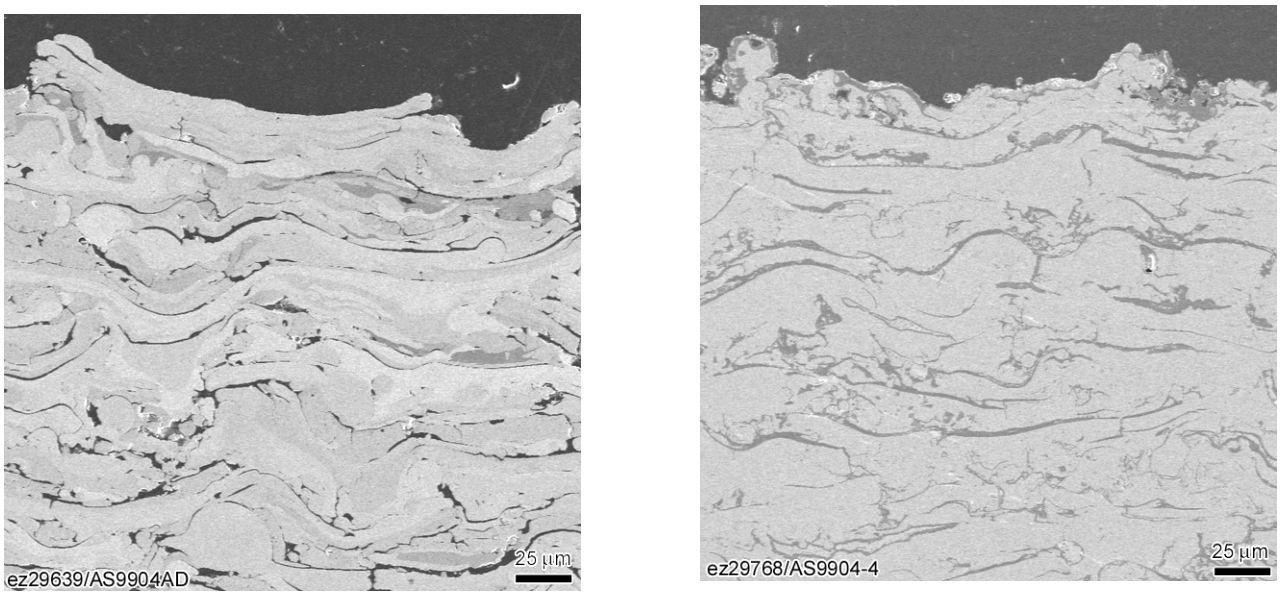

Fig. 7. SEM micrographs of wire arc spray deposits made in a N-filled glove box: as-deposited (left) and after exposure in air at 900°C for 100 h (right).

The deposit made in the N-filled glove box contained fewer oxides in the as-deposited condition (see Fig. 7, left). Also, the contrast of the metallic matrix suggested that it was more chemically inhomogeneous than the deposit made in air, and this was confirmed by microchemical analysis. No pure Al particles were found in the deposit, but a few pure Fe particles were observed. Most of the deposit was alloyed, but the variations in contrast correlated with variations in Al and Fe concentrations. As for the air-deposited specimen, exposure at 900°C produced significant oxidation throughout the thickness of the deposit with most of the films being aluminum oxide. In addition, homogenization of the metallic matrix was promoted during the exposure.

DISCUSSION

The composite wire of composition Fe-26Al-0.25Mo-0.25Zr-0.1C wt % was adequate for use with the wire arc spray process from an operational point of view. In addition, it appears adequate in metallurgical terms because it produced spray deposits that were either alloyed as-deposited or quickly alloyed during elevated temperature exposure. In addition, Al loss during processing was minimal, especially when the spraying was done under a more protective atmosphere. The higher Al losses associated with air processing, 18.35 wt % compared with 24.37 wt % for deposition in the N-filled glove box, correlated with higher O concentrations and with higher fractions of aluminum oxides in the deposits. Carbon recovery was also lower for air processing, and this is consistent with an increased tendency to form CO_X. The N concentrations in the deposits were relatively constant irrespective of atmospheric conditions, suggesting that they saturate at a propellant gas concentration lower than that of air, which consists of about 78% N.

The weight gain data from the four specimens that were directly exposed at 900°C for 100 h are compared with data from monolithic Fe-Al alloys (see Fig. 8.) (Pint et al., *Oxidation of Metals*, vol. 51, 1999, pp. 181-97). The wire arc spray deposits had much higher weight gains than would be expected for monolithic alloys of identical Al concentrations. The reasons for this, however, seem clear in light of the deposit microstructures. First, the deposit surfaces are highly irregular so that their actual surface areas are much larger than those that are determined from specimen size measurements. Perhaps more importantly, the cracks in the deposits and their general lack of integrity expose even much higher surface areas to environmental attack than can be accounted for by surface roughness. The overwhelming influence of through-thickness oxidation must account for both the inordinately large weight gains and for the lack of a dependence on atmospheric conditions during deposition.

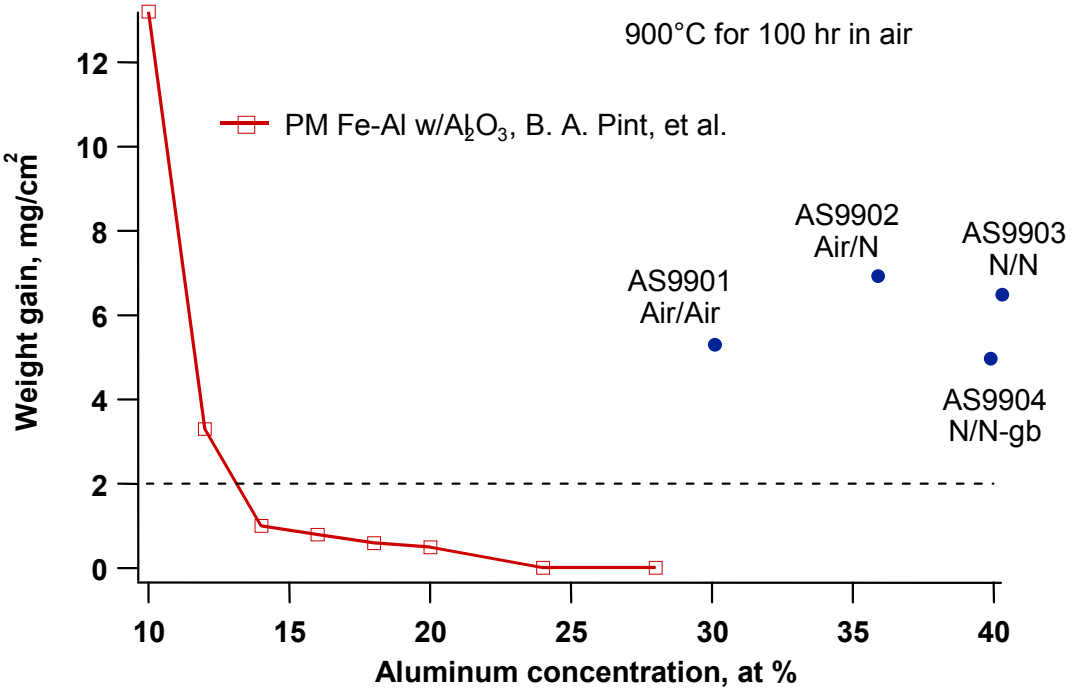

Fig. 8. Comparison of the oxidation weight gains of wire arc sprayed Fe-Al deposits with the variation of weight gain during oxidation at 900°C for 100 h in air with Al concentration for monolithic Fe-Al alloys. (Source: Pint et al., *Oxidation of Metals*, vol. 51, 1999, pp. 181-97.)

CONCLUSIONS

The oxidation behavior of wire arc spray deposits was evaluated. The deposits were made with a composite wire of nominal chemical composition Fe-26Al-0.25Mo-0.25Zr-0.1C wt %. The deposits were exposed in air to temperatures of 500°C and 900°C for times of 24 h and 100 h, both with and without a pretreatment of 1000°C for 1 h in air. The following conclusions resulted from this study.

1. The composite Fe-Al wire was suitable for the wire arc spray process.
2. Substantial alloying of the various elemental components of the wire occurred during the spraying process and elevated temperature exposure.
3. The oxidation behavior of the deposits was not influenced significantly by the variation in atmospheric conditions used for making the deposits. Specimens sprayed with air propellant behaved similarly to those sprayed in a N-filled glove box.
4. The oxidation weight gains were higher than those expected for monolithic alloys of identical Fe-Al composition. This was attributed to the lack of integrity of the deposits, which exposed much higher surface areas to oxidation than the apparent surface areas determined from specimen dimensions.

ODS ALLOYS FOR HIGH-TEMPERATURE APPLICATIONS

I. G. Wright, C. G. McKamey, and B. A. Pint

INTRODUCTION

Oxide-dispersion-strengthened (ODS) alloys have the potential for safe operation at temperatures significantly higher than possible with current heat-resistant alloys. Essentially, these alloys represent the maximum temperature capability of metallic alloys that can be used in tube and sheet form, and they allow operation at the lower end of the temperature range for which it is usually assumed that ceramic materials would be required. The incorporation of ODS alloys into the design of advanced heat-transfer modules, for instance, would not only increase the system temperature capability but would also reduce the size of any downstream ceramic heat transfer component, if even higher temperatures were required. Two prototype ferritic ODS alloy heat exchangers[1,2] have already demonstrated the ability to operate at metal temperatures of approximately 1100°C (2102°F).

ODS alloys have not attained wide usage to date because they are made by a powder metallurgy process and so are relatively expensive, and the unique microstructure necessary to develop their exceptional high-temperature strength leads to difficulties in joining, which results in restricted fabrication options. The prototype ODS heat exchangers mentioned above employed less than optimum configurations to allow the use of available joining techniques.

The goal of this program is to develop a detailed understanding of the behavior of ODS alloys in all phases of their use, including relevant properties, fabrication and joining, service performance, oxidation life prediction, mode of failure, repair, and refurbishment. These data are needed to provide designers of components requiring exceptional high-temperature strength (such as heat-transfer modules) with the basis from which to consider ODS alloys in their initial component designs. The peculiar properties of these alloys do not allow their strength benefits to be fully exploited when retrofitted into existing designs based on the properties of current heat-resistant alloys. The successful outcome of this project will result in developments that allow ODS alloys to be used with confidence in a variety of applications previously not possible with metallic materials.

The alloys of interest are indicated in Table I, which also gives their typical chemical compositions.

Table 1. Nominal compositions of available ferritic ODS alloys (weight percent)

Alloy	Fe	Cr	Al	Mo	W	Ti	Si	RE*
ODS-Fe_3Al	Bal	2.2	15.9	—	—	0.07	0.1	Y_2O_3-Al_2O_3
INCO MA 956	Bal	20.0	4.5	—	—	0.5	—	Y_2O_3-Al_2O_3
INCO MA956HT	Bal	21.6	5.9	—	—	0.4	0.07	Y_2O_3-Al_2O_3
Plansee PM 2000	Bal	20.0	5.5	—	—	0.5	—	Y_2O_3-Al_2O_3
Dour Alloy ODM 751	Bal	16.5	4.5	1.5	—	0.6	—	Y_2O_3-Al_2O_3
Kanthal APM**	Bal	20.0	5.5	—	—	0.03	0.23	ZrO_2-Al_2O_3

*reactive element addition, in the form of an oxide dispersion

**Kanthal APM is manufactured by a powder process but is not strictly speaking an ODS alloy; ZrO_2 and Al_2O_3 are not added as oxide species, but result from the processing route used.

DISCUSSION OF CURRENT ACTIVITIES

MECHANICAL PROPERTIES

As was shown elsewhere[3], the prototype ODS-Fe_3Al alloy exhibits tensile and creep properties that are similar to those of the commercial ODS-FeCrAl alloys. One of the peculiarities of ODS alloys is that, although they possess excellent high-temperature creep strength, the creep behavior is unusual in that the progressive stages of creep exhibited by conventional alloys are typically not observed. Instead, creep loading results in long periods of no measurable activity, as shown in Fig. 1 for ODS-Fe_3Al, with occasional small step fluctuations (possibly machine noise) or increases in elongation, as shown by the inset in Fig. 1. At lower stress levels, essentially no creep is observed for extremely long times. However, at sufficiently high levels of applied stress such activity is terminated by an abrupt failure with essentially no warning, as shown in Fig. 2. This strain rate sensitivity of ODS alloys is an important feature which must be fully appreciated when considering their application.

These results suggest that a threshold stress might be defined below which the alloy will have a very long creep life (still to be determined), but above which failure will be relatively rapid. The values of the failure stress from creep tests in which specimens were incrementally loaded in 100 h intervals until failure are plotted in Fig. 3. It is suggested that the area below the resulting curve may be taken to indicate the temperature-stress regime where advantage could be taken of the superior creep behavior of this alloy. Obviously, to be of much practical value, such diagrams should also indicate the strain rate-sensitivity, but this information is scarce at present.

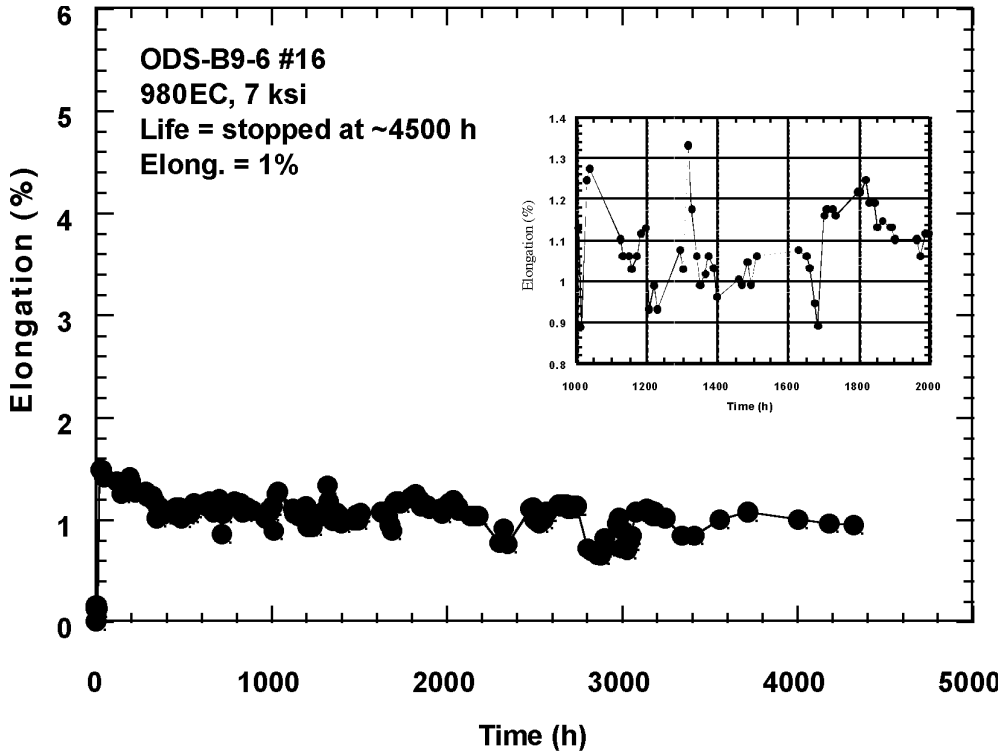

Fig. 1. Creep curve for ODS-Fe_3Al at 980°C and a load of 48 MPa (7 ksi).
The test was stopped after 4500+ hours

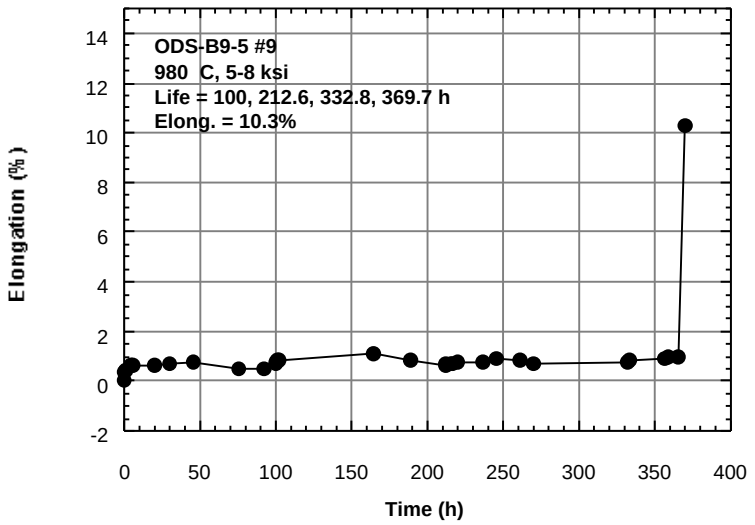

Fig. 2. Typical creep curve for ODS-Fe_3Al. Load was increased from 34 to 55 MPa (5 to 8 ksi) in 7 MPa (1 ksi) increments at 100-hr intervals until failure.

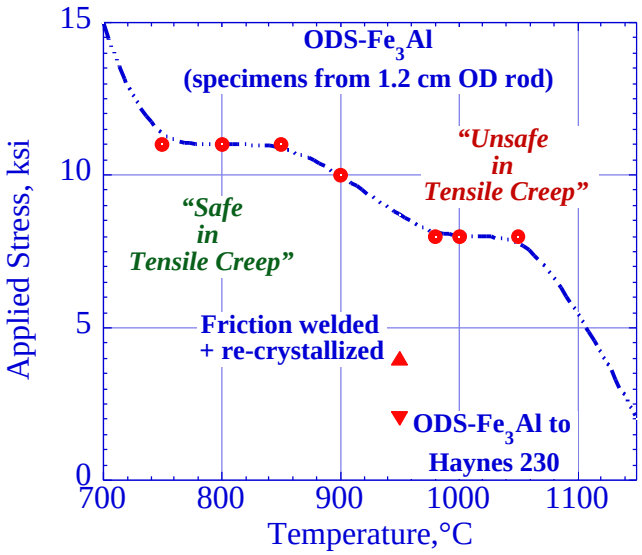

Fig. 3. Suggested representation of regimes of safe/unsafe application of ODS alloys.

JOINING

Initial tensile tests of ODS-Fe_3Al rod stock joined by rotary friction welding[4] were made using as-joined rods (not tensile bars) and indicated, surprisingly, that the joints retained from 54 to more than 69 percent of the strength of the parent alloy[3]. Subsequent creep testing using the incremental loading technique of specimens machined from such joints has indicated that an ODS-Fe_3Al-self joint (in which the alloy was recrystallized after joining) retained about half the strength of the parent alloy. The strength of an ODS-Fe_3Al-to-Haynes 230 (conventional high-temperature wrought alloy) joint was only approximately 25 percent of that of bulk ODS-Fe_3Al. These data are shown by single points in Fig. 3.

Fig. 4 shows a cross section of the fracture surface of an ODS-Fe_3Al self-joint (alloy recrystallized after joining); the failure occurred in the joint, and the distortion of the microstructure (swirl pattern) resulting from the friction welding is discernable. The fracture surface exhibited a dimple pattern indicative of a ductile mode of failure (elongation was 3.4 percent) (Fig. 5a), with large numbers of small particles in the bottoms of the dimples (Fig. 5b). These particles were found by energy dispersion spectroscopy (EDS) to contain yttrium. A possible explanation of this observation is that the Y_2O_3 dispersion in the alloy may have been redistributed to the joint interface during the friction welding. Hence, the reduced creep strength of the joined material probably resulted not only from realignment of the alloy grain structure such that some grain boundaries in the welded region were transverse to the loading direction[3], but also from localized depletion of the dispersoid phase.

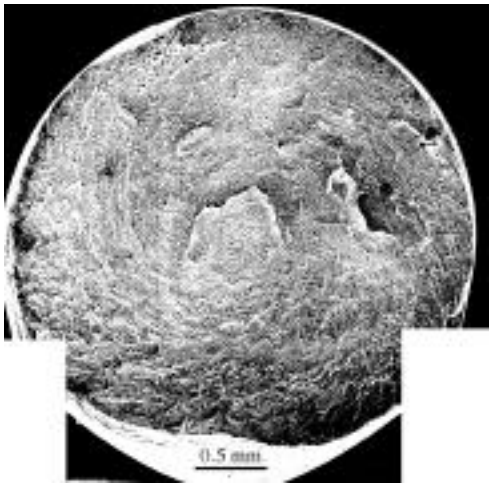

Fig. 4. Macro-view of the fracture surface of an ODS-Fe_3Al self-joint

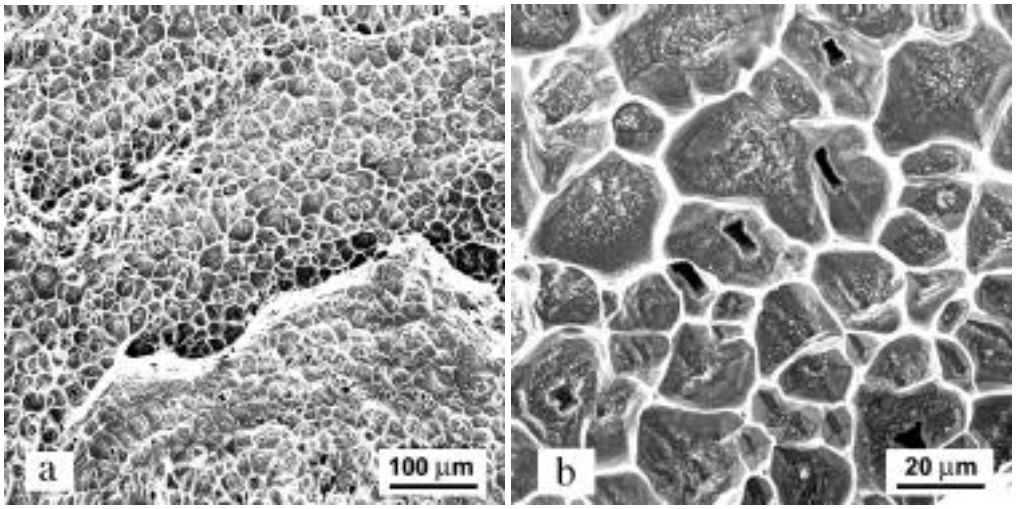

Fig. 5. Details of the fracture surface showing (a) ductile dimpling, and (b) Y-rich particles at the bottom of the dimples

The fracture of an ODS-Fe_3Al-to-Haynes 230 weld also ran straight across the joint, but actually occurred just inside the Haynes 230 half of the specimen. Fig. 6 shows the appearance of the two halves of the fracture surface, and the identical detailed structure of these surfaces is shown in Fig. 7. Analysis of these surfaces indicated mostly elements from the Ni-base alloy.

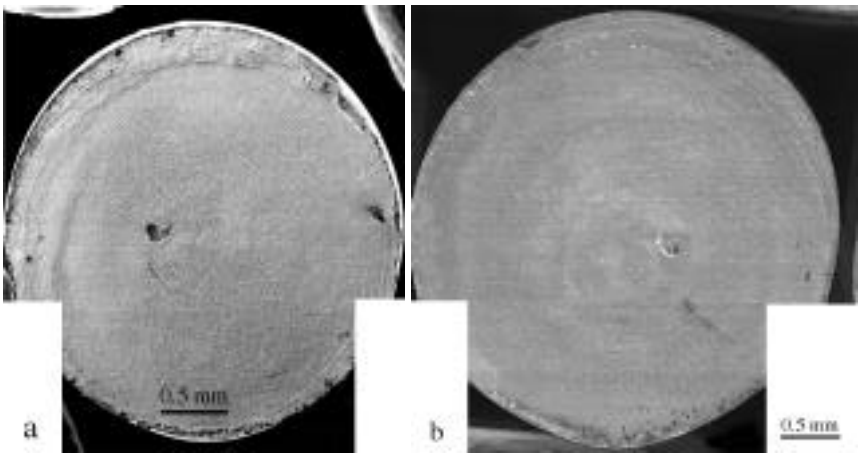

Fig. 6. Macro-views of the two fracture surfaces from an ODS-Fe_3Al-to-Haynes 230 joint (a) ODS-Fe_3Al-side (b) Haynes 230-side

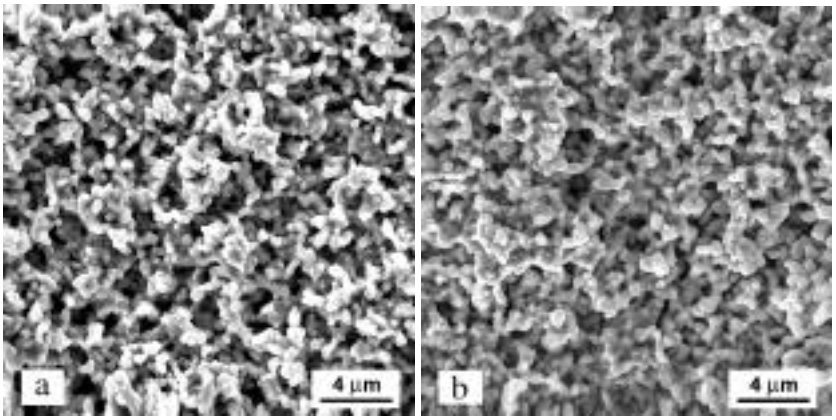

Fig. 7. Details of the fracture surfaces (a) on ODS-Fe_3Al side, and (b) on Haynes 230 side, showing that both have the same structure

PHYSICAL PROPERTY DETERMINATION

Thermal expansion measurements were made on ODS-Fe_3Al (PMWY-2) using a Theta Industries dual push-rod differential dilatometer, which employs high-density alumina push rods and sample holder in a horizontal configuration. The temperature dependence of the mean coefficient of thermal expansion (CTE) of ODS-Fe_3Al is shown in Fig. 8, in comparison to literature values for MA956[5], PM2000[6], and polycrystalline alumina[7]. It is clear that the CTE of ODS-Fe_3Al is significantly greater than for the ODS-FeCrAls, and that it has a different temperature dependence as a result of the DO_3-to-B2, and B2-to-α (disordered) phase changes which occur at 533°C and 821°C, respectively. The values are slightly different for those measured earlier[8] for a cast Fe_3Al alloy (FA-129: 16Cr-5Cr-0.05C-0.1Zr, weight percent), which were DO_3-to-B2 at 543°C, and B2-to-disordered α at 924°C. The ΔCTE between ODS-Fe_3Al and polycrystalline alumina, shown in Fig. 9, indicates that a maximum (approximately 12 x 10^{-6}/°C) exists at approximately 900°C; this value is some 2.4 times that for the ODS-FeCrAls.

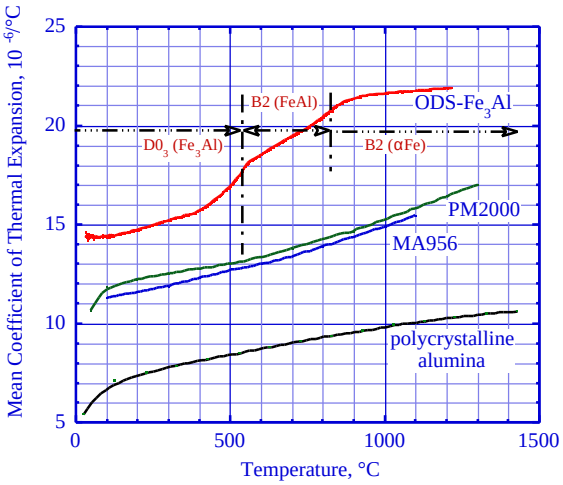

Figure 8.Comparison of mean coefficients of thermal expansion of ODS-Fe_3Al and ODS-FeCrAl alloys with that of alumina.

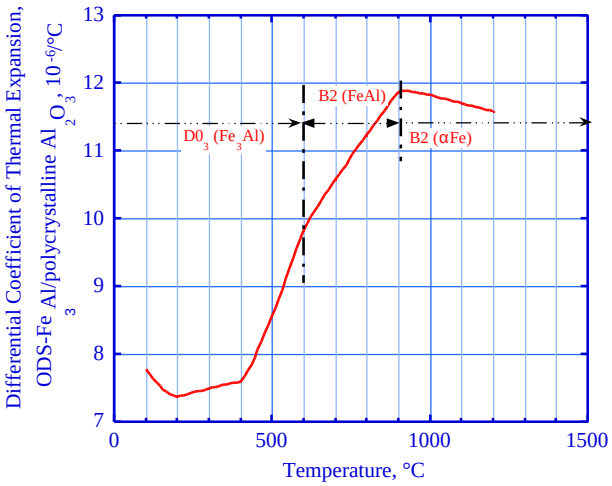

Figure 9. Variation with temperature of the difference between coefficients of thermal expansion of ODS-Fe_3Al and alumina.

OXIDE SPALLATION

The major characteristic of the cyclic oxidation behavior of ODS-Fe_3Al is the tendency for significantly more scale spallation to occur than observed on the FeCrAl alloys. Although the adherence of the oxide to ODS-Fe_3Al appears to be tenacious, at temperatures of 1100°C and higher, spallation of small fragments of scale occurs in amounts that increase with increasing time and temperature, so that the overall oxidation rate is higher compared to ODS-FeCrAl alloys[9]. Scale spallation from ODS-Fe $_3$Al appears to result from cracking associated with undulations in the alloy-oxide interface[9]. While such undulations are small at 1000 and 1100°C, they increase in size at 1200°C, and at 1300°C the stresses generated are sufficient to cause gross local deformation of the substrate. The changes in plane caused by the surface undulations result in cracking of the oxide and scale loss. Similar undulations are present in the metal-oxide interfaces on Kanthal APM (and on the commercial ODS-FeCrAls)[14], but they are typically much smaller than on ODS-Fe_3Al after similar exposures.

The basic driving forces for scale spallation are the stresses resulting from the accommodation of the increased volume of oxide compared to the alloy from which it was formed, and from the thermally-induced stresses from the difference in the coefficient of thermal expansion of the oxide and the alloy substrate. The stress from the former source increases with increasing scale thickness (time at temperature), but may be ameliorated to some extent by deformation of the substrate (or oxide) at temperature. The macro yield and tensile strengths of ODS-Fe $_3$Al are very similar to those of the ODS-FeCrAl alloys at temperatures up to 1100°C, while the creep strength of ODS-Fe_3Al is similar to that of MA956, and somewhat less than for PM2000 in the range 800 to 1100°C[3,6,11], and are expected to be greater than for Kanthal APM. Hence, it would be expected that, for a given rate of scale growth, relaxation of the Pilling-Bedworth stresses would occur at a similar, or greater rate, on Kanthal APM than on ODS-Fe_3Al and the ODS-FeCrAls.

The stress from the CTE mismatch is exerted during the cooling cycle of the oxidation exposure since the oxide is grown at temperature. It is clear from Fig. 8 that the CTE of ODS-Fe_3Al is significantly greater

than of the ODS-FeCrAls, and that it has a different temperature dependence as a result of the phase changes which occur at 533°C and 821°C. The stress (σ_{ox}) resulting from the different coefficients of thermal expansion of the oxide (α_{ox}) and alloy (α_{alloy}) can be estimated[12] from:

$$\sigma_{ox} = -E_{ox}\Delta T(\alpha_{alloy} - \alpha_{ox})/(1-\nu)$$

where E_{ox} and ν are the elastic modulus (360 GPa[13]) of the oxide and the Poisson's ratio of the oxide and metal (assumed equal, estimated to be 0.3), respectively. The estimated compressive stress from cooling an ODS-Fe_3Al specimen from 1300°C to 25°C is 7.6 GPa. Recent measurements have indicated a residual compressive stress of 9 GPa in the scale formed on this alloy after exposure for 20 h at 1200°C[14]. This stress level suggests a corresponding strain in the scale of approximately 2 percent and, since a strain of only 0.1 to 0.2 percent is sufficient to fail an alumina scale in compression, it is clear that conditions for scale failure exist. Hence, the large CTE mismatch between ODS-Fe_3Al and alumina appears to be the major inherent reason for the increased tendency for scale spallation of this alloy.

It is apparent that the CTE mismatch problem will not be solved by small modifications of the alloy composition. Minimization of the growth rate of the oxide scale is, nevertheless, a worthwhile goal for maximizing its service lifetime. It is also important to have an accurate knowledge of the temperature dependence of oxidation in environments of interest to allow calculation of the rate of consumption of Al, and the minimum Al level to which the substrate can be depleted before non-protective behavior ensues. Oxidation lifetime models, such as that due to Quadakkers, et al.[15] equate the oxidation lifetime (t_b) to the time required to deplete the alloy Al reservoir from the initial level (C_o) to some critical level (C_b), where the Al is consumed in the formation of the protective oxide scale:

$$t_b = [4.44 \times 10^{-3} \cdot (C_o - C_b) \cdot \rho \cdot d/k]^{1/n}$$

where ρ is the density of the alloy, d the section thickness, k is the oxidation rate constant, T is the oxidation temperature, n is the time-dependence exponent (0.5 for parabolic oxidation behavior), and R is the gas constant. Clearly, t_b will be increased by decreasing both C_b and k.

OXIDATION DATA FOR ODS ALLOYS IN STEAM AND WATER VAPOR

The oxidation kinetics of ODS-Fe_3Al and ODS-FeCrAl alloys in an interrupted test in steam at 1.7 MPa (250 psia) and 899°C, and in an air-90% water vapor mixture at 0.1 MPa (1 atm) in a thermal cycling test (cycled from approximately 100°C to 1200°C, with 1h at temperature), are illustrated in Figs. 10 (a) and (b), respectively. The test at 899°C was stopped at the intervals indicated, and the specimens were removed, examined, and weighed before being either removed or replaced. The data for Kanthal APM indicate that parabolic kinetics were followed for more than 4000 h, with an indicated parabolic rate constant of 5.5 x 10^{-14} $g^2cm^{-4}s^{-1}$. This compares to rates of 7.0 x 10^{-14} $g^2cm^{-4}s^{-1}$ and 0.35 x 10^{-14} $g^2cm^{-4}s^{-1}$ at 899°C extrapolated from isothermal oxidation in oxygen and from 100-hr cyclic oxidation in air, respectively[9], and suggests that the oxidation rate of this alloy is essentially unchanged in the high-pressure steam environment. The reason why the data points at 722 h for ODS-Fe_3Al indicate higher weight gains than for APM is not known. The slightly lower weight gains for ODS-Fe_3Al at longer times suggest some loss of scale by spallation; similar behavior was observed in long-term, 500-hr cycle tests in air at 1000°C[16].

The data in Fig. 10 (b) also suggest that the oxidation behavior of both alloys in air is not obviously modified by the addition of water vapor in 1h cyclic tests at 1200°C (at least to 200 cycles). These tests

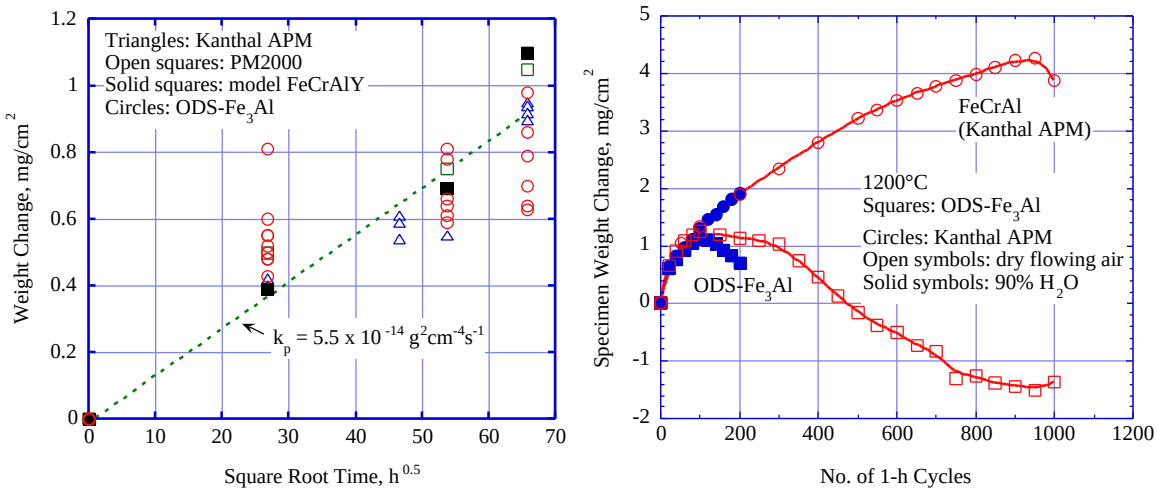

Fig. 10. Oxidation kinetics in (a) steam at 1.7MPa and 899°C, parabolic plot, and (b) air-90% water vapor at atmospheric pressure and 1200°C (1 hr cyclic tests)

also are continuing. As discussed earlier, the tendency for greater scale spallation from ODS-Fe_3Al is very obvious, both in air and air-water vapor at this temperature.

.

CONCLUSIONS

The observation that below some critical stress level ODS-Fe_3Al undergoes essentially no tensile creep whereas at a higher stress it fails very rapidly (apparently by ductile yielding), suggests that a limiting stress can be defined below which this alloy can be expected to exhibit the exceptional creep resistance typical of ODS alloys. The development of a threshold stress-temperature diagram could be a useful method of depicting the range of applicability of this alloy. The commercial ODS-FeCrAl alloys exhibit similar behavior in creep to that observed for ODS-Fe_3Al, but this has not been documented to indicate a threshold behavior. The technique used to generate the data for this diagram also proved useful for evaluating the creep strength of joints in a relatively short time. A friction-welded joint of ODS-Fe_3Al to itself failed at a stress some 50% of the threshold value for a monolithic specimen. There were indications that the highly elongated alloy grains were misaligned due to the welding process, and that significant redistribution occurred of the yttria dispersion strengthening phase in the joint area. Both of these features would be expected to contribute to the observed reduction in strength.

ODS-Fe_3Al was found to have a much larger CTE than ODS-FeCrAl alloys. Observations of the morphologies of surfaces from which scale spallation had occurred suggested that the mode of spallation is consistent with the need to accommodate large CTE stresses. Hence, the large ΔCTE between ODS-Fe_3Al and alumina appears to be the major inherent reason for the increased tendency for scale spallation of this alloy. Initial results from exposures to air-water vapor at 1200°C and to high-pressure steam at 899°C suggest that the oxidation behavior of ODS-Fe_3Al and the ODS-FeCrAl alloys is not significantly changed from that in air.

ACKNOWLEDGMENTS

This research was sponsored by the Fossil Energy Advanced Research Materials (ARM) Program, U.S. Department of Energy, under contract DE-AC05-96OR22464 with UT-Battelle, LLC. Program of the U.S. Department of Energy. Mr. L. D. Chitwood was responsible for the oxidation lifetime tests, Mr. W. Porter measured the coefficients of thermal expansion of the alloys, and Mr. C. A. Carmichael performed the creep tests.

REFERENCES

1. F. Starr, A. R. White, and B. Kazimierzak, in *Materials for Advanced Power Engineering 1994*, D. Coutsouradis, et al., Eds., (Kluwer Academic Publishers, 1994) pp. 1393-1412.
2. D. J. Seery and J. Sangiovanni, "Engineering Development of a Coal-Fired High-Performance Power Generating System," Paper No. 1.7 in *Proc. of the Advanced Coal-Based Power and Environmental Systems'98 Conference*, Morgantown, West Virginia, July 21-23, 1998, DOE/FETC-98/1072.
3. I. G. Wright, C. G. McKamey, B. A. Pint, and P. J. Maziasz, "ODS Alloys for High-Temperature Applications," Paper No. 4.1 in *Proc. 13th Annual Conference on Fossil Energy Materials*, Knoxville, Tennessee, May 11-13 1999.
4. P. L. Threadgill, Friction Welding of an Fe_3Al-based ODS Alloy, ORNL/Sub/97-SX373/01, July 1998. See, also, B. J. Inkson and P. L. Threadgill, "Friction Welding of Fe-40Al Grade 3 ODS Alloy," *Mat. Sci. and Eng.*, A258, 313-318 (1998).
5. INCO Data Sheet PP-1: Physical Properties of INCOLOY alloy MA956.
6. Material Data Sheet ODS-Superalloy PM 2000, Metallwerk Plansee GmbH/Lechbruck, Feb. 1993.
7. Y. S. Touloukian, R. K. Kirby, R. E. Taylor, and T. Y. R. Lee, *Thermal Expansion—Nonmetallic Solids, Vol. 13 of Thermophysical Properties of Matter,* IFI/Plenum, New York (1970).
8. W. Porter, unpublished data; measurements made at the Oak Ridge National Laboratory, 1999.
9. I. G. Wright, B. A. Pint, and P. F. Tortorelli, "The High-Temperature Oxidation Behavior of ODS-Fe_3Al Alloys," submitted to *Oxidation of Metals*, 2000.
10. J. P. Wilbur, J. R. Nicholls, and M. J. Bennett, "Assessment of Defects in Alumina Scales Formed on Ferritic ODS Alloys," pp. 207-220 in *Microscopy of Oxidation-3*, S. B. Newcomb and J. A. Little, The Institute of Materials (1997).
11. J. Fischer, J. J. deBarbadillo, and M. J. Shaw, "MA Alloys for Industrial Applications," pp. 79-87 in *Structural Applications of Mechanical Alloying*, F. H. Froes and J. J. deBarbadillo, Eds., ASM International (1990).
12. M. Schütze, Chapter 4.2 in *Protective Scales and Their Breakdown*, Edited by D. R. Holmes, Translated by R. B. Waterhouse, The Inst. of Corrosion and Wiley Series on Corrosion and Protection, John Wiley & Sons Ltd. (1997).
13. M. A. Janney, H. D. Kimrey, W. R. Allen, and J. O. Kiggans, *J. Mat. Sci*., 32, 1347-55 (1997).
14. M. Lance and B. A. Pint, Oak Ridge National Laboratory, unpublished work, 1999.
15. W. J. Quadakkers, K. Bongartz, F. Schubert, and H. Schuster, in *Materials for Advanced Power Engineering 1994*, D. Coutsouradis et al., Eds., (Kluwer Academic Publishers, 1994) pp. 1533-1542.
16. I.G. Wright, B.A. Pint, C.S. Simpson, and P.F. Tortorelli, "High-Temperature Life Characteristics of ODS-Fe_3Al," pp. 195-202 in *High-Temperature Corrosion and Protection of Materials 4*, R. Streiff, J. Stringer, R. C. Krutenat, M. Caillet and R. A. Rapp, Eds., Materials Science Forum Vol. 251-54 (1997).

PROCESSING AND PROPERTIES OF MOLYBDENUM SILICIDE INTERMETALLICS CONTAINING BORON

J. H. Schneibel and H. T. Lin

ABSTRACT

Alloys with the nominal composition Mo-12.Si-8.5B (at. %) were prepared by arc-melting and drop-casting. They consisted of approximately 38 vol % α-Mo in a brittle matrix of Mo_3Si and Mo_5SiB_2. Their high-temperature strength was investigated in tensile creep (constant applied stress) and in compression (constant applied cross-head speed) at temperatures ranging from 1200 to 1350°C. In order to improve the oxidation resistance, the α-Mo volume fraction was reduced. Since castings with low α-Mo volume fractions were prone to macro-cracking, powder-metallurgical processing techniques were explored. Processing based on elemental powders resulted in inhomogeneous microstructures. Processing based on arc-cast ingots ground into particles or powder gave better results. Hot isostatic pressing resulted in fully dense materials, even for large particles with sizes on the order of 1 mm. As expected, the room-temperature strength and fracture toughness tended to decrease with decreasing α-Mo volume fraction.

INTRODUCTION

The objective of this task is to develop new-generation corrosion-resistant Mo-Si alloys for use as hot components in advanced fossil energy combustion and conversion systems. The successful development of Mo-Si alloys is expected to improve the thermal efficiency and performance of fossil energy conversion systems through increased operating temperature, and to increase the service life of hot components exposed to corrosive environments at temperatures as high as 1600°C. While $MoSi_2$ is highly oxidation resistant at elevated temperatures, it is extremely brittle at ambient temperatures and has poor creep resistance at elevated temperatures. Molybdenum compounds with lower Si contents, such as Mo_5Si_3 or Mo_3Si, are potentially less brittle and exhibit higher strengths at elevated temperatures, but do not have the required oxidation resistance. Boron additions appear to alleviate the oxidation problem. As early as 1957, Nowotny et al.[1] pointed out that boron-containing silicides possess high oxidation resistance due to the formation of borosilicate glass on their surface. Based on Nowotny et al.'s work, boron-containing molybdenum silicides based on Mo_5Si_3 were recently developed at Ames Laboratory.[2-4] These silicides consist of approximately 25 vol. % Mo_3Si, 50 vol.% Mo_5Si_3 (T1), and 25 vol. % Mo_5SiB_2 (T2). A typical composition is Mo-26.7Si-7.3B, at. % (unless indicated otherwise, compositions will be given in at. %). This alloy has an oxidation resistance comparable to that of $MoSi_2$, and it does not appear to show catastrophic oxidation ("pest reaction") at intermediate temperatures such as 800°C.[4] Also, its creep

strength is superior to that of $MoSi_2$. Since these types of alloys consist exclusively of brittle phases, they tend to be brittle. Another class of Mo-Si-B alloys of interest are those developed by Berczik,[5,6] which consist of α-Mo, Mo_3Si, and T2. These types of alloys have also been studied recently by Perepezko and co-workers.[7-9] While their oxidation resistance is inferior to that of the Mo_3Si-T1-T2 alloys, it is likely that it can be improved by reducing the α-Mo volume fraction, by suitable alloying additions, and/or by silicide or mullite coatings. The main advantage of the Mo-Mo_3Si-T2 alloys is that they do not consist exclusively of brittle phases and have therefore reasonable room-temperature fracture toughness values on the order of 10 MPa $m^{1/2}$. On the other hand, the α-Mo in these alloys will be weak at elevated temperatures and may thus reduce the creep strength. In the work described here, the high- temperature creep strength of cast and annealed Mo-12Si-8.5B was determined to provide a base-line for future alloy development aimed at increasing the creep strength of Mo-Si-B alloys. Since cast Mo-Si-B alloys with small α-Mo volume fractions such as 20% exhibited macro-cracks, powder-metallurgical (PM) techniques were explored to process those alloys. Their room-temperature strength and fracture toughness were determined as functions of the α-Mo volume fraction.

RESULTS AND DISCUSSION

OXIDATION RESISTANCE OF CAST MO-SI-B ALLOYS

Cast Mo-Si-B alloys with different compositions were screened for their oxidation resistance by annealing pieces with a known surface area for 1 day at 1300°C in air. After annealing, the weight losses per unit area were determined (see Fig. 1). Initially these alloys lost large amounts of Mo in the form of volatile MoO_3. Later on, the oxidation rate slowed down and the weight losses per unit time became probably lower than those inferred from Fig. 1. These data exhibited a lot of scatter because the cast alloys were not completely homogeneous and exhibited some casting segregation as well as macro-cracking. However, the data serve to illustrate the general trends in the oxidation resistance of these alloys. First, the binary silicides in the Mo-Mo_3Si region of the phase diagram have very poor oxidation resistance. Second, Mo-12Si-8.5B has also a very poor oxidation resistance (195-387 mg/cm^2). Third, if the Si and B concentrations are increased to 14 and 10 at. %, respectively, the oxidation resistance improves dramatically. However, arc-cast alloys with these more oxidation resistant compositions exhibited always macro-cracks. This is the reason why the cast alloy Mo-12Si-8.5B, which does not macro-crack significantly, was chosen for the creep measurements to be described later. Fourth, the oxidation resistance tends to increase with increasing boron concentration, which is the reason why boron is added to these alloys in the first place.

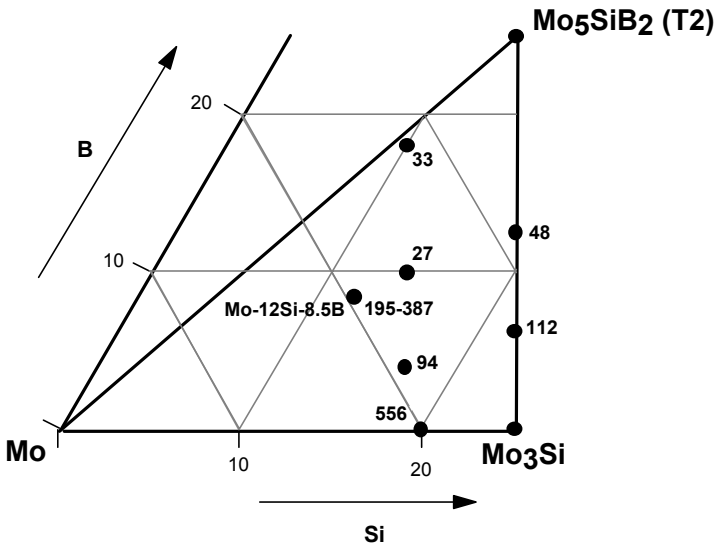

Fig. 1: Oxidative weight losses for cast Mo-Si-B alloys annealed for 1 day at 1300°C in air. The weight losses (mg/cm^2) are indicated next to the data points. Since the density of these alloys is on the order of 9 Mg/m^3, 1 mg/cm^2 corresponds to a surface recession of approximately 1 μm.

CREEP STRENGTH OF MO-12SI-8.5B (AT. %)

Since Mo-Si-B alloys are being considered for high-temperature structural applications, knowledge of their high-temperature strength and creep properties is of importance. A combination of tensile creep and slow compression tests was used to assess the creep properties of cast and annealed (24 h/1600°C/vacuum) Mo-12Si-8.5B. Flat dog-bone specimens with gage lengths and cross sections of 8 mm and 1.5 × 2 mm, respectively, were electro-discharge machined. They contained a circular hole on each end to attach them to the SiC load train with SiC pins. The tests were carried out in flowing argon at 1200°C in a $MoSi_2$ - element-heated furnace at various constant stresses. The elongation was measured through a quartz window with a laser extensometer directed at the gage length of the specimen. Since Mo-12Si-8.5B contained too much Mo to be oxidation resistant, MoO_3 vapor formed even though protective gas was used. As a consequence, MoO_3 needles deposited at the cool quartz window and eventually interfered with the laser measurement system. While an initial creep test was successful, later creep tests were discontinued prematurely because of measurement problems. Therefore, only few tensile creep data were obtained. In order to generate additional data, slow compression tests were carried out in a screw-driven testing machine at a constant displacement rate (initial strain rate 10^{-5} s^{-1}) and at temperatures ranging from 1200 to 1350°C. The deformation was measured via the crosshead displacement. After an initial rise an approximately

constant stress was reached, which was taken to be the steady-state creep stress associated with the imposed strain rate and temperature.

The data were interpreted in terms of a creep equation of the form

$$\dot{\varepsilon} = A\sigma^n \exp[-Q/(RT)], \quad (1)$$

which describes the strain rate in terms of a materials constant A, the applied stress , the stress exponent n, the activation energy Q, the gas constant R, and the absolute temperature T. From a double-logarithmic plot of the creep rate as a function of the applied stress, the stress exponent was found to be approximately 2.7. Using this value, the values of the unknown activation energy and the constant A were obtained by a nonlinear fit of Eq. (1), solved for the stress, to a plot of the plateau stresses vs temperature (at 10^{-5} s^{-1}). In order to improve the agreement with the creep data, a value of 2.6 was chosen for the stress exponent. This value suggests that viscous dislocation glide, not dislocation climb (which would have a value of 4 to 5), are rate-controlling[10]. In view of the low dislocation mobilities in Mo_3Si and the T2 phase, this conclusion appears to be reasonable. The analysis resulted in the following creep equation:

$$\dot{\varepsilon} = 0.012 s^{-1} (\sigma / MPa)^{2.6} \times \exp[(-285.6 kJ/mol)/(RT)]. \quad (2)$$

Note that the stress σ in this equation has been non-dimensionalized by its unit, MPa. Alternatively, the equation can be written as

$$\dot{\varepsilon} = 2.6 \times 10^{12} s^{-1} (\sigma / E)^{2.6} \times \exp[(-285.6 kJ/mol)/(RT)], \quad (3)$$

where E is the room temperature Young's modulus of Mo-12Si-8.5B, namely, 327 GPa[11].

Table 1 shows that the fitted creep rates calculated from Eqs. (2) or (3) agree well with those measured. This suggests that Eqs. (2) and (3) are good descriptions of the creep rates for the particular range of stresses and temperatures explored. For comparison, the creep rates (at an applied stress of 100 MPa and a temperature of ≈1300°C) of two other silicides are listed in Table 1. The Mo_3Si-Mo_5Si_3-T2 PM material investigated by Meyer et al.[3] has a somewhat lower creep rate than Mo-12Si-8.5B. Since it did not contain α-Mo and only little Mo_3Si (which Meyer et al. believe to be weak as it contains dislocations after creep), one might have expected a much lower creep rate. The fact that its creep rate is not much lower than that of cast and annealed Mo-12Si-8.5B may be the result of its small grain size (4 μm). The grain size of Mo-12Si-8.5B is difficult to determine quantitatively, but it is on the order of 10 to 20 μm for the Mo_3Si and

T2 phases. Subramanian et al.'s single-phase Nb_5Si_3[12], on the other hand, had a very low creep rate under these conditions. It also had a large grain size, on the order of 50 μm. The large grain size, and the absence of α-Nb, are among the reasons for its high strength. In view of the high strength of Nb_5Si_3, Nb may be an effective alloying addition to Mo-Si-B alloys to improve their high temperature creep strength.

Table 1. Comparison between fitted and measured creep rates for Mo-12Si-8.5B, and comparison with other high temperature alloys

Composition, at. %	T, °C	$\dot{\varepsilon}, s^{-1}$	σ_{fitted} MPa	σ_{exp}, MPa
Mo-12Si-8.5B	1200	1×10^{-5}	514	500, 520
"	1250	1×10^{-5}	383	391
"	1300	1×10^{-5}	291	313
"	1350	1×10^{-5}	224	226
"	1200	2.1×10^{-8}	48	50
"	1200	4.5×10^{-8}	64	75
"	1200	1.4×10^{-7}	100	100
"	1300	6.2×10^{-7}	100	
Mo-31.4Si-8.1B[a]	1302	2.1×10^{-7}		100
Nb_5Si_3[b]	1300	7×10^{-9}		100

[a] M. K. Meyer, M. J. Kramer, and M. Akinca [sic], "Compressive Creep Behavior of Mo_5Si_3 with the Addition of Boron," *Intermetallics* 4 (1996) 273

[b] P. R. Subramanian, T. A. Parthasarathy, M. G. Mendiretta, and D. M. Dimiduk, "Compressive Creep Behavior of Nb_5Si_3, *Scr. Metall. Mater*. 32 [8] (1995) 1227.

POWDER-METALLURGICAL MO-SI-B ALLOYS

The purpose of the PM processing was two fold. First, PM processing can provide sound materials with lower α-Mo volume fractions than those produced by melting and casting. Second, PM processing allows more microstructural control than melting and casting. Casting typically results in α-Mo particles in a brittle matrix of Mo_3Si and T2. Powder processing can produce such a structure and it is also suitable for embedding particles of Mo_3Si and T2 in a ductile, continuous α-Mo matrix. While a continuous intermetallic matrix tends to favor oxidation and creep resistance, a continuous α-Mo matrix tends to improve ductility and fracture toughness. In the following, a few examples of microstructures produced by powder metallurgy will be described.

The microstructure of a Mo-15Si-10B alloy hot isostatically pressed (HIPed) from elemental powders was inhomogeneous. It contained large Mo_3Si particles (e.g., 30 μm) in a fine-grained matrix of α-Mo, Mo_3Si, and T2 (see also Table 2). Black spots in the microstructure contained silicon and oxygen and were presumably borosilicate glass. No evidence was found for a continuous α-Mo matrix.

Table 2. Processing details and oxygen contents for HIPed Mo-15Si-10B (2 h/1600°C/30 MPa)

	Mo	Si	B	Mo-15Si-10B
Powder size (μm)	2-8	< 45	< 45	
Purity, wt % (metallic)	99.98	99.99	99.99	
Oxygen concentration, wt %	0.163		3.03	0.156

In a previous report[13] a mixture of coarse Mo_3Si and T2 particles was HIPed with fine Mo powders (see specimen #544 in Table 3). This alloy exhibited a continuous α-Mo matrix. However, the α-Mo volume fraction was too high to result in adequate oxidation resistance. Attempts were made to produce finer microstructures with a lower α-Mo volume fraction. Although the Mo_3Si and T2 powders were wet screened to a mesh size of –325/+635 (20 < size < 45 μm) it appears that many finer particles survived the screening process. These fine particles resulted in fine-grained regions (≈1-2 μm) in the microstructure (Fig. 2, see also specimen #580 in Table 3). The black spots in Fig. 2 are again silica contamination. In another experiment, coarse particles (0.85 mm < size < 2 mm) were prepared from a casting with the composition Mo-18Si-9B and HIPed for 2 h at 1600°C and 200 MPa. Metallographic examination indicated that full densification was achieved. Only few dark spots containing Si and O were found, suggesting a low oxygen content for this alloy.

Intuitively, one would expect the room-temperature strength of Mo-Si-B alloys to decrease with decreasing α-Mo content because there will be less ductile α-Mo to offset the effect of detrimental flaws in the brittle silicide phases. Also, one would expect the fracture toughness to decrease. Figs. 3 and 4 (plotted from the data listed in Table 3 and data from previous reports) verify these trends. In combination with more detailed oxidation and creep data, the fracture toughness trend shown in Fig. 4 will be useful for optimizing the fracture toughness of these alloys while retaining adequate oxidation and creep resistance.

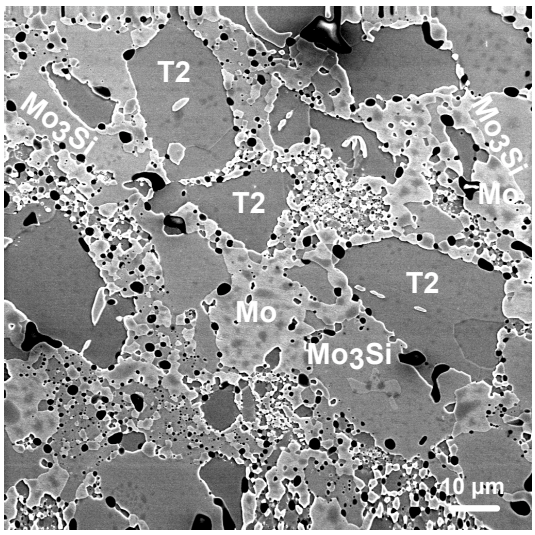

Figure 2: SEM micrograph of polished and etched section of Mo-15.3Si-11.5B hot-pressed from Mo_3Si, T2, and Mo powders (see specimen #580 in Table 3).

Table 3. Processing details, room-temperature fracture toughness, and 3-point flexure strength of Mo-Si-B alloys with different α-Mo volume fractions

Specimen number	Nominal compositions, at. %	α-Mo content, vol %	KQ, MPa $m^{1/2}$	Flexure strength, MPa	Processing details[a]
#562	Mo-18.2Si-13.6B	0	3.3	167	50 wt % Mo_3Si & 50 wt % T2 (-325/+635, dry), HP 1.5 h/30 MPa/1600°C
#561	Mo-15.3Si-11.5B	18	6.2	418	40 wt % Mo_3Si & 40 wt % T2 (-325, dry), 20 wt % Mo, (2-8 µm), HP 1.5 h/30 MPa/1600°C
#571	Mo-15.3Si-11.5B	18	5.8	399	40 wt % Mo_3Si & 40 wt % T2 (-325/+635, dry), 20 wt % Mo (2-8 µm), HP 1.5 h/30 MPa/1600°C
#571	Mo-15.3Si-11.5B	18	6.1	426	
#580	Mo-15.3Si-11.5B	18	7.2	284	40 wt % Mo_3Si & 40 wt % T2 (-325/+635, wet), 20 wt % Mo (2-8 µm), HP 1.5 h/30 MPa/1600°C
#580	Mo-15.3Si-11.5B	18		304	
#531	Mo-12Si-8.5B	38	9.1	484	Cast & annealed (24 h/1600°C/vacuum)
#531	Mo-12Si-8.5B	38	9.8	539	
#544	Mo-12Si-8.5B	38	14.0	384	30.3 wt % Mo_3Si & 28 wt % T2 (-100, dry), 41.7 wt % Mo (2-8 µm), HIP 1 h/200 MPa/1650°C
#544	Mo-12Si-8.5B	38	15.6	376	
#544	Mo-12Si-8.5B	38		412	
#544	Mo-12Si-8.5B	38		408	

[a]Prior to consolidation by hot-pressing (HP) or HIPing, the powders were screened either dry or wet with the indicated screen sizes (-100 mesh = <150 µm; -325 mesh = <45 µm; -635 mesh = <20 µm).

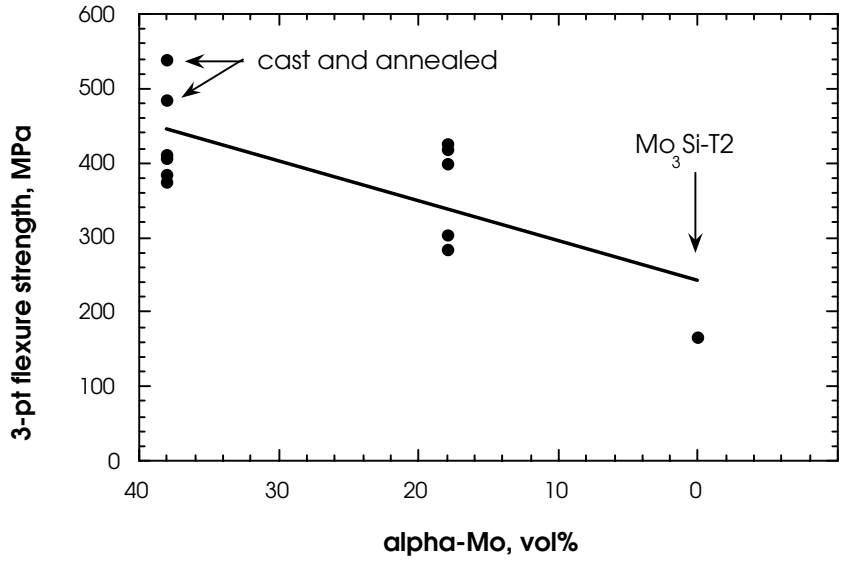

Fig. 3 Room-temperature flexure strength vs α-Mo volume fraction for PM alloys and cast and annealed Mo-12Si-8.5B.

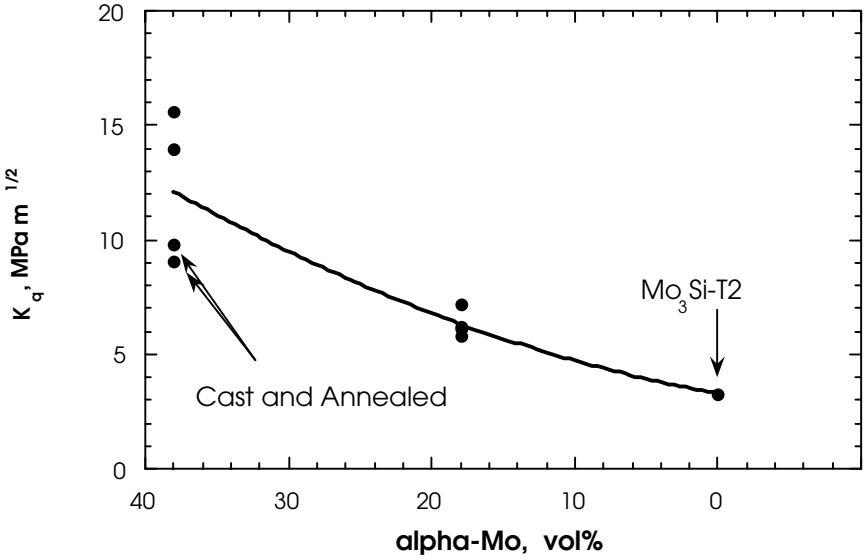

Fig. 4 Room-temperature fracture toughness vs α-Mo volume fraction for PM alloys and cast and annealed Mo-12Si-8.5B.

ACKNOWLEDGMENTS

This research was sponsored by the Office of Fossil Energy, Advanced Research and Technology Development (AR&TD) Materials Program, U.S. Department of Energy, under contract DE-AC05-00OR22725 with UT-Battelle, LLC. The help of C. A. Carmichael in the alloy preparation is greatly appreciated.

REFERENCES

1. H. Nowotny, E. Kimakopoulou, and H. Kudielka, "Untersuchungen in den Dreistoffsystemen: Molybdän-Silizium-Bor, Wolfram-Silizium-Bor und in dem System: VSi_2-$TaSi_2$," *Mh. Chem.* 88 (1957) 180.
2. A. J. Thom, M. K. Meyer, Y. Kim, and M. Akinc, "Evaluation of $A_5Si_3Z_X$ Intermetallics for Use as High Temperature Structural Materials," in *Processing and Fabrication of Advanced Materials III*, V. A. Ravi et al., eds., TMS, 1994, p. 413.
3. M. K. Meyer, M. J. Kramer, and M. Akinca [sic], "Compressive Creep Behavior of Mo_5Si_3 with the Addition of Boron," *Intermetallics* 4 (1996) 273.
4. M. Meyer, M. Kramer, and M. Akinc, "Boron-Doped Molybdenum Silicides," Adv. Mater. 8 (1996) 85.
5. D. M. Berczik, United States Patent 5,595,616 (1997), "Method for enhancing the oxidation resistance of a molybdenum alloy, and a method of making a molybdenum alloy."
6. D. M. Berczik, United States Patent 5,693,156 (1997) "Oxidation Resistant Molybdenum Alloy."
7. J. H. Perepezko, C. A. Nunes, S.-H. Yi, and D. J. Thoma, "Phase Stability in Processing of High Temperature Intermetallic Alloys," *MRS Symposium Proceedings* Vol. 460, C. C. Koch et al., eds., 1996, pp. 3-14
8. C. A. Nunes, R. Sakidja, and J. H. Perepezko, "Phase Stability in High Temperature Mo-rich Mo-B-Si Alloys, in *Structural Intermetallics 1997*, eds. M. V. Nathal et al., TMS, 1997, pp. 831-839.
9. R. Sakidja, H. Sieber, and J. H. Perepezko, "Microstructural Development of Mo-rich Mo-B-Si Alloys, in *Molybdenum & Molybdenum Alloys*, A. Crowson, E. S. Chen, J. A. Shields, and P. R. Subramanian, eds., TMS, Warrendale, PA, 1998, pp. 99-110.
10. J.-P. Poirier, *Creep of Crystals*, Cambridge University Press, Cambridge, 1985.
11. J. H. Schneibel, C. T. Liu, L. Heatherly, Jr., and C. A. Carmichael, "Processing and Properties of Molybdenum Silicide Intermetallics containing Boron," *Proc. 12th Annual Conference on Fossil Energy Materials*, R. R. Judkins, ed., Knoxville, TN, 1998.
12. P. R. Subramanian, T. A. Parthasarathy, M. G. Mendiretta, and D. M. Dimiduk, "Compressive Creep Behavior of Nb_5Si_3, *Scr. Metall. Mater*. 32 [8] (1995) 1227.
13. J. H. Schneibel and C. A. Carmichael, "Processing and Properties of Molybdenum Silicide Intermetallics containing Boron," *Proc. 13th Annual Conference on Fossil Energy Materials*, R. R. Judkins, ed., Knoxville, TN, 1999.

DEVELOPMENT OF INTERMETALLIC-REINFORCED AND OXIDE-DISPERSION DUCTILIZED CR ALLOYS FOR AGGRESSIVE HIGH-TEMPERATURE ENVIRONMENTS

M. P. Brady, C. T. Liu, J R. Keiser, P. F. Tortorelli, V. K. Sikka, E. Lara-Curzio, C. A. Walls, C.G. Westmoreland, C. A. Carmichael, J. L. Wright, J. D. Vought, M. Howell, H. Longmire, and K. L. Crowley Oak Ridge National Laboratory and M. L. Weaver, The University of Alabama

INTRODUCTION

A new family of structural Cr alloys based on Cr-(6-10)Ta (at.%) is under development for high-temperature use (900-1300°C) in the oxidizing and aggressive hot corrosion environments encountered in advanced fossil energy conversion and combustion systems[1,2]. The microstructures of these alloys consist of a Cr solid solution matrix reinforced with the intermetallic Cr_2Ta Laves phase (for high-temperature strength) as a dispersed second phase particle or in a lamellar Cr solid solution-Cr_2Ta eutectic structure (Fig. 1). The compositions of interest are in the range of: Cr-(6-10)Ta-(3-6)Mo-(0.5-3)Si-(0.2-1.0)Ti-(0.05-0.2)La/Ce at.% [3]. The Mo is added for solid solution strengthening, Si (primarily) for oxidation resistance, Ti for interstitial gettering, and La or Ce for oxidation resistance and interstitial gettering.

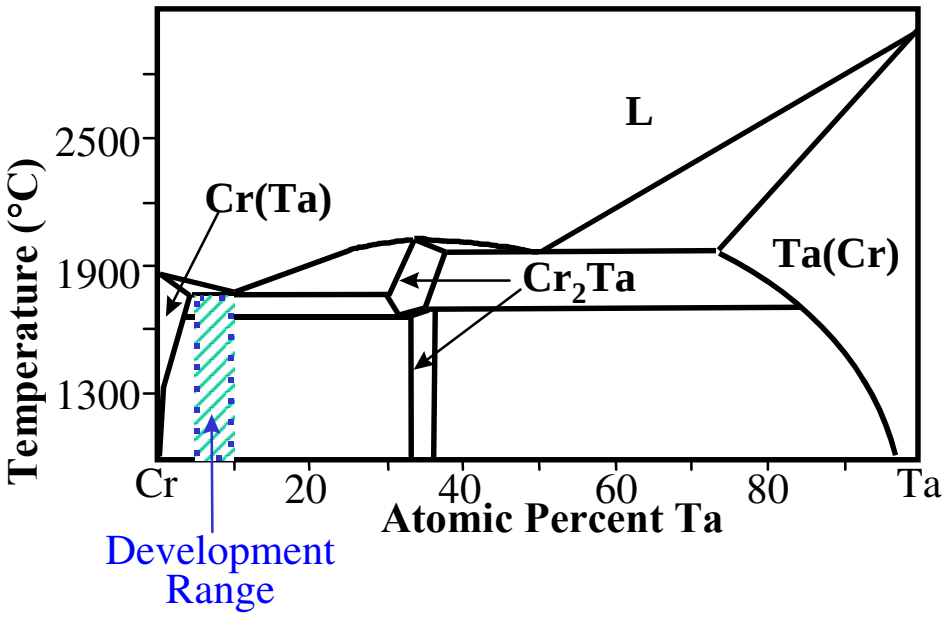

Fig. 1- Schematic binary Cr-Ta phase[4,5].

Substantial progress has been made in developing attractive high-temperature properties. Microalloying with Si and La has yielded alloys with oxidation resistance in the range reported for commercial Cr_2O_3-forming alloys (900-1100°C, air, 1000 h duration)[2]. The alloys exhibit tensile fracture strengths in excess of 700 MPa at 1000°C and in excess of 400 MPa at 1200°C [1.] Further, cast Cr-8Ta-5Mo-0.5Ti-0.01Ce at. % was creep tested up to 1438 h at 1000°C in humid room air under a load of 138 MPa, at which point the test was stopped due to failure of the grip rods[2]. However, room temperature fracture toughness remains the key challenge for development. Current compositions exhibit a brittle to ductile transition temperature in the range of 800 to 1000°C[1,2]. At room temperature, tensile fracture strengths are in excess of 700 MPa, but no plastic tensile elongation is observed and fracture toughness is generally in the range of 11to 12 MPa $m^{1/2}$ [1].

Three approaches for improved ductility and toughness at room temperature are under investigation: directional solidification[6], microalloying/microstructure control[7], and interstitial nitrogen gettering[2,8] via spinel-based oxide dispersions. This paper presents the results of room-temperature tensile and fracture toughness studies of microalloyed Cr-Cr_2Ta-based alloys and MgO/$MgCr_2O_4$ spinel-dispersed Cr and Cr-Cr_2Ta alloys. Sufficiently promising mechanical behavior has been achieved to initiate consideration of these alloys for low-impact, high-temperature component applications such as thermowells, spouts, and brackets. The results of high-temperature corrosion screenings in alkali molten salt and coal slag environments relevant for such components are also presented.

ROOM-TEMPERATURE MECHANICAL PROPERTIES

Subsized chevron-notched three-point bend samples approximately 3 × 4 × 25 mm were used to evaluate fracture toughness at room temperature. The samples were prepared to a 600-grit surface finish and then notched using a low speed diamond saw. The crosshead speed was 0.6 mm/min. A modulus of 250 GPa was estimated for Cr-Cr_2Ta-based alloys and 300 GPa for Cr-based alloys. Fracture-toughness values obtained by this technique should be considered semiquantitative; details are provided in reference 9.

Room-temperature tensile properties were evaluated using dogbone tensile samples approximately 0.6 to 0.7 mm thick with a gage length of 12.7 mm. The samples were prepared to a surface finish of 600 grit, and a crosshead speed of 2.54 mm/min was used.

Microalloying/Microstructure Effects For CR-CR_2TA Alloys

The Cr(Ta)-Cr_2Ta eutectic occurs between approximately 9.5 and 10 at. % Ta (Fig 1)[5], which is at a lower Ta level than the currently accepted Cr-Ta phase diagram, which shows this eutectic composition

at approximately 13 at.% Ta[4]. The fracture toughness values of cast, binary near hypo- and hyper- eutectic alloys (Cr-8Ta, Cr-9.8Ta, Cr-11Ta at. %) showed no major differences at room temperature and ranged from 9 to 10 MPa $m^{1/2}$ [10]. However, preliminary evaluation of Cr-Ta alloys with additions of Mo, Ti, and Ce suggests that the primary Cr(Ta) regions present in hypoeutectic compositions may be detrimental to room-temperature fracture toughness (Fig. 2).

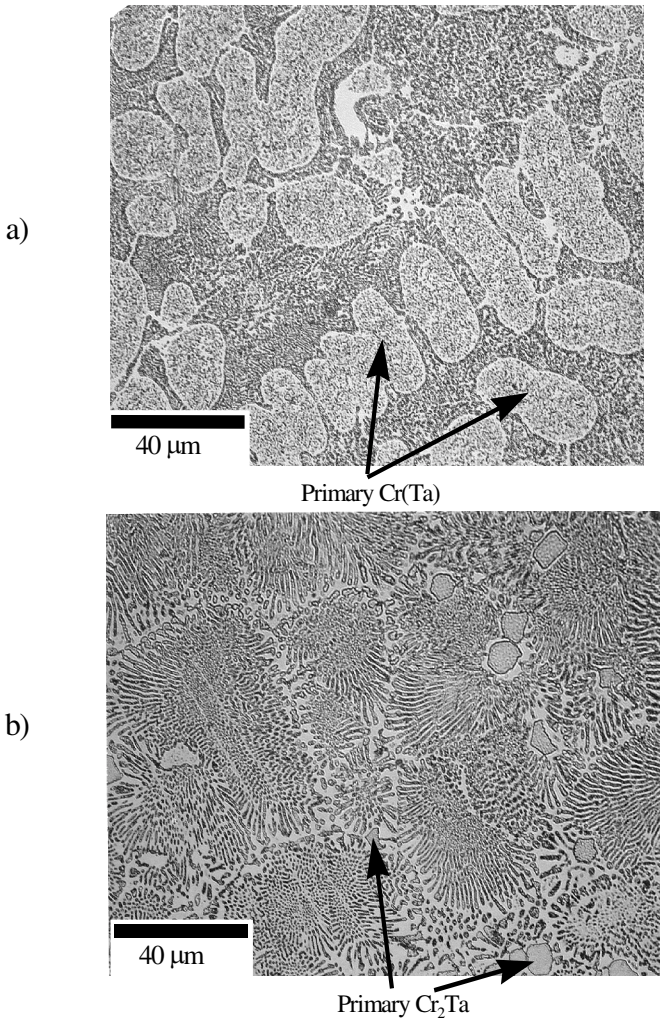

Fig. 2. Optical (light microscopy) microstructures. The Cr(Ta) phase appears light and the Cr2Ta phase appears dark. (a) Hypoeutectic Cr-8Ta-5Mo-0.5Ti-0.01Ce. (b) Hypereutictic Cr-10Ta-5Mo-0.5Ti-0.01Ce.

Cast and heat-treated Cr-8Ta-5Mo-0.5Ti-0.05Ce at. % exhibited toughness values of 7.4 and 8.3 while similarly processed Cr-10Ta-5Mo-0.5Ti-0.01Ce at. % exhibited values of 9.4 and 12.8 (two test samples per composition). It is speculated that the large volume fraction of fine Cr_2Ta precipitates in the primary

Cr(Ta) microstructural regions, which form due to the decreasing solubility of Ta in Cr with decreasing temperature, may degrade ambient toughness. Microalloying of the (just) hypereutectic composition Cr-9.85Ta-5Mo-0.5Ti-0.1La with 1 at.% Si yielded an additional increase in room-temperature toughness from 11.3-11.5 to 12.7-14.3 (two test samples per composition). Detailed study and confirmation of these effects are in progress.

Spinel Dispersed Ductile CR

A major contributor to the ambient brittleness of Cr is the presence of nitrogen interstitials. Work by Scruggs and co-workers in the 1960s demonstrated that plastic tensile elongations up to 20% could be achieved at room temperature in Cr via the addition of MgO[8,11,12]. The baseline composition of these alloys was Cr-(3-6)MgO-0.5Ti wt. %. During powder processing, the MgO particles convert to a $MgCr_2O_4$ spinel, which was hypothesized to getter nitrogen from the Cr, rendering it ductile[8,11,12]. A sintered and extruded ingot of Cr-6MgO-0.5Ti wt.% provided by Scruggs was found to exhibit an average plastic tensile elongation of 8.2% (three samples) with a 600-grit surface finish and a strain rate of 3.33×10^{-3}/s, despite a nitrogen impurity level of 0.03 wt. % (Fig. 3)[2]. When polished to a 180-grit finish, under the same test

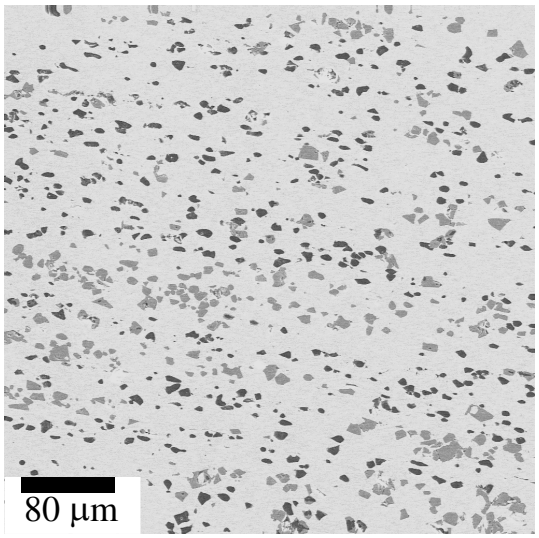

Fig. 3. SEM (backscatter mode) micrograph of sintered and extruded Cr-6MgO-0,5Ti provided by Scruggs. The dark particles are MgO and the light particles are $MgCr_2O_4$ spinel.

conditions, plastic tensile elongation was reduced to below 2 to 3% (i.e., the material exhibited a degree of notch sensitivity). The fracture appeared to be predominately cleavage-type in all cases, regardless of the surface finish or the extent of plastic tensile elongation.

Table 1 summarizes room-temperature mechanical properties for a series of hot-pressed or hot-pressed and extruded Cr-6MgO-wt.%-based alloys produced from MgO and elemental Cr, Ti, or Ta powders. As with the original Scruggs extrusion (Fig. 3), approximately one-half to two-thirds of the MgO particles in the Cr-MgO and Cr-MgO-Ti alloys were converted to the $MgCr_2O_4$ spinel phase (identification based solely on composition).

Only modest tensile ductility was exhibited by as-hot-pressed material. Subsequent extrusion more than doubled the plastic tensile elongation at room temperature. The increase in tensile ductility with extrusion may be the result of a finer, more uniform distribution of $MgO/MgCr_2O_4$ particles in the microstructure (large agglomerations of particles may act as local notches). The texture introduced by extrusion may also contribute to the higher ductility, as the gage section of the tensile samples was oriented parallel to the extrusion direction.

Table 1. Room-temperature mechanical properties for Cr-6MgO-based alloys

	Tensile strength (MPa)			
Alloy (wt. %)	**Yield**	**Fracture**	**% Elongation**	**Toughness (MPa $m^{1/2}$)**
		Hot-pressed 1590°C for 2 h		
Cr-6MgO				28, 20.1
	220	324	5.2	
	209	290	3.5	
Cr-6MgO-1Ti				16.7, 15.5
	201	344	5.4	
	210	322	3.1	
Cr-6MgO-2.2Ti				Not measured
	338	372	1-1.5 range	
	283	338	1-1.5 range	
		Hot-pressed 1590°C for 2 h and extruded 1300°C 3 in. compact to 1 in. die		
Cr-6MgO-0.75Ti				27.3, 17.2
	227	393	12.9	
	243	388	10.7	
		Hot-pressed 1500°C for 2 h (melted during 1590°C hot press)		
Cr-6MgO-15.5Ta				13.5, 13.1
	255	255	<1	
	253	253	<1	

The Ti addition does not appear to play a critical role in the ductilization mechanism: similar tensile elongations were exhibited by Cr-6MgO and Cr-6MgO-1Ti. This was surprising because Ti was observed to segregate to the $MgCr_2O_4$ spinel and was initially suspected of playing a key role in the nitrogen-gettering process. Interestingly, although tensile ductility was similar, these preliminary data suggest that the fracture toughness of Cr-6MgO was significantly higher than that of Cr-6MgO-1Ti. A Ti-rich phase consistent with that of the $TiCr_2$ Laves phase was observed in a Cr-0.5Ti wt.% control alloy[13], and, if present in the Cr-6MgO-1Ti wt. % alloy, may be the source of the decreased toughness. The formation of a $TiCr_2$ Laves phase with additions of Ti in Cr-6MgO is consistent with the increased strength and decreased ductility exhibited by the Cr-6MgO-2.2Ti wt. % alloy.

Attempts to introduce the ductilizing MgO effect into the high-strength Cr_2Ta-reinforced Cr alloys have not yet been successful. The addition of 15.5 wt. % Ta to Cr-6MgO resulted in complete loss of tensile ductility, with no increase in strength. Initial microstructural analysis suggests that Ta interferes with the formation of the $MgCr_2O_4$ spinel phase, resulting instead in the formation of a Mg-Ta-O phase. It is not clear whether the absence of nitrogen gettering by the Mg-Ta-O phase, the presence of a small amount of Ta in solution in the Cr phase, or the presence of a significant volume fraction of the Cr_2Ta Laves phase caused the poor room-temperature ductility exhibited by Cr-6MgO-15.5Ta wt. Evaluation of the use of prealloyed Cr-Ta powders, mechanical alloying, and direct addition of spinel phases such as $MgAl_2O_4$ is ongoing[8,11].

HIGH-TEMPERATURE CORROSION SCREENINGS

The mechanical properties achieved to date in both the Cr_2Ta-reinforced Cr and spinel-dispersed ductile Cr are sufficiently encouraging to initiate evaluation of these alloys for low-impact, high-temperature components such as thermowells, spouts, and brackets for aggressive environments (as well as corrosion-resistant coatings). Of particular interest are molten alkali salt and coal slag environments, in which conventional alumina- and chromia-forming alloys are rapidly attacked. While ceramics and/or refractories often offer improved performance with respect to metals in such environments, high-temperature corrosion is still a major issue, and, further, ceramics/refractories are brittle and exhibit poor fabricability. The developmental Cr alloys may represent an attractive alternative for such applications. High-temperature corrosion screening was initiated in two environments: molten alkali salt (smelt) and molten coal slag.

Exposure in Molten Smelt

Smelt is the molten alkali salt byproduct of the burning of the black liquor product of the kraft pulping process. Traditionally, the Tomlinson recovery boiler is used to burn black liquor to dispose of organic

waste, recover inorganic chemicals, and produce electric power for the paper and pulp plant. Black liquor gasification represents a more cost-effective and efficient alternative to recovery boilers. With combined-cycle black liquor gasification, it is predicted that two to three times more electricity can be produced, giving the mill the opportunity to generate all of its own energy needs[14]. However, numerous materials-related issues have surfaced in pilot-scale testing of black liquor gasification[15]. In particular, the molten smelt has been found to be extremely corrosive, and currently available metallic materials are aggressively attacked and corroded in this environment. There is a great need for smelt-resistant alloys and coatings for components ranging from thermowells and brackets to spouts and structural components.

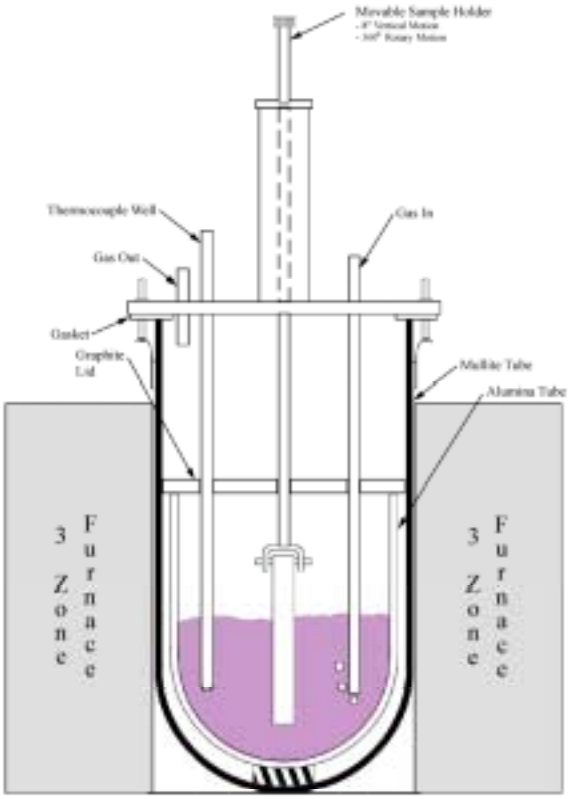

Fig. 4. Schematic of smelt immersion test rig.

The smelt is based on Na_2CO_3 and typically contains significant amounts of Na_2S, Na_2SO_4, and KCl. It becomes molten above about 700 to 800°C and can reach temperatures of up to 1000 to 1100°C during operation. Lab-scale smelt-immersion screenings were conducted between 850 and 1000°C in smelt collected at a commercial papermill. A schematic of the laboratory smelt immersion test apparatus is shown in Fig. 4. Argon gas was bubbled into the molten smelt for agitation. Oxygen gettering was accomplished by the addition of graphite coupons to the molten smelt in combination with a graphite

lid on the furnace. Comparison with in-plant exposed material of both conventional alloys and refractories suggests that this screening apparatus provides a reasonable evaluation of corrosion resistance in molten smelt[16].

Little attack was observed for sintered and extruded Cr-6MgO-0.5Ti wt.% and cast Cr-9.8 Ta at.% (27.4 wt.% Ta) in an initial 100-h smelt immersion screening at 850°C. At 1000°C, a 500-h immersion in molten smelt resulted in the formation of a Cr-Na-O rich scale approximately 0.3 mm thick on hot-pressed and extruded Cr-6MgO-0.75Ti wt.% [Fig. 5(a)]. Underneath the scale, a 0.2-mm-thick zone of hardened metal (Vicker's hardness of 900; 100-g load, 15 s), which separated from the underlying, unaffected metal (Vicker's hardness of 150) during metallographic preparation, was evident [Fig. 5(a)]. For comparative purposes, a 3.2-mm-thick rectangular bar of alloy 671 (Ni-48Cr wt.% base), generally considered the most smelt-resistant metallic material available, was immersed in the molten smelt for only 100-h at 1000°C. The depth of attack in alloy 671 ranged from 0.6 to 0.8 mm [Fig. 5(b)]. Assuming linear corrosion kinetics for both alloys (and including the hardened zone in Cr-6MgO-0.75Ti as scale), this screening suggests that Cr-6MgO-0.75Ti wt.% may be at least 6 to 7 times more resistant to molten smelt than alloy 671. Based on these promising preliminary results, more detailed lab-scale testing and evaluation of Cr-MgO and Cr-Ta base alloys in molten smelt environments are planned, including microalloying for optimization of corrosion resistance and in-plant exposure of test coupons.

Exposure in Molten Coal Slag

There is a great need for coal-slag-resistant materials for use in coal-gasification systems. Such environments are extremely aggressive, with temperatures routinely in the 1250 to1400°C^{+} range. The Cr_2Ta-reinforced Cr alloys are potentially attractive for low-impact load components, such as thermowells, in locations where coal slag is constantly present (assuming the coal slag would act as a physical barrier to Cr_2O_3 scale volatilization). As a simple first-step screening, coupons were loaded into a SiC crucible filled with Baldwin Illinois #6 coal slag (53.4 SiO_2-18.6 Al_2O_3-17.6 Fe_2O_3-7.1CaO-1.7 K_2O-0.9 MgO-0.7 TiO_2 wt.%). The mixture was heated in air for the desired temperature/time conditions. It is recognized that the actual coal gasification environment is much more complex and much more aggressive than this simple screening test implies. Further, significant interaction of the molten slag with the SiC crucible was observed. The goal of this experiment was simply to ascertain whether sufficient promise exists to pursue more rigorous coupon exposures in coal-slag environments.

a)

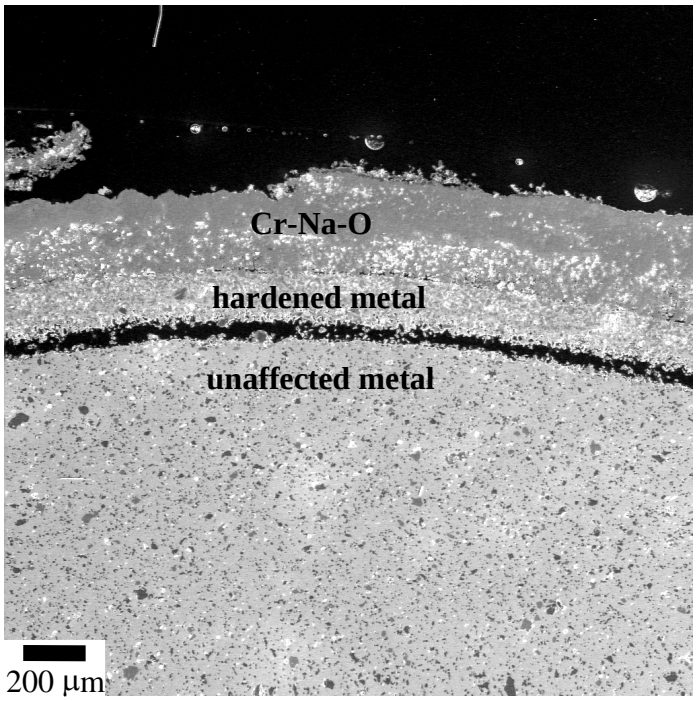

b)

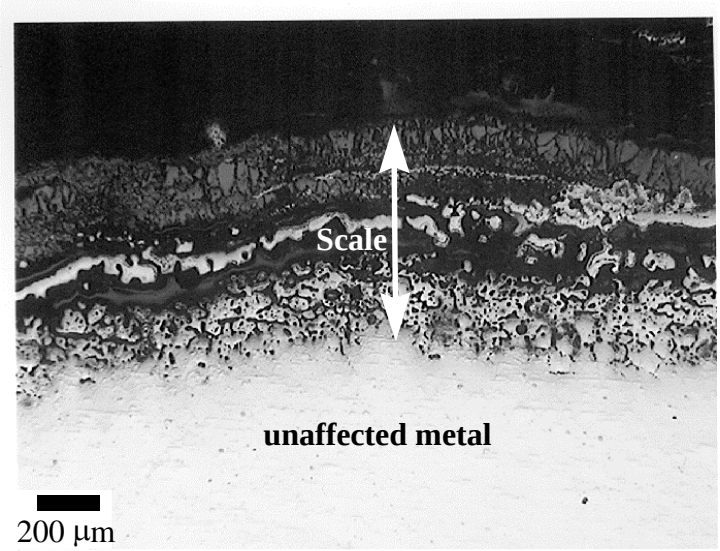

Fig. 5. Cross-section micrographs after immersion in molten smelt at 1000°C. (a) Region of greatest attack for Cr-6MgO-0.75Ti wt. % after **500 h** (secondary mode SEM). (b) Region of least attack for Alloy 671 after **100 h**(light microscopy).

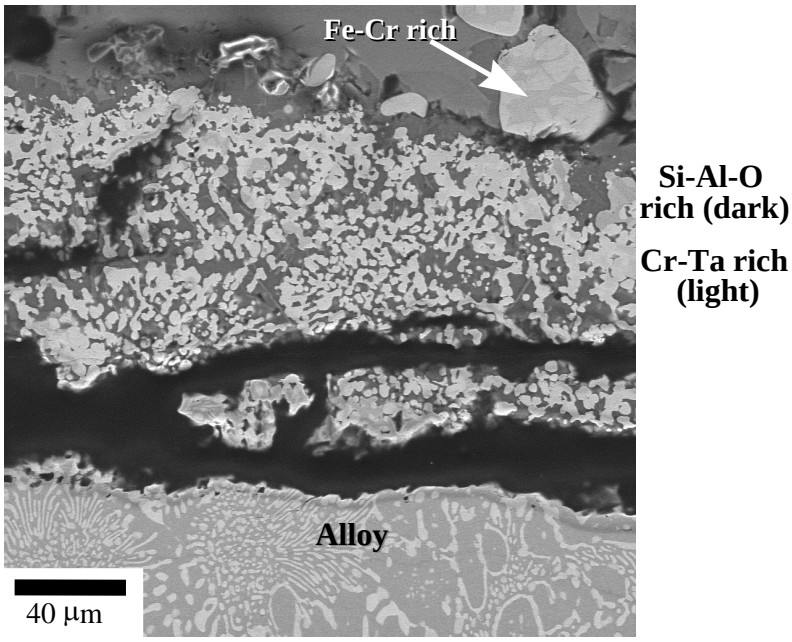

Fig. 6. SEM (secondary mode) cross-section micrograph of Cr-8Ta-5Mo-3Si-0.5Ti-0.1La after immersion in molten coal slag at 1275°C for 168 h. The Cr(Ta) phase appears dark and the Cr_2Ta phase appears light in the alloy region.

The microstructure of Cr-8Ta-5Mo-3Si-0.5Ti-0.1La at. % after immersion in the coal slag at 1275°C for 168 h is shown in Fig. 6. A complex scale consisting of a Cr-Ta rich phase and a Si-Al-O rich phase was formed. Nodules of a Fe-Cr rich phase were also observed. (The preliminary analysis was not able to definitively distinguish whether the Cr-Ta and Fe-Cr rich phases were oxide or metallic). The scale thickness varied between approximately 0.1 and 0.2 mm. At 1350°C, more extensive attack was observed. After only 50 h, the scale thickness was already approximately 0.25 mm on the bottom portion of the coupon, which was completely immersed in the slag. The upper portions of the coupon appeared to have been partly exposed to air, and suffered from extensive attack (1-mm scale thickness). The behavior at 1275°C was considered sufficiently positive that exposures in simulated coal combustion and gasification slagging environments are planned. However, based on the extent of attack observed at 1350°C, it is unlikely that these alloys could be used in slagging environments above 1300°C.

ACKNOWLEDGMENTS

The authors thank D. M. Scruggs for donation of a Cr-MgO alloy ingot and helpful discussions regarding his efforts in the 1960 to ductilize Cr. The authors also thank D. F. Wilson and J. H. Schneibel for their reviews of this manuscript. This research was sponsored by the U.S. Department of Energy, Fossil Energy Advanced Research Materials (ARM) Program and by the Assistant Secretary for Energy

Efficiency and Renewable Energy, Office of Industrial Technologies, Advanced Industrial Materials Program. Oak Ridge National Laboratory is managed by UT-Battelle, LLC, for the U.S. Department of Energy under contract No. DE-AC05-00OR22725.

REFERENCES

1. M. P. Brady, J. H. Zhu, C.T. Liu, P. F. Tortorelli, J. L. Wright, and C. A. Carmichael, in *Proc. of the Twelfth Annual Conference on Fossil Energy Materials*, Knoxville, R. R. Judkins (comp.), U. S. Department of Energy, paper 4.9 (1998).
2. M. P. Brady, J. H. Zhu, C.T. Liu, P. F. Tortorelli, L.R. Walker, C G. McKamey, J. L. Wright, C. A. Carmichael, D. J. Larson, M. K. Miller, and W. D. Porter, *Materials at High Temperatures*, vol. 16, no. 4, pp. 189-193 (1999).
3. C. T. Liu, M. P. Brady, J. H. Zhu, and P. F. Tortorelli, "Dual Phase Cr-Ta Alloys for Structural Applications", submitted to U.S. Patent Office.
4. M. Venkatraman and J. P. Neumann, in *Binary Alloy Phase Diagrams* Vol. 1, T. B. Massalaski, J. L. Murray, L. H. Bennett, and H. Baker eds., ASM, p. 867 (1986).
5. J. H. Zhu and C. T. Liu, unpublished research (1997).
6. Y. He, P. Liaw, C. T. Liu, L. Heatherly, and E. P. George, to be published in the *Proceedings of the Fourteenth Annual Conf. on Fossil Energy Materials* (2000).
7. C. T. Liu, J. H. Zhu, M. P. Brady, C. G. McKamey, and L. M. Pike, "Physical Metallurgy and Mechanical Properties of Transition-Metal Laves Phase Alloys", *Intermetallics*, in press.
8. D. M. Scruggs, L. H. Van Vlack, and W. M. Spurgeon, *J. Amer. Ceram. Soc.*, 51, 9, pp. 473-481 (1968).
9. J. H. Schneibel, C. A. Carmichael, E. D. Specht, and R. Subramanian, Intermetallics, 5, p. 61 (1997).
10. M. P. Brady, J. H. Zhu, C.T. Liu, P. F. Tortorelli, and L. R. Walker, "Oxidation Resistance and Mechanical Properties of Laves Phase Reinforced Cr In-Situ Composites", *Intermetallics*, in press.
11. D. M. Scruggs, 'Ductile Chromium Composition", U.S. Patent 3, 175, 279 (Mar. 30, 1965).
12. D. M. Scruggs, *American Rocket Society Journal*, 31, 11, pp. 1527-1533 (1961).
13. I. M. Anderson, M. L. Weaver, and M. P. Brady, unpublished research (1999).
14. E. D. Larson, W. Yang, K. Iisa, E. W. Malcom, G.W. McDonald, W.J. Frederick, T.G. Kreutz, and C. A. Brown, in *Proceedings of the International Chemical Recovery Conference*, TAPPI Press, Atlanta, GA, pp. 1-18 (1998).
15. C. A. Brown and W. D. Hunter, in *Proceedings of the International Chemical Recovery Conference*, TAPPI Press, Atlanta, GA, pp. 655-662 (1998).
16. J. R. Keiser, unpublished research, 1999.

EVALUATION OF IRON-ALUMINIDE COATINGS FOR HIGH-TEMPERATURE CORROSION PROTECTION

B. A. Pint, P. F. Tortorelli, I. G. Wright, J. A. Haynes, and W Y. Lee*

*present address
Stevens Institute of Technology
Hoboken, New Jersey 07030

ABSTRACT

Initial results on the oxidation performance of three types of iron-aluminide-based coatings are presented. The coatings were fabricated by a conventional plasma spray process, high-velocity oxy-fuel (HVOF) deposition, and chemical vapor deposition (CVD). The latter two techniques show promising results in terms of oxidation performance at 800°C on substrates including mild steel, a tool steel, Fe-9Cr-1Mo and type 304 stainless steel. While chromia-forming steels possess some degree of corrosion resistance, the presence of SO_2 and water vapor in combustion environments can greatly degrade their corrosion resistance. An aluminide coating forms an alumina scale that has been shown to be less affected by the presence of sulfur or water vapor than chromia or silica scales. Thus there is particular interest in fabricating a reliable alumina-forming coating. One source of difficulty may be the high coefficient of thermal expansion observed in iron aluminides. This may represent a problem in mechanical integrity during thermal cycling at high temperatures.

INTRODUCTION

This work comprises part of an effort focused on evaluation of metallic coatings for high-temperature corrosion resistance. The ultimate goal is to identify candidate material systems for significantly extending corrosion-limited lifetimes of high-temperature components in advanced fossil systems. The general approach is based on matching an appropriate synthesis technique (developed elsewhere) with the composition and microstructure required for fossil environments associated with Vision 21 concept technologies. It involves coordination with the appropriate coating efforts sponsored by the Advanced Research and Technology Development Program, as well as by others.

Given the excellent high-temperature oxidation-sulfidation resistance of iron aluminides in many prototypic fossil environments (e.g., Refs.1-4), this work has focused on an examination of iron-aluminum coatings on steel substrates as prepared by plasma spray (PS) processing and high-velocity oxy-fuel (HVOF) deposition at Idaho National Engineering and Environmental Laboratory (INEEL) and by chemical vapor deposition (CVD) at ORNL. Previous studies have presented results on weld-overlay coatings[5-8] and conventional air thermal spraying.[9] Preliminary characterization of the present coatings involved relatively simple high-temperature oxidation exposures, which are sufficient for

first-stage evaluation of the protectiveness afforded by the various coatings to the steel substrates. In these initial tests, both HVOF and CVD showed promising results.

RESULTS

HVOF Coatings

Coatings were fabricated by two methods at INEEL. The first technique involved thermal spraying of Fe_3Al powder by HVOF.[10] Fig.1 shows the as-sprayed microstructure of the FAS (nominally Fe-28at%Al-2Cr) coating on a mild steel (A36, nominally Fe-1Mn-0.2Si-0.2C) substrate. The maximum use temperature of mild steel in oxidizing environments is limited to ≈500°C, because of the rapid metal consumption that occurs when FeO can form. The FAS HVOF coating on A36 had a significant beneficial effect on the oxidation performance at 800°C. However, because the coating is only on one side of the substrate, mass gains of the test coupons do not show the true effect of the coating. (Attempts to protect the uncoated faces with a ceramic coating have not been successful so far.) A metallographic cross-section of the exposed specimen is shown in Fig. 2. After 24 h at 800°C, the uncoated face formed a very thick oxide, while the coated face formed an oxide too small to be detected by light microscopy. The edge of the specimen showed heavy attack of the substrate beneath the coating and virtually no attack of the coating itself [Fig. 2(c)]. The only indication of an adverse reaction was a small amount of localized oxide observed at the coating-substrate interface [arrow in Fig. 2 (a)]. However, further characterization by electron probe microanalysis (EPMA) showed either no oxide formation or a thin (<1 μm) Fe-rich oxide at the coating-substrate interface in most locations [Fig. 3 (a)]. More extensive characterization and testing is planned for this class of coatings.

Plasma-Sprayed Coatings

The same FAS powder composition also was deposited on a type 304 stainless steel substrate by plasma spraying (PS) under two different process gases, argon-helium and argon-hydrogen. Previous work with coatings plasma-sprayed in air did not show good

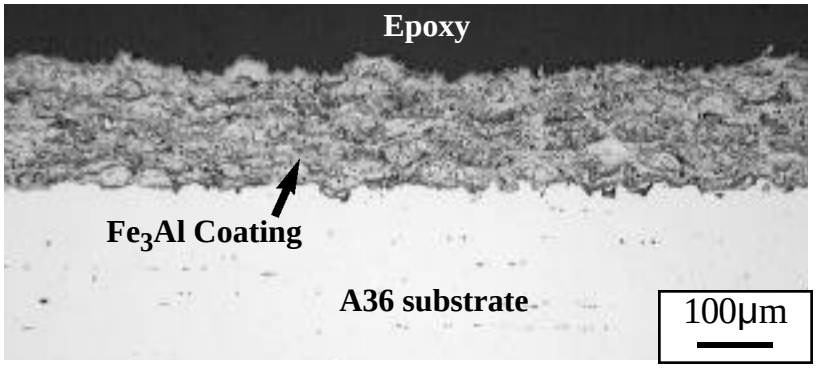

Fig. 1. Metallographic cross-section of the as-deposited HVOF iron aluminide coating on a mild steel (A36) substrate.

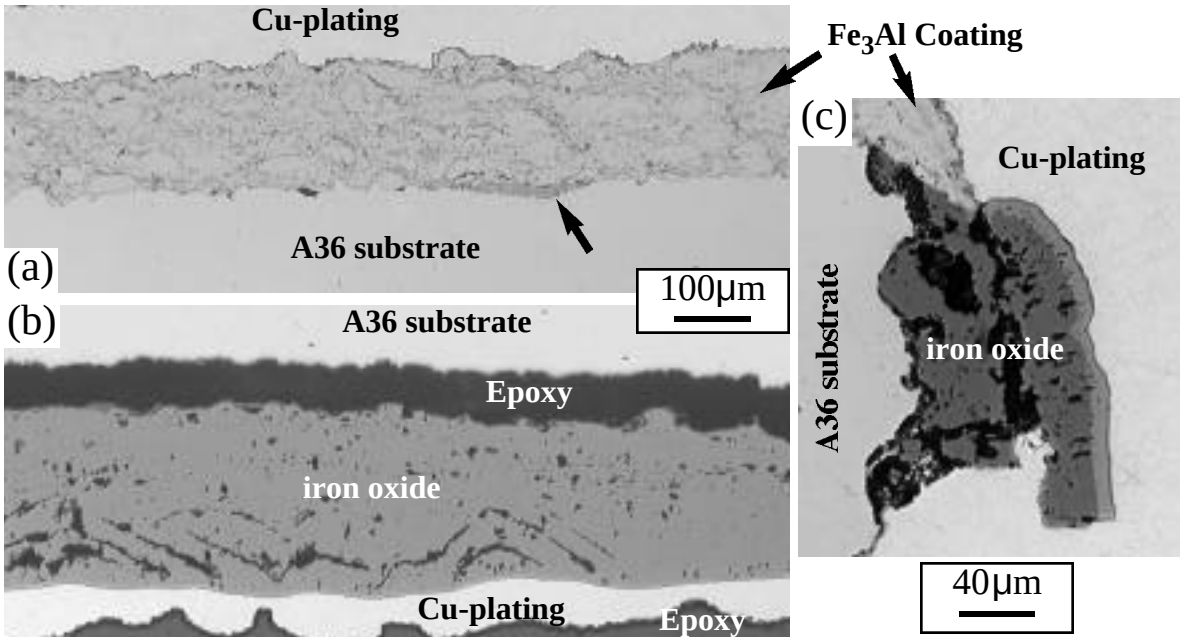

Fig. 2. Copper-plated metallographic section of a mild steel coupon HVOF coated with Fe_3Al oxidized for 24 h at 800°C. (a) the coated face formed only a very thin oxide (not visible by light microscopy), (b) the uncoated face formed a very thick iron oxide which separated from the substrate and (c) at the edge of the specimen the substrate beneath the coating was consumed but only a fragment of the scale remained attached. In one area (arrow in (a)), a thicker oxide was observed beneath the coating.

results, likely due to excessive depletion of Al oxidation during deposition.[9] Type 304 stainless steel (nominally Fe-18Cr-9Ni) has a much higher corrosion resistance than mild steel so no voluminous iron oxide forms at 800°C, instead a relatively thin oxide formed after 24 h, Fig. 4c. After 24 h, the PS coatings appeared to be generally protective. However, the coating deposited with an Ar-He process gas appeared to be less dense (Fig. 4 (a)

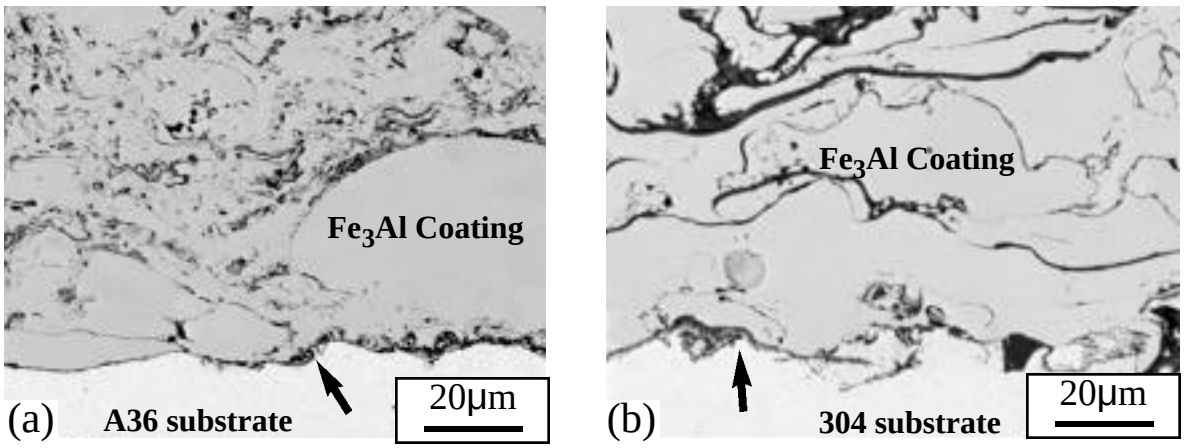

Fig. 3. EPMA secondary electron images of the coating-substrate interface after 24 h at 800°C for (a) HVOF FAS on A36 and (b) PS FAS on 304 fabricated with Ar-He process gas . A thin oxide was noted in some areas in both cases (arrows).

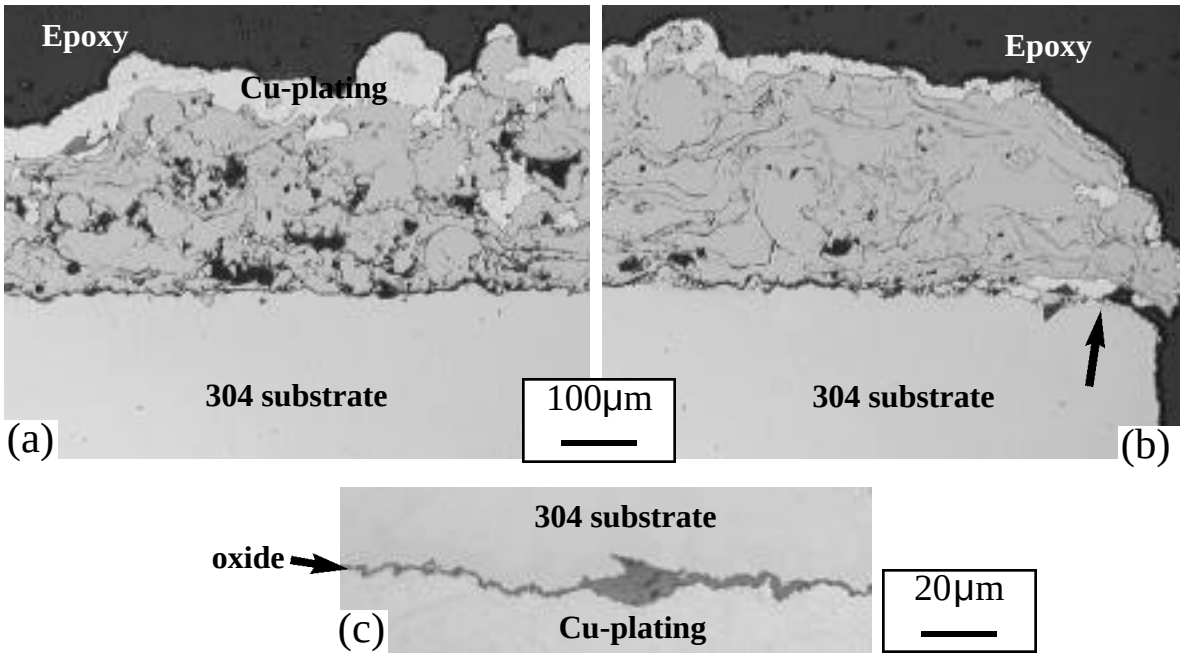

Fig. 4. Copper plated metallographic section of two 304 stainless steel coupons plasma spray coated with Fe_3Al and oxidized for 24 h at 800°C. The coatings were made with (a) Ar-He and (b) Ar-H_2 process gases; (c) uncoated 304 forms a relatively thin oxide under these conditions. The reaction product on the iron aluminide coating is too thin to observed by light microscopy.

than one deposited with an Ar-H_2 process gas, Fig. 4b. The denser coating would likely exhibit superior long-term performance. At the specimen edge, a slight delamination was noted after the exposure, arrow in Fig. 4b. However, this may have occurred during specimen preparation or by oxidation along the coating-substrate interface from the uncoated edge. These coatings were also evaluated by EPMA and a thin oxide was found along the substrate-coating interface, [arrow in Fig. 3 (b)]. Also, a significant amount of Al_2O_3 was observed within the as-deposited coating in both cases. Because of the much greater oxidation resistance of the 304 substrate, this type of oxide formation reflects a much larger oxygen penetration than in the case of the HVOF coating on A36. Thus, these results are not as promising as those for HVOF. Further work will be required to develop a denser coating and limit the oxidation of the FAS powder during deposition.

CVD Coatings

The third type of coating was fabricated by CVD. This process involves flowing H_2+$AlCl_3$ over the specimens at 100 Torr in a controlled atmosphere reaction tube at 850°-900°C. The high Al activity in the gas results in enrichment of Al in the substrate. The experimental equipment and general process is described elsewhere.[11]Coatings were fabricated on a tool steel (H13), Fe-9Cr-1Mo and type 304L stainless steel substrates. The as-deposited coating formed on H13 after 2h at 850°C is shown in Figure 5. The aluminum rich layer was 40-50μm thick. Initial depositions on Fe-9Cr-1Mo and 304L resulted in a thinner (<10μm) aluminide layer. These thinner coatings were identified by x-ray diffraction (XRD) as β-FeAl. A second deposition run at 900°C formed a thicker layer (based on mass gain). Using energy dispersive x-ray analysis in a scanning electron

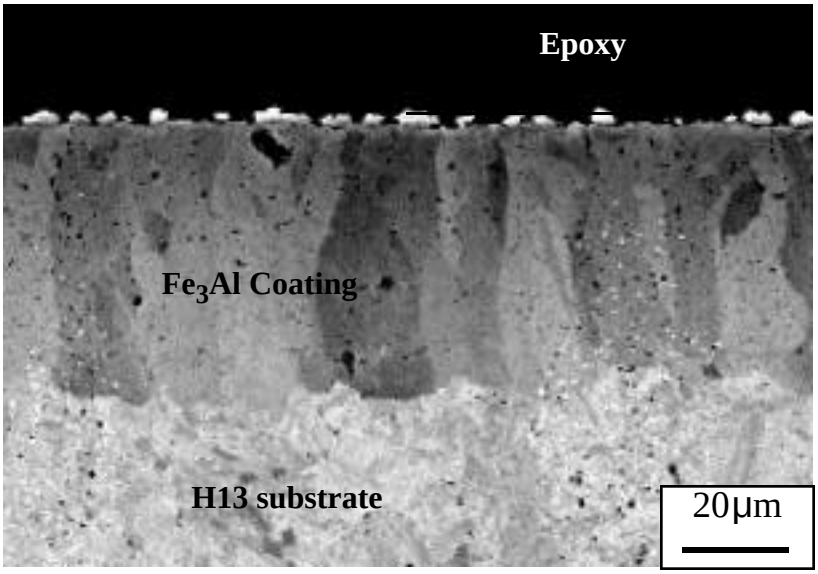

Fig. 5. Metallographic cross-section of the CVD iron aluminide coating deposited on a tool steel (H13) substrate.

microscope (SEM/EDX), both Fe and Al were detected on Fe-9Cr-1Mo but Al and a strong Ni signal were detected on the 304L substrate indicating a possible enrichment of Ni (from the substrate) in the aluminide layer. When the coating deposition conditions are optimized, additional characterization work of the as-deposited coatings will be performed.

The coating on H13 tool steel showed excellent oxidation performance during a 100 h exposure at 800°C. Without a coating, H13 forms a voluminous, 200-300µm thick iron oxide, while the coated specimen formed an alumina scale less than 2µm thick, Figure 6. Because the CVD process coats the entire substrate, these specimens are more amenable to thermogravimetric analysis. Coated and uncoated specimens were isothermally exposed at 800°C using a Cahn model 1000 microbalance. Fig. 7 shows the performance for Fe-9Cr-1Mo. Without a coating a reasonably slow oxidation rate is observed in dry air. However, with the addition of 10vol% water vapor to the environment, the rate was greatly accelerated after an initial incubation period. This type of effect has been observed in other

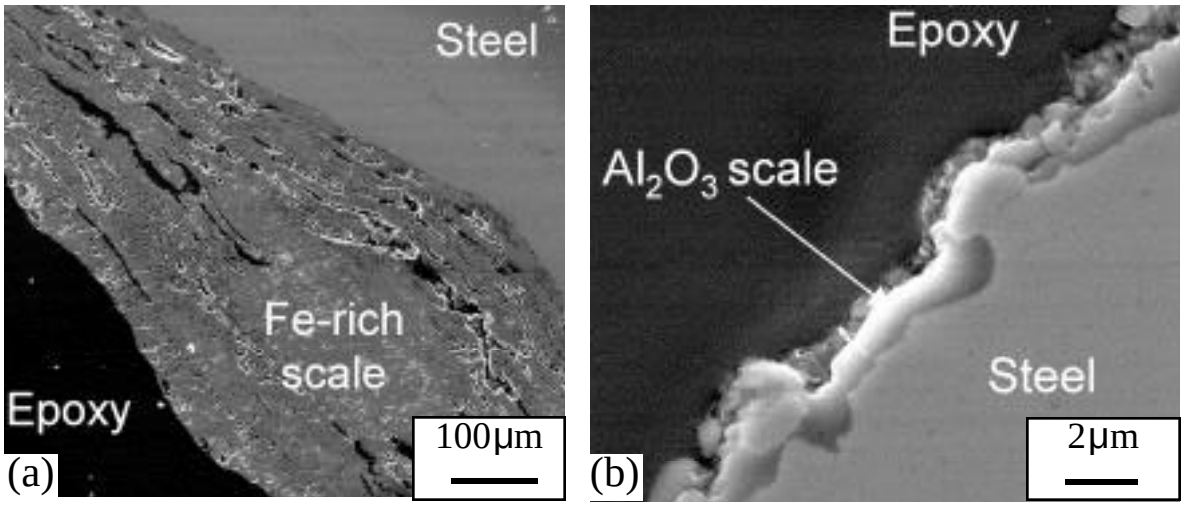

Fig. 6. Metallographic cross-sections of the scale formed after 100 h at 800°C on (a) uncoated H13 and (b) CVD aluminized H13. A thin alumina layer forms on the aluminized tool steel.

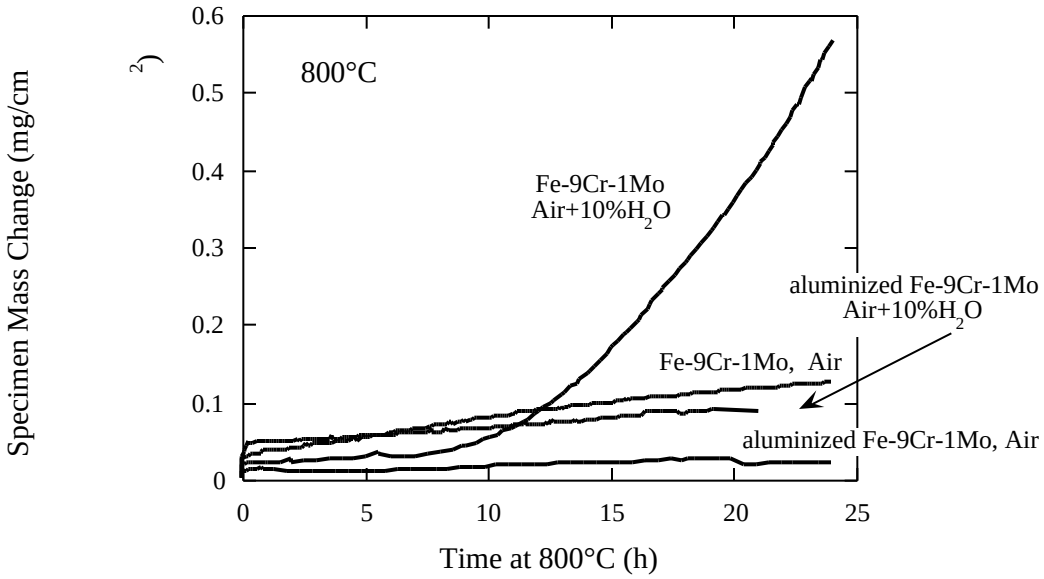

Fig. 7. Mass gain data for Fe-9Cr-1Mo at 800°C. The addition of water vapor significantly increased the specimen mass gain. A CVD aluminide coating significantly reduced the rate of attack in both environments.

water vapor corrosion studies.[12-14] Ingot-processed Fe_3Al also showed very low mass gains at this temperature, Fig. 8. With a CVD coating on Fe-9Cr-1Mo, the mass gain was very similar to that for Fe_3Al. When a CVD coated Fe-9Cr-1Mo specimen was exposed to the same water bearing environment, a slightly higher mass gain was observed, but far less than that for the uncoated material, Fig. 7. Most of the additional mass gain occurred initially and may reflect an accelerated formation of a transient (cubic) alumina scale. Previous work has suggested that water vapor can increase the formation of transient alumina phases[15] but testing of alumina-forming alloys at 900°-1100°C[16] showed no long-

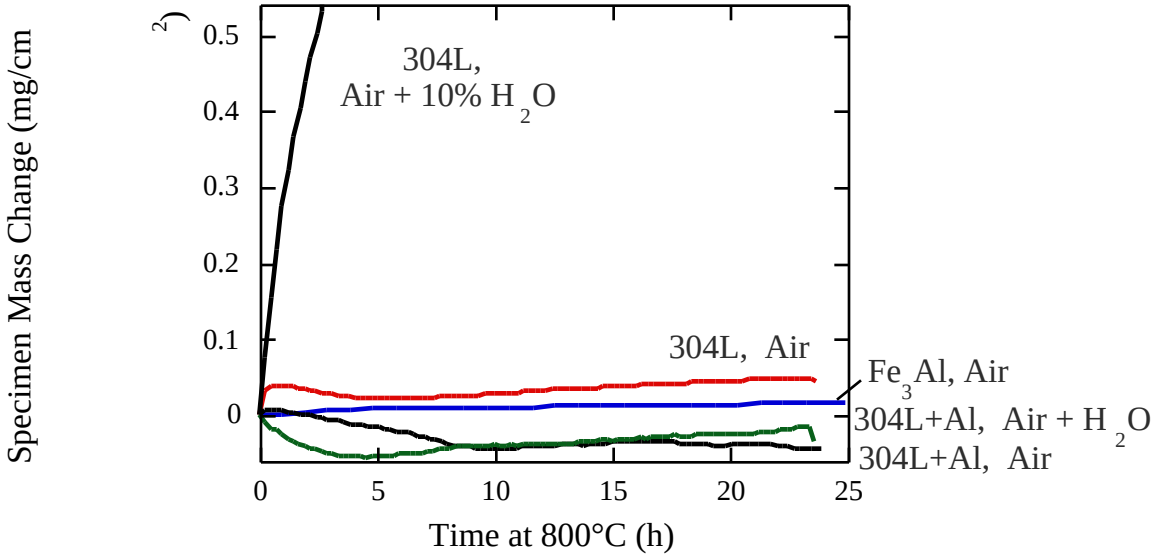

Fig. 8. Mass gain data for type 304L stainless steel at 800°C. A CVD coating showed an initial mass loss during the test but overall showed very little attack.

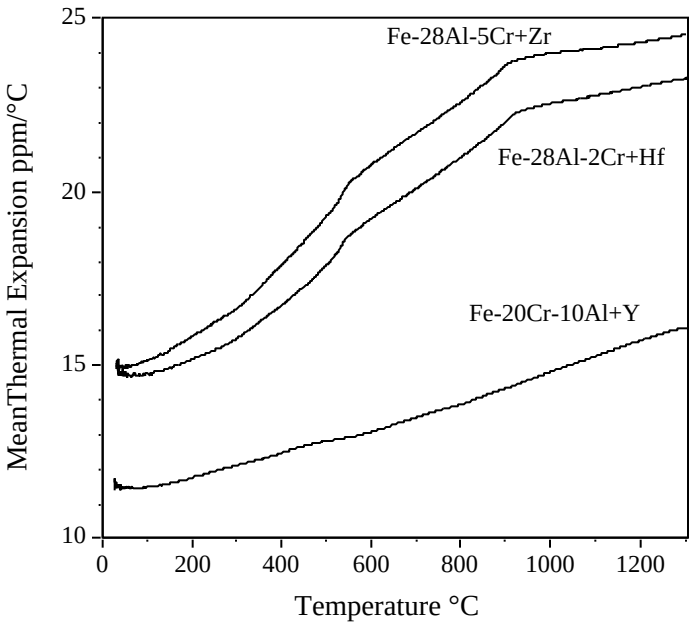

Fig. 9. Thermal expansion as a function of temperature for several iron-base alloys. Iron aluminides have a significantly higher thermal expansion coefficient than a ferritic FeCrAl-base material.

term effect of water vapor on the scale growth rate.

Fig. 8 shows data for type 304L stainless steel with and without a coating. Without a coating, this alloy formed a protective chromia scale with a relatively low mass gain in air, but, again, when water vapor was added to the environment, the rate was highly accelerated (although at longer times the rate slowed such that the total mass gain was 2.4mg/cm^2 after 24h at 800°C). With a CVD coating, an initial mass loss was observed in air and in air+10%H_2O, followed by very little mass change, Fig. 8. Because of these promising results, further work will be conducted to optimize the coatings on Fe-9Cr-1Mo, type 304L stainless steel and mild steel and further testing will include sulfur containing environments.

DISCUSSION

Unlike most previous work[5,6,9] on weld overlay and conventional thermal spray iron- aluminide coatings, these HVOF and CVD coatings appear to be dense, adherent and, in initial testing, tended to form a protective alumina scale. Further testing is required to determine the time and temperature limitations of these coatings.

The need for a coating on mild and tool steels is obvious. These alloys form thick, non-protective oxides at 800°C [Figs. 2 (b) and 6 (a)] and require a coating for extended service at high temperatures or in sulfur-bearing environments. Fe-9Cr-1Mo and type 304 stainless steel have reasonably good oxidation resistance at 800°C. However, it is well-known that these alloys are heavily attacked in sulfidizing environments where iron

aluminides show significantly better oxidation resistance.[1-4] Another reason that these alloys may need coatings is the accelerated attack observed in the presence of water vapor (Figs. 7 and 8). In this case, a coating which forms an alumina scale has the benefit of a lower oxidation rate but, more importantly, lower susceptibility to water vapor attack[15,16]. The oxidation rate of silica-forming alloys also can be accelerated in the presence of water vapor. Thus, in high-temperature combustion environments, aluminum-containing coatings which form protective alumina scales appear to be the most attractive option.

Previous iron-aluminide coating work[5-6] has indicated that good performance in sulfidizing environments required the coating to contain >18 at.% Al. However, cracking of weld overlay coatings was a recurring problem. Recent thermal expansion results indicate that the cracking may be exacerbated by the high coefficient of thermal expansion of Fe_3Al compared to ferritic alloys, Fig. 9. (The two kinks in the iron aluminide curves are from the phase transformation from $D0_3$ to B2 at ≈550°C and then from B2 to α-Fe at ≈850°C.[17]) Previous work has shown that the mean thermal expansion of the B2 phase is even higher.[18] Thus, there is an inherent physical compatibility problem between iron aluminides and most ferritic and austenitic alloys at high temperatures. Given the high thermal expansion and low strength of Fe_3Al, the alloys are likely to flow and then crack during cooling. This is an issue that will need to be addressed in future work. One possible option is to explore aluminum contents below the $D0_3$ phase (≈16 at.%) in order to avoid the high thermal expansion mismatch. Castings and coatings of such compositions have shown promising results at lower temperatures.[8] Lower Al content powders can be sprayed by HVOF. A more difficult task may be avoiding the formation of aluminide phases by CVD.

SUMMARY

Initial results were presented for HVOF, PS and CVD coatings on various Fe-base substrates. Both HVOF and CVD appear promising for further testing and characterization. Although iron aluminides may be difficult to produce as coatings, the formation of an alumina scale is a desirable goal for both oxidation and sulfidation resistance in combustion environments and, for this type of substrate, an aluminum-rich coating appears to have the highest potential for success.

ACKNOWLEDGMENTS

The authors wish to thank M. Howell, H. Longmire, L. R. Walker and G. W. Garner for assistance with the experimental work; S. J. Pawel and C. G. McKamey for comments on the manuscript; and R. N. Wright at INEEL for providing HVOF and PS coatings. The research was sponsored by the Fossil Energy Advanced Research and Technology Development (AR&TD) Materials Program, U. S. Department of Energy (DOE), under contract DE-AC05-00OR22725 with UT-Battelle, LLC.

REFERENCES

1. J. H. DeVan and P. F. Tortorelli, *Corr. Sci*. 35 (1993) 1065.
2. P. F. Tortorelli and J. H. DeVan, *Mater. Sci. and Eng*. A153 (1992) 573-7.
3. P. F. Tortorelli and K. Natesan, *Mater. Sci. and Eng*. A258 (1998) 115-25.
4. B. A. Pint, P. F. Tortorelli, and I .G. Wright, *Mater. High Temp*. 16 (1999) 1-13.
5. G. M. Goodwin, pp. 381-92 in *Proc. Tenth Annual Conf. Fossil Energy Materi*als, N. C. Cole and R. R. Judkins (comp.), U. S. Department of Energy, August 1996.
6. P. F. Tortorelli, J. H. DeVan, G. M. Goodwin, and M. Howell, pp. 203-12 in *Elevated Temperature Coatings: Science and Technology I*, N. B. Dahotre, J. M. Hampikian, and J. J. Stiglich (eds.), TMS, Warrendale, PA, 1995.
7. K. Natesan and R. N. Johnson, pp. 591-99 in *Heat-Resistant Materials II*, K. Natesan, P. Ganesan, and G. Lai (eds.), ASM International, Materials Park, OH, August 1995.
8. S. W. Banovic, J. N. Du Pont, and A. R. Marder, *Mater. High Temp*. 16 (1999) 195-9.
9. B. A. Pint, C. Leyens, J. R. Regina, P. F. Tortorelli, and I. G. Wright, "High-Temperature Corrosion Behavior of Iron Aluminide Alloys and Coatings," paper 1.3 in *Proc*. *Thirteenth Annual Conf. Fossil Energy Materials*, R. R. Judkins (comp.), U. S. Department of Energy, 1999.
10. R. N. Wright, to be published in *Proc*. *Fourteenth Annual Conf. Fossil Energy Materials*, 2000.
11. W. Y. Lee, Y. Zhang, I. G. Wright, B. A. Pint, and P. K. Liaw, *Met. Trans*. 29A (1998) 833-41.
12. W. J. Quadakkers and P. J. Ennis, pp.123-38 in *Materials for Advanced Power Engineering 1998*, J. Leconte-Beckers, F. Schubert, and P. J. Ennis, Eds, Forschungszentrum, Jülich Germany, 1998.
13. H. Nickel, Y. Wouters, M. Thiele, and W. J. Quadakkers, *Fresenius Journal Analytical Chemistry* 361 (1998) 540-4.
14. B. A. Pint and J. M. Rakowski, NACE Paper 00-259, Houston, TX, presented at NACE Corrosion 2000, Orlando, FL, March 2000.
15. P. T. Moseley, K. R. Hyde, B. A. Bellamy, and G. Tappin, *Corr. Sci*. 24 (1984) 547-65.
16. B. A. Pint, Oak Ridge National Laboratory, unpublished research, 2000.
17. I. G. Wright, B. A. Pint, and P. F. Tortorelli, submitted to *Oxid. Met*.
18. W. D. Porter and P. J. Maziasz, *Scripta Met. et Mater.* 29 (1993) 1043-8.

OXIDE DEFECTS AND DAMAGE PROCESSES IN IRON-BASED ALUMINA FORMERS

P.F. Tortorelli, B.A. Pint, E.A. Kenik, K.L. More, and I.G. Wright

INTRODUCTION

The nature of the defects and damage processes leading to oxide scale cracking and spallation (failure) has been the subject of fairly extensive study over the past ten years. Because of this, a number of mechanical, defect, and chemical scale-failure models have been proposed based on various analytical considerations and/or empirical observations (see, for example, refs. 1-5). Yet, there is still much uncertainty about the mechanisms of scale spallation, particularly as related to predictions of failure modes as a function of substrate composition and strength and the nature of imposed stresses. To help evaluate a deterministic role of scale defects and damage on spallation, this study utilized an experimental approach based on a microstructural comparison of isothermally and cyclically oxidized specimens exposed for the same time and temperature. Oxidation conditions were chosen so that exposures were terminated prior to the onset of general macroscopic scale spallation (as determined visually and by net mass losses). In this way, differences in incipient scale damage can be investigated, and, depending on what is observed, conclusions about the relevance of defects in setting the ultimate scale-failure mode can be made. As such, this study, which evaluates iron-based alumina-formers, follows a similar approach used for alumina scales on Ni-based alloys.[6]

EXPERIMENTAL PROCEDURES

The two alloys used in this study are an oxide-dispersion-strengthened (ODS) Fe_3Al alloy consisting of Fe-27.1% Al-2.1% Cr-0.2% Y (as Y_2O_3)-30 ppma S and an ingot-processed FeCrAlY, Fe-20.2%Cr-9.9%Al-0.08%Y-16 ppma S. (Unless otherwise noted, all compositions are listed in atomic percent. Chemical compositions were measured by inductively coupled plasma analysis and combustion analysis.) These alloys were chosen for this study because they showed substantially different mass-change behavior during cyclic oxidation (Fig. 1) but had approximately the same oxidation rate under isothermal exposure conditions. The ingot-processed alloy was made by vacuum induction melting and solidified in a water-chilled copper mold. Standard powder metallurgy techniques were used to fabricate the ODS Fe_3Al alloy.[7] After casting, the FeCrAlY was annealed for 4 h at 1300°C in a quartz ampoule. Coupons (1-1.5 mm thick, typically 15 mm in diameter) were polished to 0.3-μm alumina and were cleaned in acetone and methanol prior to oxidation.

Isothermal exposures were performed in dry, flowing O_2 at 1200°C, and mass gain was measured using a Cahn Instruments model 1000 microbalance. Automated cyclic oxidation exposures were

conducted in the same environment using a cycle consisting of 60 min at temperature and 10 min out of the furnace. For these experiments, specimens were attached to alumina rods with Pt-Rh wire; mass changes were measured every 20-50 cycles using a Mettler model AG245 balance.

After oxidation, specimens were examined by field emission gun scanning electron microscopy (FEG-SEM) equipped with energy dispersive X-ray analysis (EDX). The scale-gas structures and polished cross sections were examined. Specimens were copper-coated before sectioning. The sections were then ground and polished to 0.3 μm alumina. For SEM examination, these were then overpolished with colloidal silica to aid in imaging the oxide scale grain structure.[8] Scanning transmission electron microscopy (STEM) was used to image cross-sectional specimens fabricated using the focused ion beam (FIB) technique.[9]

RESULTS

GRAVIMETRIC DATA

The long-term mass changes measured for the two subject alloys under cyclic oxidation conditions at 1200°C are shown in Fig.1(*a*), which also includes data for a ZrO_2-dispersed FeCrAl (Kanthal alloy APM) that represents a superior alumina-former in terms of spallation resistance.[10] The ODS iron aluminide suffered mass losses after about 100 cycles, thereby indicating significant scale spallation. The shape of its mass curve (extended period of little change followed by steep mass gains after ~1800 cycles) is indicative of formation of fast-growing spinels and the influence of the deformation of the specimen, which can lead to more retained scale.[11] The FeCrAlY alloy continued to exhibit overall mass gains out to 700 cycles before substantial spallation. The more rapid onset of spallation for the iron aluminide is most likely due to the much higher thermal stresses in the alumina scale during cooling; its coefficient of thermal expansion is significantly higher than that of the FeCrAlY alloy.[7] Furthermore, FeCrAlY is less creep resistant than the ODS iron aluminide and, thus, some stress relief may occur during cooling.[2]

Because the intent of the present study was to compare the scales and oxide-metal interfaces of isothermally and cyclically exposed specimens before the onset of any appreciable spallation, the gravimetric data were used to select the oxidation times for the two alloys. Accordingly, the ODS iron aluminide was oxidized under both conditions for 20 h. At this point, the mass gain of the thermally cycled specimen was still similar to its isothermally exposed counterpart. This indicated that 20 h was a reasonable time period after which to compare scale microstructures for incipient damage. In a similar manner, an exposure time of 200 h was chosen for the FeCrAlY specimens [Fig. 1(*b*)].

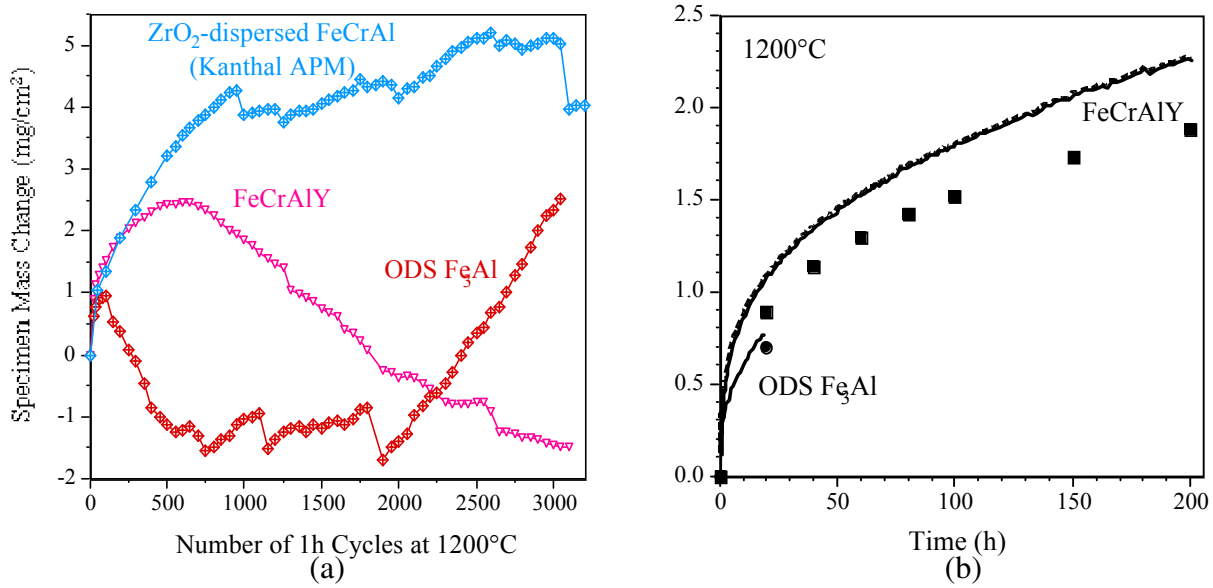

Fig. 1. Specimen mass change as a function of time for exposures in O_2 at 1200°C (a) long-term cyclic oxidation data; (b) comparison of short-term cyclic data (symbols) shown in (a) with isothermal data (lines).

MICROSTRUCTURAL CHARACTERIZATION

ODS Iron Aluminide

After 20 h of oxidation at 1200°C, scales approximately 5 µm thick formed on both the isothermally and cyclically oxidized iron-aluminide specimens, and there was no significant difference in oxide-metal adherence or interfacial roughness (Figs. 2 and 3). No evidence of scale spallation was observed in the cross sections of the isothermally and cyclically oxidized specimens. However, SEM of in-plan oxidized surfaces showed that the iron-aluminide specimens tended to have some isolated spalled areas. These were on the order of 10 µm laterally and were not more prevalent on the thermally cycled specimen than the isothermally exposed one.

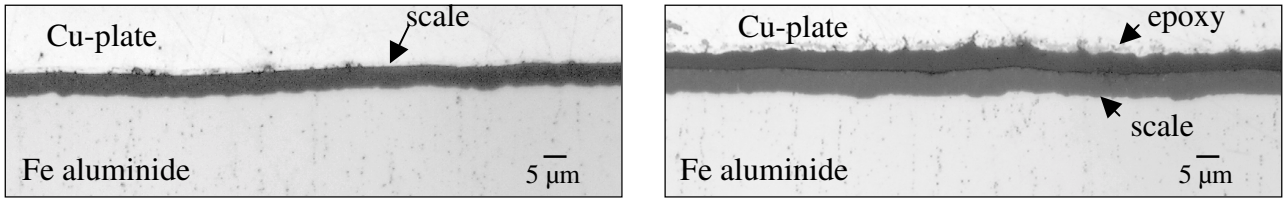

Fig. 2. Polished cross sections of ODS iron aluminide exposed at 1200°C. (a) 20-h isothermal exposure (b) 20 1-h cycles.

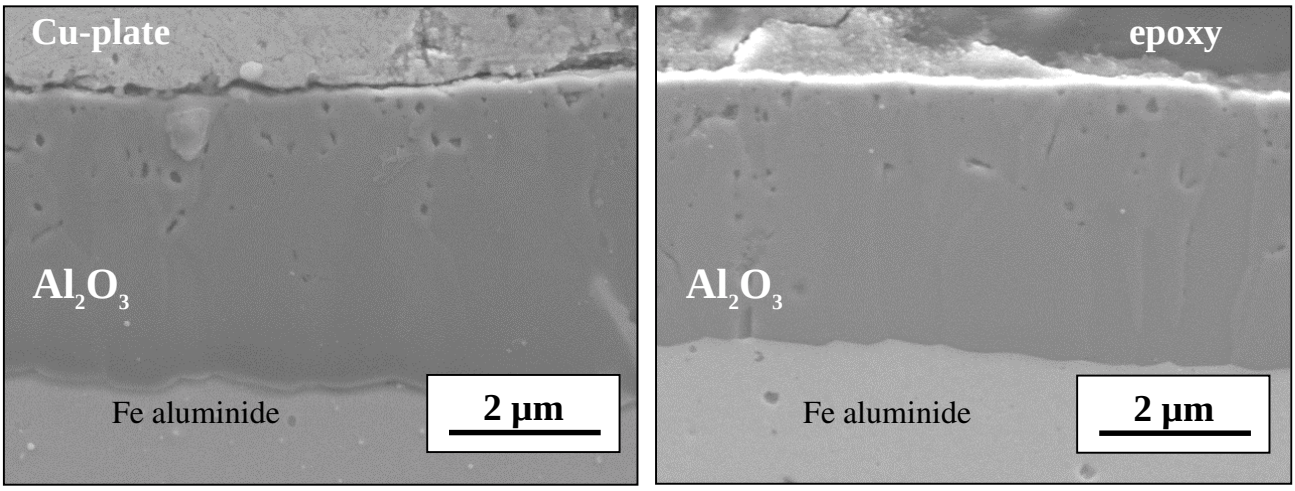

(a) (b)

Fig. 3. SEM images of polished cross sections of ODS iron aluminide exposed at 1200°C. (a) 20-h isothermal exposure (b) 20 1-h cycles

Under both oxidation conditions, the scales grown on the ODS iron aluminide specimens consisted of mainly columnar grains with some finer equiaxed grains near the gas-oxide interface (Fig. 4). Such alumina scale microstructures are indicators of reactive element (RE) doping and, consequently, alumina

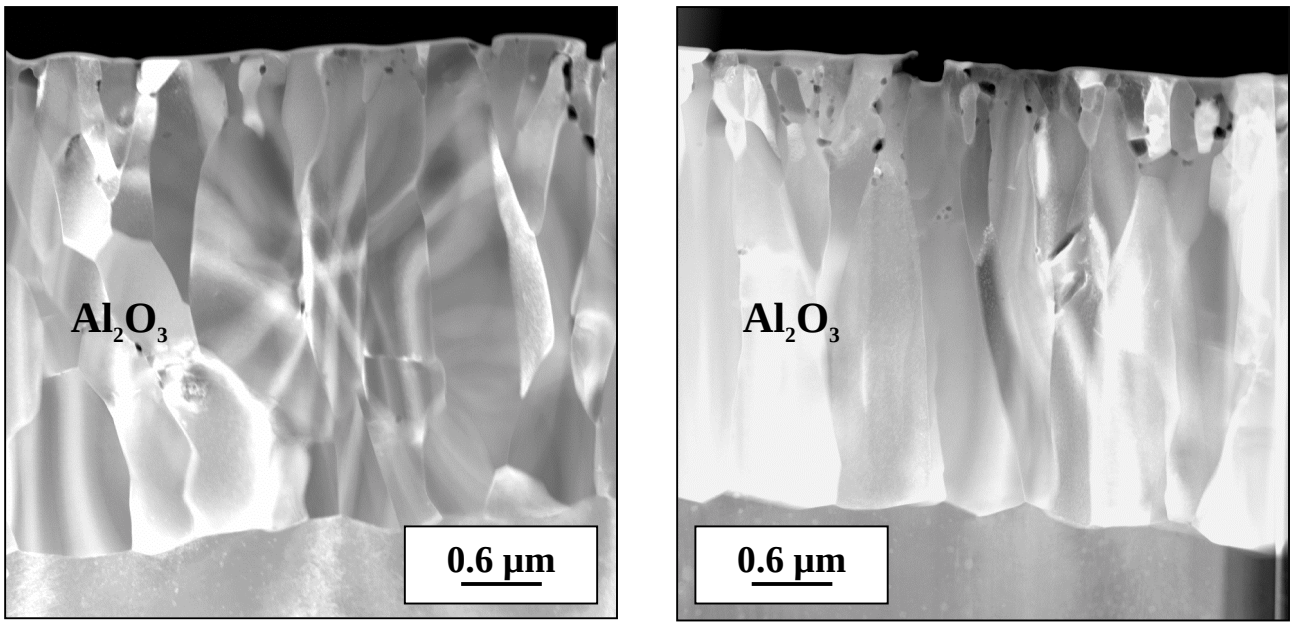

(a) (b)

Figure 4. Cross-section STEM images of cross sections of ODS iron aluminide exposed at 1200°C. (a) 20-h isothermal exposure (b) 20 1-h cycles

growth by anion diffusion such that new oxide is predominately formed at the interface with the alloy substrate.[12] Imaging by SEM and STEM clearly showed preferential pore formation near the gas-scale interfaces (Figs.3 and 4), but little porosity elsewhere. Nevertheless, at every spatial level of imaging, there is virtually no difference in scale structures between the isothermally and cyclically oxidized ODS iron aluminide (Figs. 2-4). The same conclusion can be made about the morphologies of the oxide-metal interfaces. While isolated interfacial pores were sometimes observed on polished cross sections, the STEM imaging of specimens prepared using the FIB technique revealed only intact interfaces under both oxidation conditions. Again, there was no difference in interfacial structure between the isothermally and cyclically exposed specimens.

FeCrAlY

As shown in Figs.5 and 6, the oxide scales on the FeCrAlY (200 h) were thicker (~ 10 μm) than those grown on the ODS iron aluminide consistent with the longer exposure time (note different magnifications for Figs. 2 and 5). As with the iron aluminide, there was little evidence of differences in oxide thickness and external scale microstructures between the isothermal and thermal cycling cases. The light phases within the alumina scales on the FeCrAlY were found to be predominately yttrium, oxygen, and aluminum and, thus, likely are yttrium aluminum garnet (YAG), which is often observed for alumina-forming alloy systems (see, for example, ref. 13).

In contrast to the ODS iron aluminide, where the yttrium is added as an oxide, significant internal oxidation of yttrium in FeCrAlY occurred under both exposure conditions. This internal oxidation can explain the higher mass gains of FeCrAlY (at a given time) relative to the iron aluminide [Fig. 1(*b*)]. The isothermally exposed FeCrAlY showed a somewhat greater tendency for localized broad internal oxide penetrations. The arrows in Fig. 5(*a*) indicate examples of such. In addition to the long stringers of

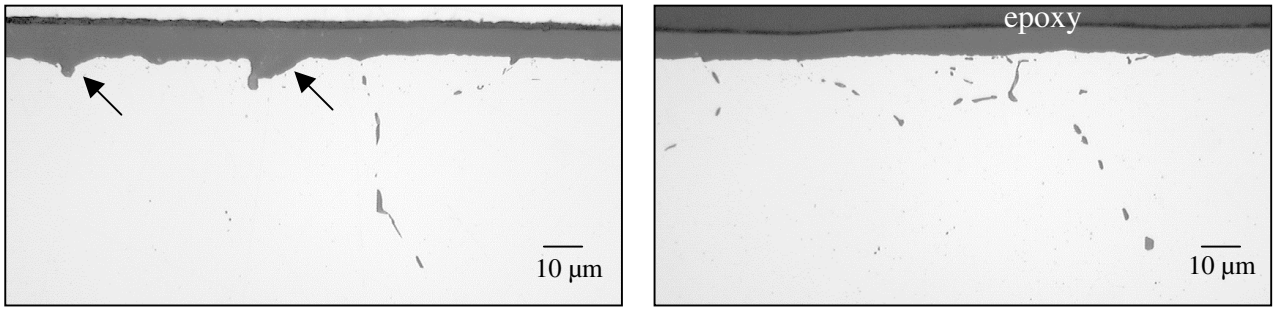

(a) (b)

Figure 5. Polished cross sections of FeCrAlY exposed at 1200°C. (a) 200-h isothermal exposure (b) 200 1-h cycles. Arrows point to selected sites of localized oxide penetrations

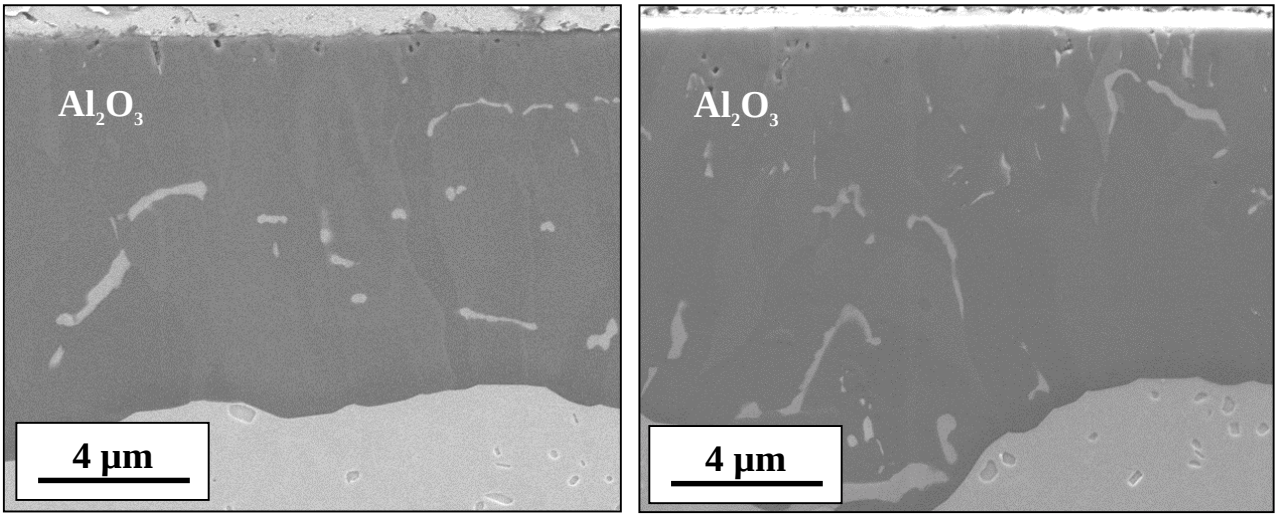

(a) (b)

Fig. 6. SEM images of polished cross sections of FeCrAlY exposed at 1200°C. (a) 200-h isothermal exposure (b) 200 1-h cycles.

internal oxide, smaller discrete yttrium-rich particles (most likely YAG) were observed near the oxide-metal interface (Fig. 7). Similar particles have been previously reported for oxidized FeCrAlY by Mennicke et al.[14]. The particle sites appear to be pits. This surface relief may be a consequence of the overpolishing procedure described in the "Experimental Procedures" section.

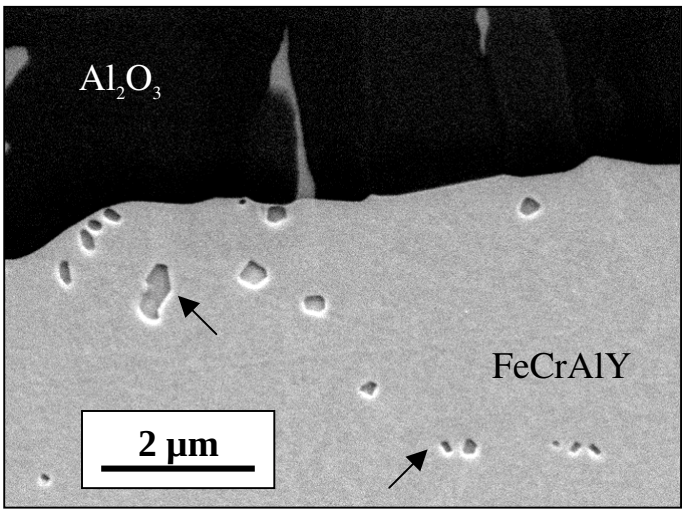

Fig. 7. SEM image of polished cross section of FeCrAlY exposed at 1200°C for 200 1-h cycles showing internal oxide particles (arrows). Similar internal oxides were observed on isothermally exposed specimen. Surface relief at these particle sites may be due to the overpolishing procedure

DISCUSSION

Oxide characterization across a wide range of imaging magnification did not indicate any significant scale or interfacial differences between isothermally and cyclically oxidized specimens for either of the two alumina-forming alloys of this study. The major defect type found in all of the scales was porosity, predominately located nearer the oxide-gas interface. As such, most of the pores were associated with the finer-grained oxide typically found at this boundary.[12] However, this type of porosity, along with isolated voids or RE oxides (for the FeCrAlY) in the scales, was observed under both isothermal and cyclic oxidation exposures and therefore could not be related to any damage accumulation during thermal cycling. Indeed, there was an absence of microstructural evidence for differences in defect or damage production between the two oxidation conditions. Cracks were not observed, nor was there any evidence for preferential void formation (or healing[3,8]) in either case. Similar findings have been reported for a NiCrAlY alloy oxidized under isothermal and cyclic conditions at 1100°C.[6]

Some implications regarding the relationship of scale defects and their development to spallation and failure can be made based on the fact that the relatively straightforward comparative approach used in both this work and the NiCrAlY study failed to reveal evidence of incipient defects or damage. One consideration involves the defect distribution. In this regard, it is important to note that the present microscopy observations probe only a part of the oxidized surfaces. It is possible that, if the defects controlling scale failure were sufficiently localized, they would not necessarily be observed by random sectioning. In this case, when the strain energy in the oxide exceeds a critical value, the defect(s) can rapidly grow and cause substantial spallation. Under such conditions where failure is controlled by very localized defects or a critical defect size is very small, a microstructural basis to differentiate oxidation performance would be problematical at this stage of scale development.

The absence of observable differences in incipient scale and interfacial defects despite different long-term oxidation performance under isothermal and cyclic conditions can be interpreted as indicating that fundamental processes associated with scaling and oxide-metal adherence do not necessarily manifest themselves in terms of early-stage damage accumulation. For example, for scale spallation by adhesive failure, changes in interfacial energies/properties can ultimately control failure without extensive defect production. In such cases, overall strain energy considerations can well be paramount. Indeed, as mentioned above, the greater spallation susceptibility of the oxidized ODS iron aluminide (Fig. 1) is at least partially due to the higher thermal stress generated in the alumina grown on this alloy, which has a significantly greater coefficient of thermal expansion (CTE) than FeCrAlY.[7] Using the measured CTE's,[7] the stress from cooling from 1200°C for an alumina scale on the iron aluminide was calculated to be about twice that for FeCrAlY (neglecting the effect of the yttria-rich phase in the scale on the CTE of the alumina).

The results of this study and a similar one with NiCrAlY[6] obviously call into question the role of early-stage defect production and damage development in determining the nature of scale failure. However, this does not mean that damage accumulation considerations are not valid at the later stage, when other observable defects form and interact.[1,8,15] In fact, such an approach has been effective in predicting spallation-related oxidation lifetimes in some cases, including a FeCrAlY.[1,15] Based on these analyses, a propensity of in-scale defects would not be expected at the relatively short exposure times of the present study.[15] While the conclusions of this work are applicable to iron-based alumina formers and NiCrAlY, definitive, widely applicable conclusions await more such systematic investigations across a wider range of alloy systems and oxidation conditions. In this regard, there is some evidence that interfacial void development may have a more prevalent role in the case of β-NiAl-type alloys.[16] It thus would be of interest to apply the same methodology in comparing alumina scales formed on isothermally and cyclically oxidized specimens of such alloys.

SUMMARY

In order to examine the nature of incipient defects and damage processes controlling the breakdown of protective alumina on an Fe-Al and an FeCrAlY alloy, the effects of thermal cycling on scale morphology and adherence were studied for 1200°C exposures that were terminated before the onset of significant spallation. Damage was characterized by use of optical imaging and scanning and transmission electron microscopy to compare oxide-metal cross sections from specimens that were thermally cycled to those that were isothermally exposed for similar times at temperature. No significant differences in scale and metal-oxide interfacial morphologies/damage were found between thermally cycled and isothermally exposed specimens. These observations suggest that, at least in some cases, the nature of ultimate scale failure is not set by early-stage oxide or interfacial defect development, but rather by chemical, diffusion, and stress processes affecting adhesion or by damage that only forms at longer times.

ACKNOWLEDGMENTS

The authors wish to thank L.D. Chitwood and G.W. Garner for assistance with the oxidation exposures, D.W. Coffey and T. Geer for specimen preparation for microstructural analysis, and J.A. Haynes and M. Lance for reviews of the manuscript. The research was sponsored by the Offices of Fossil Energy and Industrial Technologies and the Division of Materials Sciences, U. S. Department of Energy, under contract DE-AC05-00OR22725 with UT-Battelle, LLC.

REFERENCES

1. P. Handcock, and J. R. Nicholls , *Mater. Sci. and Technol*. 4 (1988) 398.
2. H. E. Evans, *Mater. High Temp.* 12 (1994) 219.
3. M. Schütze, *Protective Oxide Scales and Their Breakdown*, John Wiley and Sons, Chichester, 1997.
4. J. R. Nicholls, H. E. Evans, and S.R. J. Saunders, *Mater. High Temp*., 14 (1997) 5.
5. B. A. Pint, P. F. Tortorelli, and I. G. Wright, *Mater. Corros*. 47 (1996) 663.
6. B. A. Pint, K. L. More, I. G. Wright, and P. F. Tortorelli, *Mater. High Temp*., 17 (2000) 165.
7. I. G. Wright, B. A. Pint, and P. F. Tortorelli, submitted to *Oxid. Met*, 2000.
8. J. A. Haynes, M. K. Ferber, W. D. Porter, and E. D. Rigney, *Oxid. Met*. 52 (1999) 31.
9. K. L. More, D. W. Coffey, B. A. Pint, K. S. Trent, and P. F. Tortorelli, to be published in *Proc. MSA*, August 2000.
10. B. A. Pint, P. F. Tortorelli, and I. G. Wright, *Mater. High Temp*. 16 (1999) 1.
11. B. A. Pint, P. F. Tortorelli, and I. G. Wright, pp. 111-32 in *Cyclic Oxidation Testing of High Temperature Materials*, M. Schütze and W. J. Quadakkers (eds.), European Federation of Corrosion Publication 27, IOM Communications, London, 1999.
12. B. A. Pint, pp. 74-85 in *Fundamental Aspects of High Temperature Corrosion*, D.A. Shores, R. A. Rapp, and P.Y. Hou (eds.), volume 96-26, The Electrochemical Society, Pennington, New Jersey, 1997.
13. J. D. Kuenzly, and D. L. Douglass, *Oxid*. Met. 8 (1974) 139.
14. C. Mennicke, E. Schumann, C. Ulrich, M. Rühle, *Mater. Sci. Forum* 251-4 (1997) 389.
15. J. P. Wilber, J. R. Nicholls, and M. J. Bennett, pp. 207-20 in *Microscopy of Oxidation-3*, S.B. Newcomb and J.A. Little (eds.), Institute of Materials, London, 1997.
16. J. A. Haynes, Y. Zhang, W. Y. Lee, B. A. Pint, I. G. Wright, and K.M. Cooley, pp. 185-96 in *Elevated Temperature Coatings: Science and Technology III*, J.M. Hampikian (ed.), TMS, Warrendale, PA, 1998.

BISMUTH OXIDE SOLID ELECTROLYTE OXYGEN SEPARATION MEMBRANES

S. D. Nunn and E. A. Payzant

ABSTRACT

β-Bi_2O_3 compositions containing mixed alkaline earth dopants, different amounts of alkaline earth dopants, and compositions with additional additives have been prepared and evaluated to compare properties with the baseline samples. While a number of factors affected the observed properties, the most important variables influencing the conductivity level and the transformation temperature were the type and the amount of the alkaline earth dopant present in the composition. Compositions were prepared having improved conductivities that were 80 to 200% greater than the baseline β-Bi_2O_3 compositions. The thermal expansion of a number of the β-Bi_2O_3 compositions was measured to temperatures above the β_2/β_1 phase transformation temperature. There is an abrupt increase in the linear expansion of about 0.3% in these materials at the phase transformation temperature. Some preliminary mechanical property measurements have been made on several of the β-Bi_2O_3 compositions. Samples showed a range of fracture strengths from less than 20 MPa to about 56 MPa. Neutron diffraction and X-ray diffraction studies were used to continue the refinement of the β-Bi_2O_3 crystal structure.

INTRODUCTION

Doped β-Bi_2O_3 exhibits oxygen ion conductivity that is much higher than yttria-stabilized ZrO_2 (YSZ) up to the maximum operating temperature of about 800°C.[1] The β-phase of Bi_2O_3 is formed by partial substitution for the bismuth atoms by divalent alkaline earth ions such as calcium, strontium, and barium. The conductivity increases by nearly tenfold due to a phase change in the temperature range of 560 to 745°C, depending upon the amount and type of dopant in the composition.[1-3] At the transformation temperature, the low-temperature β_2 phase transforms to the high-temperature β_1 phase. Test results for baseline samples containing 28 mol% dopant (CaO, SrO, or BaO) were presented in the previous report.[4] Above the transformation temperature, the ionic conductivity of β-Bi_2O_3 is 35 to 65 times greater than that of YSZ at the same temperature. The divalent cation substitutions change the structure and properties of Bi_2O_3 through the creation of oxygen-site defects and lattice distortions due to charge and ionic size effects. The general chemical formula for β-Bi_2O_3 is $Bi_{(1-x)}M_xO_{(3-x)/2}$ where M = Ca, Sr, or Ba. The solid solution range[3] of the alkaline earth doped β-Bi_2O_3 phase is shown in Table 1. The present study evaluated a broad range of compositions containing mixed alkaline earth dopants, varying amounts of alkaline earth dopants, and additional additives having different ionic sizes and valance charges to

determine the effect of these variations on the conductivity and the transformation temperature of the compounds.

Table 1. The range of beta-phase solid solution for alkaline earth doped bismuth oxide.

	Solid solution range		
Alkaline earth dopant	***x***	**mol. %**	**wt. %**
CaO	0.120-0.183	21.5-31.0	3.2-5.1
SrO	0.093-0.274	17.0-43.0	4.4-14.4
BaO	0.146-0.170	25.5-29.0	10.1-11.0

EXPERIMENTAL

β-Bi_2O_3 compositions containing 28 mol% of the alkaline earth oxides CaO, SrO, or BaO were used as the baseline materials for comparison in this study. Mixed alkaline earth compositions were prepared in which the alkaline earth oxides were combined in pairs and added in equal molar amounts, again with a total of 28 mol % dopant. Compositions containing varying amounts of single alkaline earth dopants were also made for comparison. Additional compositions were prepared in which the ionic size of the additive was smaller (Mg, Cu, Zn) or larger (Cs) than the alkaline earth cation and where the size was similar to the alkaline earths but the valence charge was greater (La). The compositions that were prepared are listed in Table 2. The starting powders were milled in a small attritor using 3-mm YSZ milling media and isopropyl alcohol as the solvent. After milling, the slurry was poured through a sieve into a glass tray and dried under low heat to evaporate the alcohol. The dried cake was crushed into loose powder using a mortar and pestle. The powder was then placed in a crucible and heated to 625°C for 12 h to decompose the carbonate and hydroxide raw materials and to react the constituents to form the desired compounds. The calcined material was again crushed to form a loose powder. Samples were fabricated by uniaxially pressing the calcined powder into disks and bars. The pressed shapes were then sintered at 700°C for 48 h to fully react the constituents and to densify the samples.

The modulus of rupture was measured in 4-point bending. The test bars were machined from sintered samples and were nominally 50 × 3 × 4 mm. A computer-controlled mechanical testing machine (Instron 4465) was used to fracture the test bars and to record the data.

The DC conductivity was measured in both 4-point and 2-point mode using a Hewlett Packard 4194A Impedance Analyzer. Small bars, which measured approximately 38 × 3 × 3 mm, were used for the conductivity tests. The conductivity of the samples was measured over a temperature range from ambient to 700-800°C, depending upon the specific composition.

Table 2. Composition and properties of β-Bi_2O_3 compounds containing various additives

Dopant content mol%	Modulus of rupture MPa	Transformation temperature, ºC	Conductivity after transformation, S/cm
10.75CaO	55.6 ±5.6	715	1.211
16CaO	41.1 ±15.5	710	1.011
22CaO	39.2 ±2.7	755	0.930
28CaO	23.9 ±3.2	765	0.673
8.5SrO	15.8 ±3.8	745	1.352
12SrO	49.1 ±6.2	740	1.203
18SrO	22.4 ±1.3	680	0.644
28SrO	40.5 ±3.7	725	0.429
42SrO		645	0.104
18BaO	24.3 ±0.5	610	0.178
28BaO	20.8 ±0.8	590	0.164
14CaO 14BaO	33.3 ±2.6	675	0.404
14SrO 14BaO	17.2 ±2.2	660	0.330
25.6BaO 1.4Cs_2O		605	0.177
21CaO 7SrO		760	0.673
14CaO 14SrO	11.6 ±1.3	760	0.573
7CaO 21SrO	24.8 ±1.8	740	0.449
21CaO 7MgO		750	0.780
21CaO 7CuO		750	0.652
21CaO 7ZnO		750	0.855
21SrO 7MgO	24.7 ±0.7	720	0.392
25.6CaO 1.4La_2O_3		785	0.789
25.6SrO 1.4La_2O_3		765	0.527
23.2SrO 2.8La_2O_3		770	0.598
16.35SrO 0.91La_2O_3		685	0.706
11CaO 9SrO	29.6	725	0.844
6CaO 6SrO 6BaO	28.8 ±11.2	675	0.699

The linear thermal expansion of the baseline samples and the compositions containing mixed alkaline earth pairs was measured using a Theta dual push-rod differential dilatometer. The samples were heated in stagnant air from room temperature to greater than the β_2-β_1 phase transformation temperature at a rate of 3°C/min. The samples were cooled at the same rate. The elongation was recorded during both the heating and cooling ramps.

Neutron diffraction measurements were made at Oak Ridge National Laboratory's High Flux Isotope Reactor (HFIR). Powder and sintered samples were also examined by X-ray diffraction analysis (XRD). Both room-temperature and elevated-temperature measurements were made using Cu Kα radiation.

RESULTS AND DISCUSSION

The formation of β-Bi_2O_3 after calcining and sintering was confirmed by XRD. The lattice parameters of the compounds varied with dopant addition due to the differences in the ionic radii. XRD data taken at

high temperatures showed an abrupt change in the lattice dimensions that is associated with the β_2- β_1 phase transformation. This transformation was also observed in the linear thermal expansion measurements and the conductivity measurements.

The mechanical property measurements are summarized in Table 2. The compositions showed a considerable variability in strength, with a low of about 11 MPa and a high of 56 MPa. The higher values should be adequate for using these materials in an oxygen separation device. These are preliminary results and mechanical testing is being continued to determine the optimum processing conditions for maximizing the strength.

Also summarized in Table 2 are the transformation temperature on heating and the conductivity after transformation for each of the compositions examined. The general trend for compositions containing a single alkaline earth dopant is that the conductivity increases as the dopant level decreases. This is an interesting finding since the presence of the dopant results in the formation of oxygen vacancies, which might be expected to enhance the ionic conductivity. It is hoped that the crystallographic analysis that is under way will lead to a better understanding of the conductivity mechanisms. The log of the conductivity versus the reciprocal temperature is plotted in Figs. 1 and 2 for the CaO-doped and the SrO-doped β - Bi_2O_3 compositions, respectively.

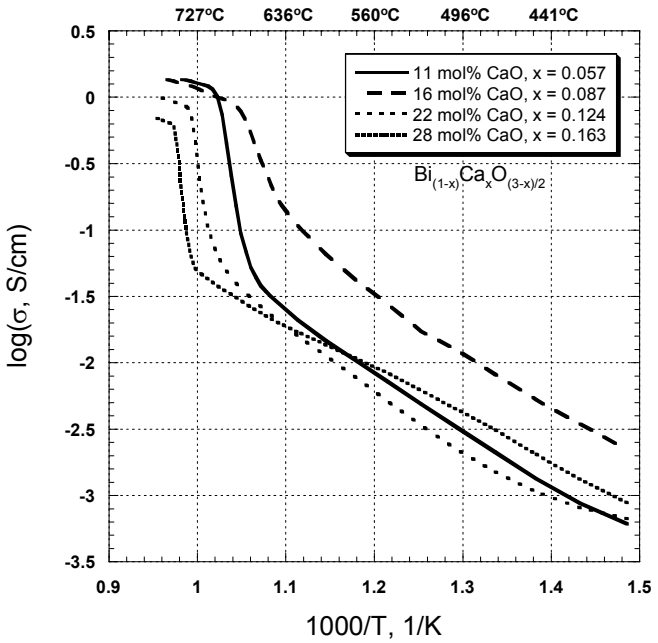

Fig. 1. The measured conductivity as a function of temperature
for the CaO-doped β-Bi_2O_3 compositions.

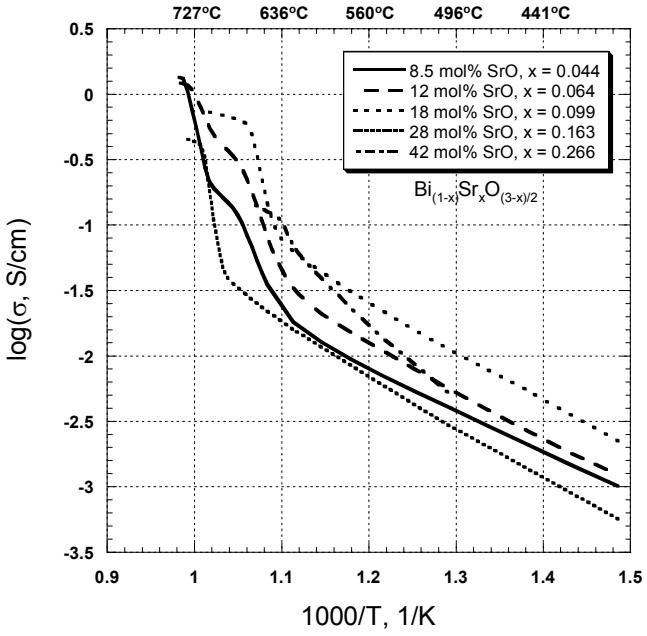

Fig. 2. The measured conductivity as a function of temperature
for the SrO-doped β-Bi_2O_3 compositions.

These plots clearly show the step increase in conductivity that occurs at the phase transformation temperature. The conductivity values for the best-performing compositions were 80 to 200% greater than the values for the baseline β-Bi_2O_3 compositions.

The mixed alkaline earth compositions showed transformation temperatures and conductivities that were intermediate between the two baseline end members. The compositions with the addition of cations having different ionic sizes and valance charges showed a change in properties compared to the baseline materials. However, these changes could not be attributed to the presence of the additives alone, since the alkaline earth content was reduced by the amount of the additive addition, and, as described above, the alkaline earth content in the composition has a very strong effect on properties.

The results of the linear thermal expansion measurements are shown in Fig. 3. The abrupt step in the thermal expansion curves corresponds to the reversible β_2-β_1 phase transformation. The thermal expansion coefficient below the phase transformation temperature is about 13×10^{-6}/°C, while above the phase transformation temperature it is about 23×10^{-6}/°C. The step increase in linear expansion at the transformation temperature is about 0.3%. The hysteresis that is seen in the phase transformation is also observed in the conductivity measurements. The transformation on heating always occurs at a higher

temperature than the transformation on cooling.

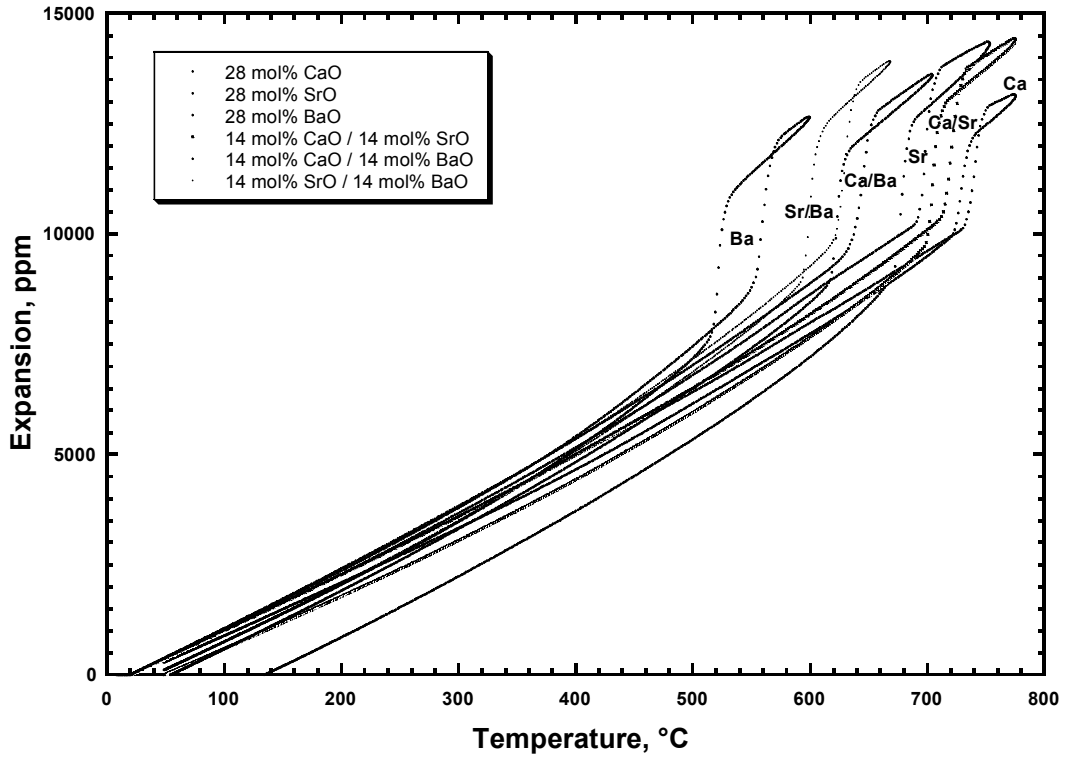

Fig. 3. Linear thermal expansion measurements of the baseline compositions and the mixed alkaline earth doped β-Bi_2O_3. The abrupt step in the thermal expansion curves corresponds to the reversible β_2- β_1 phase transformation. Note the hysteresis in the phase transformation temperature. The transformation on heating always occurs at a higher temperature than the transformation on cooling.

An illustration of the refined crystal structure that has been determined for β -Bi_2O_3 is shown in Fig. 4. The rhombohedral β-phase structure is composed of layers of the defect-fluorite δ-phase structure, but with the partially doped layers sandwiched between two exclusively bismuth-occupied layers. Although the divalent alkaline earth ions can be expected to increase the number of oxygen defects in the structure, the most oxygen-deficient positions are located in the vicinity of the bismuth-occupied layers.

At high temperatures there is a phase transformation from the β_2-phase, which is stable at room temperature, to the closely related β_1-phase. By diffraction methods this transformation is characterized by an increase in the *c*-axis of the unit cell, which corresponds to the large (>10×) increase in ionic conductivity. Recent high-temperature neutron diffraction studies have shown that this is an order-disorder transformation involving both the cation and anion sublattices.

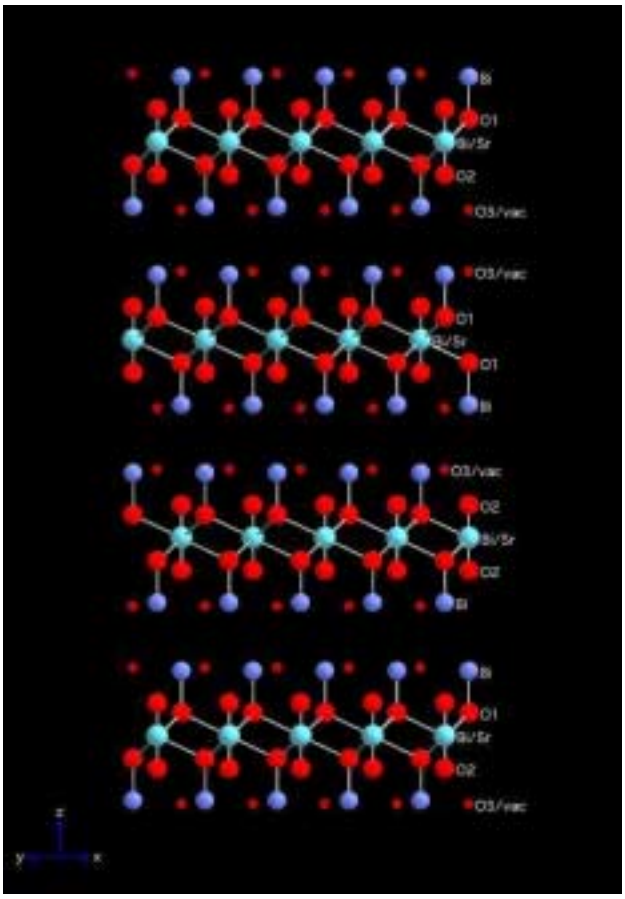

Fig. 4. The proposed crystal structure of β -Bi_2O_3 as determined by neutron and X-ray diffraction analysis.

CONCLUSIONS

β-Bi_2O_3 compositions containing mixed alkaline earth dopants, different amounts of alkaline earth dopants, and compositions with additional additives have been prepared and evaluated to compare properties with the baseline samples. While a number of factors affected the observed properties, the most important variables influencing the conductivity level and the transformation temperature were the type and the amount of the alkaline earth dopant present in the composition. Compositions were prepared having improved conductivities that were 80 to 200% greater than the baseline β-Bi_2O_3 compositions. The thermal expansion of a number of the β-Bi_2O_3 compositions was measured to temperatures above the β_2/ β_1 phase transformation temperature. There is an abrupt increase in the linear expansion of about 0.3% in these materials at the phase transformation temperature. Some preliminary mechanical property measurements have been made on several of the β-Bi_2O_3 compositions. Samples showed a range of fracture strengths from less than 20 MPa to about 56 MPa. Neutron diffraction and X-ray diffraction studies were used to continue the refinement of the β-Bi_2O_3 crystal structure.

ACKNOWLEDGEMENTS

Research sponsored by the Office of Fossil Energy, Advanced Research and Technology Development Materials Program, U.S. Department of Energy under contract number DE-AC05-00OR22725 with UT-Battelle, LLC.

REFERENCES

1. T. Takahashi, H. Iwahara, and Y. Nagai, "High Oxide Ion conduction in Sintered Bi_2O_3 Containing SrO, CaO or La_2O_3," *J. Appl. Electrochem*. **2** 97-104 (1972).
2. J. C. Boivin and D. J. Thomas, "Structural Investigations On Bismuth-Based Mixed Oxides," *Solid State Ionics* **3**/**4** 457-462 (1981).
3. P. Conflant, J. C. Boivin, G. Nowogrocki, and D. Thomas, "High Temperature X-ray Structural Study of the Anionic Conductor $Bi_{0.844}Ba_{0.156}O_{1.422}$," *Solid State Ionics* **9&10** 925-928 (1983).
4. S. D. Nunn and E. A. Payzant, "Bismuth Oxide Solid Electrolyte Oxygen Separation Membranes," *Fossil Energy Program Annual Progress Report*, April 1, 1998 - March 31, 1999.

EFFICIENT ZIRCONIA ELECTROLYTE FABRICATION

**V. Varanasi and T. M. Besmann, T. L. Starr, University of Louisville,
and T. J. Anderson, University of Florida**

ABSTRACT

Current yttria-stabilized zirconia (YSZ) electrolyte materials are inefficiently processed or lack sufficient quality. The highest-quality material is currently produced by chemical vapor deposition (CVD) at reduced pressures. Such processes are capital and operationally intensive, and thus cannot meet cost goals. At ORNL we are studying atmospheric-pressure chemical vapor deposition (APCVD) techniques that would be significantly less costly and would lend themselves to continuous processing. As an initial step in that work a thermochemical analysis has been performed and a preliminary reactor design has been developed.

INTRODUCTION

Solid oxide electrolytes have been in use for many years in fuel cells and oxygen sensors. Specifically, yttria-stibilized zirconia (YSZ) has been one of the most widely used solid oxide electrolyte materials due to its desirable properties, which include high ionic conductivity, thermal expantion coefficient compatibility, hermeticity, and long-term stability.

The most common method of fabricating YSZ electrolyte material is by chemical vapor deposition (CVD) using chloride precursors. A possible reaction sequence is as follows:

$$ZrCl_{4(g)} + Ar_{(g)} + 2H_{2(g)} + 2CO_{2(g)} = ZrO_{2(s)} + Ar_{(g)} + 4HCl_{(g)} + 2CO_{(g)} \quad (1)$$

$$2YCl_{3(g)} + Ar_{(g)} + 3H_{2(g)} + 3CO_{2(g)} = Y_2O_{3(s)} + Ar_{(g)} + 6HCl_{(g)} + 3CO_{(g)}. \quad (2)$$

In the present design, in situ chlorination of the yttrium and zirconium metals will be used to provide precursors for deposition. Deposition of ten mole %YSZ will be accomplished using a stagnation point flow reactor. Stagnation point flow constrains the flow in all directions to be zero at the substrate, ensuring uniform deposition over the whole substrate.

The purpose of this work is to demonstrate the feasibility of performing atmospheric pressure chemical vapor deposition (APCVD) of 10 mole % YSZ using metal chloride precursors through a thermochemical analysis. The ultimate goal is to combine the computational fluid dynamic analysis by T.L. Starr et al.[1] and thermochemical analysis to obtain high deposition rates, have good deposition uniformity, have low-cost operation, and be commercially scalable for continuous processing.

THERMODYNAMIC MODEL

Before beginning equilibrium calculations, it is necessary to assure that the phase diagram for the Y_2O_3-ZrO_2 (YSZ) system is well understood. Suzuki.experimentally determined a phase diagram for the region of 0 to 50 mole % of Y_2O_3 using conductivity (Fig. 1). His results are in reasonable agreement with Stubican et al. (1988), Pascual and Duran (1983), and Degtyarev and Voronin (1987).[2]

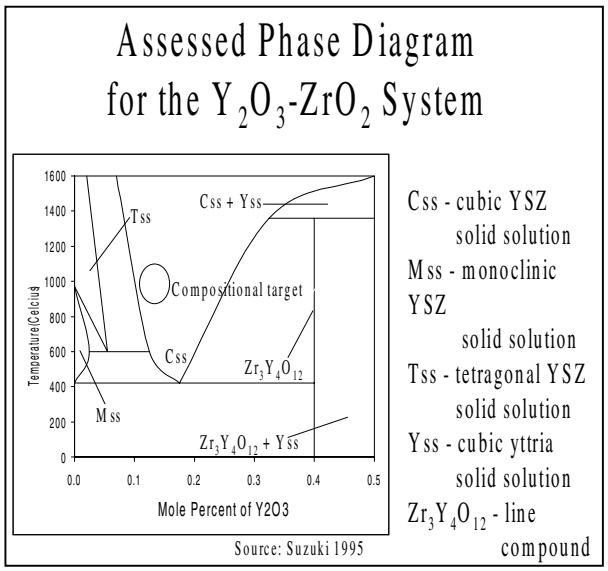

Fig. 1. Assessed phase diagram for the Y_2O_3-ZrO_2 system.

Du et al. in 1992[3] used the substitutional solid solution model to calculate the phase diagram based on the authors mentioned above (except Suzuki). The formalism for the Gibbs free energy of the mixture (G_m), based on stable element reference enthalpies (H^{SER}) at 298 K, is

$$G_m - H^{SER} = {}^{me}G_m + {}^{id}G_m + {}^{ex}G_m. \qquad (3)$$

The first term on the right-hand side of the equation is the mechanical mixing term, which is described by the compositional addition of the pure component molar Gibbs free energies as

$${}^{me}G_m = x_{ZrO2}\,(G_{ZrO2}(T) - H_{Zr}{}^{SER} - 2H_O{}^{SER}) + x_{YO1.5}\,(G_{YO1.5}(T) - H_Y{}^{SER} - 1.5H_O{}^{SER}), \qquad (4)$$

where H_{Zr}^{SER}, H_{Y}^{SER}, and H_{O}^{SER} are the stable element reference enthalpies at 298 K for zirconium, yttrium, and oxygen, respectively, and x is the mole fraction of each component. The second term is the ideal mixing term, which is described by the entropic contribution of the mixture as

$$^{id}G_m = RT[x_{ZrO2}\ln(x_{ZrO2}) + x_{YO1.5}\ln(x_{YO1.5})], \quad (5)$$

where R is the ideal gas law constant and T is the absolute temperature. The third term is the excess mixing term, which is just a truncated version of the Redlich-Kister polynomial[4]:

$$^{ex}G_m = x_{ZrO2}\, x_{YO1.5}\, [^{0}L(T) + {}^{1}L(T)(x_{ZrO2} - x_{YO1.5})], \quad (6)$$

where the terms $^{0}L(T)$ and $^{1}L(T)$ are interaction parameters between $YO_{1.5}$ and ZrO_2. This model predicts the following reactions very well:

$$Css = Mss + Zr_3Y_4O_{12} \quad (7)$$

$$Tss = Mss + Css \quad (8)$$

and introduces a new eutectoid reaction,

$$Zr_3Y_4O_{12} = Mss + Yss, \quad (9)$$

where Yss is the cubic yttria solid solution, $Zr_3Y_4O_{12}$ is the line compound at 0.4 mole fraction of Y_2O_3, and Css, Mss, and Tss are the cubic, monoclinic, and tetragonal YSZ solid solutions, respectively (Fig. 1). This solid solution model will be used in the thermochemical analysis to predict the formation of 10 mole % YSZ.

Several issues in the design of a reactor system were addressed. First, the chlorination and reaction temperatures must be determined so that an efficient system can be designed. Second, the optimal initial reacting gas flow rate and overall flowrates must be determined so that deposition rates are adequate. Finally, the conditions under which other solid phases may co-deposit must be determined so that second phase formation can be avoided.

Fig. 2 compares the vapor pressures of both chlorides[5], showing a large disparity between the vapor pressure curves for these precursors. Using the thermochemical analysis, achlorination temperature of at least 800°C allows for the partial pressure of YCl_3 to be of a sufficient value (~.001 to .004 atm) to allow Table 1 lists a reasonable set of processing conditions for the reactor

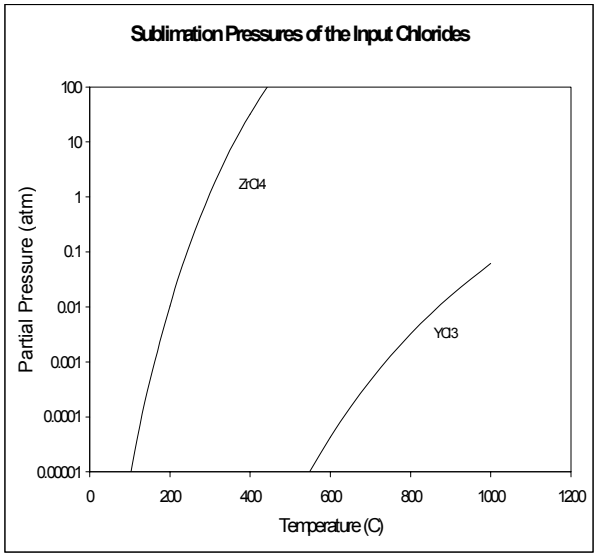

Fig. 2. Sublimation Pressures of the Input Chlorides

Table 1. Initial conditions for thermochemical analysis and reactor design

Condition	Value
P_{H2}/P_{CO2}	3.0
$P_{YCl3} / (P_{YCl3} + P_{ZrCl4})$	0.2
Temperature, ^{o}C	800
Overall flow, sccm	1500
Flow of YCl_3, sccm	2
Flow of $ZrCl_4$, sccm	4.7
Flow of CO_2, sccm	20
Flow of H_2, sccm	60

design. The thermochemical analysis yields a deposition rate of ~200 μm h^{-1} from these parameters. Calculations indicate that the reaction is essentially 100% efficient. This conclusion is supported by the calculated gas species at equilibrium presented in Fig. 3, showing that the $ZrCl_4$ and YCl_3 gases have been completely consumed. Fig. 4 illustrates the required conditions to avoid second phase (carbon) formation. Thus, from a thermochemical viewpoint, the reactions are very efficient.

A model flow scheme (Fig. 5) and a model reactor design (Fig. 6) were obtained from a combination of the thermochemical and computational fluid dynamic analyses for the chloride APCVD of YSZ.

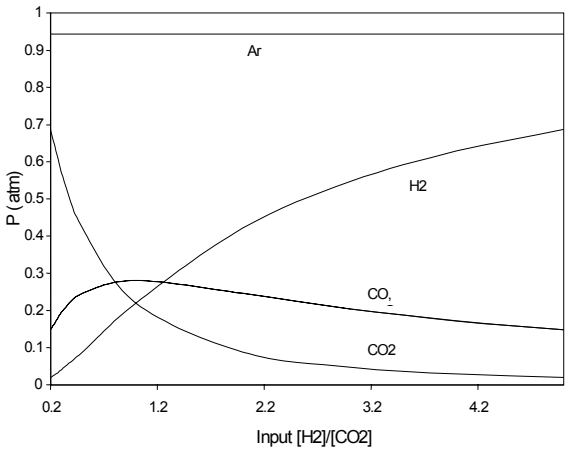

Fig. 3 Calculated partial pressures of the gas species at equilibrium.

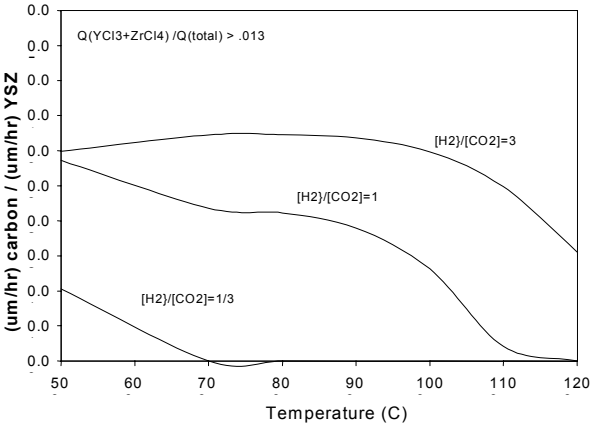

Fig. 4. Controlling carbon co-deposition during YSZ deposition requires low H_2:CO_2 ratios.

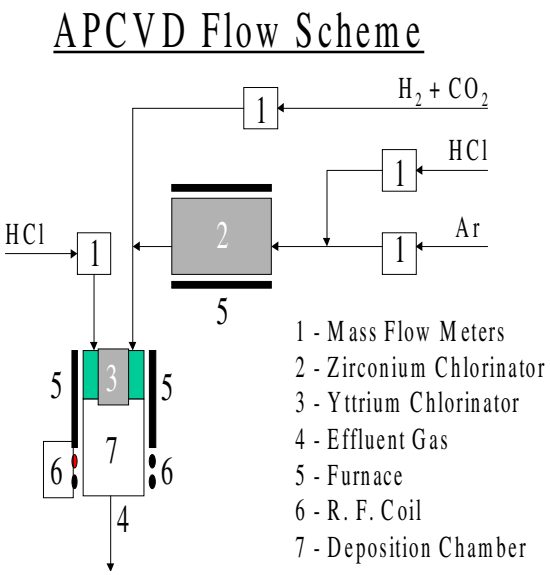

Fig. 5. APCVD flow scheme.

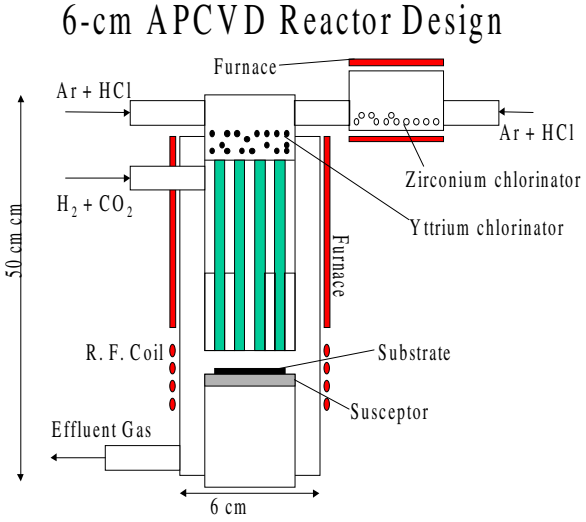

Fig. 6. 6-cm APCVD reactor design.

GAS SEPARATION USING A CARBON FIBER COMPOSITE MOLECULAR SIEVE

Timothy D. Burchell

INTRODUCTION

A novel monolithic carbon adsorbent material has been developed, and its use for the separation of gasses has been demonstrated[1]. Because the material exhibits a continuous carbon skeleton, it is electrically conductive, allowing for the electrical stimulation of desorption of adsorbed gasses. This phenomenon has been utilized in a gas separation process we have named *Electrical Swing Adsorption* (ESA), which is analogous to pressure swing adsorption and temperature swing adsorption, except that the process is driven by swinging and applied voltage on the adsorbent rather than pressure or temperature [2]. Recently, we have been investigating the modification of our adsorbent monoliths to increase their selectivity for O_2/N_2 separations. The separation of O_2/N_2 is kinetic, and, therefore, the size of the pores must closely match the size of the O_2/N_2 molecules. A carbon vapor deposition process has been used to reduce the micropore size of the material. Two mechanisms of pore size reduction are postulated: (1) the formation of a microporous carbon membrane over the porous fibers or (2) the partial "plugging" of pore openings to form "inkbottle" pores (Fig 1). The development of our novel adsorbent carbon and the ESA process is reviewed, and preliminary data on the modification of the micropore structure are reported.

EXPERIMENTAL

Carbon fiber composite molecular seive (CFCMS) samples were fabricated via the process outlined in Fig. 2[1]. The substrate CFCMS was activated to 35 to 38% burn-off and had a BET surface area of 1000 to 1800 m^2/g, and a D-R micropore volume of 0.4 to 0.6 cm^3/g. The carbon was deposited from the vapor phase (CH_4) at a pressure of 12 torr and a temperature of 900^oC. Post-chemical-vapor-infiltration (CVI) examinations included SEM characterization and N_2 adsorption at 77K.

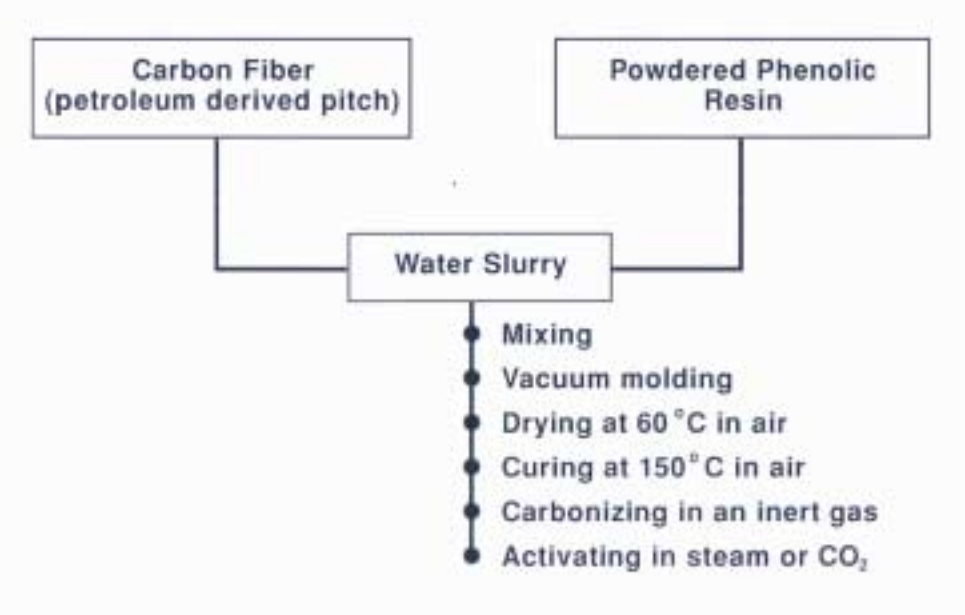

Fig. 2. The manufacturing process steps for ORNL's CFCMS.

RESULTS AND DISCUSSION

The preliminary results from this work are reported in Tables 1 and 2 below. Significant weight gains occurred during CVI processing. The BET surface area and D-R micropore volumes were substantially reduced, but the mean micropore size increased. It is speculated that this latter phenomenon was due to the complete closure of the smaller micropores, moving the distribution to larger pore sizes.

Table 1. Micropore parameters and CVI weight gain for the CFCMS samples studied

Sample	BET surface area (m^2/g)	D-R micropore volume (cm^3/g)	D-R micropore width (nm)	Mass gain on CVI (%)
13-1 (B)	1155	0.44	2.0	7.4
13-3 (M)	1591	0.58	2.1	16.8
13-5 (T)	1541	0.56	2.2	20.7
13-2 (B)	1390	0.51	2.0	14.0
13-4 (M)	1528	0.55	2.2	21.3
13-6 (T)	1647	0.60	2.2	22.3
15-1 (B)	1381	0.52	2.0	11.9
15-3 (M)	-	-	-	18.9
15-5 (T)	-	-	-	19.3

Table 2. Pre- and post-CVI micropore characterization data

Sample	BET surface area (m^2/g)		D-R micropore volume (cm^3/g)		D-R micropore width (nm)	
	Pre	Post	Pre	Post	Pre	Post
13-1 (B)	1155	263	0.44	0.10	2.0	2.8
13-3 (M)	1591	262	0.58	0.11	2.1	2.8
13-5 (T)	1541	718	0.56	0.27	2.2	2.3

The observations made during this experimental work are summarized below.

1. 24 hours deposition time gives 10-20% weight gain of carbon.
2. Weight gain increases with BET area and/or position in furnace (bottom to top).
3. CVI deposit reduces BET surface area and D-R micropore volume (micropore filling).
4. CVI deposit increases mean D-R micropore size by preferentially filling the smallest pores.
5. Lower weight gains will be targeted in future work since the amount of carbon deposit that was achieved here caused excessive surface coverage (Fig 3).

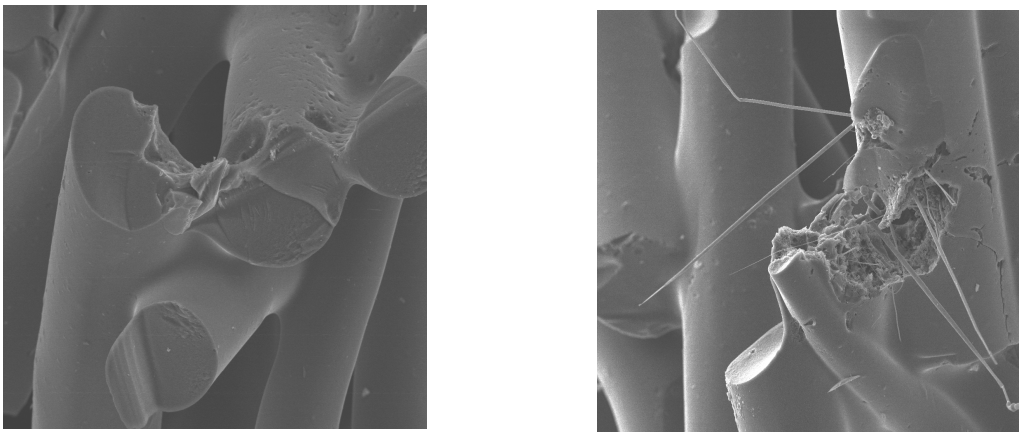

(*a*) (*b*)

Fig. 3. The structure of CFCMS before (*a*) and after (*b*) CVI treatment, indicating the excessive amount of carbon deposit attained.

CONCLUSIONS

A novel monolithic carbon adsorbent called carbon fiber composite molecular sieve (CFCMS) has been developed. The electrical conductivity of the monolith allows for a swing separation process based on electrical (self) heating (electrical swing adsorption, ESA). Research in the area of air separation is ongoing at ORNL.

REFERENCES

1. T.D. Burchell, R.R. Judkins, M.R. Rogers, and A.M. Williams, "A Novel Process and Material for the Separation of Carbon Dioxide and Hydrogen Sulfide Gas Mixtures," *CARBON* Vol. 35(9) pp. 1279-1294 (1997).
2. T.D. Burchell and R.R. Judkins, "A Novel Carbon Fiber Based Material and Separation Technology," *Energy Convers. Mgmt* **38 Suppl**., pp. S99-S104, (1997).

ESTIMATION OF CARBON CREDITS IN CARBON DIOXIDE SEQUESTRATION ACTIVITIES

K. T. Klasson and B. H. Davison

INTRODUCTION

The approach for the new activity for FY 2000, "Estimation of Carbon Credits in Carbon Dioxide Sequestration Activities," will be based on the proposed approaches for forest systems. The desired result is a general methodology for evaluation of other sequestration options, which may result in temporary or permanent carbon fixation. In the first year, the scope will be to develop the model in a series of small focus group meetings. The scope during the second year will address the collection of pertinent data for various sequestration scenarios, which will require input from other researchers and organizations worldwide. Initially, this will focus on data collection from projects currently funded by Fossil Energy. To accomplish this task a focused workshop with participants representing various FE-sponsored projects will be held in the spring of 2001. Continued work in a third year will incorporate data from other agencies.

A process that involves sequestration of carbon, either from the atmospheric carbon dioxide (or other carbon-based greenhouse gas) or from the stack gases of a plant, should be evaluated on the same basis so that it can be compared to other sequestration options. As an example we are providing the following discussion of some of the variables that may be evaluated.

NET MASS OF CARBON SEQUESTERED

It is important to have accurate estimates for the mass of carbon sequestered. For example, if a pond is used for heavy algae growth on atmospheric carbon dioxide, it is necessary to estimate any amount of methane that may be formed and emitted from the pond during anaerobic digestion in the sediments. Also, if a substantial amount of lime is used to control the pH, it may be appropriate to assign a carbon equivalent corresponding to the amount of carbon dioxide (or other carbon) emitted during the production of the lime. To address these issues it is important to draw distinct boundaries and account for all the carbon flows.

DURATION OF CARBON SEQUESTRATION

It is intuitive that a long sequestration period is advantageous. However should it be expected that any sequestration activity should pass a threshold duration (e.g., 100 years) before being considered? Or, should the carbon sequestration activity receive full credit the year it is effective, and later receive a debit

when possibly the carbon is released? The latter approach corresponds to some of the accounting strategies that are discussed in support of the Kyoto protocol. However, it does not allow for a priori comparison when two alternative activities are considered for the sequestration. If the time factor is important, several approaches may be taken. The threshold method is one. A linear relationship between the credit assigned and the duration sequestered is a second method. A third and fourth method may be to consider progressive approaches to bring incentives for longer- or shorter-term sequestration activities. It is possible that a threshold sequestration time (e.g., 100 years) is common among all methods, after which full credit is given. When discussing time it is also important to realize that the sequestration and the emissions may be spread out over time and that a life-cycle approach for the activity is used. For example, if the algae pond is used for several decades before it is harvested and the algae is converted into bio-fuels, the activity will have sequestered a net amount of carbon each year, but it is being released all at once. It is probably appropriate to take into account that some of the carbon was sequestered for a long time, but other portions were not. An attractive method to approach the time factor may be to define the "time value of carbon" (analogous to the time value of money) and to use present-value-type calculations to bring all carbon flows to a single time.

ENERGY USE FOR CARBON SEQUESTRATION

The use of easily distributed energy (e.g., electricity) during the sequestration or maintenance of the stored carbon may be important to consider. This is energy that most likely resulted in carbon dioxide emissions during its generation. Thus, the energy can be converted into carbon equivalence and taken into account in the same fashion that other carbon flows are considered with respect to time. The use of waste energy that cannot be distributed (e.g., geothermal heat or process plant waste heat) should be considered "carbon neutral."

LAND USE FOR CARBON SEQUESTRATION

If the sequestration activity will occupy a significant amount of land and if that land is a sink for carbon, this has to be taken into account.

Others

Cost, regulatory issues, environmental impact, and social impact fall into this category. These are items very important for any undertaking and should be considered. However, it is in some cases very subjective and they should be kept separate from the carbon metrics evaluation. They each have strong merit and should be addressed, but it may be appropriate to abstain from assigning any value to these factors. Cost represents a separate factor that can be evaluated through standard cost estimation methods.

Costs will be part of this work if data are available. For example, if the cost for an algae pond has been estimated, it will be noted, but it will not be part of the carbon metrics.

In order to investigate whether the above factors are appropriate to consider when a carbon sequestration activity is being evaluated, several focus-group meetings will be held with others who are working on carbon credit trading and carbon credits for Land Use Change and Forestry. Both ORNL internal and external focus-group meetings will be held. This will make sure that the initial approach taken gains support and understanding.

DISCUSSION OF CURRENT ACIVITIES

The funds for this task were received in April 2000. To initiate this project we have had one informal lunch discussion in the Biochemical Engineering Research Group on the topic and the project review meeting on March 7–8, 2000. Also, a presentation was given at a discussion session on Special Topics on CO_2 Sequestration at the 22nd Symposium on Biotechnology for Fuels and Chemicals on May 9, 2000. In all the discussion, the general consensus was that the variables chosen were appropriate. It was pointed out that when evaluating sequestration activities, not only should the clear carbon flows be accounted for, but also the latent carbon dioxide emissions associated with construction of equipment and facilities as well as for material used or generated via the process. It was also clear that the cost aspect was an important variable, but no consensus was reached about how that could be incorporate into one metric for a specific activity. Most were in favor of a tier approach, where carbon and energy balance and sequestration duration would come in the top tier and that costs, environmental issues, and potential other consequences would be a lower-tier evaluation. Some felt that some preference should be given to technologies that produced a usable product.

PRESENTATIONS AND PUBLICATIONS

K. T. Klasson and B. H. Davison, "Estimation of Carbon Credits in CO_2 Sequestration Activities," presented at the 22nd Symposium on Biotechnology for Fuels and Chemicals, Gatlinburg, TN, May 7–11, 2000.

ENVIRONMENTAL SUPPORT TO THE CLEAN COAL TECHNOLOGY PROGRAM

R. L. Miller

Work for the National Energy Technology Laboratory (NETL) during this period included the preparation of an environmental impact statement (EIS) to evaluate the potential environmental impacts associated with constructing and demonstrating a new circulating fluidized bed (CFB) combustor fueled by coal and petroleum coke to repower an existing steam turbine to generate nearly 300 MW of electricity. The EIS will be used by the U.S. Department of Energy (DOE) in making a decision on whether or not to provide cost-shared funding to design, construct, and demonstrate the CFB technology under the Clean Coal Technology (CCT) Program. The proposed project would be located at JEA's (formerly the Jacksonville Electric Authority's) Northside Generating Station in Jacksonville, Florida, which currently consists of three heavy oil- and natural-gas-fired steam generation units and four diesel-oil-fired combustion turbine units. Demonstration of the proposed project would be conducted during a 2-year period, from March 2002 until March 2004. In addition, JEA plans to repower a second Northside steam turbine about 6 to 12 months after the proposed project without cost-shared funding from DOE.

The overall objective of the project is to demonstrate the feasibility of CFB technology at a size that will be attractive for large-scale utility operation. In a CFB combustor, coal and coal/fuel blends, air, and limestone are introduced into the lower portion of the combustor, where initial combustion occurs. As the fuel is reduced in size through combustion and breakage, it is transported higher in the combustor, where additional air is introduced. Ash and unburned fuel and limestone pass out of the combustor, collect in a particle separator, and recirculate to the lower portion of the combustor. Sulfur reacts with limestone added in the furnace to form ash that can be marketed as a useful by-product such as roadbed material. The project is expected to provide JEA with a low-cost, efficient, and environmentally sound generating resource.

The EIS evaluates the principal environmental issues, including air quality, traffic, noise, and ecological resources, that could result from construction and operation of the proposed project. Key findings include that maximum modeled increases in ground-level concentrations of sulfur dioxide (SO_2), nitrogen dioxide (NO_2), and particulate matter (for the proposed project alone or in conjunction with the related action) would always be less than 10% of their corresponding standards for increases in pollutants. For potential cumulative air quality impacts, results of modeling regional sources and the proposed project indicate that the maximum 24-h average SO_2 concentration would closely approach the corresponding Florida standard (i.e., 97%) but would not exceed it. After the Unit 1 repowering, results indicate that the maximum 24-h average SO_2 concentration would be 91% of the Florida standard.

Concentrations for other averaging periods and pollutants would be lower percentages of their standards. Regarding toxic air pollutants from the proposed project, the maximum annual cancer risk to a member of the public would be approximately 1 in 1 million; given the conservative assumptions in the estimate, the risk would probably be less.

With regard to threatened and endangered species, impacts to manatees, gopher tortoises, and other species would be negligible or nonexistent. Construction-induced traffic would result in noticeable congestion. In the unlikely event that all coal were transported by rail, up to three additional trains per week would exacerbate impacts associated with noise, vibration, and blocked roads at on-grade rail crossings. Additional train traffic could be minimized by relying more heavily on barges and ships for coal transport, which is likely to be a more economical fuel delivery mode. During construction of the proposed project, noise levels would increase from the current operational levels. Except possibly during steam blowouts and possibly during operation of equipment used to construct a nearby segment of a conveyor, construction noise should not appreciably affect the background noise of nearby residences or exceed local noise limitations. The preferred alternative for management of the combustion ash would be to sell it as a by-product to off-site customers. If more than approximately 70% of the ash could be sold over the 30-year lifetime of Northside Generating Station, the 40-acre storage site would be sufficient for complete containment.

BIOLOGICAL QUALITY OF SOILS CONTAINING HYDROCARBONS AND EFFICACY OF ECOLOGICAL RISK REDUCTION BY BIOREMEDIATION ALTERNATIVES

A. J. Stewart

INTRODUCTION

This project, FEAC303, was supported by the U.S. Department of Energy (Fossil Energy Program, National Petroleum Technology Office, Tulsa, OK; Dexter Sutterfield, Project Manager). It provided data and technical guidance to Petroleum Environmental Research Forum (PERF) project 94-06, "Cooperative Bioremediation Program," sponsored by Exxon. Participants in PERF project 94-06 included Exxon, Shell, Conoco, BP Amoco, Texaco, Chevron, Unocal, the Gas Research Institute (GRI), Alcoa, DuPont, the Canadian Association of Petroleum Producers (CAPP), and the American Petroleum Industry, in addition to the Department of Energy. The central research issue being addressed by research in PERF project 94-06 was on environmentally acceptable endpoints for petroleum hydrocarbon residuals in soil, from a risk-based perspective. Various studies have shown that various chemicals present in petroleum hydrocarbon mixtures may be able to permeate into soil particles. If this occurs, the particle-embedded hydrocarbon compounds may be extractable by organic solvents, and yet be essentially unavailable to biota. Risk to ecological receptors from petroleum hydrocarbons in soils would be lessened accordingly, which should be taken into account in setting risk-based cleanup standards or when developing and verifying efficacy of bioremediation cleanup techniques.

DISCUSSION OF CURRENT ACTIVITIES

PERF Project 94-06 was completed on schedule, in 2000 ,[1] so funding to support FEAC303 also ended. We are now essentially wrapping up the project's last loose ends; many of the activities supported by FEAC303 are incorporated into the PERF Project 94-06 final report.[1] During 1999, key activities in FEAC303 included project-related travel; completion of a report on toxicity benchmarks for petroleum hydrocarbons; and development and field-testing of methods for characterizing biological conditions at petroleum exploration and production (E&P) sites. Additional details about each of these three areas are given below.

Project-related communication and interaction with petroleum industry representatives have been important aspects of FEAC303. In August 1999, the project's principal investigator attended PERF 97-08, 94-06, and 99-01 project meetings in San Francisco, California. In November 1999 he attended the annual Society for Environmental Toxicology and Chemistry meeting in Philadelphia, Pennsylvania; and in April

2000 he attended a PERF Project 99-01working-group meeting in Houston, Texas. Excellent technical exchange occurred in each of these meetings.

One area of interest by petroleum industry partners in PERF Project 94-06 was that of developing simple field-based methods that could be used to characterize biological conditions at E&P sites. Such methods could be used to provide evidence for the idea that conventional operational procedures were sufficient to preclude the necessity of a formal ecological risk assessment. The idea corresponds approximately to what we at ORNL might refer to as a "Best Management Practices" operation: a means to document operational status, with the objective being to reduce the potential for inadvertent damage to the environment. Documentation, in the form of a checklist, might also make it easier for environmental regulators to consider alternative uses of land associated with E&P operations when the fields are no longer productive. We developed a brief protocol that could be used to evaluate biological conditions at petroleum E&P sites, and performed preliminary testing of that protocol at several small E&P sites in south-central Kentucky. The protocol and the results of its application were submitted to the project manager and the PERF project point-of-contact as a project (Task 3) milestone in April 2000. A photograph of the E&P site where the protocol was applied is shown in Fig. 1.

Fig. 1. E&P site in south-central Kentucky, where we tested a checklist protocol for assessing biological conditions.

The third main accomplishment for FEAC303 during this annual reporting period was the preparation of a document titled "Review of Data and Proposed Benchmarks For Evaluating the Potential Ecotoxicity of Petroleum-Contaminated Soil."[2] This report was sent to petroleum industry representatives for review and comment, and is presently being revised to manuscript form. When revision is complete, the manuscript will be sent to *Environmental Toxicology and Chemistry* for publication.

The "benchmarks report" noted above contains total petroleum hydrocarbon toxicity data and no-effects concentrations and doses for plants, soil invertebrates, mammals and birds; these data were compiled from published studies and summarized. Screening ecotoxicity benchmarks for plants and soil invertebrates were calculated as the 10th percentile of Lowest Observed Adverse Effects Concentrations and other effects concentrations from tests in published studies. One significant finding was that toxicity to invertebrates generally occurred at concentrations of total petroleum hydrocarbons that were lower than those associated with toxicity to plants (Fig. 2).

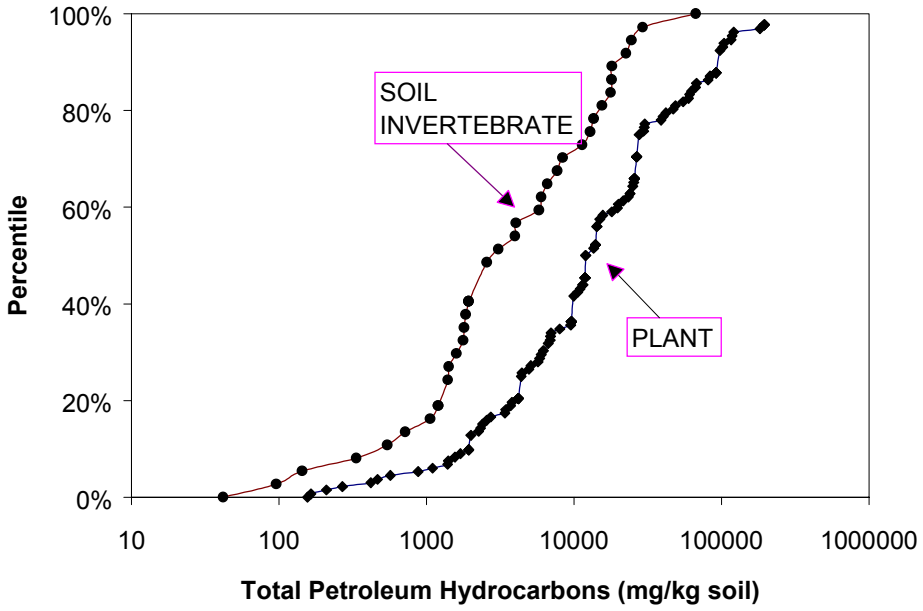

Fig. 2. Plot showing percentile of studies reporting effects levels for total petroleum hydrocarbons in soil to soil invertebrates and plants. Note that data for total petroleum hydrocarbon concentrations (*x*-axis) are expressed on a log scale. [From Efroymson et al., 2000. *Review of Data and Proposed Benchmarks for Evaluating the Potential Ecotoxicity of Petroleum-Contaminated Soil*. (Manuscript, in revision).]

Materials associated with the lowest toxic-effects concentrations (and benchmark concentrations) for plants and soil invertebrates were bioremediated crude-oil-contaminated soils. Mixtures associated with the highest toxic-effects concentrations (i.e., the least toxic mixtures) were diesel fuel, home heating oil, lube oil, and jet fuel. Interestingly, the variability in toxic effects concentrations that were used to derive the screening benchmarks for plants and soil invertebrates was no greater than that for many single chemicals for which screening benchmarks have been derived previously. Data summarized in the toxicity benchmarks report clearly reveal the biological value of bioremediation, and provide strong support for the idea that plants are generally more tolerant than soil invertebrates to petroleum hydrocarbons in soil.

REFERENCES

1. ThermoRetec. 2000. *Final Report: Environmentally Acceptable Endpoints for Hydrocarbon-Contaminated Soils.* (GRI Contract No. 5094-250-2863, PERF Project 94-06, Research Area 1). Released in February 2000.

2. Efroymson, R. A., B. E. Sample, M. J. Peterson and A. Saterbak. 2000. *Review of Data and Proposed Benchmarks for Evaluating the Potential Ecotoxicity of Petroleum-Contaminated Soil.* (Manuscript, in revision).

NATURAL GAS AND OIL TECHNOLOGY PARTNERSHIP

T. W. Schmidt

PARTNERSHIP SUPPORT

The Natural Gas and Oil Technology Partnership (NGOTP) expedites development and transfer of advanced technologies through technical interactions and collaborations between nine national laboratories and the petroleum industry (majors, independents, and service companies), and universities.

The Partnership combines the expertise, equipment, facilities, and technologies of the U.S. Department of Energy's national laboratories with those of the U.S. petroleum industry. The laboratories utilize unique capabilities developed through energy and defense research and development, including electronics, instrumentation, materials, computer hardware and software, engineering, systems analysis, physics,
and expert systems. Industry contributes specialized knowledge and resources and prioritizes Partnership activities.

The areas of advanced technology are as follows.

- **Diagnostics and Imaging Technology** addresses cutting-edge geophysical methods for improved reservoir characterization with a focus on improved borehole hardware and computational efforts for seismic processing and other exploration issues. The Partnership catalyzed formation of a 25-company collaboration that has become the industry focal point for this technology.
- **Oil and Gas Recovery Technology** addresses a broad range of technologies aimed at improving production from existing fields and with specific emphasis on assisting independent producers. The industry interface is an Industry Review Panel consisting of more than 20 individuals representing independents, majors, and the service companies.
- **Drilling, Completion, and Stimulation Technology** aims at better access to the reservoir through improved drilling and completion technologies. Currently, the laboratories participate in several joint industry projects fostered by two industry organizations: the Drilling Engineering Association (DEA) and the Completion Engineering Association (CEA).
- **Environmental Technology** addresses new technologies that are needed to produce more oil and gas from mature domestic sources while safeguarding the environment. Key issues to be addressed include
  - produced water,
  - stationary source emissions,

  - risk assessment,
  - tank bottoms and sludge,
  - naturally occurring radioactive material (NORM),
  - soil remediation,
  - vapor recovery,
  - offshore structure decontamination and dismantlement (D&D), and
  - drilling wastes.
- **Downstream Technology** is a new area of technology that was funded under the NGOTP for the first time in fiscal year 1999. Projects were funded in the areas of bioprocessing heavy oils and the monitoring of $PM_{2.5}$ particulate.
- **Ultra-Clean Fuels Technology** is a new area of technology that is being coordinated under the NGOTP for the first time in fiscal year 2000 with projects to be funded in fiscal year 2001. A technology roadmap has been prepared based on the stated needs of the petroleum industry. On the basis of that roadmap, a solicitation to the members of the NGOTP is to be prepared and proposals are to be submitted, reviewed, and recommended for funding.

NATURAL GAS AND OIL TECHNOLOGY PARTNERSHIP COORDINATION OF BIOPROCESSING PROJECTS

T. W. Schmidt

The Natural Gas and Oil Technology Partnership Bioprocessing program involves projects at four national laboratories: Oak Ridge National Laboratory, Brookhaven National Laboratory, Idaho National Engineering and Environmental Laboratory, and Lawrence Livermore National Laboratory. To ensure coordination between the different projects, two meetings involving the four laboratories and their collaborating industry partners are held each year. A review of the current projects and a solicitation for new projects is scheduled for fiscal year 2000.

DISCUSSIONS OF CURRENT ACTIVITIES

T.W. Schmidt and S. M. Robinson

During 2000, T. W. Schmidt participated in the development of the recommendations for funding of the Partnership Programs on behalf of Oak Ridge National Laboratory. In addition, to existing projects in Diagnostics and Imaging Technology and Downstream Environmental Technology, T. W. Schmidt and S. M. Robinson assisted in the continued funding of the In-Well Oil and Water Separation Project, the Physical Property Measurement of Produced Water Project, and the funding of a new project to develop an ecological framework to evaluate the impacts of the releases at petroleum exploration and production sites. Other activities include program planning with the Partnership, selection of a Partnership Steering Committee, coordination of the Partnership projects in Bioprocessing of Crude Oils, coordinating all of the national laboratory participation in the Downstream Technology Area, and the development of a new technology area in Ultra-Clean Fuels through the coordination of an industry workshop and project review.

BIOLOGICAL UPGRADING OF PETROLEUM FEEDSTOCKS AND HEAVY OILS VIA MICROBIAL AND ENZYME BIOCATALYSIS

Abhijeet P. Borole

INTRODUCTION

Biological removal of organic sulfur from crude oil offers an attractive alternative to conventional thermochemical treatment due to the mild operating conditions afforded by the biocatalyst. Our previous work has included development of an electro-spray bioreactor to improve oil-water contacting,[1,2] determination of sulfur removal from crude oils using microbial biocatalysts,[3] and comparison of gram-negative and gram-positive organisms as hosts for biodesulfurization enzymes[4].

In our continued efforts toward development of alternate technologies for heavy oil upgrading, we are currently investigating enzymatic methods for upgrading crudes via partial oxidation and bioconversion. The objective of this program is to develop new technologies for upgrading of heavy oils, using novel enzyme-based bioprocessing concepts. This project is being conducted in collaboration with Texaco, Chevron, and Phillips via a cooperative research and development agreement and it is funded by the National Petroleum Technology Office, U.S. Department of Energy.

A combined chemical-biological desulfurization process for sulfur removal from diesel and middle distillates was investigated in collaboration with Petro Star and Dr. Eduardo Diaz from Consejo Superior de Investigaciones Cientificas (CSIC), Madrid, Spain. This project was funded by Petro Star, Inc., a refiner located in Anchorage, Alaska. The researchers at Petro Star have developed a process to selectively oxidize organosulfur compounds present in diesel followed by extraction of the oxidized sulfur compounds with an organic solvent, resulting in a high-sulfur diesel extract. ORNL performed experiments to develop the biological desulfurization step for removing sulfur from the high sulfur diesel extract.

DISCUSSION OF CURRENT ACTIVITIES

Enzymatic Upgrading of Heavy Crudes via Partial Oxidation or Conversion of PAHs

Enzymes, naturally occurring in aqueous environments, can be adapted to work in organic media by chemical modification and genetic engineering, making them stable and active in the organic media. Initial focus is on the use of oxidative reactions as model reactions to study conversion of polyaromatic hydrocarbons (PAHs) to partially oxidized products in organic media.

In order to develop biocatalysts that are stable and active in organic media, enzymes and heme-containing proteins capable of partial oxidation of PAHs were screened for activity in pure solvents and mixtures of organic solvents in water. Pyrene, methyl-anthracene and dibenzothiophene were used as model compounds for these reactions. The typical products from these bioconversions were quinones or sulfones. Lignin peroxidase (LiP) and cytochrome c (cyt c) were found to have a high rate of reaction and were chosen as candidates for improvement of activity. These proteins were found to be inactive at higher concentrations of organic solvent (30% acetonitrile for LiP, and 50% for cyt c). In order to improve activity of the proteins in organic solvents, chemical modification of the proteins with hydrophobic groups was studied. Groups such as polyethylene glycol (PEG), or surfactants such as Brij were attached covalently to the protein. The modified protein was purified and either lyophilized for storage at -20^{o}C or stored as a solution at 4^{o}C. Experiments to determine the activity of the surfactant-modified proteins is in progress. Modification of the proteins with PEG was found to increase the activity of cyt c for conversion of pyrene by a factor of four at 20% acetonitrile[5]. However, it did not improve the activity of the protein at 50% and higher acetonitrile concentrations. Experiments with other substrates indicated the hydrophobicity and polarity of the substrate; possibly the enzyme active site played a role in conversion of polyaromatic compounds. In order to achieve the transformation of polyaromatic structures in an oil or similar hydrophobic solvent environment, future work is being planned to alter the active site of the enzymes. In order to accomplish active-site modification, both chemical and molecular biology techniques will be employed. Peroxidase enzymes and other catalytic proteins such as chloroperoxidase, cytochrome c or lignin peroxidase are being considered for modification. Preliminary experiments investigating attachment of small hydrophobic groups such as methyl and ethyl groups at the active sites via chemical means have been initiated. The second means to alter proteins is via genetic manipulation of the DNA expressing the enzyme. This requires expression of the enzyme in a suitable host, which would allow easy manipulation of the DNA. Host organisms such as yeast are being considered for expression of the fungal peroxidases being investigated.

Biological Desulfurization of Diesel Extract

The diesel extract produced from Petro Star's chemical oxidation and extraction process consists of aromatic sulfones as the major species. In order to remove sulfur from these organosulfur compounds ORNL investigated aerobic as well as anaerobic processes. Sulfur removal using anaerobic organisms such as sulfate-reducing bacteria revealed marginal sulfur conversion. Aerobic microbial biocatalysts were developed by our collaborator, CSIC, by inserting the genes for the desulfurization enzymes into

hosts such as *Pseudomonas putida* and *P. aeruginosa*. These biocatalysts were tested by ORNL against model sulfone compounds to determine the extent of desulfurization[6]. Considerable desulfurization was observed using the aerobic biocatalysts as compared to the anaerobic organisms; therefore, further work was focussed on aerobic biocatalysts. Figure 1 shows the results from biological treatment of diesel extract with the aerobic biocatalyst, *P. putida*, KTH2. The distinct peaks representing the major sulfur compounds in the extract were eliminated across the whole spectrum of the extract as seen in the sulfur-specific chromatogram. These compounds were converted to desulfurized products as demonstrated by the appearance of new peaks on the flame ionization detector (FID) chromatogram. The extent of desulfurization, however, was not very deep since only marginal reduction of the hump was observed. This indicates the need for further development in biocatalyst, especially for broadening the substrate specificity of the biocatalyst to improve desulfurization of complex and highly substituted compounds such as alkyl and aryl thiophenic sulfones present under the hump.

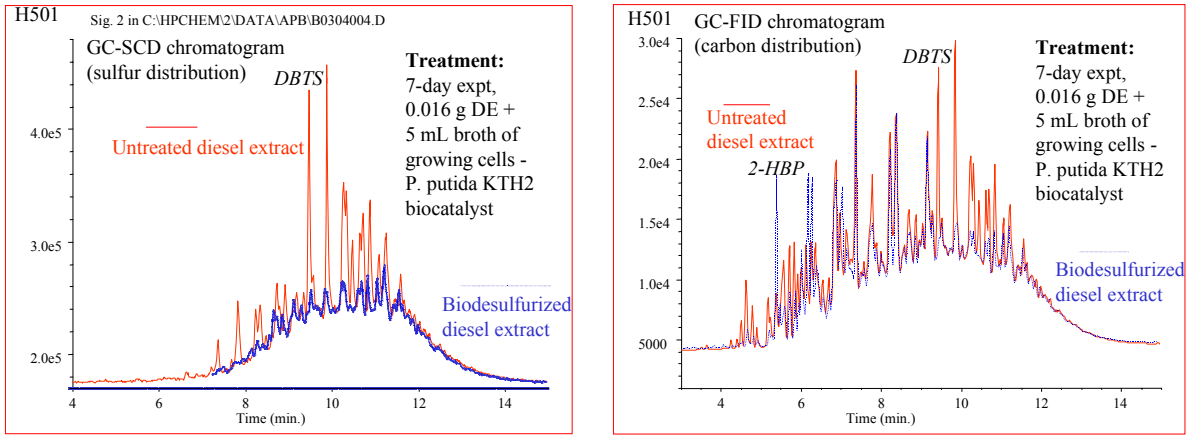

Fig. 1. Biological desulfurization of diesel extract using *P. putida* KTH2 biocatalyst. (*left*) sulfur distribution by GC-SCD. (*right*) GC-FID chromatogram.

ACKNOWLEDGMENTS

The multi-oil company CRADA project was supported by the National Petroleum Technology Office, U.S. Department of Energy under a contract DE-AC05-00OR22725 with UT-Batelle, LLC. The desulfurization of diesel project is being supported by Petro Star, Inc.

REFERENCES

1. C. Tsouris, A. P. Borole, E. N. Kaufman, and D. DePaoli, "An Electrically-Driven Gas-Liquid-Liquid Contactor for Bioreactor and Other Applications," *Ind. & Eng. Chem. Res.*, 1999. **38**: 1877-1883.
2. E. Kaufman, J. Harkins, and A. Borole, Comparison of Batch-Stirred and Electro-Spray Reactors for Biodesulfurization of Dibenzothiophene in Crude Oil and Hydrocarbon Feedstocks, *Applied Biochemistry and Biotechnology*, 1998. 73(2-3), 127-144.
3. E. N. Kaufman, A. P. Borole, R. Shong, J. L. Sides, and C. Juengst, "Sulfur Specificity in the Bench Scale Biological Desulfurization of Crude Oil by *Rhodococcus* IGTS8," *J. Chem.Technol. & Biotechnol.*, 1999. **74**, 1000-1004.
4. A. P. Borole, E. N. Kaufman, M. J. Grossman, V. Minak-Bernero, R. Bare, and M. K. Lee, "Emulsion Formation and Breakage in a Biodesulfurization Process: Effect of Biocatalyst Hosts," submitted to *Biotech. and Bioeng*. for publication, 2000.
5. A. P. Borole, C. L. Cheng, B. H. Davison, J. M. Cosgrove, and E. N. Kaufman, "Bioconversion of Polyaromatic Hydrocarbons in Organic Media Using Chemically Modified Enzymes," *AIChE Annual Meeting*. 1999. Dallas, TX.
6. A. P. Borole, C. L. Cheng, B. H. Davison, M. D. Travis, and S. E. Bonde, "Biological Desulfurization of Chemically-Oxidized Sulfur Species in Middle Distillate Fuels," *American Chemical Society Annual Meeting, Division of Petroleum Chemistry Preprints*. 2000.

PHYSICAL PROPERTIES MEASUREMENTS OF PRODUCED WATER

D. A. Bostick

INTRODUCTION

Oak Ridge National Laboratory (ORNL), Shell, BP, Chevron, Phillips, Marathon, and Statoil have initiated a collaborative Petroleum and Environmental Research Forum (PERF) project to characterize and evaluate water solubles aimed at reducing future production of these contaminants. ORNL will identify water-soluble organics in produced water and will characterize these compounds quantitatively by accurate measurements of equilibrium solubilities and associated thermophysical properties for deep-water crudes at high pressures and temperatures. Industrial partners will provide samples of deep-water crudes and produced water, select methods to characterize the water-soluble organics, compare the data with industrially obtained data from low-pressure wells, and evaluate the data for trends. Industrial partners will develop a model to predict the production of water-soluble organics as a function of crude composition and formation characteristics.

The primary tasks for FY 1999 and 2000 include (a) devise an integrated testing plan to determine the effect of water cut, produced water pH and salinity, and crude oil properties on the type and content of water-soluble organics; (b) obtain from industrial partners samples of actual crude/produced water; (c) begin to characterize the water-soluble organics by methods to be selected by industrial partners; and (d) provide data to industrial partners as data become available.

DISCUSSION OF CURRENT ACTIVITIES

BACKGROUND

Soluble organics in produced water and the resulting refinery effluents are treatment problems for the petroleum industry. Production facilities and refineries take special efforts to meet regulatory discharge requirements for dissolved organics. These problems are expected to increase as environmental regulations become stricter and as production from deepwater operations increases. Deepwater crudes are more polar, which increases the amount of dissolved hydrocarbons in the produced water and refinery effluents. Early data from the Gulf of Mexico wells indicate that the dissolved hydrocarbons will increase significantly as deepwater production increases.

Neither the chemistry involved in the production of soluble organics in the petroleum industry nor the impact of these compounds on total effluent toxicity is well understood. Several industrial companies, including Shell, BP, Chevron, Phillips, Marathon, and Statoil, are developing the collaborative PERF project to characterize and evaluate water solubles aimed at reducing future production of these contaminants. The project will increase the understanding of the production of water-soluble organics and

will ultimately result in reduced production of water solubles and development of guidelines for effluent treatment. Quantitative characterization data are needed as the first step in this activity. ORNL will identify water-soluble organics in produced water and will characterize these compounds quantitatively by accurate measurements of equilibrium solubilities and associated thermophysical properties.

ORNL is uniquely well suited to do research on the characterization of crude oils and water solubles, by virtue of its strong in-house concentration of equipment and expertise in high-temperature solution chemistry. In addition to a wide range of analytical instrumentation, equipment formerly under the control of the U.S. Department of Energy (DOE) National Institute for Petroleum and Energy Research (NIPER) program and the ORNL High-Temperature Aqueous Chemistry group is available. The Acoustic Resonance Spectrometer/Calorimeter, one of five units in the world that is on loan to ORNL from Phillips, can make ultrasensitive physicochemical property measurements. Additionally, a Vapor-Liquid Equilibria (VLE) system has been made available to ORNL from Chevron. This enables ORNL to perform a full spectrum of experiments on the liquid mixtures of interest over a wide range of temperatures and pressures to simulate field conditions.

PROGRESS

Several meetings were held among PERF members throughout the year to further define the scope of this project and to systematize analytical procedures. Laboratory work began in late fiscal year 1999. Input from industrial partners over the past year has been used to develop a detailed scope of work for sample analysis needed to support the industrial partners' development of a model for produced water contamination. Barrel quantities of crude oil will be obtained from industrial partners for analyses in 2000 and 2001. An experimental work plan for their analysis was developed to ensure comparability between data generated by ORNL and industrial partners. The U.S. Environmental Protection Agency (EPA) Methods protocol has been selected to analyze individual organic species in actual produced water and actual crude samples received from industrial partners. These methods include the following protocol for organic constituents:

- EPA Method SW-846 8260 B (Volatile Organic Compounds),
- EPA Method SW-846 8270C (Semivolatile Organic Compounds and Polyaromatic Hydrocarbons),
- EPA Method 1664 (Total Recoverable Petroleum Hydrocarbons) as the benchmark protocol for environmental regulation requirements, and
- BTEX in sample head space to be analyzed by GC/FID.

Inorganic constituents will be analyzed using the following methods:

- Ion chromatography (EPA Method 429) for anions,
- Inductively coupled plasma optical emission spectrophotometry (EPA Method 305) for dissolved metal, and
- titrimetry (EPA Method 403) for pH and carbonate/bicarbonate ratio.

In addition to actual crude and produced water, a series of laboratory-prepared water samples have also been planned. In this case, real crude oils will be contacted with brine simulant to create produced waters representing reaction conditions to be encountered under a variety of drilling conditions. During the course of this fiscal year, PERF industrial partners set the following ranges for preparing the produced water samples:

- 1-100 atm (15-1500 psi);
- 90-200°F (25-100°C);
- pH 6.5 plus or minus 2 units;
- water cut of 20, 50, 80 %; and
- 35,000-150,000 ppm total dissolved solids.

Because of the extensive number of samples that will be generated in this study, ORNL staff will use a less-expensive, open-column liquid chromatographic procedure to characterize the organic content in these samples. The open-column protocol will determine total, asphaltene, saturated and aromatic petroleum hydrocarbon, and organic-acid fractions on a weight basis. Individual fractions will then be archived in the event that analysis by full EPA method protocol is deemed necessary in the future.

Thus far, ORNL has received 20 L of a crude oil, sampled at ambient pressure, to begin laboratory preparation of performed water samples. Additionally, industrial partners have provided chemical characterization data for brine from the Gulf of Mexico and a spreadsheet that will delineate the preparation of a simulant of brine from the Gulf of Mexico based on their characterization data. An oil/water contact vessel has been fabricated, based on design criteria described in ASTM D6081 (Proposed Standard Practice for Aquatic Toxicity Testing of Lubricants: Sample Preparation and Results Interpretation). Solvent extraction/concentration equipment is being set up. Once certified, the extraction/concentration and chromatographic equipment will be used to analyze the produced water samples from crude/brine simulant contacts.

Additionally, two pressurized crude oil samples have been received; the half-liter samples are being archived until ambient-pressure studies are completed. VLE equipment is currently being assembled to determine the distribution and partitioning of organic components at high temperatures and pressures for crude/simulant brine samples and in the two pressurized crude oils.

Finally, a confidentiality agreement between ORNL and industry participants was developed and signed this year. This agreement will give ORNL staff access to the confidential information from industry needed to perform the characterization tasks.

FUTURE PROGRESS

Analyses of the crude/produced water samples obtained in 1999 and 2000 will be completed in 2001. ORNL will assist industrial partners in the development of models to predict the production of water solubles from formation, crude, and water properties and will obtain additional data required for the model in 2001-2002. ORNL will evaluate the potential impact of increased water solubles on produced water treatment methods and down-stream processing and will evaluate the toxic effects of water solubles in the out years if the information obtained from the project warrants the additional activities.

REAL-TIME CHARACTERIZATION OF METALS IN GAS AND AEROSOL PHASES

Mengdawn Cheng

INTRODUCTION

Continuous monitoring is needed to provide data for real-time engineering control of the emissions of hazardous air pollutants and to meet future regulatory requirements; however, many technical difficulties are present for continuous measurement. Fluid conditions of a source emitting toxic metals can be hot, humid, and/or corrosive, thus creating problems for instrumentation. The toxic metals include arsenic, beryllium, cadmium, nickel, mercury, selenium, vanadium, radionuclides, and their organo-metallic species, which could be more toxic in terms of bioavailability than their elemental forms. Many metals can be found in the aerosol phase, elemental mercury being the only exception. Most reactive mercury and organo-mercury species are found in aerosol. To measure aerosol and the elemental composition of the particles in a source environment, one traditionally employs a filter-pack sampling train followed by instrumental analysis in a laboratory. This practice has several inherent problems, which include (1) bias due to sampling, (2) error due to sample handling, and (3) collection of nonrepresentative data due to an inadequate number of samples. The sampling bias could result when conditions inside a source (e.g., a stack) are different from the ambient conditions where the samples are taken. Particle nucleation, agglomeration, and coagulation can alter particle-size distribution and chemical composition, leading to inaccurate data when sample dilution is employed. The sample-handling errors could be human errors that are common even for a skillful technician. The cost involved in source sampling and analysis is high and prohibits the collection of a large number of samples. A small sample number may not be adequate to fully describe the source emission and its temporal variation, making the data less representative. Furthermore, for hazardous sources the samples are better contained inside without being drawn to the ambient. These factors have encouraged development of continuous-emission measurement techniques for emission sources.

A number of instrumental techniques currently exist for the measurement of trace elements associated with airborne particulate matter or aerosols.[1] These include X-ray fluorescence (XRF), proton-induced XRF, inductively coupled plasma atomic emission spectroscopy (ICP/AES), instrumental neutron activation analysis, and graphite-furnace atomic absorption spectroscopy, to name a few. To meet the requirements of developing a one-person field-portable and rugged instrument for continuous aerosol measurement, the laser-induced plasma emission spectroscopy (LIPS) was found to be the best candidate among several promising techniques.[2] The LIPS technique requires *no* alteration of sample condition

because the measurement is done in situ. The short cycle time (~ 100 ms) between each measurement makes the LIPS observation nearly *real time*.

LIPS, also called laser-induced breakdown spectroscopy, has been investigated for a large number of chemical analyses.[2-16] The LIPS technique has advantages over the other traditional analytical techniques. These advantages include the rapid turnaround time; nonintrusive, in situ, and flexible probe configuration; and availability as a compact trace metal analyzer. These strengths make LIPS a suitable candidate for the development of a small-footprint field-portable multi-element monitor to be used in hazardous environments such as a radiological hot cell, a mixed-waste contaminated area, and a high-temperature combustion chamber.

To raise the analytical performance of LIPS, a number of techniques had been tested, although none was specifically for aerosol measurements. Sattmann et al.[17] demonstrated the use of double or multiple laser pulses to achieve a higher signal-to-noise ratio for detecting Si in solid steel samples. They found that double pulses enhanced the signal over single pulses used in traditional LIPS by two orders of magnitude. Gornushkin et al.[18] suggested the use of LIBS/laser-excited atomic fluorescence spectrometry technique for the determination of cobalt in solid matrices: graphite, soil, and steel. They found this combination technique to have linearity over four orders of magnitude in the parts-per-billion to parts-per-million range, and the result was comparable with that for ICP/AES. These interesting techniques are harder to develop for a field-portable, rugged unit using current laser and gated detector technologies than a single-shot LIPS technique. Thus, alternative designs were pursued to improve LIPS performance for aerosol measurement. In this paper, we demonstrate that the sensitivity of single-pulse LIPS for aerosol measurement can be significantly improved by a new probe configuration called "Aerosol Beam Focusing" (ABF). The ABF technique was adopted from a similar design by Fernandez de la Mora and Riesco-Chueca.[19.]

ACCOMPLISHMENTS IN APRIL 1999 THROUGH MARCH 2000

1. Designed and tested several ABF configurations operated under different sampling conditions: pressure drop, flow rate, nozzle height, and convergence boundary geometry.
2. Completed system integration for the field-portable ABF-LIPS into a box of physical dimensions no bigger than the size of carry-on luggage and a weight of less than 50 lb.
3. Calibrated the ABF-LIPS against aerosol particles of known chemical composition and sizes.
4. Submitted two manuscripts for peer-reviewed publication. One has been accepted by *Applied Spectroscopy* and is in press; the other one, submitted to *Aerosol Science and Technology*, is currently in review.
5. The Lockheed Martin Energy Research Corporation (the former manager of Oak Ridge National

Laboratory for DOE) filed a patent for the ABF-LIPS design.

6. Identified and successfully made contact for conducting field tests on the instrument in the summer of 2000.

LABORATORY EXPERIMENTAL SETUP

LIPS uses a pulsed laser beam that is tightly focused onto an aerosol sample. This focused energy creates a micro-plasma that has a peak temperature four to five times higher than that of other plasma emission spectroscopy. Excited atoms release light at their characteristic wavelengths as they relax from the plasma-excited states. Only the bright broadband light can be observed a few nanoseconds after the plasma ignition. In a few microseconds after the plasma is ignited, the broadband emission background subsides significantly. The fine line structure of a spectrum resulting from the emissions of excited elements becomes prominent. The pattern and duration of an emission light at a specific wavelength depends on several factors, such as the atomic species, the surrounding ionic cloud and gas, and the laser characteristics (e.g., wavelength, pulse length, and energy). These factors together determine the physical characteristics (such as size, shape, residence time, temperature, and ion density) of the plasma. The time-resolved LIPS technique takes advantage of the time-dependent spectral behavior specific to an atom to improve the detection and sensitivity of LIPS.

An intensified detector was used to collect the emission light. The identified wavelengths of an atom were compared with those in an atomic spectroscopic library obtained from the National Institute of Science and Technology to qualitatively determine the identity of the atom. The background-corrected photon counts were recorded and evaluated against a calibration curve to quantitatively determine the amount of the element in the aerosol sample. The calibration curve was established for this study using prepared solutions of known concentrations. The repetition rate of the laser is 10 Hz; therefore all the processes involving the material breakdown, plasma ignition, triggering, gating, spectral analysis, and digital signal processing are completed within a 100-ms timeframe. With such a high data-throughput rate, the time-resolved LIPS system can be employed as a nearly continuous metal-aerosol monitor.

RESULTS AND DISCUSSION

LASER-INDUCED PLASMA SPECTRUM

A screen-capture of the emission spectrum of chromium in air is shown in Fig. 1. The delay time used for this detection was 18 μs after the laser was fired; the gatewidth was 8 μs. The presence of the wavelength triplet at 425, 427, and 429 nm is essential for a positive identification of aerosol chromium

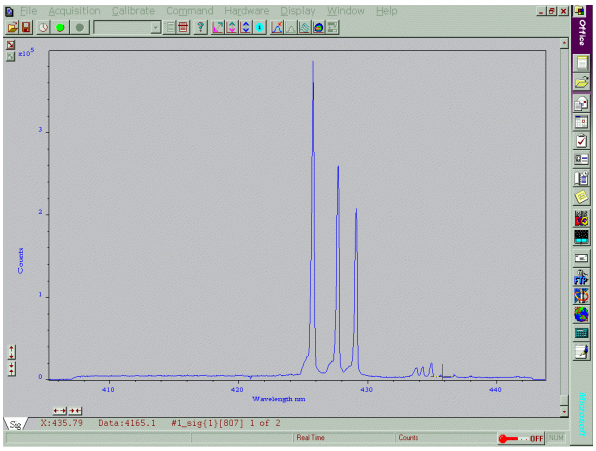

Fig. 1 A LIPS spectrum of aerosol chromium. Aerosol particles are produced by a nebulizer. The number density of the aerosol particles is on the order of 105 cm-3, and the median size is 300 nm with a geometric standard deviation of 1.29.

The 425-nm line of the triplet was used to quantitatively determine the amount of chromium in the aerosol. A total of 1000 shots (equal to 1 min and 40s) were accumulated to yield this measurement at the aerosol chromium concentration of 100 ng m^{-3}.

DESCRIPTION OF ABF NOZZLE

A properly operated focusing nozzle effectively concentrates particles and improves the odds for successful laser shots. This improvement is significant (as shown in the following section) and is critical for the development of a highly sensitive field-portable LIPS aerosol spectrometer. A flow velocity simulation result for the focuser using a commercially available computational fluid dynamics code is shown in Fig. 2. The focal length of the nozzle was approximately 2.4 mm from the exit and the focal-point cross section was about 50 micrometers. The flow downstream from the nozzle exit was operating at about 2.5 l min^{-1}. This creates a negligible pressure drop across the nozzle exit and minimizes any possible damage to the particle integrity without losing the focusing capability. A detailed comparison and characterization of different nozzle geometry and operating conditions with respect to the LIPS detection is presented in Cheng and Martin.[20]

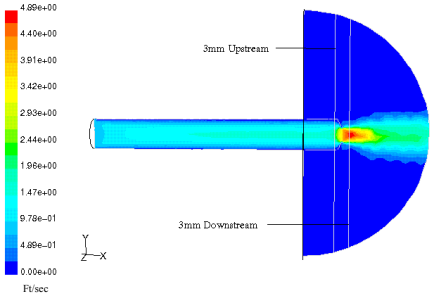

Fig. 2 Velocity distribution of an aerosol beam focuser.

EFFECTS OF THE ABF CONFIGURATION ON LIPS

Comparison of LIPS results between with and without ABF is presented in Fig. 3. The aerosol chromium concentration was maintained constant at 100 ng m^{-3} so we could examine the focusing effects. The 532-nm wavelength was used, and a total of 1000 shots was recorded. The energy levels of three bar pairs were at 50, 75, and 250 mJ per pulse. At the 50-mJ level, we collected no quantifiable signals [defined as the signal-to-noise (S/N) ratio ≥ 10] from the 1000 shots. The signal (S) is taken as the background corrected counts (BCC) at 425.5 nm. The noise (N) is the total noise for a measurement consisting of CCD pixel readout noise in counts, the electronic dark current noise in counts, and the shot

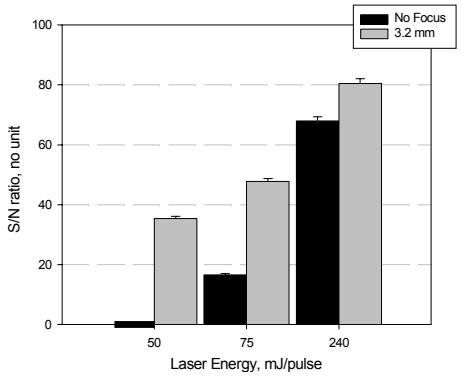

Fig. 3 Signal-to-noise ratio of LIPS measurement as a function of 532-nm laser energy with aerosol focusing and without. Concentration of chromuim on aerosol particles is 100 ng m^{-3}.

background noise in counts at a selected wavelength representing the background (i.e., 432 nm in this case).

When a 3.2-mm nozzle exit size was used, we could detect the chromium, and the S/N ratio was registered at 35 ± 0.7 for a 1000-shot sample. Where the laser energy was increased, one could in practice ignite a plasma and generate a LIPS signal at low particle mass, as shown in Fig. 3. The S/N ratio for the non-focusing cases goes from 17 ± 0.3 at 75 mJ to 68 ± 1.4 at 250 mJ. The S/N ratio for the focusing cases goes from 47 ± 1.0 at 75 mJ to 81 ± 1.6 at 250 mJ. The increases of the S/N ratios from non-focusing to focusing configuration were significant. Note that the increase in the S/N ratio for the non-focusing configuration from 50 to 250 mJ appears to be a nonlinear function of laser energy. This could be due to significant variation in the amount of the material present inside the plasma. The focusing configuration produces a linear relationship between the S/N ratio and the laser excitation energy input, indicating that the focusing nozzle maintains a rated material supply to the plasma that enables a precise quantification using LIPS.

EFFECTS OF LASER WAVELENGTH ON ABF-LIPS

A similar bar chart is presented in Fig. 4 for the 266-nm wavelength laser energy. All operating conditions remain fixed except the wavelength. The two bar pairs were for 50 mJ and 75 mJ, respectively. We noticed that no LIPS signal could be obtained without the focusing nozzle at 50-mJ energy using the 266-nm wavelength. Detection became possible when 75-mJ of energy was used in the non-focusing case.

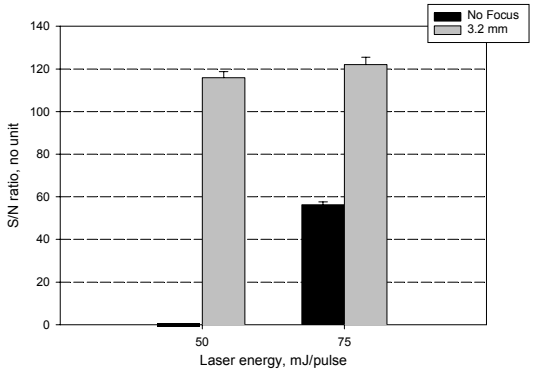

Fig. 4 Signal-to-noise ratio of LIPS measurement as a function of 266-nm laser energy with aerosol focusing and without. Concentration of chromuim on aerosol particles is 100 ng m^{-3}.

The increase of the S/N ratio as a function of the 266-nm laser energy in the energy range was minimal compared with that at 532 nm. This could be due to different ionization mechanisms postulated for the 266-nm wavelength that was mostly multiphoton ionization, while at 532 nm, both multiphoton and thermal cascade ionization were present.[2] If the coupling of energy to matter via multiphoton ionization saturated with the amount of material inside the plasma, the linearity as seen in Fig. 3 would not be present in Fig. 4. This result also indicates that 266 nm would not be a good choice of wavelength to use in the source emissions measurement that generally have high concentration, although it did provide a better S/N ratio compared with the 532-nm wavelength in our study.

The S/N ratios of the 1064-nm laser energy chart shown in Fig. 5 are similar to that of Fig. 3 (532 nm) and 4 (266 nm). Studies by Radziemski et al.[13] and Martin et al.[2], for example, noted that most of the LIPS signal from the interaction of the 1064-nm wavelength with aerosol resulted from thermal cascade ionization. The results in Figs. 3, 4, and 5 show that the LIPS signal might not be a linear function of laser energy. For instance, the S/N ratios for the focused cases level off when the laser energy increases from 200 to 400 mJ per pulse. This behavior is inconsistent with those seen in the other two wavelengths, where more energy leads to a higher S/N ratio. However, the energy inputs of the 1064-nm laser were about twice to four-time higher than that of the 532- or 266-nm wavelengths. This result indicates the ability of the focusing nozzle to regulate the retrievable amount of LIPS signal by controlling the amount of material available for plasma consumption. This also shows that using more laser energy cannot

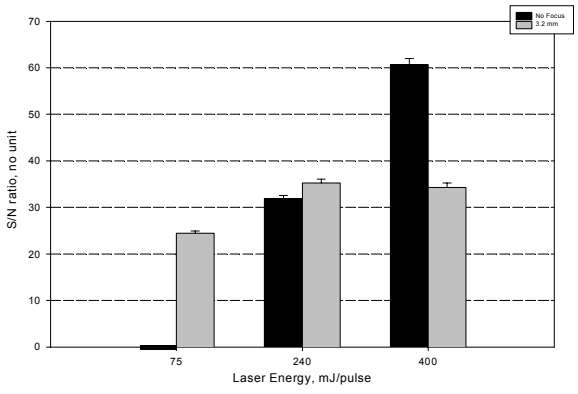

Fig. 5 Signal-to-noise ratio of LIPS measurement as a function of 1064-nm laser energy with aerosol focusing and without. Concentration of chromium on aerosol particles is 100 ng m-3.

possibly produce more signals exceeding what is available from the material inside the plasma. On the other hand, more laser energy leads to a higher S/N ratio in the non-focusing case consistent with those non-focusing cases in Fig. 3 and 4. This raises a question regarding the analytical performance of the LIPS measurement. In other words, if the analyte quantity cannot be controlled as in the non-focusing case, the LIPS signal would have to be normalized somehow at the different excitation energy levels for an unknown (or uncontrollable) analyte mass. That can be quite challenging in a field operation.

EFFECTS OF CHEMICAL SPECIATION ON ABF-LIPS

The ratios of BCCs for chromium (VI) to chromium (III) are shown in Fig. 6. The tri-chromium chloride salt [$CrCl_3$] provided the Cr (III), while the hexachromium salt ($Na_2Cr_2O_7$) provided Cr (VI) for LIPS analyses. Two solution concentrations were used, 4.8 and 11.5 M. The objective of this experiment was to test whether ABF-LIPS is matrix dependent. The ratio of BCC of the aerosol that was made from the hexachromium salt to that of the tri-chromium salt should be approximately 2 at both molar concentrations because there are two chromium atoms in the aerosol made of $Na_2Cr_2O_7$ while only one is in the $CrCl_3$ aerosol. We show in Fig. 6 that the LIPS signals are consistent with the ratio of 2 and that LIPS can precisely quantify irrespective of the wavelength used.

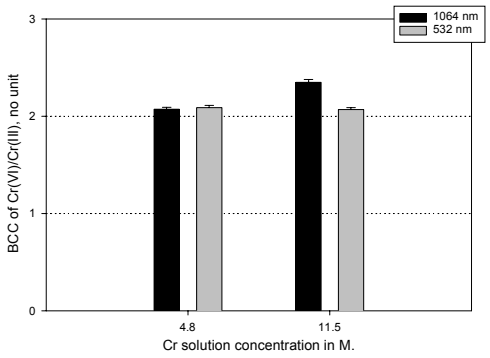

Fig. 6. LIPS signal as a function of chromium molar concentration.

We did not convert this solution concentration to aerosol concentration (ng m^{-3})as we did in other experiments for the sake of simplicity. When the solution concentration increased from 4.8 to 11.5 M, the BCC ratios of the 1064- and 532-nm wavelength are different. While the 532-nm wavelength still yields a ratio close to 2, which is the correct number, the 1064-nm wavelength configuration yields a higher ratio around 2.35, which is 17% higher than 2. The uncertainty of the ratios was on the order of 0.03, so 17% deviation is significant. We currently do not know what caused this discrepancy but hypothesize that the 1064-nm wavelength may be more sensitive to the plasma optical thickness than the 532-nm wavelength. As more material present inside the plasma as in the case of 11.5 M, the thermal cascade ionization tends

to depend more on the material mass present thus activating the same chromium atoms more than once. Since the repetitive collision of photons with the same atoms has a small probability, one would not expect a substantially higher (on the order of magnitude type) BCC ratio. These results demonstrate that ABF-LIPS does not speciate but it provides a true total elemental concentration in the aerosol sample.

CONCLUSIONS

Aerosol beam-focused laser-induced plasma spectroscopy was employed as the principle in the design of a field-portable instrument for the measurement of trace metals associated with airborne particulate matter. Operational parameters examined in the design phase included the laser wavelength, laser energy, and the use of ABF. It was found that more laser energy used in plasma generation could produce a higher LIPS signal. However, the optimal or maximum signal appears to be regulated by the focusing nozzle, which provides precise control for quantitative determination of aerosol metal content. It was also found in this study that the LIPS technique alone, without ABF, was insufficient to detect trace metals in aerosol at a level comparable to those found in source emissions. This is due to the discrete nature of aerosol mass distribution inside a source, a property that is unique to aerosol sampling. By coupling an ABF technology, we have enhanced the LIPS sensitivity by more than 250% while consuming much less laser energy than previously needed. A rugged, compact ABF LIPS was successfully developed. Finally, LIPS was proven to be a non-species-specific analysis. The ABF-LIPS technique measures the true total elemental composition associated with aerosol rather than the concentration of speciated metals. To measure speciated metals associated with aerosols in real time and in situ at emissions, other techniques have to be developed.

REFERENCES

1. Hopke, P. K. (1985) *Receptor Modeling*, John Wiley & Sons, New York, NY.
2. Martin, M. Z. et al. (1999) *Aerosol Sci. Technol*. 31: 409-421.
3. Aragon, C. et al. (1993) *Appl. Spectrosc*. 47,606.
4. Belliveau, J. et al. (1985) *Appl. Spectrosc*. 39,727.
5. Cheng, M. D. (1999) *Fuel Process. Technol*. in press.
6. Grant, K. J. et al. (1991) *Appl. Spectrosc*. 45, 701.
7. Kirchheim, R. et al. (1976) *Anal. Chem*., 48, 1505.
8. Millard, J. A. et al. (1986) *Appl. Spectrosc*. 40, 491.
9. Niemax K., and W. Sdorra (1990) *Appl. Opt*. 29: 5,000.
10. Neuhauser, R. E. et al. (1999) *Fresenius J. Anal. Chem*. 364:720-726.
11. Panne, U. et al. (1998a) *Spectrochimica Acta Part B*. 53:1,957-1,968.
12. Panne, U. et al. (1998b) *Spectrochimica Acta Part B*. 53:1,969-1,981.
13. Radziemski, L. J. et al. (1983) *Anal. Chem.* 55, 1246.
14. Simeonsson, J. B., and A. W. Miziolek (1994) *Appl. Phys*. B, 59, 1.
15. Wisburn, R. et al. (1993) *Anal. Methods Instrument*. 1, 17.

16. Yalcin, S. et al. (1996) *Hazardous Waste Hazardous Materials*, 13: 51.
17. Sattmann, R. et al. (1995) *J. Phys. D: Appl. Phys*. 28, 2181-2187.
18. Gornushkin, I. B. et al. (1997) *Appl. Spectrosc*. 51: 1055-1059.
19. Fernandez de la Mora, J. and Riesco-Chueca, P. (1988) *J. Fluid Mech*. 195, 1-21.
20. Cheng, M. D. and Martin, M. Z. (2000) *Aerosol Sci. Technol*., in review.

ENVIRONMENTAL COMPLIANCE ASSISTANCE SYSTEM

S. M. DePaoli

The Environmental Compliance Assistance System (ECAS) is a web site provided through the National Petroleum Technology Office (NPTO). This web site is targeted at the independently owned and operated oil and gas exploration and production (E&P) industry. In general, these E&P facilities are small, family-owned operations and therefore do not have the capital to support the personnel needed to research and maintain information regarding environmental compliance issues concerned with their industry. This web site has been provided to aid these and other interested parties with regulatory information on the E&P industry; local, state, and federal contacts; waste handling/treatment/disposal options; and to direct them to other related web sites. A link to the ECAS can be found at http://www.aimsicorp.com/ECAS_frames/frame_b.htm.

This NPTO-funded project is tasked with updating the ECAS system that is currently on the web. The new, completed website is currently on a server at Advanced Integrated Management Services, Inc. (AIMSI) (accessed through the above address). The NPTO is working on a new environmental webpage to be accessed from their main website. The ECAS website will be a link from this page, and will be incorporated when the NPTO's environmental website is complete.

A logo was designed for the ECAS website by Karen Billingsley of AIMSI in Oak Ridge under a subcontract on this project, and is shown above. Work on updating the website began in January 1999. A fully updated and approved website format was completed in March 1999. The "draft" website was completed in December 1999. A formal review was held in March 2000, and formatting changes were completed on the ECAS site in April 2000. The new site now includes information regarding links to other pertinent sites, federal regulatory contacts, regulatory/legislative changes that are pending, and other links to sites within the NPTO. Information on regulations is provided through the site. Work is continuing on updates to the site's section concerning applicable treatment for wastes generated within the oil and gas Industry.

Final approval for the incorporation of the website on NPTO's homepage has not yet been received. When the website is linked to the NPTO homepage, mailings to independent oil producers will go out to advertise the site. A draft brochure to advertise the site has also been completed and awaits approval through the NPTO.

GEOLOGIC CONTROLS OF HYDROCARBON OCCURRENCE IN PART OF THE APPALACHINA BASIN IN TENNESSEE, SOUTHWESTERN VIRGINIA, SOUTHERN WEST VIRGINIA, AND EASTERNMOST KENTUCKY

Robert D. Hatcher, Jr.
Environmental Sciences Division, ORNL
and
Department of Geological Sciences, University of Tennessee, Knoxville

The Appalachian basin has produced hydrocarbons for almost a century and a half (the Drake well was drilled in Pennsylvania in 1859), and several early concepts, such as the anticlinal theory of hydrocarbon occurrence, were also developed in the Appalachians. The southeastern parts of the basin that are not overmature remain poorly explored. A new discovery in northeastern Tennessee has demonstrated that the potential exists in this region for development of major oil and gas fields. The application to the southern Appalachian basin of new technologies developed in this project and existing state-of-the-art technologies developed in other basins (e.g., the petroleum system concept) is proving useful for drawing attention to this area as an unexplored but now a potential area of interest by the petroleum industry. We have an active research partner in the U.S. Geological Survey and several participating industry partners.

Our current intent with this project is to quantitatively retrodeform and reconstruct the stratigraphic column on the Appalachian margin prior to end of Paleozoic deformation and incorporate into the reconstruction critical data on thermal maturation (USGS data), geochemistry (USGS data), and basement structure in order to better evaluate fluid generation and migration, reservoir geometry, reservoir properties, and reservoir development. We are accomplishing this by making detailed analyses of palinspastic locations of facies boundaries situated on a rigorously reconstructed basement surface (Fig. 1). Through detailed fracture investigations of several important structures (triangle zones, specific thrust blocks, and duplexes), we are now beginning to be better able to make definitive statements about fluid generation and migration. The timing of hydrocarbon migration and entrapment remains an important question for current and future exploration, for if the hydrocarbon source beds in the study area matured and hydrocarbons migrated before the rocks were deformed during the Alleghanian (Appalachian) orogeny, there would be no hydrocarbons left for the resulting structures to trap. We currently know that that may not have been the case because a new major oil and gas field has been discovered during the past two years and is currently being developed in Ordovician rocks in the thrust belt.

To date we have drawn the attention of industry to the hydrocarbon potential in the southern Appalachian basin in eastern Tennessee, southwestern Virginia, easternmost Kentucky, and southern

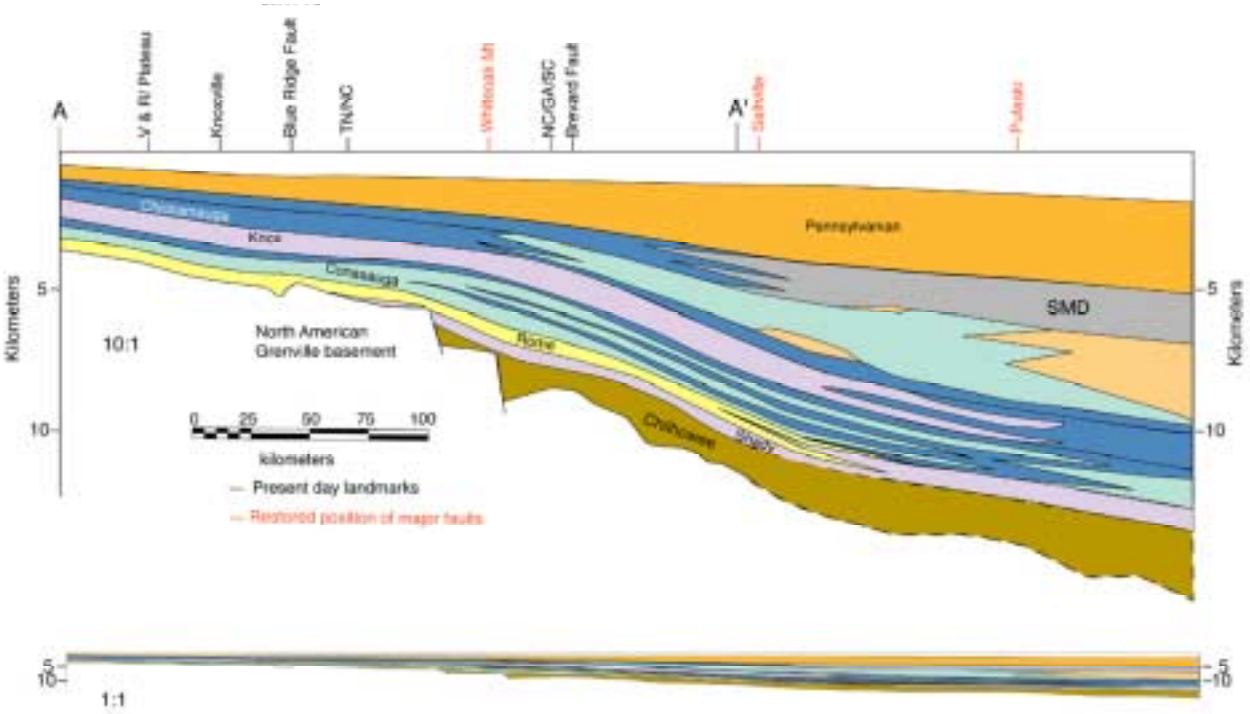

Fig. 1. Palinspastically Restored Facies in East Tennessee

West Virginia by making a number of presentations at professional meetings (including by USGS partner Dr. R. C. Milici) during 1998-2000. Detailed field and laboratory structural (including fracture) analysis of a newly recognized triangle zone in the southern Appalachians has been completed; we are able to conclude that fluid migration is favored in the intensely deformed core of the triangle zone and that the potential for hydrocarbon accumulation in this structure extends through much of the early Paleozoic carbonate section. We also have collected new data on an exposed duplex in Lower Ordovician carbonate rocks and have demonstrated that intensely fractured zones develop in particular parts of the faulted structure, small faults develop that mimic the larger structure and that increase the reservoir capacity of the main structure, and interconnected fracture systems increase in all the deformed components. Duplexing is possibly the most common deformational style in the main deformed subsurface part of the southern Appalachian foreland fold-thrust belt and accounts for numerous structures that potentially could contain hydrocarbons.

We have developed a new technique for sequential analysis of the hydrocarbon potential of a deformed foreland belt; this technique involves first reconstruction of the undeformed (with respect to foreland

deformation) basement surface beneath the deformed foreland using mostly geophysical data, then palinspastically restoring the thrust belt and locating major facies boundaries in their predeformational state; reconstruction takes place along several 2-D lines that will then be connected into a 3-D arrayed polygon for reservoir analysis.

Initial results of organic geochemical analysis (gas chromatograph, USGS lab in Denver) of four oil samples collected by partner Tengasco from their new Swan Island field have yielded an Ordovician source for oil that is trapped in Ordovician rocks; this is a monumental result because of the regional implications for exploration by confirmation of an older (pre-Devonian) source for major accumulations of hydrocarbons in the southern Appalachian basin. This result should open up numerous new potential hydrocarbon plays throughout the southeastern part of the Appalachian basin.

We will continue to be able to make definitive statements about the relationships between the location and character of hydrocarbon reservoirs, regional stratigraphic and structural boundaries, and the T-P regime that has been superimposed on the stratigraphic assemblage present here. In addition, we will begin to be able to better define the movement directions within individual thrust sheets and the thrust belt as a whole in order to better understand the processes that generate reservoirs and produce migration. The relationships of all of these parameters to the oil-gas window and reservoir architecture should begin to emerge from our investigations during FY 2001. At this time we will be able to (1) begin to define the stratigraphic intervals for deep plays; (2) evaluate the structural and stratigraphic data from seismic and limited deep drilling in the deeper parts of the basin to determine the extent and parameters for new hydrocarbon plays; (3) complete the reconstruction of the basement surface from seismic-reflection data beneath the deformed foreland (Valley and Ridge) in Virginia; (4) continue to evaluate the regional transition from purely brittle to more penetrative failure modes in the Paleozoic section and the relationships of these failure modes to thermal maturation parameters and their controls on hydrocarbon distribution and the oil-gas window; (5) begin 3-D analysis of this part of the Appalachian basin and identify potential reservoirs; and (6) continue to assess reservoir characteristics through fracture studies (e.g., fracture-dominated vs primary porosity-dominated) and identify potential fluid migration pathways related to movement vectors of thrust sheets; in addition, we expect continued collaboration with partners on this and related projects. We also will continue to present results at professional meetings and submit papers for publication.

OZONE TREATMENT OF SOLUBLE ORGANICS IN PRODUCED WATER (FEAC307)

K. Thomas Klasson, David W. DePaoli, and Costas Tsouris

OVERVIEW

Oil production is shifting from "shallow" wells (0-650 ft water depth) to offshore, deep-water operations (>2,600 ft). Production from these operations is now approaching 20%. By 2007, it is projected that as much as 70% of the U.S. oil production will be from deep-water operations. The crude oil from these deep wells is more polar, thus increasing the amount of dissolved hydrocarbons in the produced water. Early data from wells in the Gulf of Mexico indicate that the problem with soluble organics will increase significantly as deep-water production increases. Existing physical/chemical treatment technologies used to remove dispersed oil from produced water will not remove dissolved organics. Operations in the Gulf of Mexico are rapidly moving toward design of high-capacity platforms that will require compact, low-cost, efficient treatment processes to comply with current and future water quality regulations.

This project is an extension of previous research to improve the applicability of ozonation and will help address the petroleum industry-wide problem of treating water containing soluble organics. The goal of this project is to maximize oxidation of water-soluble organics during a single-pass operation. The project investigates (1) oxidant production by electrochemical and sonochemical methods, (2) increasing the mass transfer rate in the reactor by forming microbubbles during ozone injection into the produced water, and (3) using ultraviolet irradiation to enhance the reaction if needed. Industrial collaborators include Chevron, Shell, Phillips, BP Amoco, Statoil, and Marathon through a joint project with the Petroleum Environmental Research Forum (PERF).

The research and demonstration program consists of three phases.

1. Laboratory testing in batch reactors to compare effectiveness of organics destruction for two types of ozone generation methods (corona discharge and water-splitting) with hydrogen peroxide generated sonochemically and to evaluate the enhancement of destruction by UV light and micro-bubble spraying.
2. Continuous-flow studies to determine the efficacy of various contactors, the dependency of organics destruction of process variables, and scale-up issues.
3. Field testing of a prototype system in close collaboration with an industrial partner to generate performance data suitable for scale-up and economic evaluation.

INTRODUCTION

Ozone is an extremely powerful oxidant that can attack organic materials and convert them to nonhazardous products. Ozone is sparingly soluble in water. It has been determined that the main limitation in ozonation systems comes from the low mass transfer rate of ozone from the gas phase to the liquid phase.[1-6] The mass transfer efficiency of ozone from the gas phase to the liquid phase depends on the mixing characteristics of the gas-liquid contactor used, the kinetics of ozone reactions in the water, and the number and size of bubbles produced.[1,6,7] The effectiveness of ozone as an oxidant can be increased by creating a higher surface-area-to-volume ratio for the contact of ozone with the solution through the generation of smaller bubbles.[8,9] A smaller bubble size results in a higher surface-to-volume ratio. In addition, smaller bubbles have higher residence times in contactors, leading to, higher gas volume fractions. These findings motivated the experimental work conducted in this project.

During the first year of study, laboratory testing in batch reactors was conducted to compare effectiveness of organics destruction using hydrogen peroxide generated sonochemically and ozone generated via corona discharge. In the batch experiments, three water matrix types were used: (1) benzene, toluene, ethylbenzenes, xylenes, and hexanoic acid (BTEXH) in deionized water; (2) BTEXH in salt water (100 g/L); and (3) salt water as described in ASTM D1141-90 (less trace metals) and mixed with light crude from the Gulf of Mexico. The results of that testing are summarized as follows.

- Sonochemical oxidation can destroy some compounds such as BTEX; however, no destruction of hexanoic acid was measured. Because of the relatively slow destruction of BTEX at significant power levels ($k \approx 0.07$ min^{-1} at 0.5 W/L), and no destruction of hexanoic acid, further testing of the sonochemical technique was not pursued.
- Effective destruction of hexane-extractable materials can be achieved by ozonation in a reasonable time period (less than 5 min). Improved ozonation rates are achieved by enhancing mass transfer through microbubble injection (see Fig. 1).
- An effective means to employ electrostatic spraying for production of microbubbles in high-ionic-strength solutions such as produced water was not found. However, small bubble sizes are readily achieved in such solutions using bubble dispersers.
- Ultraviolet (UV) irradiation contributes significantly to destruction of BTEX by ozonation; however, UV irradiation was not found to significantly improve ozonation of simulated produced water.

- The ozonation of hexanoic acid is highly pH dependent, which may have significant processing implications.

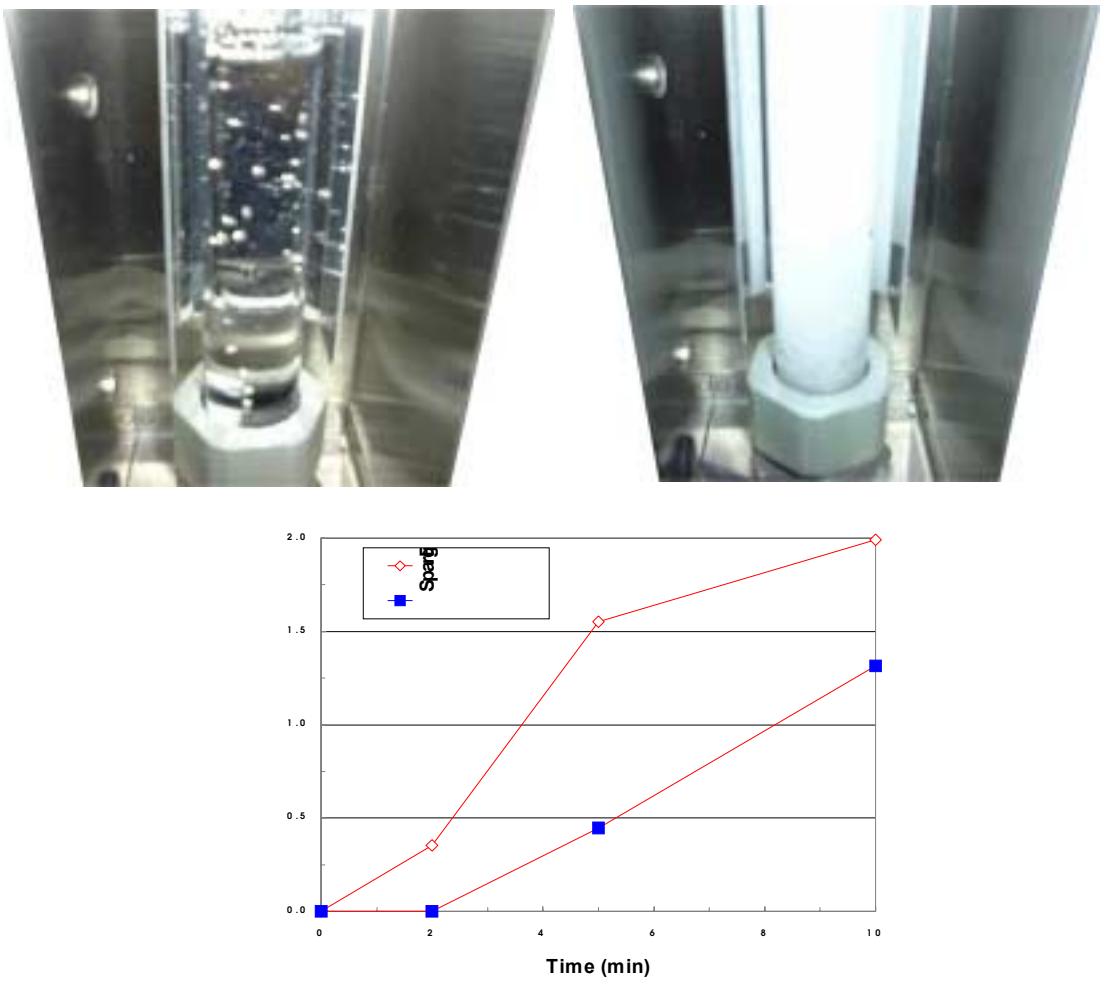

Figure 1. Illustration of the effect of bubble size on organic destruction by ozonation. Top images compare bubbles produced by a sparger (left), and a fine bubble diffuser (right); graph below shows ozonation representative ozonation results.

DISCUSSION OF CURRENT ACTIVITIES

An initial set of continuous-flow testing was performed using BTEXH and simulated produced water feed. The tests involved countercurrent gas-liquid contacting in 350-mL and larger reactors, with ozonated gas injection using porous injectors for microbubble formation. The results (see Fig. 3) indicated that good removal efficiency, as measured by the reduction of hexane-extractable materials quantified by fluorometry, is possible at reasonable residence times and ozone loading.

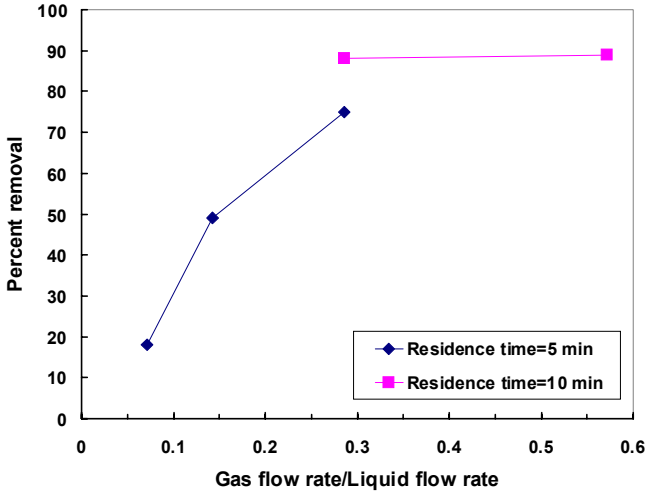

Figure 2. Example results from continuous-flow tests. Experimental conditions: Feed – simulated produced water (25 ppm hexane-extractable); 350-mL reactor, ozone concentration – 40 mg/L ozone; no UV.

On October 7-8, 1999, the PERF steering committee reviewed the results obtained to date in this project. They recommended that additional bench-scale research be conducted prior to scale-up and demonstration to answer several technical questions that remain regarding the feasibility of field application of ozonation. The continuous-flow study task was rescoped to meet those needs.

The focus of current activities is on two types of testing: microbubble formation and oxidation performance. Several experiments have been conducted so far using simulated produced water, and a limited number of tests were also performed with samples of actual produced water collected by our industrial partners. Microbubble formation tests have involved long-term experiments to determine the impact of, and means for avoiding, possible fouling during ozonation by materials such as ferric oxide, calcium carbonate, and evaporative salt deposits. Oxidation tests were continued using laboratory-scale continuous-flow column reactors. The work involved multiple experiments with improved synthetic solutions to determine the effect of major process variables, including gas flow rate, use of air or oxygen as the feed gas, presence of immiscible oil droplets in the water, and solution pH.

EXPERIMENTAL SYSTEMS

A continuous-flow column reactor of 25.4-mm internal diameter and jacketed wall for temperature control has been employed in this work. For the majority of tests, simulated produced water was prepared as directed by industrial partners by continuously homogenizing 1 g/L of light crude oil in salt water

(containing 35 g/L sea salt and 65 g/L sodium chloride). The homogenized feed solution was pumped from the bottom of the source vessel and flowed downward through a vertical reactor. A gas mixture containing either pure oxygen, oxygen and ozone, air and ozone, or air was introduced through a porous glass injector at the bottom of the reactor and was removed at the top. Due to the high ionic strength of the solution, small bubbles on the order of 100 μm were formed by the porous material. The exit gas was directed through a flow meter to a spectrophotometer for ozone concentration measurements. Gas and liquid samples were obtained every 30 min for concentration measurements of carbon dioxide using a gas chromatograph and organics using infrared spectroscopy. Typical conditions used in these experiments were 200 mL of simulated produced water in the reactor, 20 mL/min liquid flow rate (10-min residence time), pH 8, room temperature, and 90-1000 mL/min gas flow rate.

Long-term experiments of microbubble formation were conducted using a similar column reactor. The input solution had the same ionic strength (35 g/L sea salt and 65 g/L sodium chloride) and a concentration of 30 ppm ferrous chloride that was oxidized, forming a precipitate phase. The histories of pressure and flow rate of the input gas were recorded to determine whether fouling occurred.

RESULTS

Long-term microbubble formation experiments indicated that after sufficient time, depending on the gas flow rate, injector area, and solution concentration, pore fouling occurs, leading to decreased gas flow rate at constant pressure or increased gas pressure required for a given flow rate (see Fig. 3). To date, fouling has been encountered only as a result of evaporative salt deposition rather than ferric oxide or calcium carbonate formation. This problem was effectively overcome by periodically flowing water through the injectors to dissolve the salt deposits in the pores. The flow rate of the water stream needed to maintain a constant gas flow rate was on the order of 0.01% of the produced water stream. By adding this flow, gas introduction has been kept uninterrupted for several days of constant operation.

Experiments with actual produced water using oxygen/ozone as the oxidant confirmed that carbon dioxide is produced. A preliminary carbon balance indicated that the reduction of soluble organics in the effluent could be accounted for by the CO_2 production.

Representative results obtained in the ozonation experiments using oil dispersed in simulated seawater at 1 g/L are shown in Fig. 4. This figure presents the fate of the carbon that was introduced into the reactor in the liquid feed stream. Each experimental condition plotted is represented by a bar with three segments; the segment labeled “residual” is the fraction of the carbon that remained in the water after treatment, the segment labeled “CO_2” is the fraction fully converted to carbon dioxide, and the segment labeled “flotation” is the amount of carbon that was removed by physical flotation of the oil droplets by the gas bubbles. The results vary greatly, depending on the process conditions. Bars A and B indicate that,

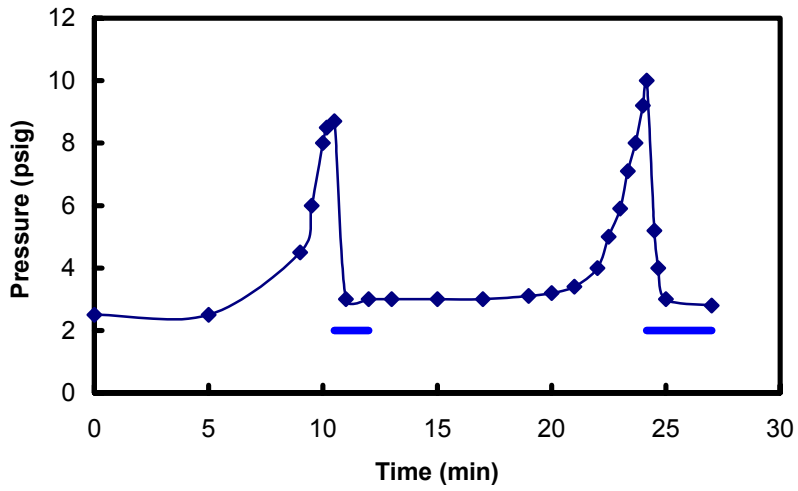

Figure 3. Example results of salt deposition and water flush for gas flow through a porous injector. Conditions: liquid flow – 10 mL/min salt water (100 g/L TDS); gas flow - 300 mL/min oxygen containing ozone, distilled water flush – 0.3 mL/min. Horizontal bars indicate time period for water flush.

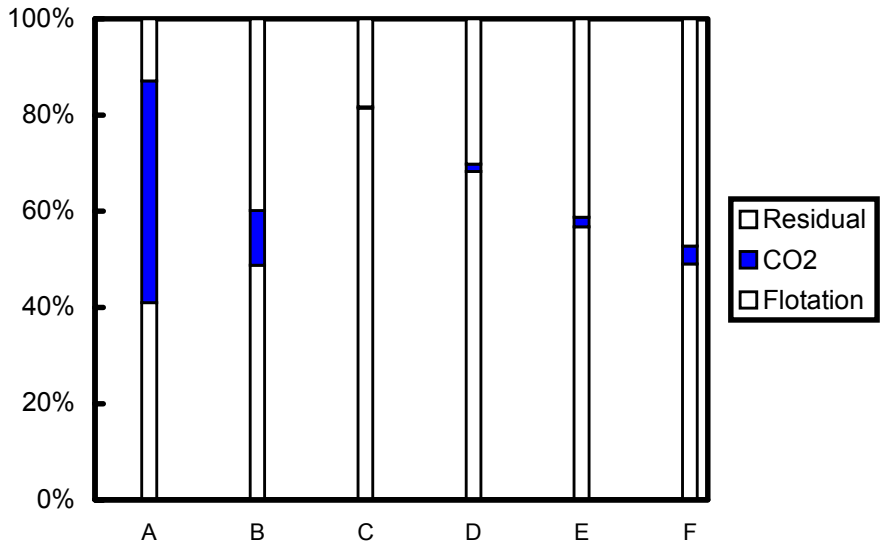

Figure 4. Representative results of continuous-flow ozonation tests with simulated produced water. All experiments run at 20 mL/min liquid flow rate and 10 min liquid residence time.
Test conditions:

A: 1000 mL/min gas flow (oxygen/ozone), pH 8
B: 90 mL/min gas flow (oxygen/ozone), pH 8
C: 500 mL/min gas flow (oxygen), pH 8
D: 100 mL/min gas flow (oxygen), pH 8
E: 100 mL/min gas flow (air/ozone), pH 8
F: 100 mL/min gas flow (air/ozone), pH 4.9

with ozone injection, a significant amount of the total carbon present in the feed solution is transformed into carbon dioxide. In these cases, the ozone is generally not completely consumed. Bars C and D indicate that little oxidation is caused by injection of oxygen instead of ozone, while Bars E and F show that a small but measurable conversion to CO_2 occurs with injection of ozone at the lower concentrations encountered with air feed to the ozone generator. In all cases, flotation is shown to be a major mechanism for dispersed oil removal. Further observations are presented below.

EFFECT OF PH

The pH of the produced water has been found to significantly affect the removal of organics from the simulated produced water prepared by dispersing oil in salt solutions. Experiments were conducted at pH values ranging from 4.3 to 10. At pH 4.3, the amount of carbon oxidized to carbon dioxide was maximum, approximately 25% higher than at other pH values. The surface potential of oil drops was measured at various pH values to investigate the removal of oil droplets by flotation. It was found that the isoelectric point (zero surface potential) is at pH 4.8, while between pH 2.8 and 10.7 the potential ranges from +60 mV to –125 mV. Despite the wide range of surface charge on the oil droplets, the oil removal obtained by flotation alone (using a low flow, 100 mL/min, of air as the feed gas) was not greatly affected by a shift in pH from 8 (60% removal) to close to the isoelectric point at 4.9 (53% removal). The fact that removal by flotation was not higher at the isoelectric point indicates that the ionic strength is sufficient to reduce the role of electrostatic forces; further work will address droplet-bubble interactions.

EFFECT OF GAS FLOW RATE

The gas flow rate plays a significant role in the removal of oil (soluble and insoluble part) from produced water. The removal efficiency by flotation is increased as the gas flow rate is increased. At higher gas flow rates, the bubble concentration is increased, as well as the collision rate of oil drops with bubbles.

PUBLICATION

A. B. Walker, C. Tsouris, D. W. DePaoli, and K. T. Klasson, "Ozonation of Soluble Organics in Aqueous Solutions Using Microbubbles," submitted to *Ozone Science and Engineering*, February 2000.

PRESENTATION

A. B. Walker, C. Tsouris, D. W. DePaoli, and K. T. Klasson, “Removal of Organics from High-Ionic-Strength Aqueous Solutions, presented at Eleventh Symposium on Separation Science and Technology for Energy Applications, Gatlinburg, TN, October 17-20, 1999.

REFERENCES

1. M. D. Gurol and P. C. Singer, "Dynamics of the Ozonation of Phenol," *Water Res*. **17**:1163–1171 (1983).
2. M. D. Gurol, "Factors Controlling the Removal of Organic Pollutants in Ozone Reactors," *J. Am. Water Works Assoc*. **77**:55–60 (1985).
3. M. D. Gurol and R. Vatistas, "Oxidation of Phenolic Compounds by Ozone and Ozone Plus U.V. Radiation: A Comparative Study," *Water Res*. **21**:895–90 (1987).
4. C. Yurteri and M. D. Gurol, "Removal of Dissolved Organic Contaminants by Ozonation," *Environ. Prog*. **6**:240–245 (1987).
5. Q. Zhu, C. Liu, and Z. Xu, "A Study of Contacting Systems in Water and Wastewater Disinfection by Ozone. 1. Mechanism of Ozone Transfer and Inactivation Related to the Contacting Method Selection," *Ozone Sci. Eng.* **11**:169–188 (1989).
6. F. Xu and C. Liu, "Mass Balance Analysis of Ozone in a Conventional Bubble Column," *Ozone Sci. Eng.* **12**: 269–279 (1990).
7. H. Zhou, D. W. Smith, and S. J. Stanley, "Modeling of Dissolved Ozone Concentration Profiles in Bubble Columns," *J. Environ. Eng*. **120**:821–840 (1994).
8. M. Ahmad and S. Farooq, "Influence of Bubble Sizes on Ozone Solubility, Utilization, and Disinfection," *Water Sci. Technol*. **17**:1081–1090 (1983).
9. M. M. Sharma, "Some Novel Aspects of Multiphase Reactions and Reactors," *Trans. Inst. Chem. Eng*. **71**:595–610 (1993).

DEVELOPMENT OF A CENTRIFUGAL DOWNHOLE SEPARATOR

P. A. Taylor and K. T. Klasson

INTRODUCTION

Produced water is the largest generated waste stream by volume in the Gulf Coast region and is typically a mixture of formation and injection process water that contains oil, salts, chemicals, solids, and trace metals. In 1991, Louisiana generated over 1 billion barrels and Texas generated 7.5 billion barrels of produced water as a result of oil and gas operations. More than 250 million barrels of produced water are discharged each year to surface waters in both Texas and Louisiana.

Two primary alternatives exist for disposal of produced water in the future: (1) improve the treatment of produced water prior to surface or subsurface disposal or (2) reduce the volumes of produced water by using downhole, or in-well, separations or reinjection. Newer technologies being considered by the industry for contaminant removal include hydrocyclones, reverse osmosis, membrane filtration, gas flotation, carbon adsorption, bioreactors, chemical oxidation, stripping/extraction, and UV oxidation. These processes are complicated and expensive, and several of these unit operations will be required to reduce the conventional, unconventional, and toxic pollutant concentrations to new discharge limits.

Therefore, emphasis should be placed on reinjection or in-well separations/recycle of produced water. Successful use of reinjection has increased in the last several years, but enhanced treatment is often required to remove oil and particulate matter to avoid damaging or plugging the rock formations. The suitability of produced water for reinjection is determined by the enhanced recovery process, the water quality, and the rock formation properties. Options for in-well separations have been evaluated, but no technology has reached maturity.

This project will extend the application of remotely operated separations equipment developed for the nuclear industry to in-well recovery of oil generated by enhanced oil recovery techniques. A conceptual drawing for the process, which combines a centrifugal separator with two downhole pumps, is presented in Fig. 1. Centrifugal separators, originally developed by the U.S. Department of Energy (DOE), have been successfully used for surface treatment of produced water and wastewater generated during environmental cleanup operations.

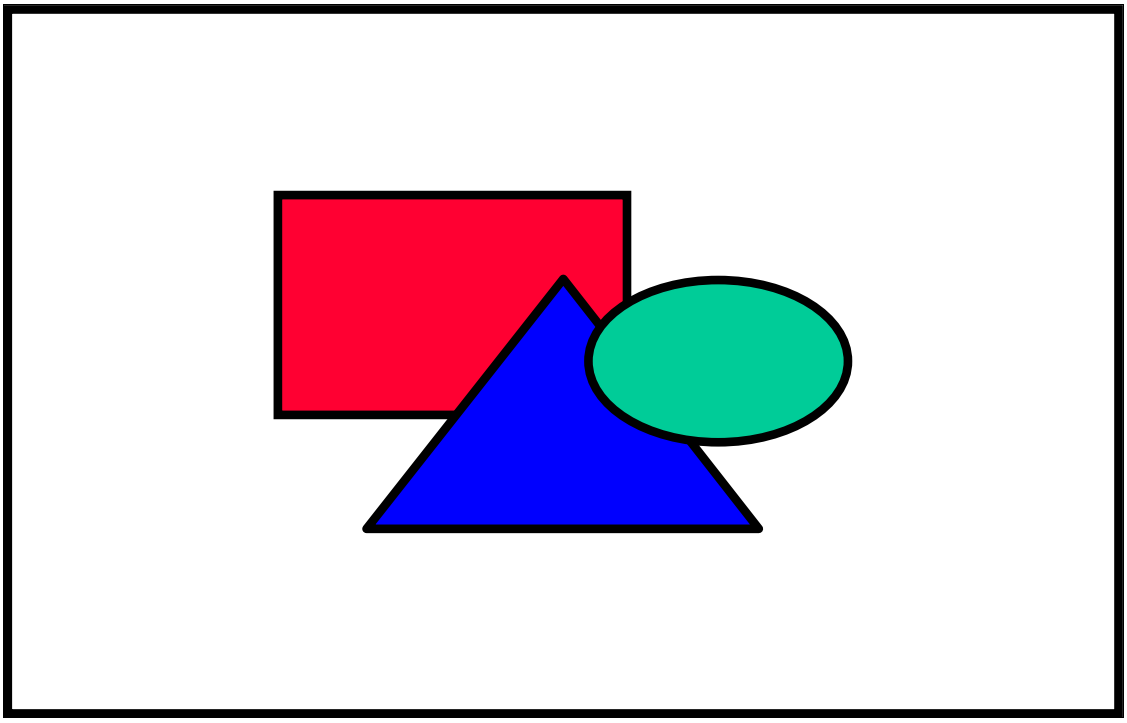

Fig. 1. A conceptual drawing for the installation of a centrifugal separator in an oil well, with the separated oil being pumped to the surface for recovery and the produced water being recycled through horizontal wells.

Centrifugal separators of various sizes (from 2- to 25-cm rotor diameter) have been built and operated over the past three decades at the Savannah River Site (SRS), Argonne National Laboratory (ANL), and ORNL for use in DOE applications. These units have several characteristics that make them attractive for consideration in downhole separation of oil and produced water. These include (1) excellent phase separation, (2) reliability in remote applications with >20,000 h of operation prior to maintenance, and (3) the ability to handle high volumetric throughput with a very low residence time. However, several modifications must be made to the design prior to successful use as a centrifugal downhole separator (CDHS). These include (1) lengthening the rotor to increase the throughput, (2) introducing the oil/water mixture directly into the bottom of the rotor to limit mixing, (3) overcoming problems associated with the accumulation of solids in the rotor, and (4) connecting the separator to downhole pumps for pumping the oil to the surface and for reinjecting the produced water. A schematic of the rotor for a centrifugal separator is shown in Fig. 2. The size of the aqueous weir can be changed to optimize the performance of the separator, depending on the properties of the oil and the ratio of water to oil in the feed. The oil and water discharges from the rotor are captured in collection channels in the separator housing, and drain by gravity through outlet ports back into the feed tanks.

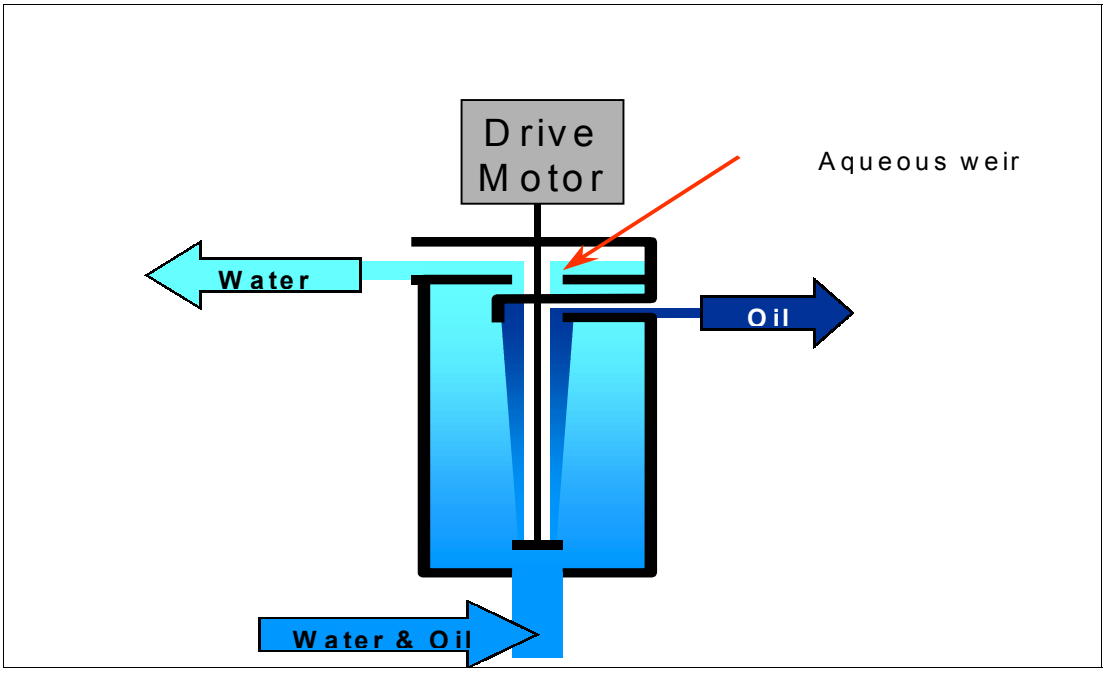

Fig. 2. Schematic drawing of the centrifugal separator rotor.

MATERIALS AND METHODS

Recent discussions with representatives from the Petroleum Environmental Research Forum (PERF) industrial partners and DOE have resulted in the formulation of a revised set of functional criteria for use in the development of the CDHS. These functional criteria are presented in Table 1.

Table 1. Functional criteria for development of the CDHS

Flow rate	2000 to 10,000 barrels per day (60 to 300 gal/min)
Diameter	6-in. O.D., to fit in 7-in. well casing
Temperature	100 to 300°F (previously 100 to 200°F)
Water-to-oil ratio	1:100 to 10:1 (previously 1:10 to 10:1)
Solids	Concentration = 0 to 3%, Size = sand to clay
Product quality	Maximum of 500 ppm (0.05 vol %) oil in water (previously 0.2 vol %)
Reliability	24 months mean time between failures (previously 18 months)

A model V-2 (2-in. rotor) centrifugal separator (CINC, Inc., Carson City, NV) equipped with a 1/6 HP motor is being used for the bench-scale tests. Tests last year with the original separator had shown that the organic collection channel overflowed at higher oil flow rates, due to the high viscosity of the oil. The housing of the separator was modified to provide larger collection channels and outlet ports. Two crude oils have been provided by a PERF industrial partner for testing. The first is a Gulf of Mexico light crude

with an API gravity of 34.06°, specific gravity at 60°F of 0.8547, and a viscosity of 9.0 cP at 77°F. The second is a heavy North Sea crude with an API gravity of 19.3°, specific gravity at 60°F of 0.948, and a viscosity of 400 cP at 77°F. The American Society for Testing and Materials (ASTM) Standard Specification for Substitute Ocean Water (ASTM: D1141-90) is being used for the aqueous phase in the bench-scale tests with these crude oils. Most of the testing has used the light crude, based on recommendations from the industrial partners. The oil companies need to add water to the heavy crude in order the pump it to the surface, so separating water from this type of oil is not required. The tests conducted with the heavy crude do show the range of crude oils that can successfully treated using the centrifugal separator.

The separator has been tested with water-to-oil feed ratios of 1:10, 1:3, 1:1 and 10:1. About 3 L each of crude oil and synthetic ocean water are used during a run, and the oil and water streams are continuously recirculated through the separator. The water and oil feed streams are mixed just before they enter the separator. The viscosity of the light crude oil increased as it was used, primarily due to evaporation of the lighter components. The viscosity increased from 9 cP to about 16 cP after being used for one day, but the performance of the separator did not change significantly. In earlier tests, where a batch of oil was used for several days, the oil had a viscosity of 55 cP and higher levels of cross contamination were measured in the discharge streams, so the oil is replaced with fresh crude each day to minimize the changes. At high oil flow rates the concentration of water in the oil increased with time, indicating that additional water was emulsified into the oil each time the oil passed through the separator. The buildup of water in the oil is an artifact of recycling the oil through the separator and would not occur in an actual operation. A water absorption filter system was installed on the oil recycle line to continuously remove the emulsified water from the oil before it entered the separator.

Samples of oil and water from the separator are collected in API Centrifuge Tubes (12.5 mL), acidified with 0.125 mL of 1 N HCl, and centrifuged at 4500 rpm for 10 min. The amount of water in the oil samples is read directly from the graduations on the centrifuge tubes. The amount of oil in the water samples is determined by dissolving the oil floating on the water in two 1-mL portions of hexane, evaporating the hexane, and weighing the oil residue.

A mathematical model, developed by ANL and modified by ORNL, that predicts the performance of centrifugal separators, was used to compare with the experimental results. The model can be used to help scale up the separator. The inputs for the model are the separator dimensions, fluid properties (viscosity and density), rotor speed, oil-to-water feed ratio, and the dispersion number, which is a measure of how readily the two fluids separate after being mixed. The dispersion number is measured by mixing the two fluids and then measuring the time required for the phases to completely separate after the mixing is

stopped. The output from the model is the predicted feed flow rate that will give 1% cross contamination in one of the discharge streams.

RESULTS

The dispersion number for the light crude oil and synthetic ocean water was found to be strongly dependent on the length of time the fluids were mixed. A plot of the results is shown in Fig. 3. The amount of water left in the oil, following an extended settling time, was also measured, which shows the same increase in water concentration that was noted during operation of the separator.

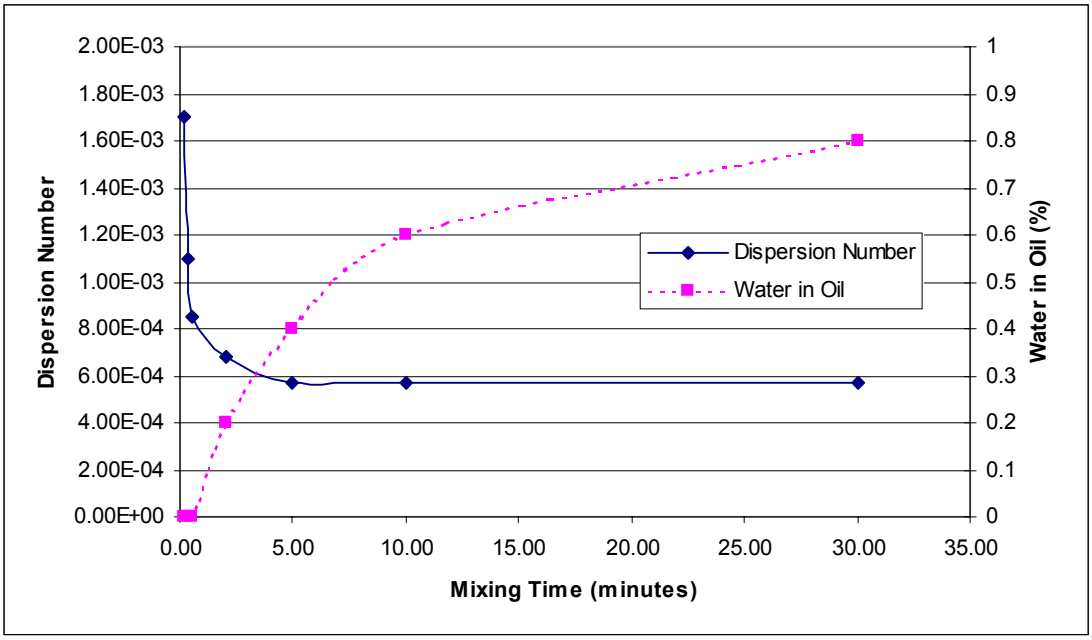

Fig. 3. Effect of mixing time on dispersion number and water content of oil.

The crude oil and water entering the separator are mixed slightly as they enter the bottom of the rotor, but the exact amount of mixing is not known. In order to determine a dispersion number to use in modeling the separator, the results from one set of operating conditions were used to calculate a dispersion number that predicted the observed results. The calculated dispersion number was 0.00082, which corresponds to a mixing time of 30 seconds in the dispersion test apparatus. This dispersion number was then used to predict the operating results for the other conditions tested. The predicted results were then compared with the operating data to determine how well the model predicts the performance of the separator.

The centrifugal separator operated effectively for the full range of water-to-oil feed ratios that have been tested to date (10:1 down to 1:10). Figure 4 shows the results for the 10:1 feed ratio using the Gulf of Mexico light crude, and also shows the model prediction for these conditions. The separator performed

slightly better than the model predicted in this test. At the maximum flow rate of 2 L/min (0.53 gpm), the residence time for the liquid inside the rotor is only about 5 seconds.

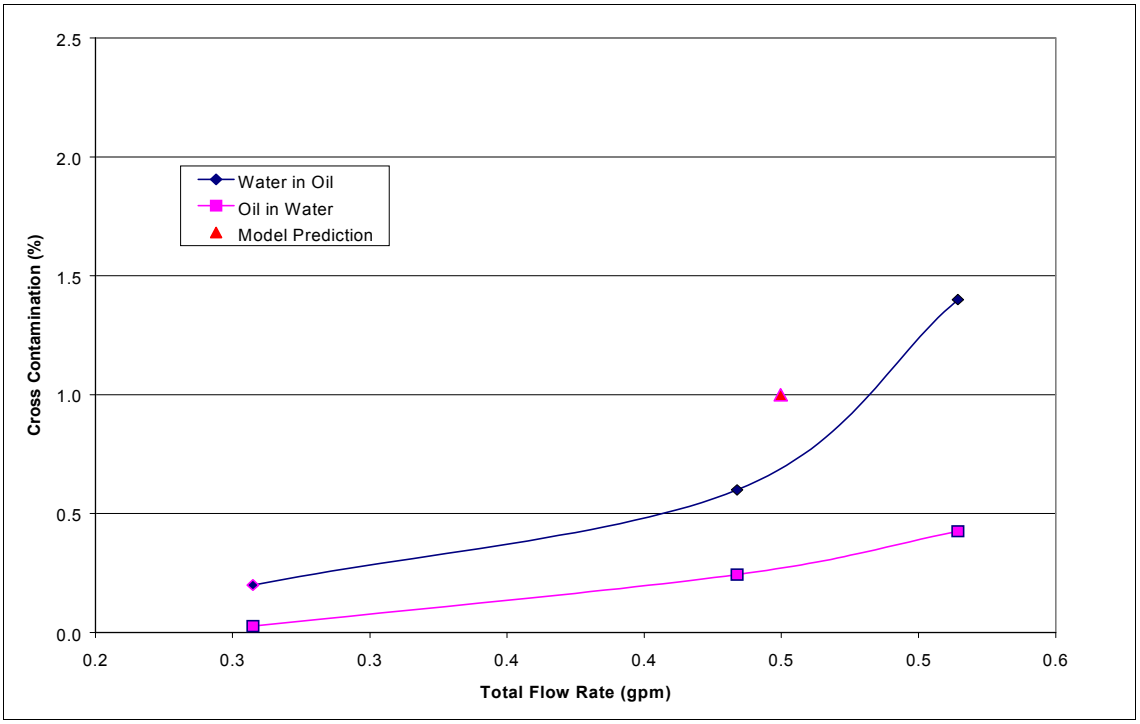

Fig. 4. Performance of separator using Gulf of Mexico light crude, 10:1 water-to-oil feed ratio, 2500 rpm rotor speed, and 1.02-in. weir.

Decreasing the water-to-oil feed ratio to 1:1 resulted in slightly higher concentrations of water in the oil discharge stream, but the separator still operated very efficiently, as shown in Fig. 5. The oil flow rate was much higher for these tests than for the 10:1 ratio, resulting in much shorter residence times in the feed tank (~20 s at the highest flow rate). The water-removal filter was needed during these runs to keep the water concentration in the oil discharge stream from increasing with time. The performance of the separator was very close to that predicted by the model.

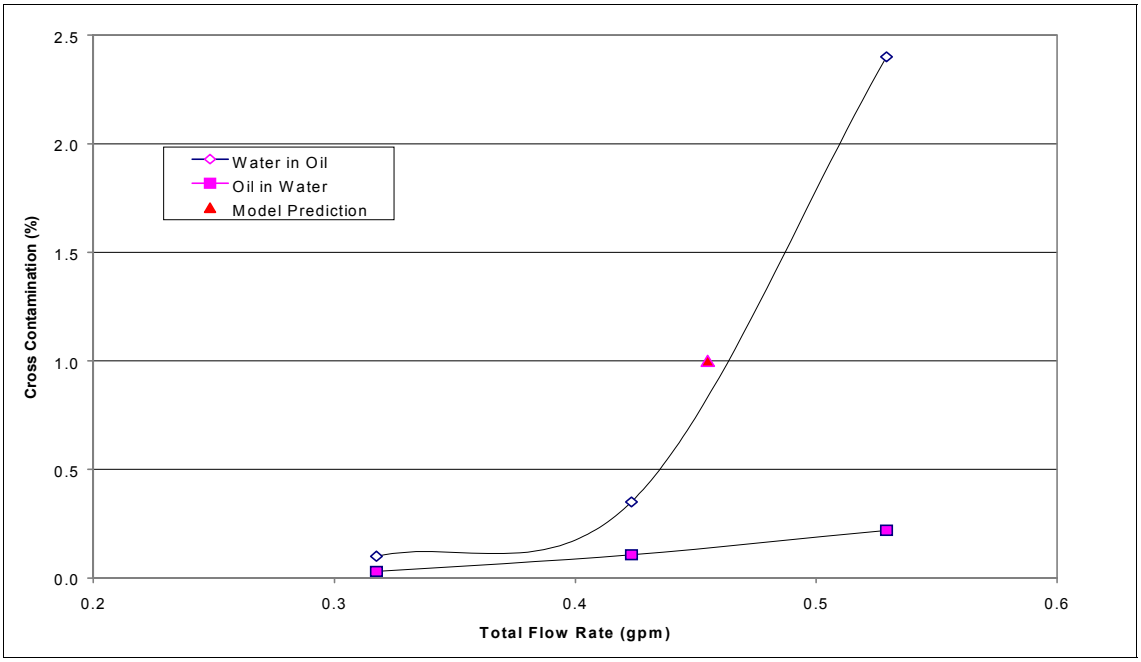

Fig. 5. Performance of separator using Gulf of Mexico light crude, 1:1 water-to-oil feed ratio, 2500 rpm rotor speed, and 0.950-in. weir.

One test each has been performed at water-to-oil ratios of 1:3 and 1:10. The water concentration in the oil discharge was < 0.2 vol % for all of the test conditions. The oil concentrations in the water discharge streams are shown in Fig. 6. Since the concentration of oil in the water increased much faster than the water in the oil as the flow rate increased, a smaller weir is needed to optimize the performance of the separator. The separator performed much better than the model predictions for both of these tests.

The effect of gas entrained in the oil stream was measured using the Gulf of Mexico crude, a feed ratio of 1:1 water-to-oil, a flow rate of 1.5 L/min, and a rotor speed of 2500 rpm. Air was added to the oil feed stream, just prior to entering the separator. The presence of gas in the oil can completely disrupt the operation of hydrocyclones, which are also being tested for downhole oil-water separation. Air additions of 0 to 20% of the total liquid flow rate did not have any impact on the operation of the separator.

The North Sea heavy crude was tested at a water-to-oil feed ratio of 10:1. The oil was difficult to pump and flowed very slowly from the outlet port, but the separator was successful in producing a water discharge stream with a very low concentration of oil. At a total flow rate of 2 L/min, the amount of water in the oil discharge was 8 vol % and the oil in the water discharge was 0.05 vol %. This crude was used to determine the effect of increasing temperatures on the performance of the separator, using a feed ratio of 10:1 and a combined flow rate of 1.4 L/min. The heavy crude was used for this test because of the high volatility of the light crude oil. The amount of water in the oil discharge stream did not change

significantly, but the amount of oil in the water decreased from 0.05% to 0.015% as the temperature increased from 25 to 65°C. The higher temperatures reduce the viscosity of the oil, which improves the performance of the separator.

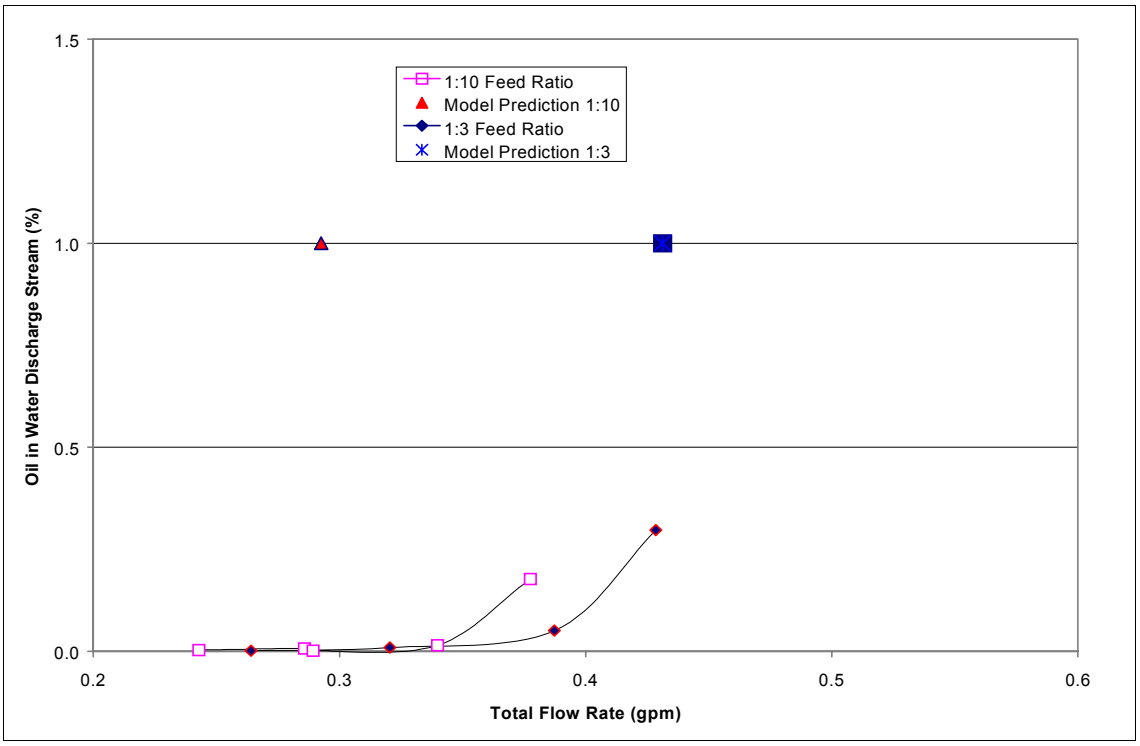

Fig. 6. Performance of separator using Gulf of Mexico light crude, 1:3 and 1:10 water-to-oil feed ratios, 2500 rpm rotor speed, weir = 0.95 in. for 1:3 ratio and 0.900 in. for 1:10 ratio.

SUMMARY

A centrifugal separator is currently being developed at ORNL that will extend the application of remotely operated equipment developed for the nuclear industry to in-well recovery of oil, with in situ recycle of produced water. A light Gulf of Mexico crude oil has been used in most of the testing. Water-to-oil feed ratios of 10:1 to 1:10 have been tested to date, and the separator operated efficiently for the full range of feed ratios. Air was added to the oil stream in one test to model the effect of gas in the oil. Air additions up to 20% of the feed flow rate (the maximum tested) did not have any impact on the performance of the separator. The separator also effectively processed a very viscous North Sea heavy crude oil. The heavy crude was used to determine the effect of higher temperatures on the performance of the separator. Increasing the temperature of the oil and water feed stream decreased the concentration of oil in the water discharge stream.

ADVANCED COMPUTATIONAL TOOLS FOR 3-D SEISMIC DATE FUSION

D. B. Reister, E. M. Oblow, and J. Barhen
J. B. DuBose, Jr. Paradigm Geophysical Ltd., Houston, Texas

INTRODUCTION

The objective of this effort is to develop and test advanced computational tools for data fusion in 3-D seismic analysis. Research focuses on two tasks: (1) application of novel global optimization methods to residual statics in seismic imaging; and (2) application of neural networks to oilfield parameters estimation. The revolutionary techniques investigated by ORNL provide a unique approach for enhancing the understanding of hydrocarbon reservoirs away from the well.

During the period covered by this report, we have made significant progress on both tasks. This report has three sections. The first two provide an overview of our progress on each of the two tasks; the third provides a mathematical introduction to our revolutionary method for systematic nonlinear incorporation of uncertainties in reservoir parameters estimation.

GLOBAL OPTIMIZATION

Since the objective function that is used to estimate surface-consistent residual statics can have many local maxima, a global optimization method is required to find the optimum values for the residual statics. As reported in several recent papers, we had developed a new method (TRUST) for solving global optimization problems and had demonstrated that it was superior to all competing methods for a standard set of nonconvex benchmark problems. The residual statics problem can be very large with hundreds or thousands of parameters, and large global optimization problems are much harder to solve than small problems. To solve the very challenging residual statics problem, we have made major improvements to TRUST (Stochastic Pijavskij Tunneling) and we have made several significant advances in the mathematical description of the residual statics problem (derivation of two novel stack power bounds and disaggregation of the original problem into a large number of small problems). Using the enhanced version of TRUST, we have performed extensive simulations on a realistic sample problem that had been artificially created by large static disruptions. Our simulations have demonstrated that TRUST can reach many plausible distinct “solutions” that could not be discovered by more conventional approaches.

During the period covered by this report, we have submitted a paper to the leading journal in the field (*Geophysics*) and submitted a patent application. We submitted a paper to *Geophysics* in May 1999. In October 1999, we received reviews of our paper. The five reviewers provided the most detailed and constructive comments that I have ever received on a paper in the 30 years since I got my Ph.D. In

response to the reviewer's comments, we made a major revision of the paper. In May 2000, the revised paper was accepted subject to minor revision. The requested revisions are extraordinary! The editors ask us to do a better job describing the importance of our contribution.

Excerpts from the editor's letter:

"The authors have done an excellent job of rewriting this paper. The authors have developed an original contribution to the subject of global optimization that should be applicable in many areas of geophysics."

"The shortcoming of the article as it stands is a basic underselling of the work at the front end of the article. If the reader completes the article, the work sells itself. However, the abstract and the introduction are very mechanical and do little to attract the geophysical reader past the beginning of the paper. I would encourage a sentence or more of salesmanship toward the end of both the abstract and the introduction."

"Once the reader reaches the interior of the paper, the authors do an excellent job of taking the reader through the technique."

In September 1999, we filed a patent application "Method for using global optimization to the estimation of surface-consistent residual statics." Our ORNL report, *Application of Global Optimization to the Estimation of Surface-Consistent Residual Statics*, was published in October 1999. A paper "SPT: A Stochastic Tunneling Algorithm for Global Optimization," has been submitted to the *Journal of Global Optimization*.

DATA FUSION

The goal of this task is to use artificial neural networks to predict pseudo-logs throughout a 3D seismic volume using data supplied by DeepLook (a collaboration of eight oil and gas producing companies and six oil service companies). The three types of pseudo-logs were gamma rays, resistivity, and porosity. The neural networks were trained using integrated datasets that include both well log data and seismic data (for the same locations as the well log data). Some of the integrated datasets are called training sets, and the remaining datasets are called validation sets. The parameters for the neural networks were determined on the training sets, and errors between the calculated results and the measured results were determined for both the training sets and the validation sets. Our main accomplishment was to develop an ultrafast neural learning paradigm that considerably reduces the computational requirements required to train the neural networks. In 1998, the ultrafast neural learning paradigm was used to train neural networks that made predictions of pseudo-logs that had very small errors.

Several papers published in journals and conference proceedings are listed in the publications section of this report. Our primary activity this year has been to develop our revolutionary method for systematic

nonlinear incorporation of uncertainties in reservoir parameters estimation. We have written a computer code in FORTRAN 95 that performs the calculations, which are described in the next section.

UNCERTAINTY ANALYSIS

Our goal is to is to estimate the parameters in a function (which could be an artificial neural network) to predict pseudo-logs throughout a 3D seismic volume. The of pseudo-logs are: gamma rays, resistivity, and porosity. The functions are trained using integrated datasets that include both well log data and seismic data (for the same locations as the well log data). At each point in the training data set, we have the measured log values (**r**) and the seismic variables (**s**) that are used to calculate our estimate of the log values (**q**).

The calculated values depend on the seismic variables and parameters (**a**):

$$\mathbf{q} = \mathbf{F}(\mathbf{s}, \mathbf{a}) \tag{1}$$

In general, there will be an error between the measured and calculated values:

$$\mathbf{e} = \mathbf{q} - \mathbf{r} \tag{2}$$

Our objective is to determine best estimates for both the calculated values and the parameters. We optimize a generalized Bayesian loss function that simultaneously minimizes the differences between the best estimate and the measured responses and the best estimate and the nominal values of the system parameters. While many uncertainty analysis methods choose a form for the probability density function (PDF), we will be more general and will only specify the first two moments of the PDF (mean value and covariance matrix).

Our methods for determining best estimates will be based on the calculation and utilization of sensitivity coefficients (**S**), which provide a systematic way to propagate uncertainties in complex non-stationary nonlinear models and are the partial derivatives of the model-derived estimates of the measurements (**q**) with respect to the parameters (**a**):

$$\mathbf{S} = \frac{\partial \mathbf{F}}{\partial \mathbf{a}} \tag{3}$$

The sensitivity coefficients relate changes in the parameters (**da**) to changes in **q** (**dq**):

$$\mathbf{dq} = \mathbf{S}\,\mathbf{da} \tag{4}$$

The nominal uncertainties in the parameters are quantified by specifying a covariance matrix:

$$\mathbf{C_{aa}} = \left\langle \Delta\mathbf{a}\,\Delta\mathbf{a}^{\mathrm{T}} \right\rangle \tag{5}$$

In Eq. (5), the brackets denote integration over the PDF.

The covariance matrix for the response vector **r** is

$$\mathbf{C_{qq}} = \left\langle \Delta\mathbf{q}\,\Delta\mathbf{q}^{\mathrm{T}} \right\rangle = \mathbf{S}\,\mathbf{C_{aa}}\,\mathbf{S}^{\mathrm{T}} \tag{6}$$

Denoting the best estimates for the parameters and responses by $\hat{\mathbf{a}}$ and $\hat{\mathbf{q}}$, the best estimates are related to the current estimates by the sensitivity coefficients [Eq. (4)]:

$$\hat{\mathbf{q}} = \mathbf{q} + \mathbf{S}\left(\hat{\mathbf{a}} - \mathbf{a}\right) \tag{7}$$

To simultaneously estimate the best values for both the parameters and the responses, we minimize an objective function that minimizes the difference between the best response and the measured response, using the inverse of the total covariance matrix:

$$\mathrm{Q} = \left[\hat{\mathbf{q}} - \mathbf{r} \middle| \hat{\mathbf{a}} - \mathbf{a}\right] \begin{bmatrix} \mathbf{C_{rr}} & \mathbf{C_{ra}} \\ \mathbf{C_{ar}} & \mathbf{C_{aa}} \end{bmatrix}^{-1} \begin{bmatrix} \hat{\mathbf{q}} - \mathbf{r} \\ \hat{\mathbf{a}} - \mathbf{a} \end{bmatrix} \tag{8}$$

To simplify our notation, we define **y** and **x** by

$$\mathbf{y} = \hat{\mathbf{q}} - \mathbf{r} \tag{9}$$

$$\mathbf{x} = \hat{\mathbf{a}} - \mathbf{a} \tag{10}$$

Using our new variables, the sensitivity coefficient constraint [Eq. (7)] becomes

$$\mathbf{y} = \mathbf{S}\mathbf{x} + \mathbf{e} \tag{11}$$

Introducing a vector of Lagrange multipliers (λ), the constrained optimization problem becomes:

$$L = Q + \boldsymbol{\lambda}^T \left[\mathbf{S}\mathbf{x} - \mathbf{y} + \mathbf{e}\right] \tag{12}$$

The necessary conditions for an optimum solution are obtained by requiring that the partial derivatives of the objective function (L) with respect to **x** and **y** are zero:

$$\frac{\partial L}{\partial \mathbf{x}} = \mathbf{0} \tag{13}$$

$$\frac{\partial L}{\partial \mathbf{y}} = \mathbf{0} \tag{14}$$

We can solve for the optimal values of **x** and **y**, which determine the best estimates for both the parameters and responses. For the best estimates, the covariance matrices have reduced uncertainties:

$$\mathbf{C}_{\hat{\mathbf{a}}\hat{\mathbf{a}}} = \mathbf{C}_{\mathbf{aa}} - \mathbf{C}_{\mathbf{xx}} \tag{15}$$

$$\mathbf{C}_{\hat{\mathbf{q}}\hat{\mathbf{q}}} = \mathbf{C}_{\mathbf{rr}} - \mathbf{C}_{\mathbf{yy}} \tag{16}$$

$$\mathbf{C}_{\hat{\mathbf{a}}\hat{\mathbf{q}}} = \mathbf{C}_{\mathbf{ar}} - \mathbf{C}_{\mathbf{xy}} \tag{17}$$

PUBLICATIONS

F. Aminzadeh, J. Barhen, C. Glover, and N. Toomarian (1999). "Estimation of Reservoir Properties Using a Hybrid Neural Network," *Computers and Geosciences* **24**, 49-56.

J. Barhen, R. Cogswell, and V. Protopopescu (2000). "Single Iteration Training Algorithm for Multilayer Feed-Forward Neural Network," *Neural Processing Letters*, **11**.

J. Barhen, D. Reister, and V. Protopopescu (1999). "DeepNet: An Ultrafast Neural Learning Code for Seismic Imaging," *Proceedings of the International Joint Conference on Neural Nets*.

E. Oblow. "SPT: A Stochastic Tunneling Algorithm for Global Optimization," *Journal of Global*

Optimization (in press, 2000).

V. Protopopescu and J. Barhen (1999). "Ultrafast Neural Learning for Intelligent Data Representation," *Proceedings of the Conference of Information Systems Analysis and Synthesis*.

D. Reister, E. Oblow, J. Barhen, and J. DuBose. "Global Optimization to Maximize Stack Energy," *Geophysics* (in press, 2000).

David B. Reister, Edward M. Oblow, Jacob Barhen, and John B. DuBose, Jr. (1999). *Application of Global Optimization to the Estimation of Surface-Consistent Residual Statics*, ORNL-1999/102,Oak Ridge National Laboratory, Oak Ridge, Tenn.

J. Barhen and N. S. V. Rao. "Information Fusion Method for System Identification Based on Sensitivity Analysis," *Third International Conference on Information Fusion* (in press, 2000).

N. S. V. Rao, D. B. Reister, and J. Barhen. "Fusion Method for Physical Systems Based on Physical Laws," *Third International Conference on Information Fusion* (in press, 2000).

FUNDAMENTAL CHEMISTRY OF HEAVY OIL

W. V. Steele

INTRODUCTION

Catalytic hydroprocessing continues to be the core method for upgrading of feedstocks with high aromatic content. European environmental organizations have already established standards in this area and the United States is expected to follow in the near future. The reduction of aromatics in heavy petroleum upgrading will require careful management of hydrogen during hydroprocessing. Effective hydrogen management requires an understanding of the relationship between the distribution of the hydrogenated products in the process streams and the conditions of their formation (i.e., temperature and pressure).

To counteract the adverse effects of carbon rejection methods, refiners have the option of hydrogen-addition (hydroprocessing) methods. However, hydroprocessing consumes large quantities of hydrogen. As refineries reconfigure to produce the new "clean fuels" ["reformulated fuels" (i.e., those with oxygenates present], hydrogen shortages are occurring, and new sources of supply are required. The addition of oxygenates to gasoline means that less octane is required from the reformer, lowering the severity of the operation and the amount of hydrogen formed. Also, the mandated reduction of aromatics content by the U.S. government in the 1990 Clean Air Act Amendments has resulted in a further reduction of reformer operating severity, hence, severely reducing hydrogen production. Other contributions to the problem in managing hydrogen result from mandated lower gasoline temperature endpoints and reduced sulfur levels. Hence, the use of hydrogen exactly where it will "do the most good" is paramount. Overhydrogenation will have to be minimized.

DISCUSSION OF CURRENT ACTIVITIES

BACKGROUND

Worldwide demand for petroleum products continues to expand as the nations develop. However, if the demand is analyzed in terms of the three major classes of petroleum cuts (light products such as gasolines and petrochemical feedstocks, middle distillates such as jet fuels and diesels, and heavy products such as fuel oils and lubricants), then there has been a drastic shift in emphasis toward the light end. Whereas in 1972 both the light products and the middle distillates accounted for approximately 30% by mass of the market, by 1990 they had each risen to approximately 36% of the market. Analysts believe

that by the turn of the century the light products will have 38%, the middle distillates 40%, leaving only 22% for the 1973 major component the heavy ends.

Within the petroleum industry, catalytic hydroprocessing continues to be the core method for upgrading of feedstocks with high aromatic content, as well as for heteroatom removal through HDS and HDN. The 3-day symposium "Recent Advances in Heteroatom Removal" presented at the Division of Petroleum Chemistry meeting as part of the ACS biannual meeting held in March 1998 in Dallas demonstrated extensive interest by the petroleum and catalysis industries in this area. In a review of fuel-quality specification for transportation fuels, Touvelle et al. of Exxon Research and Engineering discussed trends in the regulation of aromatics in fuels. Although benzene content is carefully scrutinized, the total aromatics content is not regulated specifically in the United States. In contrast, European environmental organizations have already established standards in this area, and the United States is expected to follow in the near future.

The reduction of aromatics in petroleum, and particularly in heavy petroleum, will require careful management of hydrogen during hydroprocessing. Effective hydrogen management requires an understanding of the relationship between the distribution of the hydrogenated products in the process streams and the conditions of their formation (i.e., temperature and pressure). To meet this need, a dual-track approach is proposed, involving both state-of-the-art property measurement and advanced *ab initio* computations.

The property measurement program previously funded by DOE Fossil Energy in Oklahoma has accumulated extensive results for partially hydrogenated two-, three-, and four-ring aromatics. The majority of these results have not been published, particularly those that allow calculation of hydroaromatic distributions under processing conditions. *Ab initio* computational coding is in its infancy in this area. Accurate atomistic modeling of hydroaromatic systems will use the codes and techniques we have developed for parallel molecular simulations on the ORNL Paragons and other parallel supercomputers. Using our simulation capabilities, we believe we can substantially surpass the best prior efforts in realism and quantitative, predictive accuracy. These simulations will build on existing ORNL world-class efforts on simulating high-temperature liquid and supercritical aqueous systems.

The experimental database and the fundamental understanding from the simulations will be brought together to develop useful models for correlating data and predicting stability under hydroprocessing conditions. The two fundamental questions to be address in this research are (1) What are the "ideal conditions" for meeting low aromatics levels and still meet criteria such as sulfur levels and smoke point? and (2) How does the model react to changes in the complex heterogeneous and multicomponent systems, such as the addition to the refinery of a new crude oil from different source (such as Nigeria)?

Results from this research will allow the industrial participants to lead the field in catalyst development and process condition controls in processing, particularly in processing middle distillates.

It can be anticipated that severe operating conditions such as high temperatures, low space velocities, and high pressures can be mediated as the result of insights developed within the program. For example, at low temperatures and high space velocities, the amount of monoaromatics in the product can be higher than that in the original feed. This is not unexpected since every mole of triaromatic compound that is saturated would add a mole to the diaromatics, and each hydrogenated diaromatic compound would add a mole to the monoaromatic category; as the number of rings decreases, the rate of saturation should also decrease. Interaction between the various options can be simulated in the mode,l and options such as increased catalytic activity can be balanced again two- or even three-stage process designs.

PROGRESS

Funding for this new task was not received in the ORNL Financial Plan until late in FY 1999. Hence this section will mainly address the planned research program. The proposed research program will consist of three phases.

In Phase 1 (FY 2000), an initial literature search is being performed to ascertain the relative importance of various aromatic compounds and sulfur-containing compounds in the range of heavy petroleum being imported to refineries in the United States. Emphasis will be placed on finding the degrees of condensation and substitution of the compound types. The results of the study will be used to define the scope of the experimental work and the reaction schemes to be studied. Available literature data are being collected, and process conditions are being defined where applicable. Properties for the majority of the species have not been published in the open literature, particularly those that allow calculation of hydroaromatic distributions under processing conditions. Hydroaromatic distributions will be derived where possible, and a list of gaps in the database will be highlighted. Phase 1 will conclude with the reporting of sets of compounds to be studied to widen the applicability of the derived correlations.

In Phase 2, the gaps in the database will be the subject of property measurement or calculation using *ab initio* computations. Accurate atomistic modeling of hydroaromatic systems will use the codes and techniques we have developed for parallel molecular simulations on the ORNL Paragons and other parallel supercomputers. Using our simulation capabilities, we believe we can substantially surpass the best prior efforts in realism and quantitative, predictive accuracy.

In Phase 3, the measured properties will be used to derive extended correlations for the optimum processing of heavy crudes. In consultation with the petroleum industry, selection of candidate catalysts for operation within the optimum process-condition windows will be pursued. In tandem, idealized process conditions and catalyst selection will both be optimized simultaneously (the only limitations are of a kinetic nature).

DETERMINATION OF ESSENTIAL THERMOPHYSICAL PROPERTIES FOR SUSTAINABLE ENERGY

W. V. Steele

INTRODUCTION

This activity is focused on the determination of thermophysical and thermochemical property measurements on hydrocarbon systems. This will include pure components as well as mixtures and spans the range of hydrocarbon mixtures from natural gases to crude oils. One of the major initial focus areas will be wax-point determination. To aid in that accomplishment, DOE Fossil Energy has agreed to partially fund the acquisition of an acoustic cavity resonance spectrometer (ACRS) for experimental measurement of thermophysical properties. The ACRS has the capability to accurately and cost-effectively obtain a wide variety of essential thermophysical properties for physical properties databases, computational molecular science modeling, and, ultimately, commercialization of industrial processes. Planning the moving and re-establishment of DOE-owned thermophysical and thermochemical equipment from Oklahoma to ORNL is included within the scope of work for this project.

The scope of the FY 2000 work includes (1) acquisition and modification of the ACRS, (2) establishment of a suite of laboratories for the measurement of thermophysical properties of heavy oil components, and (3) using the ACRS for the measurement of thermophysical properties for wax point determinations in systems typical of underground petroleum reservoirs. Advanced computational techniques will be used to predict the thermophysical properties measured by the ACRS. This will serve as a mechanism to improve and validate the models of intermolecular potential energy used in molecular simulations that are otherwise exact. The ultimate goal is to be able to rely substantially or entirely on computational results when necessary.

DISCUSSION OF CURRENT ACTIVITIES

BACKGROUND

Worldwide demand for petroleum products continues to expand as the nations develop. However, if the demand is analyzed in terms of the three major classes of petroleum cuts (light products such as gasolines and petrochemical feedstocks, middle distillates such as jet fuels and diesels, and heavy products such as fuel-oils and lubricants) then there has been a drastic shift in emphasis toward the light end. Whereas in 1972 both the light products and the middle distillates accounted for approximately 30%

by mass of the market, by 1990 they had each risen to approximately 36% of the market. Analysts believe that by the turn of the century the light products will have 38% and the middle distillates 40%, leaving only 22% for the 1973 major component the heavy ends.

The development of methods for refining light crudes required property data on a relatively narrow set of compound classes for which data up through a carbon number of about C_{10} were carefully evaluated and correlated. The data evaluation was undertaken in the American Petroleum Institute (API) Project 44. Those data have been incorporated in a number of correlations devised and used by chemical engineers in process development in the petroleum industry in the manufacture of our present fuel slate. Those data also have been used as the basis of numerous computations derived to estimate the properties of related compounds for which data have not been measured. The fruits of Project 44 have ensured a petroleum industry operating at 95% thermal efficiency with light crudes.

Whether it is an East Coast refinery importing crude oil from Nigeria, or a U.S. Gulf Coast refinery importing crude oil from Saudi Arabia, or even a U.S. West Coast refinery operating on Alaskan North Slope crude, over the last decade or more for which records are available (1986-96), the quality of the crude oil processed by refineries has declined. If the decline in the quality of crude processed in U.S. refineries is denoted in terms of the API gravity, the gravity has decreased by an average of 0.15° per year in the decade 1986–95.[1] Furthermore, the decline appears to have accelerated back to the rate applicable in the early 1990s. Measured as a five-year average (1989–93), the API gravity had declined by 0.22° per year. After leveling at 31.3° for the next four years, in 1996 it was back on the line pointing to a value of 30.5° for the API gravity in the year 2000. As the API gravity of crude oil falls, the aromatic content (carbon content) increases and the correlations derived for the light crudes begin to breakdown. The failure of the correlations is well documented in the literature. New or revised correlations are necessary for continued high thermal efficiency in the refining of present and future crudes.

The heavier crudes contain more carbon, oxygen, sulfur, and nitrogen (polycyclic aromatics and heteroatom-containing compounds) than the benchmark West Texas Intermediate. These heteroatom-containing compounds are difficult to remove. Processing crudes containing increasing levels of oxygen, sulfur, and nitrogen using present-day technology has produced fuels with high heteroatom contents and a tendency toward instability. The refractory nature of the heteroatom-containing compounds is the main reason for the increase in coke production. Using heavy oil to make quality transportation fuels requires an understanding of the chemistry and the thermodynamics of adding hydrogen to the feedstocks. The major goal of this research project was to aid in that understanding.

WAX POINT DETERMINATIONS

Wax formation and deposition in pipelines and process equipment results in significant operational difficulties for the petroleum industry. The understanding of the crystallization of paraffin deposits from selected crude oils and the relationship of paraffin inhibitor structure to performance are essential to develop improved classes of inhibitors to reduce the production costs in the early stages of the petroleum production from some deep- and ultra-deep-water wells. Although it is known that the paraffin deposits are formed from long straight-chain alkanes that can crystallize from the crude under some conditions of temperature, pressure, composition, and shear rate, conventional molecular simulations have failed to give significant insight into this behavior, mainly because of the prohibitive computational costs for the systems required for realistic modeling. However, with recent advances in computer hardware and computational techniques to study such systems, it is now possible to tackle these large problems in a reasonable time period.

ACRS DEVICE

The ACRS is a novel instrument that appears to have broad application and to provide higher degrees of accuracy over wide ranges of pressure and temperature than conventional methods of determining physical properties. The literature on the ACRS promotes that it can precisely measure many thermophysical properties of materials that are required in recovery, separation, and processing (e.g., heat capacities, dew points, bubble points, viral coefficients, vapor pressures, critical points, solubilities, and diffusion coefficients). It can maintain temperature to within 0.001 K, pressures to within 0.005 psia of the setpoint, and system volumes to within
1 microliter while operating over a broad range of temperatures and pressures (typically 100-700 K and 0-25,000 psia). In addition, it is much faster and easier to use than more traditional instruments.

PROGRESS

During the period April 1998 to March 2000 the activities within this project have shifted from acquisition of the ACRS, preparing laboratory facilities to house the thermophysical property measurement equipment from the previously DOE-owned Oklahoma site, obtaining key staff, moving and setting up the equipment, to bringing the equipment on-line ready for calibration and then experimental measurements.

Last fiscal year arrangements were completed to acquire the ACRS from Phillips Petroleum Company, Bartlesville, Oklahoma. The ACRS was collected from Phillips at the end of December 1998 and was shipped to Florida University (Professor Colgate) for refurbishment. Modifications including the implementation of updated computing techniques for instrument control via LABVIEW were completed by December 1999.

To accommodate the equipment from the previous DOE Oklahoma site, and the ACRS, four (4) rooms within Building 4501 at ORNL were refurbished in FY1999. Refurbishment included decommissioning two of the rooms previously under radiation restrictions. Three (3) of the rooms required removal of benches, hoods, and sinks to accommodate the specialized equipment. The fourth room required installation of a new HVAC, floor, ceiling, lights, and sprinkler system. ORNL program development funds were secured for the refurbishment. Work in the area was completed by the end of 1999.

At that time the equipment from the Thermodynamics Section of what was the National Institute for Petroleum and Energy Research (NIPER) in Oklahoma was dismantled, packaged, and shipped in two tractor-trailers to ORNL. On arrival the equipment was allocated to the laboratory space and the required facilities (water, vacuum, blanket gas, and electric power requirements) were made available for each piece of equipment.

To aid in the installation of the "one-of-a-kind" equipment and instrumentation, Stephen E. Knipmeyer was contacted and agreed to spent some time at ORNL in early 1999. Steve was a Senior Experimentalist for over 20 years responsible to construction and maintenance of the majority of the equipment when it was in operation in Oklahoma. During a 10 day period in February 1999 the most the "skeletons" of the equipment was assembled within the laboratory complex. As of the end of the reporting period all the equipment has been reassembled and work on assuring that it meets ORNL Safety Codes was initiated.

Initial efforts at equipment calibration focused on Laboratory 110 where refurbishment was completed first. The Differential Scanning Calorimeter (DSC) was recalibrated. Physical property measurements for a DOE non-Fossil Energy project using the DSC proved very successful initiating moves to make the laboratories a DOE User Facility (see below). Also in Laboratory 110, the rotating-bomb combustion calorimeter was refurbished and passed ORNL Electrical Safety Codes. Initial tests on the constant temperature bath control system associated with the apparatus gave excellent results. Control within +/- 0.001 K over a period of 24 hours was obtained rivaling the best previous operation of the equipment.

Throughout the year (April 1999 to April 2000) other experimental techniques transferred from Oklahoma have came on line and have passed ORNL Safety Codes. Equipment for vapor pressure measurements includes 1) an ebulliometric system operating in the pressure range 2 to 260 kPa 2) an inclined frictionless rotating piston operating in the pressure range 0.010 to 3.5 kPa and 3) a torsion/mass loss Knudsen effusion system capable of measurements in the pressure range 0.0001 to 0.1 kPa. A vibrating-tube densimeter for the measurement of liquid-phase densities along the saturation line capable of measurements to temperatures greater than 600 K has been troubleshot and calibrated.

In the fall the thermophysical properties laboratories were designated a DOE User Facility. The full range of the equipment available at the Physical Properties User Facility and details on each individual

piece, including measurement type, range of property measurements, and application of results can be found on the World Wide Web at http://www.ornl.gov/divisions/ctd/pprf/ppgroup.htm.

FUTURE PROGRESS:

As of April 2000 the work under this project was rolled-up into that funded under FEAC309 "Fundamental Chemistry of Heavy Oil." Work to be continued in FEAC309 includes measurements to establish the ACRS's capabilities in wax point determinations, and testing to ascertain its range of measurement, accuracy and precision. The wax point determination effort will be directed at establishing the foundations for understanding the interaction of specific wax formation inhibitor - crude oil combinations. This will form a foundation for the subsequent modeling effort. In addition advanced computational techniques will be used to predict the thermophysical properties measured by the ACRS. This will serve as a mechanism to improve and validate the models of intermolecular potential energy used in molecular simulations that are otherwise exact. The ultimate goal is to be able to rely substantially or entirely on computational results when necessary. Results obtained will be of use to the petroleum production and refining industries in the development of new processes whilst invoking stringent pollution control, waste minimization, and environmental regulations.

REFERENCES

1. E. J. Swain, *Oil & Gas Journal,* November 10, 1997: pp. 79-82.

FUNDAMENTAL CHEMISTRY AND PROPERTIES OF IMPORTANT INDUSTRIAL CHEMICALS

W. V. Steele

INTRODUCTION

The purpose of the cooperative work between the Design Institute for Physical Property Data (DIPPR)® and the Thermophysical Property Group within the Chemical Technology Separations Group at ORNL is to develop thermodynamic and thermophysical property data for use in leading-edge chemical technology. The property measurements are directed by the DIPPR Project Steering Committees responsible for Project 821, "Pure Component Liquid-Phase Vapor Pressure Measurements," and Project 871, "Pure Component Ideal-Gas Enthalpies of Formation." The objective of Project 821 is to obtain precise and accurate liquid-phase vapor pressure data for selected pure components. The objective of Project 871 is to measure the enthalpies of combustion and to derive the enthalpies of formation in both the condensed and the ideal-gas phases of "key" compounds that have been chosen to elucidate the enthalpy of particular atomic groupings. These group contributions can then be used to estimate data on large families of related compounds, each containing that particular atomic arrangement.

DIPPR, now in its twenty-second year of funded research, is the oldest of the America Institute of Chemical Engineers' (AIChE's) active Industry Technology Alliances. In 2000, DIPPR has 31 sponsors from industry and government bodies. Its purpose is to make possible, through joint sponsorship, thermophysical property data measurement, correlation, and dissemination. The objective of DIPPR® is to develop the world's best set of critically evaluated thermophysical and environmental property data to satisfy industry needs. Data developed in DIPPR projects have become the data of choice for leading chemical process simulators and are used throughout the world. To quote from Dr. Mary Good (then Senior Vice President, Technology, AlliedSignal, Inc.),

> The US chemical process industry had a record trade surplus of $19 billion in 1991, with indications it will be close to that for 1992 demonstrating its continued global leadership position. One of the key factors contributing to this is the development and use of leading edge chemical process technology. AlliedSignal has relied heavily on the DIPPR databases in design of its chemical and polymer processes, and finds great value in sharing the costs of developing and verifying data.

DISCUSSION OF CURRENT ACTIVITIES

BACKGROUND

DIPPR had conducted two experimental property measurement projects in Bartlesville, Oklahoma for over a decade:

- Project 821 - Pure Component Liquid Vapor Pressure, and
- Project 871 - Determination of Pure Component Ideal Gas Heat of Formation.

DIPPR describes these projects using the following words: "We use top national research facilities to carry out specific projects."

DIPPR's Project Steering Committees recognized the Bartlesville facility as the only remaining thermodynamics laboratory in the United States with the full-range capability to obtain the type and quality of data required by the sponsors. With the transfer of senior staff and equipment from Bartlesville to the Thermophysical Property Group within the Chemical Technology Separations ORNL the full range capability is maintained.

The project has been setup in the cooperative research and development agreement (CRADA) form with an initial lifetime of three years. Subcommittees comprised of DIPPR Project supporters, DOE Fossil Energy staff, and ORNL staff will decide at the annual AIChE/DIPPR meeting in November a list of compounds for study in the following year in each of the two Project areas. Compounds will be chosen to represent whole families containing the necessary functionalities and to facilitate extension of available databases, rather than to fulfill the specific needs of any one member company.

PROJECT 821 - PURE COMPONENT LIQUID VAPOR PRESSURE

While vapor pressures are important in themselves for characterizing chemicals to ensure that they meet specifications, to determine suitable storage conditions, and to meet safety considerations, they are also required for Material Safety Data Sheets (MSDSs) and other regulatory reporting such as the new Occupational Safety and Health Administration (OSHA) process safety requirements. One of their major uses, however, is to define reference states for vapor-liquid equilibrium and activity-coefficient calculations. Such calculations are requisite for the design of separation processes, particularly distillation. Vapor pressures are also used throughout chemical-engineering thermodynamics to calculate a wide variety of quantities, such as acentric factors, enthalpies of vaporization, and solubilities.

Under guidance of DIPPR 821 Project Steering Committee, the Thermophysical Property Group at ORNL will conduct measurements of vapor pressure for selected compounds. The vapor pressures will be determined over a wide range of temperatures and pressures, utilizing the specialized equipment obtained from Bartlesville. Pressures as low as 0.01 kPa (0.75 mm Hg) can be measured accurately using an

inclined-piston gauge apparatus. The upper range of pressure obtained is 270 kPa in a twin ebulliometric apparatus. The vapor-pressure data are fit to a wide-range vapor-pressure equation and are verified and compared with any existing measured or predicted data. Sample purities are checked, and the materials are usually purified if necessary. Critical temperatures, critical volumes, liquid-phase densities, heat capacities, melting points, enthalpies of fusion, and vaporization can be measured, and critical pressures can be derived. Stringent efforts are made to ensure thermodynamic consistency in the derived results so that the data can be used with confidence in a wide range of process development simulations.

PROJECT 871 - DETERMINATION OF PURE COMPONENT IDEAL GAS HEAT OF FORMATION

This project utilizes ORNL's unique capability for precise and accurate measurements of enthalpies of combustion of a wide range of organic and organometallic compounds. The evaluation of chemical plant safety has never been as important as it is today. The enthalpy of formation is the thermodynamic property most needed for evaluation of the energy hazard potential of an organic compound. A second-order group-contribution methodology for the calculation of ideal-gas properties has been outlined in detail in *Thermochemical Kinetics*.[1] However, the text lacks parameters for a number of important groups and correction terms for several important ring structures. Parameters for some structural groups were derived from data that have since been shown to be incorrect. In the absence of data, application of the methodology for the estimation of thermochemical properties for some important organic compound types is impossible. Whereas the condensed-phase enthalpy of formation of a compound is of greatest interest in the calculation of energy balances for a given chemical process, the enthalpy of formation for the ideal-gas state is of greatest interest in the general case. This single value can give sufficient information to enable estimations for a large group of compounds containing that molecular entity. In summary, the objective of this project is to expand the group-additivity method of calculation of thermodynamic properties by determining thermochemical data on compounds containing unique groups or atomic environments.

Under guidance of the DIPPR 871 Project Steering Committee, the Thermophysical Property Group at ORNL will conduct measurements of the energies of combustion and hence enthalpies of formation in both condensed and ideal-gas phases for selected compounds. Such other thermophysical property measurements as will be required to derive the ideal-gas enthalpies of formation will also be made. Stringent efforts will be made to ensure high purities of the samples studied since small levels of impurity can result in order-of-magnitude errors in derived enthalpies of formation.

For both Projects ORNL staff will analyze the data obtained with special regard to the development of correlations suitable for the estimation of the properties for wide families of like compounds.

Additionally, DIPPR and ORNL staff will develop impact statements of the results on pollution control, waste minimization, and environmental regulation and control. Results of these studies will be available to the chemical industry and the general public through the DIPPR's databases.

PROGRESS

As of the information cutoff date for this report, the lists of compounds for study in the first year of FEAC315 had just been formalized. Samples of each of the chemicals have been obtained, and purification via spinning-band distillation or (in case of solid samples) zone-refining are in progress. The property measurements are due to commence in early May 2000.

Results from earlier work completed at Bartlesville, Oklahoma, has cleared subcommittee review, and submissions are in preparation for publication in the *Journal of Chemical & Engineering Data*. The titles of the six submissions are as follows.

- DIPPR Project 821. Vapor Pressure of Organic Compounds of Industrial Interest. The 1995 Project Results. Vapor pressure, heat capacity, and density along the saturation line measurements for benzenamine, butylbenzene, sec-butylbenzene, tert-butylbenzene, 2,2-dimethylbutanoic acid, tridecafluoroheptanoic acid, 2-butyl-2-ethyl-1,3-propanediol, 2,2,4-trimethyl-1,3-pentanediol and 1-chloro-2-propanol. By W. V. Steele, S. E. Knipmeyer, and A. Nguyen.
- DIPPR Project 821. Vapor Pressure of Organic Compounds of Industrial Interest. The 1996 Project Results. Vapor pressure, heat capacity, and density along the saturation line measurements for e-caprolactam, pyrazine, 1,2-propanediol, triethylene glycol, phenylacetylene, and diphenylacetylene. by W. V. Steele, S. E. Knipmeyer, and A. Nguyen.
- DIPPR Project 821. Vapor Pressure of Organic Compounds of Industrial Interest. The 1997 Project Results. Vapor pressure, heat capacity, and density along the saturation line measurements for cyclopropane carboxylic acid, N,N-diethylethanolamine, 2,3-dihydrofuran, 5-hexen-2-one, perfluorobutanoic acid, and 2-phenylpropionaldehyde. By W. V. Steele, S. E. Knipmeyer, and A. Nguyen.
- DIPPR Project 871. Thermodynamic Properties and Ideal-Gas Enthalpies of Formation. The 1995 Project Results. Methyl benzoate, ethylbenzoate, (R)-(+)-limonene, tert-amylmethyl ether, trans-crotonaldehyde, and diethylene glycol. By W. V. Steele, A. B. Cowell, S. E. Knipmeyer, and A. Nguyen.
- DIPPR Project 871. Thermodynamic Properties and Ideal-Gas Enthalpies of Formation. The 1996 Project Results. Trans-Methyl cinnamate, α-methyl cinnamaldehyde, methyl methacrylate, 1-nonyne, trimethylacetic acid, trimethylacetic anhydride, and ethyltrimethylacetate. By W. V. Steele, A. B. Cowell, S. E. Knipmeyer, and A. Nguyen.

- DIPPR Project 871. Thermodynamic Properties and Ideal-Gas Enthalpies of Formation. The 1997 Project Results. 1,4-Diisopropylbenzene, 1,2,4,5-tetraisopropylbenzene, cyclohexanone oxime, dimethyl malonate, glutaric acid, and pimelic acid. By W. V. Steele, A. B. Cowell, S. E. Knipmeyer, and A. Nguyen.

REFERENCES

1. S. W. Benson, *Thermochemical Kinetics: Methods for the Estimation of Thermochemical Data and Rate Parameters*, 2d ed., New York: Wiley, 1976.

ADVANCED TECHNIQUE FOR IMPROVING THE BIOLOGICAL QUALITY OF PETROLEUM-CONTAMINATED SOILS

A. J. Stewart

INTRODUCTION

Project FEAC317 started in May 1999 with support by the U.S. Department of Energy (DOE) Fossil Energy Program, National Petroleum Technology Office, Tulsa, Oklahoma (Nancy Comstock, Project Manager). It provides data and technical guidance to Petroleum Environmental Research Forum (PERF) project 99-01, "Ecological Evaluation for Upstream Site Remediation," sponsored by Chevron (see http://www.perf.org/). Participants in PERF Project 99-01 currently include Chevron, Exxon, Phillips Petroleum, Texaco, and BP Amoco, in addition to DOE. Two other companies are expected to formally join PERF Project 99-01 soon, and the project is likely to involve participation of the Gas Research Institute (GRI) and the American Petroleum Institute (API). The objective of PERF Project 99-01 is, at this point, general: it is to develop and/or improve methods for ecological risk evaluations and assessments via the development of early exit criteria for excluding sites from ecological risk assessment, and using field surveys to determine appropriate cleanup standards for total petroleum hydrocarbons (TPH) or salts in site soils. Project FEAC317 began in May 1999 to determine what types of soil amendments might be used to improve the biological quality of oily soils found in petroleum landfarming operations.

Petroleum landfarms are sites where waste petroleum hydrocarbons are biotreated by direct application to the ground. The materials are tilled into the soil, along with nutrients, to encourage biodegradation of the hydrocarbons by soil microbes. Soil "bulking agents" and gypsum are usually applied as well, to improve ion balance and physical properties of the soil. One problem associated with petroleum landfarming is that while lower-molecular-weight petroleum compounds volatilize and/or are biodegraded efficiently, higher-molecular-weight petroleum compounds tend to biodegrade much more slowly. With continued applications of petroleum hydrocarbons to the landfarm soil, the net result is the gradual accumulation of high-molecular-weight petroleum compounds. These materials are not very toxic, but at high concentrations they can increase the soil's water repellency, which can in turn affect the growth of plants. As a result, bioremediated oily soils may be less productive than desired and may not support a diverse community of soil invertebrates. Ultimately, the concentration of petroleum hydrocarbons approaches the upper-bound permitted limit (typically 10,000 ppm as TPH). When this occurs, the landfarm can no longer be used for treating additional waste petroleum; alternative uses for the land are then desired. The perception is that regulators could be more willing to consider various alternative land-

use possibilities if the soils are of demonstrably good quality with respect to their ability to support communities of plants and soil invertebrates.

An early objective of project FEAC317 is to identify beneficial types of organic matter amendments that might be applied to an oily landfarm soil to hasten the soil's ecological recovery. Amendments of animal manures, for example, might encourage the development of sustainable populations of earthworms. By virtue of their tunneling and soil-working habits, earthworms can improve desirable soil properties, which in turn should expedite the rate and extent of the soil's ecological recovery. During this reporting period, our main effort has been on conducting laboratory experiments with an oily landfarm soil to explore these ideas.

DISCUSSION OF CURRENT ACTIVITIES

PERF Project 99-01 was formalized recently (see http://www.perf.org), and funding for FEAC317 became available in May 1999. Immediately, several drums of an oily landfarm soil (and one drum of noncontaminated reference soil) were sent to ORNL for testing. We sent samples of the landfarm and reference soils to a contract laboratory for analysis of a suite of physicochemical properties, then conducted seed germination tests and earthworm soil-preference tests to initially judge soil biological quality. We then conducted an experiment to determine the relative (biological) merit of five different organic amendments, by use of an earthworm survival, growth, and reproduction test.[1]

During June through August 1999, a community college student (Ms Susan Humphries; Midlands Technical College, Columbia, South Carolina) worked on the project at no cost to FEAC317. Her stipend was provided by the DOE's Community College Initiative (CCI). A manuscript summarizing the results of her summer research project was prepared, sent to petroleum industry representatives for review, and then submitted to *Environmental Toxicology and Chemistry* for peer review and publication.[2] Near the end of her internship program, Ms Humphries was selected as a CCI-participant representative from ORNL; she participated in a CCI program review at DOE Headquarters in Washington, D.C., in August 1999.

The seed germination tests were inconclusive: germination rates of the seeds were low, both in the landfarm soil and the reference soil, for all four high-desert plant species we tested. We found that earthworms avoided the landfarm soil and preferred the reference soil, in 24- and 48-hour two-soil choice tests. Although earthworm (21-day) survival was high in non-amended landfarm soil, they did not reproduce. But when the landfarm soil was amended (10% on a dry mass basis) with cow manure, horse manure, or sheep manure, earthworms survived and reproduced. Earthworms did not reproduce in landfarm soil that had been amended with either tall fescue grass tissues or pulverized tulip poplar leaves (also on a 10% dry mass basis). This outcome suggests that some types of organic amendments may

measurably improve the biological quality of the landfarm soil, as assessed by earthworm survival and reproduction. An experiment now in progress will place the landfarm soil more definitively into a biological quality context by comparing earthworm survival, growth, and reproduction in landfarm soil (diluted to a 70% concentration with reference soil), a commonly used artificial soil, and a commercially available topsoil.

We also made progress on task 2, an economic cost-benefit analysis for the use of organic amendments to improve the biological quality of landfarm soils. Activity on this task consisted of preparing an extended outline of issues that will need to be addressed to determine (1) which amendment techniques meet or exceed the criteria for success, and (2) the cost of each amendment technique. The outline was sent to PERF Project 99-01 industry representatives for review in February 2000.

During April 13 and 14, 2000, the project's principal investigator attended a PERF Project 99-01 technical meeting in Houston, Texas.

REFERENCES

1. M. H. Gibbs, L. F. Wicker, and A. J. Stewart. 1996. "A Method for Assessing Sublethal Effects of Contaminants in Soils to the Earthworm, *Eisenia foetida*,"*Environ. Toxicol. Chem*. 15:360-368.
2. S.S. Humphries, K.D. Gwinn, and A.J. Stewart. 2000. "Effects of Endophyte Status of Tall Fescue Tissues on the Earthworm, *Eisenia foetida*," *Environ. Toxicol. Chem*. (manuscript submitted).

STRATEGIC PETROLEUM RESERVE PLANNING AND MODELING

P. N. Leiby

INTRODUCTION

The Strategic Petroleum Reserve (SPR) is a government-owned stockpile of crude oil intended to serve as a buffer against possible oil market disruptions. The overall purpose of this project is to assist with SPR planning and management, through the development and application of improved models and tools. Current project efforts emphasize developing new modeling tools to explicitly and flexibly portray oil market uncertainty and SPR planning risk.

DISCUSSION OF CURRENT ACTIVITIES

Oak Ridge National Laboratory (ORNL) conducts model development and planning analyses for SPR drawdown, distribution, and other management activities in support of the Office of Management Operations, Petroleum Reserves. The roles and objectives are

1. to evaluate SPR planning alternatives and roles of SPR;
2. to support development of SPR oil valuation and bid-analysis tools;
3. to evaluate potential applications of DIS-Risk model approach to related energy policy issues;
4. to study role and value of risk information in SPR planning;
5. to utilize, maintain, modify, and report on SPR analysis models; and
6. to provide analytical support for the SPR office.

ACTIVITIES THIS YEAR

Study of the Merits of Expanding the U.S. Strategic Petroleum Reserve Completed

The world oil market has endured at least 18 significant oil supply shocks since 1951. The most memorable of these, the four largest world oil shocks between 1973 and 1991, are now recognized to have cost the U.S. economy hundreds of billions of dollars. These costs occurred as lost gross domestic product (GDP) and as higher payments for oil imports. Since oil is traded globally, a major oil price increase soon spreads throughout the world, with disruptive effects on most energy-using economies. Within each economy, the shock costs are spread economy-wide. For this reason, oil-using firms and private consumers acting individually on their own behalf do not have sufficient motivation to take the actions necessary to adequately ensure against the widespread costs of price shocks. Most of the economy-wide costs of disruptions are, understandably, “external” to the cost-benefit considerations of

private agents. Private agents cannot justify holding large oil stocks for the long term as a contingency against unlikely but potentially dramatic market upheavals or geopolitical struggles. Thus, it may be more efficient for the U.S. government to hold strategic oil reserves since private agents are either unwilling or unable to do so. Strategic oil stocks, by buffering supply losses and mitigating sudden major price shocks, are a direct and effective means for dealing with the risk to economies of persistent supply and price volatility.

This study evaluated the estimated net benefits of expanding U.S. strategic oil stocks from the current 580 million barrel (MMB) size, and analyzed the efficient reserve size. It recognized that substantial strategic oil reserves already exist, both in the United States and elsewhere. An assessment of alternative U.S. reserve sizes was done with a numerical simulation model and a probabilistic cost-benefit analysis.

The analysis indicates that a substantial addition to U.S. reserves is worthwhile under a wide range of conditions (see Fig. 1), including a number of conditions ordinarily unfavorable to strategic storage. The results provide convincing support for at least filling the existing unused SPR capacity (i.e., filling the reserve to its current capacity of 700 MMB). This is because the currently unused facilities represent a substantial and valuable investment and because the next few years may present an opportunity to acquire oil at a comparatively low price.

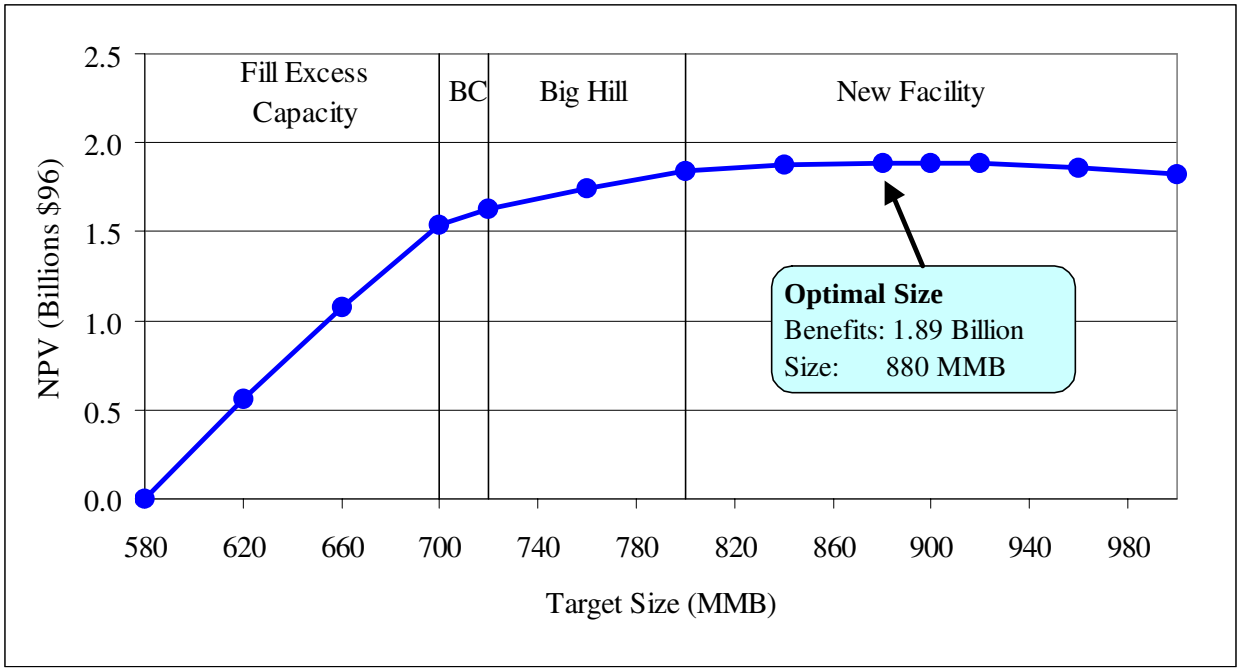

Fig. 1. Base case results: net economic benetfis of expanded U.S. strategic oil storage. (Mid-case inputs. For details, see Leiby and Bowman 2000.)

The results on efficient size are certainly robust for variations in GDP elasticity up or down by 30%, or within one standard error of the estimate. Perhaps surprisingly, if all other assumptions are held fixed, expansion to 700 MMB still yields benefits for variations in GDP elasticity of plus or minus 70%, or over two standard errors of the estimate.

The results may even underestimate the efficient expansion size because they presume that all of the existing global "strategic stocks" (both government-owned and government-controlled commercial stocks) will be promptly used and well-coordinated in the event of a disruption. They also only account for the specific economic consequences that we can easily include in the cost-benefit analysis, omitting other, less tangible or quantifiable, potential benefits

Finally, we can note that many other oil importing and consuming countries will benefit from the price-moderation effect of the U.S. reserve without in any way reducing the ability of the United States to benefit from its own stockpile investment. Rather than being a cause for concern, these "spillover benefits" provide added motivation for expanding the reserve because they assist many countries with which we have mutually beneficial trade and diplomatic relationships.

Economic Consequences of Expanding the Drawdown Capabilities of the SPR

An analysis of the economic consequences of expanding the drawdown capabilities of the SPR was begun. This study is considering a range of alternative drawdown rate capabilities for the U.S. oil reserve and their net economic benefit. The SPR draw capability expansion benefits will be estimated for some key sensitivities, notably GDP elasticity, the availability of slack (excess) supply capacity, and disruption length. This study should be completed in draft form by August 2000.

PUBLICATIONS

Paul N. Leiby and David Bowman, *The Value of Expanding the U.S. Strategic Petroleum Reserve*, ORNL/TM-2000/179, Oak Ridge National Laboratory, January 23, 2000.

Paul N. Leiby and David Bowman, "The Value of Expanding the U.S. Strategic Petroleum Reserve," presented at the 20th Annual USAEE/IAEE North American Conference, August 30, 1999.

Inja Paik, Paul Leiby, Donald Jones, Keiichi Yokobori, and David Bowman, "Strategic Oil Stocks in the APEC Region," April 6, 1999. Proceedings of the 22nd IAEE Annual International Conference, International Association for Energy Economists, Rome, Italy, 9-12 June, 1999.